Effects of carbonation on the pore structure of granulated blastfurnace slag concrete

Seppo Matala

Dissertation for the degree of Doctor of Technology to be presented
with due permission for public examination and debate in Auditorium R4
at Helsinki University of Technology (Espoo, Finland)
on the 19th of May, 1995, at 12 o'clock noon.

Helsinki University of Technology
Faculty of Civil Engineering and Surveying
Concrete Technology

Espoo 1995 - Report 6

Matala, S.P. 1995. Effects of carbonation on the pore structure of granulated blast furnace slag concrete. Espoo. Helsinki University of Technology, Faculty of Civil Engineering and Surveying, Concrete Technology, Report 6. 162 p. + app. 49 p.

UDC
Keywords: Concrete, slag, carbonation, Portland cement, microstructure, pore structure, porosity, low-temperature calorimetry, thermoporometry, mercury intrusion porosimetry, frost-salt resistance, models, durability, service life, deterioration.

ABSTRACT

The objective of the research was to characterize the pore structure and carbonation-induced changes in granulated blast furnace slag concretes activated by ordinary Portland cement used as a reference binder throughout the study. The secondary objective was to clarify the effects of aging-induced pore structure changes on the frost-salt resistance of concretes. The experimental program comprised tests with concrete, mortar, and paste samples cured and carbonated in different atmospheric conditions. The mixes were cast with water binder ratios from 0.35 to 0.75 with slag contents of 0, 50 and 70%. Compressive strength grades varied between 20 and 90 MPa. Low-temperature calorimetry, mercury intrusion porosimetry, thermogravimetry, gas analysis, infra-red spectroscopy, X-ray diffractiometry, and optical methods were used to characterize the pore structure and the microstructure in non-aged and aged states. A thermoporometric method was proposed for analysis of the results by LTC, enabling measurements of total porosity and pore size distribution in porous materials. Further research is needed to clarify the significant implications of uncertainties associated with semi-empirical calculation parameters. The LTC method allows the pore structure to be studied in its natural water-containing state. Changes in pore structure due to aging were clearly visible with LTC but only slightly detectable with MIP, where vacuum drying of the specimens dramatically alters the non-aged pore structure.

Carbonation had a marked effect on porosity and its distribution throughout the overall gel and capillary porosity. In the non-aged state GBFS showed a lower fine and higher coarse gel porosity than OPC. After carbonation the fine gel pore volume was fairly independent of the binder type. Capillary porosity increased more after carbonation the higher the slag content. OPC binder gave the highest decrease in total porosity. The results indicate a strong binder-dependent redistribution of porosity. In OPC mixes the increased capillary porosity is caused by a decrease in the finest gel porosity. In contrast, in GBFS blends reduction of the coarsest gel pores brings about a very clear increase in coarse capillaries. The gel structure and greater liability of GBFS concretes to carbonation of the CSH gel, and the lack of CH in GBFS mixes, were the main reasons for the coarsening phenomenon observed in GBFS concretes. Due to the lower amount of CH, GBFS compositions are more disposed to carbonation of the CSH gel, which transforms the initially relatively dense gel to a more porous silica hydrate gel. A high level of carbonation affects transformation of the CSH gel to SH gel in the inner slag hydrate. The dominant pore dimensions in the ISH gel before carbonation are typical for coarse gel pores, which reach the capillary pore dimensions after carbonation increasing the coarse capillary pore continuity in GBFS mixes. Permeability increases as a result. The lack of open pore space in the ISH gel prevents precipitation of carbonates in the gel, which remains permanently in its coarse state if further hydration is prevented.

The CH and CSH phases carbonate simultaneously, and there is evidence of compositional changes also in AFt and AFm phases. All morphologies of calcium carbonates; vaterite, aragonite and calcite are present in carbonated OPC and GBFS concretes, the vaterite content being higher in the latter, which reflects the differences in overall microstructures and hydration products. Enriched Mg^{2+} ions in the skeleton hydrate of GBFS compositions partly explains the higher vaterite amounts. Aging lowers the frost-salt resistance of concretes. This phenomenon is stronger in GBFS concretes. Rapid deterioration in the frost-salt test was explained by the gel and pore structural changes in the inner slag hydrate. Carbonation coarsens the densest part of the gel spaces in GBFS concretes, changing the gel porosity towards coarser capillaries, where water becomes freezable at moderate temperatures. The increased frost susceptibility of GBFS concretes is very difficult, perhaps impossible, to compensate by conventional air-entrainment. No threshold value for the allowed slag content in this respect could be presented.

Dedicated to the Memory of Finland
on her Last Independence Day
on December 6, 1994

PREFACE

This dissertation is part of a research project, started in 1990, on the pore structure characterization of by-product concretes in the course of aging processes, and on the effects of aging on the durability properties and service life estimation of ordinary and high strength concretes. Advanced research facilities at the Concrete Laboratory of Helsinki University of Technology, and the financial support of the Finnish National Road Administration, made this research possible. This work and its results could never have been realized without these organizations and without the cooperation in a free research atmosphere afforded and created by Professor Vesa Penttala, Mr. Mauno Peltokorpi and Mr. Ossi Räsänen, to whom I wish to express my sincere gratitude. The Jenny and Antti Wihuri Fund is gratefully acknowledged for its financial aid toward preparation of manuscript.

Professor Vesa Penttala afforded the appropriate balance between research and teaching work for this project. He provided encouragement and guidance throughout the work and offered most valuable assistance with tests in his special fields, the FTIR and EPMA methods. For these and for the revision and criticism of this report he is gratefully acknowledged.

I am grateful to Professor Erik Sellevold, of the Norwegian Institute of Technology, and to Professor Lars-Olof Nilsson, of Chalmers University of Technology, for their pre-examination of the report and for their valuable advice and criticism of it. I would like to thank so many Nordic researchers for their cooperation and for the stimulating discussions we have had on the durability problems of concrete over the years. Especially Mr. Erkki Vesikari, who will be remembered as one of the discoverers of the studied phenomenon, is most gratefully acknowledged for his interest in this work and for the inspiring and stimulating discussions through which he opened up this field to me twelve years ago.

The linguistic revision of the text was done by Mrs. Adelaide Lönnberg, to whom I am deeply grateful.

I wish to express my thanks to Ms. Leena Kallio, Mrs. Tarja Merikallio, Ms. Virpi Mikkonen and Ms. Sari Talla, and to Mr. Karri Mäkinen, Mr. Esko Varis and Mr. Juha Vähäkoski for their assistance in the project. Mr. Veli-Antti Hakala is greatly acknowledged for the valuable help he provided with the computer programming. Special respect goes to Mr. Jarl Lindholm who indefatigably and conscientiously tested 100 frost-salt series over three years, and to Mrs. Pipsa Vuolevi for the preparation of high quality thin sections.

Finally, the deepest gratitude is given to my wife Marjo. Without her patience and encouragement throughout these years, and without her significant financial sacrifice, this work could never have been attempted, let alone completed.

Seppo Matala

CONTENTS

APPENDICES:

NOTATION

AFm	Monosulfate phase
AFt	Trisulfate phase
A_{xy}	Area of the interphase x-y
C	CaO
$C\overline{C}$	$CaCO_3$
Calcite I	Vaterite polyform of calcium carbonate that transforms slowly in normal atmospheric conditions to calcite, and decarbonates at ordinary decomposition temperatures of well-crystallized calcite.
Calcite II	Vaterite polyform of calcium carbonate that transforms rapidly at around 500^o C to the calcite resembling polyform and decomposes at temperatures of 600^o C to 750^o C.
CaF	Degree of carbonation, Carbonation factor
CH	$Ca(OH)_2$
CoF	Coarsening factor
CSH	Calcium silicate hydrate
DTA	Differential thermal analysis
EDX	Energy dispersive X-ray spectrometry
EPMA	Phase map analysis by EDX element maps
EGA	Evolved gas analysis
ESEM	Environmental scanning electron microscope
FTIR	Fourier transmission infra-red spectroscopy
GBFS	Granulated blast furnace slag
H	H_2O
H_f	Heat flow
IR	Infra-red spectroscopy
ISH	Inner slag hydrate
LTC	Low temperature calorimetry
MIP	Mercury intrusion porosimetry
NMR	Nuclear magnetic resonance
OPC	Ordinary Portland cement
OSH	Outer slag hydrate
P	Pressure
R_n,r	Radius of ice nucleus
R_p	Pore radius
S	SiO_2 (chemical expressions), Entropy (thermodynamic abbreviations)
SAXS	Small angle X-ray scattering
S_{cap}	Degree of saturation
SH	Silicate hydrate
SHP	SH gel fraction of total solid gel
SKH	Skeleton slag hydrate
T	Temperature [^oK]
$\dot{T}$	Rate of block temperature change [$^oC/sec$]
TG	Thermogravimetry
TZ	Transition zone
UHS	Unhydrated slag
V,v	Volume
$V_{p,nf}$	Pore volume of w_{nf}

W_a	Solidification energy
W_a^f	Heat of fusion
WI	Water immersion test
W_{th}	Enthalpy
XRD	X-ray diffractometry

c	Specific heat
ca	Carbonation at RH 45%, aging treatment, also as subscripts
cy	Repeated drying and wetting treatment, also as subscripts
g	Weight of sample
s	Slag content
t_{ad}	Thickness of adsorbed water layer
t_{cap}	Saturation time at nick point in capillary test
w	Water content
w_{cb}	Chemically bound water
w_{nf}	Non-freezable water in LTC test

Subscripts:

f	freezable water at -20^{o} C
g	gas (thermodynamic state)
i	ice
l	liquid (thermodynamic state)
mc	micro capillarity (1.5 nm<R_p<4 nm)
mp	micropores (R_p<1.5 nm)
n	nucleation
nf	non-freezable water in LTC test at -63^{o} C
np	nucleation point
s	solid (thermodynamic state)
ssd	saturated surface dry state
tot	total
v	vapor
w	water

Superscripts:

bl	baseline
f	fusion
IM	iteration method
lbl	lower baseline
LM	linear method
s	solidification
ubl	upper base line

Ratios:

A/S	Al_2O_3/SiO_2 molecular ratio
C/S	CaO/SiO_2 molecular ratio
C/S+A	$CaO/(SiO_2+Al_2O_{3)}$ molecular ratio
H/S	H_2O/SiO_2 molecular ratio

M/S	MgO/SiO_2 molecular ratio
w/b	Water-binder ratio in weight

Greek letters:

ΔS_f	Entropy change
$\Delta S_{f_{sup}}$	Additional entropy due to superficial phase transformations
$\eta_{e_{sup}}$	Correction factor for additional entropy variation $\Delta S_{f_{sup}}$
η_{carb}	Correction factor for effect of carbonation on microporosity
α_x	Degree of hydration at age x days
ρ	Density
γ	Surface tension, surface extension energy
θ	Temperature depression [^{o}C] $=T-T_0$
δ	Thickness of liquid-like layer on ice sphere
η_C, η_H , $\eta_{S,}$	Correction factors for H_2O, CO_2 and SO_2 gases in TG/EGA test

1 INTRODUCTION

In recent years, fast rising total service life costs - including the costs of production, maintenance and use of structures - have elicited a number of research projects in the life cycle behavior of building materials. A case in point is a number of Finnish studies on the durability of slag concretes. Users of concrete found that knowledge afforded by research reports of projects sponsored by the producers did not include relevant research data for estimating the life cycle behavior of slag concretes. This gave birth to a series of research projects involving studies on the frost and frost-salt resistance of concrete. This long-term work was initiated and primarily supported for fifteen years by the Finnish National Road Administration, responsible for the construction, maintenance and use of most of the bridges in Finland. These projects resulted, in the mid-80s, in the first deterministic models by which the service life of bridge structures could be estimated, also with regard to frost action. VESIKARI's model comprised the calculation of the so-called frost resistance value, also with the use of industrial by-products such as fly ash, silica fume and granulated blast furnace slag.

In the first projects, where testing of the frost-salt resistance of granulated blast furnace slag (GBFS) concrete was performed traditionally at age 28 days, the binder behaved even better than ordinary Portland cement (OPC). VESIKARI repeated these tests with concretes exposed to normal atmospheric laboratory conditions for about 1 year and found an increase in the deterioration rate of slag concrete. This finding evoked a fresh series of research projects concerning the effects of curing and aging on the durability of by-product concretes. Again, abnormal deterioration was observed in the frost-salt tests with aged normal strength and high strength blast furnace slag concretes (MATALA 1988). Pore structural changes were also detected in this research. German studies reported changes in the pore structure of carbonated GBFS pastes that could partly explain the decreased frost resistance of aged GBFS concrete (BIER ET AL. 1987). LITVAN AND MEYER (1986) reported increased capillary porosity in GBFS concrete wall panels after 20 years of exposure time to natural climatic conditions, and expressed doubts concerning the frost resistance of GBFS concretes. Rapid deterioration was also observed in Canadian tests performed in a marine environment (MALHOTRA ET AL. 1987 and 1988).

Blast furnace slag has been used as an alternative binding material for Portland cement in concrete production for over 100 years. Several of its properties make it an excellent binder: A by-product of the iron industry, its price is clearly lower than that of clinker-based binders; its chemical resistance is good, especially to sulfates, and due to its low heat of hydration it is an appropriate alternative in massive structures.

In order to clarify the reasons for the unusual behavior of aged by-product concretes, the Finnish National Road Administration and the Concrete Laboratory of Helsinki University of Technology established a project focusing primarily on characterization of the pore structure in by-product concretes in the course of aging, and on the effects of aging on durability properties. Also included in the project were studies on the durability properties of silica fume concrete. These, however, are outside the scope of the present report, which deals only with GBFS. The studies with condensed silica fume represent roughly half the breadth of the project; their results, along with those needed for the service life estimation of GBFS concretes, will be presented elsewhere at a later date.

2 SCOPE OF THE RESEARCH

Pore structure can be regarded as a primary determinant for the durability of concrete. Its continuum controls the ingress of deleterious substances into concrete and its volume and distribution the behavior at low temperatures. Any concrete with extra low permeability and appropriate pore size distribution, and with the reasonable strength, can withstand severe climatic conditions. Unfortunately, the aforementioned properties are extremely difficult to achieve in practice. Concrete is a complex multiphase system where a chemically, physically and mechanically stable state cannot be achieved in reasonable time, even in a controlled environment, and never in real practice. Utilization of concrete material presumes that it must be taken into use in the "green" state in which the mechanical compatibility of different phases is far from perfect. Creep- and shrinkage-induced flaws at the paste aggregate interface and in a heterogeneous cement paste matrix cause a particular permeability of concrete. Thus another aging phenomenon, carbonation of cement paste, cannot be wholly prevented in concretes exposed to a climatic atmosphere.

Carbonation may alter the pore structure of concrete, and the extent of these changes may be associated with binder type. The scope of this investigation is limited to the study of carbonation effects on the pore structure of GBFS concrete activated by OPC, the latter being a reference material throughout the study. Different types of GBFS are not studied. The type used in this study is representative of the typical quality with high magnesia and low alumina content and high glass content produced by the Finnish iron industry.

Generally, carbonation can be defined as an aging process where dissolved or free carbon dioxide in pore solution or in pores attacks the unhydrated or hydrated products of cement, either by a through-solution process or by a topochemical process, changing the chemical, mineralogical, microstructural and pore structural characteristics of the binding component of concrete. As with all chemical processes in cement chemistry, carbonation is strongly dependent on the moisture state in the space of reaction. The process is controlled by the number of different time-dependent transport processes, which gives rise to testing problems. Carbonation reactions of hydrated and hydroxylated phases release water. This is important for further reaction in the liquid phase, but also a significant factor in the transformation of the gel structure. This, associated with drying in appropriate testing conditions, affects shrinkage-induced deformations in the cement matrix, leading to microstructural changes in the cementitous composition. Separation of carbonation effects from those of drying throughout the range of internal moisture states is experimentally possible, but the comprehensive experimental program required was not possible within the financial framework of this study. Thus carbonation was studied simultaneously with drying as a single aging process in experimental conditions of controlled moderate relative humidity and ordinary climatic CO_2 concentration.

Consideration of pore structural characteristics such as pore volume and pore size distribution are in the primary focus of study. The effects of carbonation on permeability were studied indirectly. In order to study how possible pore structural changes affect the durability of GBFS concretes, frost-salt scaling tests were performed to evaluate earlier results of laboratory tests. However, it should be pointed out that this investigation is not a comprehensive study of the frost or frost-salt resistance of GBFS concretes.

As the study covers only carbonation effects on the compositional changes of the microstructure and on the changes in the pore structure, a closer examination of carbonation models, compositional, environmental and geometric variables affecting carbonation, and the effect of carbonation on the mechanical and chemical properties of concrete are excluded. Instead, the rate of carbonation of GBFS and OPC concretes was studied in four different climatic conditions. The frame of this report outlines this interesting and important item for service life modeling. Carbonation depths were measured regularly during 4 years, but this time was considered too short for reliable modeling of the carbonation rate.

Selection of the methodology for measuring porosity is of great importance. Mercury intrusion porosimetry (MIP) is the method of choice despite of its limitations due to the sample preparation process. Low-temperature calorimetry was selected as a parallel test method, as no sample preparation is needed. Detected pore structural changes should therefore be considered in light of the limitations of these two methods.

3 REVIEW OF THE LITERATURE

The review of literature is divided into two parts, dealing with microstructure and carbonation respectively. The first part (3.1) looks at the microstructure formed in GBFS concrete activated by OPC - in fact by calcium hydroxide liberated during the hydration of alite and belite phases of clinker compositions. This part does not include slag concretes produced by other activators such as sodium hydroxide, sodium carbonate, sodium silicates or by the sulfate-comprising activators outlined in the scope of the study. The activator type has a significant effect on the hydration products formed, and evidently also on the overall gel structure obtained. Hence, the effects of different aging processes on the microstructure, and especially on the pore structure, differ from each other depending on the activator used in the production of GBFS concrete.

The microstructure of GBFS concrete is considered in non-aged concrete by comparison with that found in OPC concrete. First the overall gel structure formed during hydration process is examined. It is then looked at on the basis of morphologies, relevant molecular ratios of C/S, H/S, A/S and M/S, and the lime content, in order to describe the hydration products in OPC and GBFS concretes before aging. Finally, the porosity of non-aged GBFS concrete after wet curing regimes is discussed and compared with that observed in OPC concretes.

The second part (3.2) looks at carbonation reactions in unhydrated, hydroxylated and hydrated phases, and the gel structures formed after carbonation. Carbonation of CSH gel is discussed in more detail, and in this context recent models by SUZUKI ET AL. (1985), BIER (1988) and ATLASSI (1993) are presented. The effects of carbonation on the porosity of OPC and GBFS concretes are examined (3.2.6) followed by a discussion of the methods generally used in the identification of carbonates.

3.1 MICROSTRUCTURE OF SLAG CONCRETE

3.1.1 Development of the microstructure

Similarities in the overall microstructure of OPC and GBFS concretes can be seen in the existence of three well-defined regions in the binder pastes, and the presence of CSH gel in these areas. There is wide consensus to the separation of these regions as follows: 1) an area of inner hydration products formed within the original grain boundaries; 2) an area of outer or external hydration products formed between the grains; 3) an area situated in the interface between the binder paste and aggregate particles. Hydration products and their proportions formed in these regions differ depending on the chemical composition of the slag and cement.

The first defined region can be thought to form within the binder grain boundaries, where the morphologies of OPC and GBFS gel structures differ significantly due to differences in hydration kinetics. In OPC pastes the formation of shells around the clinker grains is the first eventual feature in the development of cement paste microstructure with regard to its later age properties. This shell is composed of CSH products and CH, and inward or outward extensions of ettringite needles or thin calcium monosulfate plates (DIAMOND 1987, p. 23). The space between the hydrated layer and the anhydrous grain is roughly 1 μm in the beginning, and is filled with highly concentrated solutions. With time the shell thickens and inner CSH forms between the shell and the anhydrous core. The inner hydrate consists of CSH gel, small quantities of CH, and AFm rather than AFt phases which are reported to exist outside the shell in the outer hydrate and in transition zones (SCRIVENER 1989, pp. 137 and 139).

The outer hydrate between the grains starts to form in OPC pastes when the shell is open and porous, allowing the migration of ions through it. CSH gel, CH and AFt phases are the primary products in this paste region forming a porous irregular network between the grains that densifies during hydration. The morphology of the inner and outer CSH gel differs clearly (REGOURD 1987, p. 188).

In the third more or less well-defined region between the outer hydrate and aggregate particle, CH is deposited in large quantities in the transition zone. This interfacial region of thickness between 25 - 50 μm is thought to form because the large anhydrous cement grains cannot pack close to the aggregate particles (SCRIVENER 1989, p. 151). CSH formed in the transition zone results from the hydration of the smallest cement particles. The area is enriched with AFt phases and is reportedly the most porous region in cement paste.

Development of the microstructure in GBFS binder differs from the above process of hydration of pure clinker grain. The glassy slag hydrated in OPC forms first a layer of Portland cement hydrates on its surface, followed by the formation of a so-called inner hydrate layer due to the attack of Ca^{2+} ions and alkali metal ions from the supersaturated solution (TANAKA ET AL. 1983, p. 969). The inner hydrate layer comprising well-crystallized hydrates becomes denser; the diffusion of Ca^{2+} ions from outside slows down, and the dissolution of Ca^{2+} and Al^{3+} ions from the unhydrated slag is accelerated. These ions are partially bound in the hydrated layer and also move to the outside aqueous phase, taking part in the formation of the outer hydrate. The surface layer of the slag particle transforms gradually into the inner hydrate by the supply of Ca^{2+} ions, developing a crystallized and dense structure. The Ca/Si ratio has been observed to be higher in the outer than in the inner hydrate, and lowest in the surface layer where concentrations of Al^{3+} and Mg^{2+} ions are highest (REGOURD 1987, p. 191). Mg-rich phases at the border of the inner hydrate have also been reported by FENG ET AL. (1989, p. 266). The space left by the original anhydrated slag particle is assumed to be occupied by the hydration products of the inner hydrate, the hydrates of the skeleton hydrated layer on the surface of the unhydrated slag, and the residual unhydrated slag grain. Once the slag grain is consumed totally, the innermost portion of the inner product forms a porous network consisting mainly of hydrotalcite (GLASSER 1989, pp. 67-68).

Hydration products formed during the hydration of GBFS/OPC blends are CSH, AFt and AFm phases, and hydrogarnet and hydrotalcite-like phases. Mixed forms of calcium aluminate and calcium magnesium hydrates have also been reported (GLASSER 1989). All these phases are not necessarily present in the same paste.

3.1.2 Gel structure

Morphology

Several morphologies for CSH have been described. Perhaps the most well-known classification is that into four groups as presented by Diamond (REGOURD 1987, p. 191). In OPC pastes the first two, Type I CSH and Type II CSH, represent morphologies existing at early ages and are of lesser importance when later age properties are considered. The outer CSH gel is typically in thick lath-shaped layers or has a fibrous resemblance, as in types I and III CSH at Diamond's classification. The inner CSH gel produced within the original grain boundaries is reported probably to form small discs or spheres closely resembling types III and IV of DIAMOND's classification. In any case, the CSH gel formed inside the shell is denser and more compact than the outer CSH gel in hydrated OPC paste.

In GBFS paste similar morphologies of CSH have been reported. In the porous space of the skeleton hydrate, Type III CSH exists together with hydrotalcite (REGOURD 1987, p. 191). Obviously the inner slag hydrate layer comprises dense and compacted Type IV CSH together with AFm phases as hexagonal plates. Also Type II CSH morphology has been observed in GBFS pastes.

Structure

Similarities in hydration products between OPC and GBFS concretes are joined by the existence of CSH gel in both materials. CSH is the principal hydration product in GBFS concretes produced by different methods although its amount and composition may vary with the choice of activator.

The structure of CSH is not fully explained. According to the Feldman-Sereda model, the gel is formed of CSH sheets with structural interlayer water and with adsorbed physically bound water on the surfaces. The CSH sheets are poorly crystallized, partly polymerized silicon tetrahedras connected with Ca^{2+} and OH^- ions as in tobermorite-like material. Distances between layers vary between 11 and 19 Å for 1.1-nm and 1.9-nm tobermorite gels, respectively. In jennite-like gel the layer thickness is reported to be 1.05 nm. In molecular ratios of C/S and H/S, CSH(I) is close to that of 1.4-nm tobermorite ($C_5S_6H_9$) and CSH(II) to that of 1.05-nm jennite ($C_9S_6H_{11}$) (TAYLOR 1990, p. 142).

Comparison of primary molecular ratios gives a particular description of the gel structural differences between OPC and GBFS pastes. According to TAYLOR (1990, p. 284), in OPC blends the Ca/Si ratio varies from 1.7 to 2.0 and in GBFS blends from 1.55 to 1.79. These ratios are markedly dependent on the age of the composition. E.g. REGOURD ET AL. (1983, p. 851) have reported a Ca/Si ratio of 1.55 for a 28 day old paste made with a cement containing 30% granulated slag with a water-binder ratio of 0.50. Correspondingly UCHIKAWA ET AL. (1991, p. 536) gives a value of 1.5 for a 91 day old paste having 50% slag content and a water-binder ratio of 0.50 and 1.8 for pure OPC paste. TANAKA and coworkers studied hydration products on the surface of a slag particle hydrated in OPC paste with a water binder ratio of 0.50 for 1 year. The Ca/Si ratio varied from 1.56 to 2.07 depending on the distance from the unhydrated particle reflecting the differences in the CSH gel in the inner and outer hydrates (TANAKA ET AL. 1983, p. 971). The Ca/Si ratio of GBFS/OPC paste decreased roughly linearly from 1.2 to 2.0 with a GBFS weight fraction of 1 to 0, and the Al/Ca ratio increased linearly with the Si/Ca ratio, being roughly 0.2 at a Si/Ca ratio of 1.0 (RICHARDSON AND GROVES 1992, p. 354). ODLER AND HINRICHS (1989) found that the hydration products formed in slag cements at ordinary temperatures are similar, but not necessarily identical, to those formed in the hydration of slag-free Portland cement. Significant differences were observed in the stoichiometry of the CHS phase formed: CSH in slag cement pastes had lower C/S and C/S+A ratios and a higher alumina content. The C/S ratio a slag content of 70% was approximately 75% of that for paste without slag replacement (ODLER ET AL. 1989, p. 16). The aforementioned ratios for Ca/Si are based on the average values of hydrated gel.

TANAKA ET AL. (1983) also studied the mole ratios of the inner and outer hydration products described above. They found that the C/S ratio in the inner product varied from 1.48 in unhydrated material to 1.64 at the boundary of the original grain and 2.07 in the outer product. The corresponding values for the A/S ratio were from 0.26 to 0.20 in the inner product and 0.18 in the outer product. and for the M/S ratio 0.22 in the unhydrated material, the enriched value of 0.53 in the skeleton layer, 0.33 in the inner hydrated layer, and 0.36 in outer hydrate.

Overall it can be concluded that the CSH gel in hydrated GBFS blends activated by OPC possesses the typical C/S ratio of roughly 1.2-1.5 to 1.7-2.0, the former belonging to the pastes of high slag contents and the latter being typical average values in pure OPC pastes and in the outer slag hydrate with moderate or low slag contents. The elemental distribution from the skeleton to outer hydrate shows increasing Ca/Si ratio, decreasing Al/Si ratio from the inner to the outer hydrate, and clear Mg enrichment in skeleton hydrate, strongly supporting the existence of a hydrotalcite-like phase in this gel space.

CH content

As a consequence of a reaction of CH with the hydrating slag, free lime is consumed faster than it is liberated in the hydration of alite and belite phases. This means that the amount of free lime in slag cements increases as hydration progresses only for a certain period, and declines thereafter (HINRICHS AND ODLER 1989, p. 13). UCHIKAWA ET AL. (1991, p. 537) have found the amount of CH for OPC pastes with water-binder ratios of 0.30 and 0.60 to fall within the range 13-23% at 7 days and 19-28% at 91 days. The corresponding values for the GBFS paste with 50% slag content were 4.5-7.5 % at 7 days and 1.5-4% at 91 days, showing a gradual decrease with curing time and water-binder ratio. A continuous increase in free lime during hydration has also been reported (SERSALE ET AL. 1980).

HÄRDTL (1992, p. 681) studied the chemically bound water and CH content of GBFS/OPC pastes with a slag content from 0 to 77% and cured for 7 to 365 days. At high slag contents of 77% and 50% the CH content was roughly 3% and 10% respectively. decreasing only slightly with longer curing times. For OPC paste the CH content increased from 20% to 25% from a curing time of 7 days to 1 year. HARRISON ET AL. (1987, p. 219) have reported the CH content of GBFS/OPC pastes with slag contents of 0% and 40% to be 19% and 11% at 28 days, 23% and 10% at 6 months, and 23% and 9% at 14 months, respectively.

The lower CH contents in hydrated GBFS pastes evidently affect the microstructural properties in non-aged and aged states. In the green state it is clear that large hexagonal CH plates formed in the outer hydrates in OPC pastes prevent the compact packing of hydration products, and the gel structure remains more open than in GBFS pastes. On the other hand, in the aged state when carbonation reaches the gel, the OPC paste becomes denser due to the precipitation of carbonates in the originally more open gel space, and the balance in pore solution is maintained for a longer time by Ca^{2+} ions liberated from CH. In contrast, in GBFS pastes the CSH gel must provide alkalinity in the pore solution due to the lack of CH. This question is discussed in grater detail in Chapter 3.2.

Chemically bound water

The differences in CSH compositions and in overall gel structures between GBFS and OPC pastes can also be observed on the basis of non-evaporable or chemically bound water contents. Generally the chemically bound water contents are clearly lower for GBFS pastes, being roughly 50-80% of those in OPC pastes depending on the mix composition.

The ratio of chemically bound water in GBFS paste with 50% slag content to that in OPC paste varied from 0.75-0.78 to higher water-binder ratios of 0.50-0.60 with all curing times from 7 to 91 days. The ratio was 0.84-0.94 for the lower water-binder ratio of 0.30, being higher the longer the curing time (UCHIKAWA ET AL. 1991, p. 537). Chemically bound water at slag contents of 77 % and 50% increased from 9% and 11% at 7 days to 13% and 15% at 365 days, respectively. The corresponding values for OPC paste were roughly 16% and 18%(HÄRDTL 1992, p. 681). In a study on the hydration kinetics of slag pastes with a water-binder ratio of 0.50 HINRICHS and ODLER (1989 p. 9) reported the relationship between chemically bound water contents in GBFS and OPC pastes at full hydration to be 0.900 and 0.755 for slag contents of 50% and 70%, respectively. After 28 days of water curing the corresponding ratios were 0.82 and 0.63. The chemically bound water of OPC paste at 28 days was as high as 25%. The values presented before are in good agreement with each other.

3.1.3 Porosity

The methodology in measuring porosity is of great importance. Most test methods presume certain preparation processes able to change or even to destroy the original pore structure. The limitations associated with different test methods are considered in Chapter 4. In the following, the results given in the literature for OPC and GBFS concretes are presented and compared. Special attention is paid to studies in which OPC has been used as an activator in GBFS concretes, pastes and mortars. The literature is considered in two categories: The first, discussed here, comprises studies in which no aging processes have been used. The second, discussed in Chapter 3.2.5, comprises studies in which samples have been exposed to aging processes where carbonation or combined carbonation and drying is an essential part of treatment. It should be mentioned here that the results of studies presented in the literature are considered mainly in the light of documented test results presented in each report. If the documentation does not allow this, the conclusions drawn by the researchers are expressed instead.

Pore structures of slag concrete have been studied by many researchers, but few studies consider the effects of aging processes. Most studies look at the pore structure or its changes during extended curing in optimal conditions in water or even in saturated CH solution. Another noticeable feature is that MIP is often the only test method used, and rarely is the preparation of samples described fully. This makes comparison of the test results very difficult.

ROY AND PARKER studied the pore structures of OPC and GBFS pastes. Slag contents were 0 and 60% of the binder, and water-binder ratios of the samples varied from 0.30 to 0.60. The samples were cured in saturated CH solution at 27-90° C for 14 to 28 days. Porosity was studied with MIP using freeze-dried samples. Measurements were also done using samples vacuum dried at 80° C for 2 hours, dried with acetone, and vacuum dried again at room temperature. Different methods showed little difference in pore structures (ROY AND PARKER 1983, p. 399). According to the results, slag blends gave a very fine pore structure for pastes cured at 27° C. A water-binder ratio of 0.40 gave peaks for the dV/dP plot at a pore radius of 5 and 4.5 nm respectively for a slag blend cured for 14 and 28 days at 27° C. The corresponding peaks for OPC blends were roughly at 11 and 9 nm. A water-binder ratio of 0.30 gave peaks at 3 and 2 nm for slag blends and at 9 and 7 nm for OPC. High water-binder ratios gave clearly higher continuous pore size distribution and slag blends showed a finer pore structure than OPC blends. Total pore volumes of slag pastes were found to be lower than for OPC pastes. ROY ET AL. (1986) have reported that cement mortars with a water-binder ratio of 0.49, containing 35-65% slag and cured in saturated CH solution for 7 or 28 days at normal or elevated temperatures, gave a finer pore structure than the control OPC mortar. The test method used was MIP.

NUMATA ET AL. (1986) used mortars with a water-binder ratio of 0.5 and 50% slag content and found, using MIP and nitrogen adsorption method, that a curing time of 28 days gave a finer pore structure in slag concrete, whereas curing for 3 days gave a coarser structure. The fineness of slag was exceptionally high at 850 m^2/kg. HWANG AND LIN (1986) also reported a finer pore structure measured by MIP for slag pastes with a water-binder ratio of 0.47 and slag content of 40 to 60%, when the curing time was 28 days or longer. The total porosity of GBFS paste was found to be higher than that of OPC paste regardless of curing time.

FELDMAN compared the pore structures of OPC pastes with those of GBFS pastes having a water-binder ratio of 0.45 and subjected to 2 to 550 days of curing at different temperatures from 21 to 55° C. Slag contents were 0 and 70% of the binder and samples were presumably cured in water. Porosity was studied with MIP, helium pycnometry, and methanol saturation using d-dried samples. The MIP results showed that OPC blends gave a finer pore structure for pastes when samples were cured at 21° C for 28 days or less. With longer curing periods, slag blends gave a slightly finer pore structure. In all cases the total pore volume was higher with slag pastes. The same conclusion can be drawn from the helium inflow curves (FELDMAN 1983, p. 415). According to FELDMAN, the total porosity of such pastes can be measured by MIP but not by helium or methanol pycnometry for slag blends, as the narrow necked pores prevent movement of methanol and retard the flow of helium. FELDMAN emphasized the structural damage that occurs at high intrusion pressures of the MIP test, commenting that the pore size distribution is therefore not necessarily correct with this method, especially with slag blends (FELDMAN 1983, p. 424).

ODLER AND HINRICHS found that the overall porosity increases with slag content, reflecting differences in the hydration kinetics of slags and clinker phases. When the overall porosities were equal, the pore size distribution and the specific surface area were only slightly affected by the slag/clinker ratio (ODLER AND HINRICHS 1989, p. 20). A higher porosity of GBFS paste with a 40% slag content has also been reported by HARRISON ET AL. (1987, p. 221). The total porosity was 17% higher leading them to conclude that the generally lower permeabilities of slag pastes are due, not to lower porosity, but to a lower degree of continuity of pores, which may be due to a lower CH content.

TENAOUTASSE AND MARION (1987, p. 36) used cement with a 65 % slag replacement, and found curing regimes below 28 days to give the higher total porosity for GBFS concrete. Longer curing times had the opposite effect, MIP showing OPC concrete to have the higher value. Pore size distribution showed a coarser capillary pore structure for GBFS concrete up to a curing time of 28 days, beyond which the capillary porosity remained the same. When styding the effect of varied water-binder ratio on the pore structure and diffusion resistance of slag pastes, mortars and concretes, UCHIKAWA ET AL. (1991) found that GBFS gave a finer pore structure for curing times of 28 days or longer with mortars and concretes, but with pastes OPC showed the finer structure for the curing times of up to 91 days. Nonetheless, the diffusion coefficient of GBFS was smaller than that of OPC paste.

GBFS decreased the air permeability compared with OPC when good curing methods were used (Austin et al. 1992, p. 165). Controversially, Grube (1987, p. 1210) has reported a 36% slag content to give the higher permeability and rate of carbonation than OPC concrete. Only after a curing period of 28 days were permeabilities and carbonation rates roughly similar. The water-binder ratio in this study was 0.60. Also Häkkinen (1993, p. 58) found a significantly higher gas permeability in GBFS concretes but no significant differences in water permeabilities. In the same study, the capillary porosity measured with the water suction test was found to be higher with GBFS concretes cured for 7 days, but the finer pore structure was detected with GBFS mortars cured for 3 months.

Roy et al. (1986) found that cement mortars containing slag showed lower penetration depths of Cl^- compared with the control OPC mortar at normal or elevated temperatures. Lowered diffusivity of chlorides with 50 % GBFS replacement has also been reported by Jackson and Brookbanks (1989, p. 648) and with 75% GBFS replacement by Philipose et al. (1991, p. 342). In the latter, decreased chloride diffusion was associated with lower solubility of CH or reduced formation of calcium hydroxide-chlorides. Lowered permeability in the form of a smaller chloride diffusion coefficient with GBFS replacement has been reported by Malek et al. (1989, p. 259). They observed that after curing for 7 days the median pore radius of slag pastes with 50 and 65% replacement was smaller than with OPC pastes of the same water-binder ratio.

Feng et al. made calculations on the distribution of porosity between the inner and outer products of hydrated GBFS/OPC paste with a water-binder ratio of 0.50 and slag content of 50%. They concluded that at fully hydrated slag grain, the inner product comprising the volume of the original slag boundaries has a porosity of 53-61% and the remaining hydration product a porosity of 20-22%. This was explained by a decrease in specific volume occurring during gel crystallization and by continuing outward migration of Ca, etc., transforming the once dense inner slag hydrate shell to a more porous microstructure (Feng et al. 1989, p. 271). This chemical transport away from the slag grain results in an accumulation of residual porosity on the site of the former slag grain. Total porosity is changed only slightly, and the lowered permeability is a consequence of the pore size redistribution. The observation is well in line with the conclusion of the total porosity and permeability in GBFS blends drawn by Harrison et al. (1987).

Table 1 summarizes the main findings in the literature referred to. According to the results two main observations can be drawn. First, GBFS seems to give a finer pore structure than OPC when the curing time exceeds 28 days but a coarser structure with shorter curing times. These results are based on the MIP test and seem to be in accordance with the differences in hydration kinetics and hydration products formed in OPC and GBFS pastes. Different results are obtained with regard to total porosity. In most cases this seems to be higher with GBFS replacement, but when the MIP test and long curing times are used it appears lower. This is explained by the test methods used. MIP measures only the capillary pore volume, but some of this may fall outside the measuring range in GBFS blends. Differences in pretreatment of samples may also have caused contradictory results. Permeability gives information on the continuity of the pore structure, and here again the results are contradictory. In all references where Cl^- diffusion or penetration were studied, GBFS blends gave the lower values, indicating lesser pore continuity. However, gas permeabilities are reported to be higher with GBFS replacement in many studies.

Only in one report in the literature (Feng et al. 1989) has the porosity of GBFS mixes been studied separately in the skeleton and inner and outer hydrates. However, many papers do suggest that the skeleton hydrate is porous and isolated by the denser inner slag hydrate layer from the other relatively porous hydrates outside the boundaries of the original slag grain. The distribution of macroscopic porosity into three well-defined parts in the GBFS gel structure is of great importance in its further behavior. If the gel structure remains in this state when hydration ends and the aging processes begins, the minor changes in the gel structure of the inner slag hydrate layer may cause changes in overall permeability and in the ability of the binder matrix to become water saturated in a moist environment.

Table 1. Effect of slag replacement on the pore structure after water curing, according to different authors.

Reference	Mix & curing & test method	Results
Roy and Parker 1983	Pastes w/b=0.30-0.60, slag 0-60%; curing 14-28 d in sat. CH at 27 to 90^{o} C; MIP	Finer pore structure and lower total porosity in GBFS pastes. No difference between preparation techniques.
Feldman 1983	Paste w/b=0.45; slag 0-70%; curing 2-550 d; MIP and Helium pyc. and Meth. rep.	Curing 28 d or less -> OPC blends gave finer pore structure. In all cases total porosity with GBFS was higher. MIP causes structural damage.
Roy et al. 1986	Mortars w/b=0.49, slag 35-65%; curing 7-28 d in saturated CH; MIP	Finer pore structure with GBFS. Lower Cl^- penetration with GBFS.
Numata et al. 1986	Mortar w/b=0.50, slag 50%, curing 3-28 d; MIP and N_2 gas ads.	28 d curing ->finer pore structure with GBFS. 3 d curing ->coarser pore structure with GBFS.
Hwang and Lin 1986	Paste w/b=0.47; slag 40-60%; curing 28 d or more; MIP	Finer pore structure but higher total porosity in with GBFS.
Harrison et al. 1987	Paste with 40% GBFS	GBFS caused higher total porosity.
Tenaoutasse and Marion 1987	Concrete with 65% GBFS; MIP	GBFS caused higher total porosity and coarser pore structure than OPC when curing time was <28d.
Odler and Hinrichs 1989	Pastes with various w/b ratios and slag contents	Total porosity increased with slag content.
Malek et al. 1989	Pastes and Mortars; w/b= 0.35-0.51 with 0, 50, 70 and 85% slag contents; curing 14 and 28 d; MIP	Finer pore structure with GBFS. Lower Cl^- diffusion coefficient in GBFS.
Uchikawa et al. 1991	Pastes, Mortars and Concretes with various w/b ratios	OPC gave a finer pore structure for mortars and concretes with curing time <28 d and for pastes up to 91 d. Lower diffusion coefficient with GBFS.
Häkkinen 1993	Mortars; w/b=0.56; slag 70%; curing time 90 d; MIP	Finer pore structure with GBFS. Lower total porosity with GBFS.
Häkkinen 1993	Concretes; w/b=0.25-0.32; slag 70 to 87%; curing 7 d; water suction and air permeability tests	Capillary porosity higher with GBFS. No significant difference in capillary water permeability. Gas permeability of GBFS greater at higher w/b ratios and similar at low w/b ratio.
Grube 1987	Concrete w/b=0.60; GBFS 36%	GBFS increased air permeability when curing time was 28d or shorter.
Jackson and Brookbanks 1989	50% GBFS replacement	Lowered Cl^- diffusivity with GBFS.
Philipose et al. 1991	75% GBFS replacement	Lowered Cl^- diffusivity with GBFS.
Austin et al. 1992		GBFS decreased air permeability.

3.2 CARBONATION

Carbonation can be defined as an aging process whereby dissolved CO_2 in pore solution or free CO_2 in pores attacks the unhydrated or hydrated products of cement by a through-solution process or by a topochemical process, changing the chemical, mineralogical, microstructural and pore structural characteristics of the binding component of concrete in the surroundings of carbonation. More than 1000 reports on the carbonation of concrete materials have been published to date. Most of these deal with OPC concretes and focus on the modeling of carbonation rate and the parameters affecting it.

In the following carbonation is considered on the basis of the literature, concentrating primarily on topics relevant to the microstructural effects of the carbonation process. As with all chemical processes in cement chemistry, carbonation is strongly dependent on the temperature and moisture conditions in the reaction space. The process is controlled by a number of different time-dependent transport processes that give rise to testing problems. In order to avoid time-consuming tests, accelerated tests with higher CO_2 concentrations have become popular. However, the 100 to 1000-fold concentrations by comparison with atmospheric values alter both the carbonation process and the products formed, making the microstructural characteristics incomparable with those detected in ordinary atmospheric conditions. As such accelerated tests are not considered in this project, the literature review includes primarily studies in which the effects of carbonation on the pore structure and on hydration products have been determined in atmospheric conditions.

The following discusses the reactions associated with carbonation, models of carbonation for different phases in concrete, the effect of carbonation on the pore structure, and the drying of concrete.

3.2.1 Carbonation reactions

Carbonation reactions between the different components of the cement paste and carbon dioxide are traditionally presented in forms for:

Unhydrated phases:

$C_3S + (3-x)\overline{C} + yH \rightarrow C_xSH_y + (3-x)C\overline{C}$ (Richardson 1988) (1)

$C_2S + (2-x)\overline{C} + yH \rightarrow C_xSH_y + (2-x)C\overline{C}$ (Richardson 1988) (2)

$C_3A + \overline{C} + CH + 11H \rightarrow C_3A(C\overline{C})H_{12}$ (Gaspar-Tebar et al. 1976) (3)

Kommentoinut [SM1]:

Kommentoinut [SM2]:

Hydroxylated phases:

$Ca(OH)_2 + CO_2 \rightarrow CaCO_3 + H_2O$ (4)

$Mg(OH)_2 + CO_2 \rightarrow MgCO_3 + H_2O$ (5)

$2\cdot NaOH + CO_2 \rightarrow Na_2CO_3 + H_2O$ (Kropp 1983 p. 15) (6)

$2\cdot KOH + CO_2 \rightarrow K_2CO_3 + H_2O$ (Kropp 1983 p. 15) (7)

Hydrated phases:

$C_xS_yH_z + x\cdot\overline{C} \rightarrow x\cdot C\overline{C} + S_yH_{z-w} + w\cdot H$ (8)

$C_xA_yH_z + x\cdot\overline{C} \rightarrow x\cdot C\overline{C} + A_yH_{z-w} + w\cdot H$ (9)

$C_x(A,F)_yH_z + x\,\overline{C} \rightarrow x\,C\overline{C} + (A,F)_yH_{z-w} + w\,H$ (10)

$C_3A(C\overline{S})_3H_{32} + 3\,\overline{C} \rightarrow 3\,C\overline{C} + 3\,C\overline{S}H_2 + AH_x + (26-x)\,H$ (Calleja 1980) (11)

$$C_3A(C\overline{S})_3H_{12} + 3\,\overline{C} \rightarrow 3\,C\overline{C} + C\overline{S}H_2 + AH_x + (10 - x)\,H \tag{12}$$

$$4\,(C_3AH_6) + 3\,\overline{C} + 12H \rightarrow 2\,Al(OH)_3 + 3\,(C_3A(C\overline{C})H_{11}) \quad \text{(SAUMAN AND LACH 1976)} \tag{13}$$

$$C_3AH_6 + 3\,\overline{C} \overset{\text{topochemical}}{\rightarrow} Al_2O_3 + C\overline{C} + 6\,H \quad \text{(CALLEJA 1976)} \tag{14}$$

$$C_3AH_6 + \overline{C} \overset{\text{topochemical}}{\rightarrow} Al_2O_3 + C\overline{C} + 10\,H \quad \text{(CALLEJA 1976)} \tag{15}$$

$$C_3A(C\overline{C})H_{11} + 3\,\overline{C} + 3\,H \rightarrow 2\,Al(OH)_3 + 4\,C\overline{C} + 11\,H \quad \text{(GASPAR-TEBAR ET AL. 1976)} \tag{16}$$

$$C_3A(C\overline{C})H_{12} + 3\,\overline{C} \rightarrow Al_2O_3 + 4\,C\overline{C} + 12\,H \quad \text{(CALLEJA 1976)} \tag{17}$$

Most of the carbonation reactions presented above are through-solution processes where CO_2 is in dissolved form. Those in which the topochemical phenomenon is present are rare (Equations 14 and 15). SMOLCZYK (1976, p. 2) has described the start of carbonation as follows: During carbonation the CO_2 gas is first absorbed by the alkali solution. The decreasing alkali hydroxide content of the solution is replaced by soluble CaO from the hydration products, and portlandite will then react with CO_2. The final result is a complete conversion of the soluble CaO in the paste to solid $CaCO_3$. The mineralogical forms of $CaCO_3$ are calcite and vaterite, and possibly also aragonite. Vaterite is the first product in the carbonation process, and is a poorly and small-crystallized form of $CaCO_3$ that converts easily to calcite if there is space enough for precipitation. In theory, carbonation can proceed as long as CaO is available in pore solution, and the final composition of the paste may be a calcium-free solid gel, pore solution with certain amounts of lime and alkalis, and carbonates in different forms as tests with pure hydration products have shown. In practice, however, a certain amount of CaO remains uncarbonated under normal conditions in which there are always several impure hydration products. According to SMOLCZYK (1976, p. 3) approximately 60% of CaO in German Portland cements is carbonable.

Carbonation reactions of hydrated and hydroxylated phases release water. This is important for further reaction in the liquid phase but also a significant factor in transformation of the gel structure. A very rough estimate for the loss in structural water of the CSH gel is 50% due to carbonation. This evidently leads to excess shrinkage-induced deformation in the paste and to changes in the microstructure.

3.2.2 Carbonation of hydroxylated phases

The phases of cement paste able to hydroxylate are calcium-, alkali- and magnesium oxides. Among these, the role of CaO is the most important. The CH content in OPC paste may reach 25 wt.-% and in GBFS paste half of that while the percentage of carbonatable alkali oxides in OPC is only 2 to 3% and in GBFS cements even lower. Furthermore the carbonated forms of alkalis are highly unstable and their precipitation is evidently impossible in ordinary pore solutions. The amount of free MgO in cements is kept to a minimum due to the demand for soundness. MgO may hydroxylate to brucite $Mg(OH)_2$ but is stable in a pore solution of high pH and hence the formation of $MgCO_3$ is possible from the brucite phase only at low pH. The MgO content in slag cements may rise to 12-14 wt.-%, and enrichment of Mg ions is observed at specified sites such as the inner and skeleton hydration products of slag binder. The exact forms of hydration or hydroxylated products at Mg rich cites are still unclear. In principle, the formation of $MgCO_3$ in low basicity solution is possible and more pronounced with concretes of high slag contents. Magnesium exists in the hydration products of slag concretes together with aluminates as hydrotalcite-type hydrates.

The carbonation mechanism of CH is generally thought to involve the dissolution of CO_2 and CH in the pore solution followed by precipitation of $CaCO_3$ as calcite, but other polymorphs such as vaterite and aragonite have also been detected (KROPP 1983, RICHARDSON 1988, JOHNSTON AND

GLASSER 1992, etc.). There is also evidence of a direct reaction between CH and CO_2 being, although this is restricted to initial stages during dry carbonation (JOHNSTON AND GLASSER 1992, p. 375).

Carbonation of CH is generally assumed to take place, and even to finish, before the carbonation of other components in cement paste begins. However, this assumption has recently been observed to be incorrect. MATSUSATO ET AL. (1992) have reported simultaneous progression of carbonation of the two main carbonable components in cement paste. This is confirmed by the simultaneous existence of silica gel as a residue of carbonated CSH gel and CH in cement paste. According to the hypothesis proposed by BIER (1988), the two CH and CSH phases carbonate simultaneously such that when CH carbonation takes place, CSH carbonates in its outer product and only a partial change occurs in the structure of the CSH gel. Also ATLASSI (1993) recently reported the simultaneous carbonation of both phases.

Carbonation of the CH phase is obviously very similar in both OPC and GBFS concretes. The main difference naturally lies in the amount of carbonates precipitated from the CH phase, GBFS concretes showing the lower amounts. According to BIER (1988) the main differences in the carbonation of GBFS and OPC concretes are the lesser formation of carbonation products from CH in small capillaries, the higher carbonation of the inner and outer hydration products of the CSH gel, and the formation of continuous areas of porous SH gel on the boundary of the inner and the outer hydration products.

3.2.3 Carbonation of CSH gel

In the literature several models have been put forward for the carbonation of CSH. In principle, the carbonation process is similar for CSH gel formed from either GBFS or OPC, although changes in the Ca/Si ratio may affect different kinetics in the carbonation process.

In their microstructural NMR study of carbonated C_3S, RICHARDSON ET AL. observed that at an early stage of carbonation some gel regions of very low Ca content form, and that a three dimensional network of silicate units develops. Calcium carbonate in a form of calcite and vaterite precipitated in the outer product of CSH gel, with a microcrystal size of the order of 100 nm. At a later stage only very fine 10 nm poorly crystalline vaterite particles formed in the inner product gel. The Ca/Si ratio of the carbonated gel was approximately 1.0. Similar features were observed in the carbonation process of OPC paste. Initially, CH was the more rapidly reacting phase but slowed due to the precipitation of carbonates on the surfaces, and the CSH reaction became dominant. Obviously the inner product of CSH suffers from a net loss of calcium due to the fact that it does not contain pores large enough to allow for the nucleation of carbonates (RICHARDSON ET AL. 1992, p. 303). According to ESSING AND HILSDORF (1976) the carbonation of CSH gel takes place in areas with high specific surfaces.

Tobermorite gel decomposed quickly in silica gel and carbonates; in the first stage vaterite and finally calcite were observed in a study by SAUMAN AND LACH (1976). The carbonation of synthetic 11Å tobermorite has recently been studied by IKEDA ET AL. (1992 and 1993). 11Å tobermorite was synthesized from quartz and CaO (Ca/Si=0.84) and carbonated by a 17% CO_2 gas flow into a mixture of tobermorite and distilled water at 60^o C. The progress of carbonation was studied by gas analyzer, XRD, IR spectroscopy and ^{29}Si NMR. Results showed that the carbonation rate in tobermorite gel is relatively fast in aqueous solution and occurs in two rate-determining steps, changing from a surface reaction to an internal diffusion process. The phenomenon was thought to be due to an increase in the diffusion resistance of the carbonated layer of tobermorite (IKEDA ET AL. 1993, p. 143). During the carbonation process, tobermorite decomposed into silica gel and calcium carbonates. All morphologies, vaterite, aragonite and calcite, were observed. As carbonation progressed the calcite fraction increased, and after complete carbonation all $CaCO_3$ was transformed into calcite. The double chain structure with Si-O-Si bridges of the silicate phase in non-carbonated tobermorite was destroyed during carbonation, a silica gel with a three dimensional cross-linked framework structure being formed instead (IKEDA ET AL. 1992, p. 1086). Noticeable in the last study was the finding that the double chain structure still exists at relatively high degrees of carbonation from 60% to 80%.

SUZUKI ET AL. (1985, p. 223) studied the decomposition of CSH in a solution exposed to atmospheric CO_2 concentration. In the first stage calcite precipitated in the solution, causing a decrease in Ca^{2+} and OH^- ions in the liquid. Thereafter CSH started to decompose, and the Ca/Si ratio of the CSH gel decreasing from 1.3 to 0.6. CSH decomposed to the modified silica gel and calcite. Finally the modified silica gel changed to pure silica gel by carbonation.

BIER (1988 p. 114) has proposed a model along the similar lines to that of SUZUKI ET AL. (1985). According to Bier's model, CO_2 ingresses into the matrix to form H_2CO_3 and reacts with CaO on the surface of the CSH gel. The reaction proceeds in stages the so-called Ca-modified CSH gel being formed first, after which CSH loses its SiO_2 to form amorphous silica gel. Bier states that although the carbonation starts as a topochemical reaction, it proceeds and ends as a through-solution process. In the process a new organization of SiO_4 tetrahedra takes place in the gel. The layered structure of CSH is bound by two of four corners in tetrahedra, but with the amorphous silica gel all corners may act as bridging components forming a three-dimensional and porous network of silicon chains. Carbonation products exist as microcrystallized material on the surface of the modified gel or as a part of it. The gel is only partly in its original form, being mostly an SH gel. The morphology, chemical composition and CO_2 concentration determine the degree of transformation of CSH to SH.

ATLASSI (1993 p. 136) has modeled the carbonation of CSH in four different conditions of relative humidity, in saturated or near saturated conditions, at intermediate relative humidities of 40-95%, at RH 11-40%, and at RH 11%. In saturated or near saturated conditions the carbonation of CSH starts when the CaO saturation level of the water phase drops below 0.020 moles per liter. The CSH gel gives away CaO to the solution in suitable amounts to maintain the metastable equilibrium between the C/S ratio of gel and the CaO saturation of the solution. When the C/S ratio drops below 1 the CSH transforms to pure silica gel and calcite. ATLASSI constructed the model to describe changes in the non-evaporable water of CSH in the course of carbonation. She states that the net loss of this reaction is only CaO, since one $CaOH^+$ ion is replaced by an H^+ ion at an oxygen corner of the tetrahedron, but this molecule has an extra corner that can polymerize with another CSH molecule, and one water molecule will be released. This part of the model is in accordance with the model presented by SUZUKI ET AL (1985).

According to ATLASSI's model parallel carbonation of CH and CSH is possible at intermediate RH. This is due to the fact that the CaO content of the water film on the CSH gel surface is lowered by carbonation, but CaO transport from the CH crystal through the thin water film is difficult, and therefore the local C/S-CaO equilibrium is maintained by the CaO released from the CSH gel. Carbonates formed at these relative humidities differ in their morphology depending on the layer thickness of the adsorbed water. It inhibits the crystallization of calcite and preferably vaterite or a CSH-$CaCO_3$ type product is formed. The minimum value of the H_2O/SiO_2 ratio in the CSH gel is 0.83, as in 11Å tobermorite. The vaterite or CSH-$CaCO_3$ may recrystallize to calcite once the pores are water filled and if the pore size allows it. If the pore is saturated and some CH is left, the partly decalcified and polymerized silica chain will again attain equilibrium with the solution and the CSH gel will be restored to its original composition (Atlassi 1993, p. 139). In this respect the model nicely fits the mechanism of realkalization of porous silica gel proposed by Bier (1988, p. 145). At lower relative humidities dissolution of CaO in the liquid phase is impossible, and the only carbonation products in Atlassi's model are a CSH-$CaCO_3$ type material or CSH plus a free $CaCO_3$ molecule. No polymerization or dehydration occurs.

All of the above carbonation models for CSH gel corroborates one another, and each has its special features describing different phenomena in the carbonation process. According to these models the final products of CSH carbonation are silica hydrate gel and carbonates representing different morphologies depending on the precipitation space and relative humidity. SH gel forms step by step as CSH releases CaO to maintain equilibrium in the pore solution, and in the remaining gel structure the corners of silicon tetrahedra act as bridging components of the structure. Layered, relatively dense CSH gel has transformed to a porous SH gel having a three-dimensional, cross-linked network.
Atlassi's model offers valuable additional understanding of the morphology of carbonates at different relative humidities and of pore size control in the carbonation process. Her concept includes the existence of a CSH-$CaCO_3$ type product at low relative humidities. This type of product could be analogous to carbonated forms of tri- and monosulfates phases, which do not necessarily change morphology during carbonation. With regard to structural changes in CSH, of particular interest are the results of the NMR study of carbonated tobermorite gel presented by Ikeda et al., according to which a threshold value exists for the degree of carbonation, below which CSH maintains its original structural state despite losing CaO. The double chain structure of the silicate phase in non-carbonated tobermorite gel was still seen at very high levels of carbonation, i.e. up to 60%. This could mean that SH formation affects the microstructure of the gel, and then also its pore structure, significantly only in severe carbonation.

3.2.4 Carbonation of other phases

The volume fraction of the CH and CSH phases in fully hydrated OPC pastes is roughly 70 to 75 wt.-% of the hydrated phases. This means that also the carbonation products of these phases represent the majority of all carbonated products in OPC and GBFS concretes. However, there exists a variety of aluminate phases able to carbonate. The most important of these are tri- and monosulfate phases and the cubic and hexagonal forms of aluminate hydrates. Carbonated forms of other phases such as ferrite phases, and in GBFS concretes magnesium containing hydrotalcite phases and also hydrogarne type phases are very rare on the basis of the literature.

Carbonation of ettringite has been suggested by Nishikawa et al. (1992a, p. 13). They proposed that in a pore solution with dissolved carbonated ions and low pH, ettringite and the liquid phase are no longer in equilibrium and dissolution of calcium and sulfate ions occurs from the surface of the ettringite. Carbonation proceeds in a diffusion process through the ettringite surface, well-crystallized gypsum and calcium carbonate forming as a result. In dry conditions the dissolution step on the surface is dominant and in wet conditions the diffusion controlled process. Johnston and Glasser (1992) also found that during the carbonation process the AFt phase no longer exists, but linked the disappearance of ettringite to the carbonation of CH. Examination of the carbonation process of AFt and AFm phases in Equations 11 and 12 shows it to involve the formation of gypsum, hydrous alumina and the release of relatively high amounts of water. The carbonated analogies for ettringite and monosulfate are $C_6A\bar{C}_3H_{32}$ and $C_4A\bar{C}H_{11-12}$, the latter being also formed by direct reaction of C_3A with $CaCO_3$. Thaumasite $C_3S\bar{C}\bar{S}H_{15}$ is one form of carbonated ettringite observed to form through the replacement of aluminium by silica at lowered temperature and at high relative humidity.

Calleja (1976) has reported the carbonation of the cubic and hexagonal forms of hydrated alumina C_3AH_6 and CAH_{10}, and also of carboaluminate $C_3ACaCO_3H_{12}$. He suggests that the reaction is topochemical by nature and that the carbonation products are calcite, Al_2O_3, and water (Equations 14, 15 and 17). Sauman and Lach (1976) have proposed a carbonation reaction according to Equation 13 for C_3AH_6, in which the cubic form of alumina hydrate decomposes relatively quickly to form $Al(OH)_3$ and a metastable carbonate complex of carboaluminate type, which decomposes later to vaterite and calcite and to $Al(OH)_3$. The decomposition of carboaluminate to $Al(OH)_3$ and calcium carbonate has also been reported by Gaspar-Tebar et al. (1976, p. 4).

Hydrogarnet phase C_3ASH_6 has been observed to be highly resistant to the effects of CO_2 (Sauman and Lach 1976). Studies describing the carbonation of magnesia- including phases are non-existent. The existence of the hydrotalcite-type phase $M_6A\bar{C}H_{12}$ in GBFS concrete has been confirmed, but the tendency of magnesia- including phases to carbonate is not discussed in the literature at all. One reason may be the undefined composition of this phase in general. Hydrotalcite type phases are reported to exist especially with slags high in MgO, and include products which may resemble meixnerite $[Mg_{0.75}Al_{0.25}(OH)_2](OH)_{0.25}(H_2O)_{0.5}$ (Taylor 1990 p. 185). Through an anion exchange reaction, meixnerite can take up CO_2 to give the carbonated form $[Mg_{0.75}Al_{0.25}(OH)_2](CO_3)_{0.125}(H_2O)_{0.5}$. Separation of this compound of layered structure has been reported to be difficult from monosulphate phases by XRD.

3.2.5 Changes in water content of carbonable phases

The carbonation reactions presented earlier show that carbonation reactions are also dehydration reactions in which varying amounts of water are released. The gel water lost during carbonation maintains an additional dissolution space for CO_2 and CaO, promoting further carbonation, or it becomes part of evaporable water or provides an opportunity for further hydration.

According to Equation 4, carbonation of CH releases one mole of water per mole of carbon dioxide absorbed. If afwillite $C_3S_2H_3$ is assumed to be a form of CSH gel and if the carbonated form of the gel has the composition of calcite and the SH gel has an S/H ratio of 0.83, roughly 0.45 moles of water per mole of carbon dioxide absorbed is released during carbonation of the CSH gel according to Equation 8. These two phases represent approximately 70-75% of the weight of hydrated phases in OPC paste. The monosulfate phase may represent about 15 wt.-%, and if calcite, gypsum and gibbsite AH_3 are assumed to be the products of carbonation in Equation 12, roughly 2.3 moles of water per mole of carbon dioxide absorbed is released during carbonation of the monosulphate phase. During carbonation of then ferrite phase (Equation 9) and the corresponding reaction including Fe_2O_3, and assuming calcite and gibbsite to be carbonation products, one mole of water per mole of carbon dioxide absorbed will be released. For example, the full carbonation of all phases in the OPC paste used in the experimental part of this study gives a value of 0.85 for the mole ratio of H_2O/CO_2 which is equivalent to the lowest H_2O/CO_2 weight ratio of 0.35 to 0.41 proposed by Pihlajavaara (1968). Chemically bound water in non-carbonated OPC paste, presented later in this report, was 24.3% of the weight of cement. This amount decreased to 18.2% and 14.0% following carbonation of the CH phase and the CH and CSH phases, respectively. If all phases are assumed to become carbonated, the final amount of chemically bound water is only 8.5%.

Carbonation of CSH gel causes loss of structural water from the gel and the structure shrinks. According to Pihlajavaara (1976) the carbonation shrinkage may be as high as 50% of the drying shrinkage. PIHLAJAVAARA (1982) reports estimated relative drying shrinkage values of 0.54, 0.51, 0.43 and 0.26 at relative humidities of 20%, 40%, 60% and 80%, respectively. Corresponding shrinkage values when carbonation shrinkage was included were 0.64, 0.65, 0.57 and 0.35. To what extent this excess shrinkage affects the pore structure is still unknown. If we assume that cement gel is a fully homogeneous isotropic body having the same strain characteristics in all directions, the volume of the solid gel decreases by the amount of volumetric shrinkage by which the changes in porosity could be estimated. However, knowing the heterogeneous characteristics of the cement gel, any estimation of carbonation shrinkage on the nanometric scale of cement gel based on volumetric calculations of the loss in gel water is rather inaccurate.

3.2.6 Effect of carbonation on pore structure

OPC concretes

The effect of carbonation on the pore structure of OPC blends has been widely studied. In the first reports from the 1960's, the pore structure with OPC binder was found to become finer and the total pore volume to decrease as a consequence of the precipitation of carbonates from CH in coarse capillary pores (PIHLAJAVAARA 1968). Several reports during the last two decades confirm this finding: Pore size distribution becomes denser due to loss of coarse capillaries; continuity of pores decreases, resulting in lowered permeability detected by air or water; and diffusion resistance increases (e.g. SAROTT & AL. 1992, p. 444). Decreased diffusion rate studied by the Cl^- and I^- through-diffusion technique was assumed to be a consequence of the precipitation of $CaCO_3$ in the near surface pore space. Some contradictory results of the effect of carbonation on the total porosity exist, but the general understanding is that overall porosity is diminished.

The second stage in the modeling of pore structural changes in OPC blends started from the findings of ESSING AND HILSDORF (1976) and ROZENTAL AND ALEKSEEV (1976). They concluded on the grounds of changes in the specific surface area of CSH gel that also this phase is attacked by carbon dioxide. In fact, ASCHAN (1963) had already presented the carbonation reactions of CSH gel 13 years earlier. ESSING AND HILSDORF (1976) found, using N_2 gas adsorption tests, that the specific surface area and also pores in the range 1.5 to 20 nm decreased due to carbonation of OPC paste with a water-cement ratio of 0.4 and 0.5. They explained their finding in terms of the carbonation process whereby CO_2 reacts with the CSH gel in areas of high specific surfaces, causing the area to decrease. Once the border zone is neutralized, pore water saturated with CH migrates to this zone where it too is neutralized. This leads to the formation of carbonates and reduction of pore volume. Thus an increase in diffusivity of the local boundary as a result of carbonation can be expected (ESSING ET AL. 1976). ROZENTAL AND ALEKSEEV (1976) also reported that the specific surface area is decreased by carbonation when measured by the water sorption method. The increased specific surface area detected by N_2 gas adsorption after carbonation was thought to be caused by the change of the fine porous structure of CSH to hydrous silica gel. The finest primary pores of silica gel are 5 to 10 nm and the coarse secondary area 260 to 400 nm.

GBFS concretes

There are only a few studies where the pore structural changes in carbonated GBFS concretes, mortars or pastes are studied. The reports of LITVAN AND MEYER (1986), BIER, KROPP AND HILSDORF (1987). BIER (1988) and MATALA (1988) were the first where this subject was considered. Thereafter DISTLER, KROPP AND HILSDORF (1992), DE CEUKELAIRE AND VAN NIEUWENBURG (1992), PARROT (1992) and HÄKKINEN (1993) have worked in the field. The effect of aging, in the form of wetting and drying treatment, on the pore structure of slag concretes was studied by HO, HINZAK, CONROY AND LEWIS (1986). Aging phenomenon with respect to the durability of slag concrete is studied also by VESIKARI (1988). In the following the before mentioned reports are considered.

BIER & AL. (1987) have noticed that carbonation in atmospheric climate coarsens the pore structure of GBFS pastes but not OPC pastes. They explain this phenomenon by the formation of a porous silica gel as a result of decomposition of the CSH. An overall decrease in porosity is observed both in total porosity and especially in capillary porosity. The decrease in capillary porosity took place especially in small capillaries where $CaCO_3$ precipitates from CH. This was observed to prevent the reliable measurement of the smallest capillaries. Bier observed that in carbonated OPC pastes the decrease in the total and capillary porosity was caused by the change of the porosity at range from 2 to 20 nm. A slight coarsening was observed at range from 100 to 200 nm being in line with the coarsest pores of SH. The smallest pores in SH are impossible to detect by MIP. Specific surface area determined by SAXS was decreased due to the carbonation in the outer CSH gel of OPC paste. Total porosity was decreased in carbonated GBFS concrete as it happened in the OPC concrete too but the decrease in the capillary porosity was not observed. The portion of the small capillaries decreased clearly. The outer CSH gel is disappeared and it has replaced by porous SH gel, and the specific surface area decreases strongly due to the carbonation.

Identical results on coarsening of the pore structure in GBFS blends was reported by MATALA (1988). The slag content in mortar samples was 30% and water binder ratio 0.45. The pore volume of pore radius > 4 nm measured by MIP decreased with all mix compositions, by 19% in OPC blends and by 25% in GBFS blends. However, in OPC mortars the relative distribution at pore radius > 24 nm unchanged but in GBFS mortar redistribution occurred to coarser pores over 50 nm. LITVAN AND MEYER (1986) studied the subject in natural atmospheric conditions in the walls of two experimental houses, one made of OPC concrete and the other of GBFS concrete. The concretes were comparable in terms of water binder ratios and compressive strengths at 28 days. After 20 years of exposure, pore structural analysis by MIP showed the pore structure in GBFS concrete to have coarsened remarkably due to carbonation, whereas that in non-carbonated concrete was very fine. Total porosity had not changed in the GBFS concrete but had decreased in the OPC concrete, where the pore structure had become denser over the entire pore range. LITVAN AND MEYER (1986, pp. 1447-1450) also observed a markedly greater freeze-thaw susceptibility in GBFS concrete compared with OPC concrete as a result of coarsening. Cement replacement by 60% GBFS caused significant coarsening of the capillary pore structure of pastes having a water-binder ratio of 0.50 and cured for 7 to 28 days under a wet burlap and carbonated in an atmosphere of 2% CO_2. The same phenomenon has also been observed with 20% slag replacement (DISTLER ET AL. 1992, p. 434). PARROT (1992, p 116) has reported identical results to the above studies. In carbonated paste the use of 50% GBFS as replacement material gave a capillary porosity (pores > 28 nm) roughly 50% higher than for pure OPC, when measured by the sorption method. The water-binder ratio was 0.59 and the initial curing time 7 days.

The only report in which coarsening of carbonated GBFS blends was not observed is that by HÄKKINEN (1993). The effect of carbonation was studied on well-hydrated GBFS mortars with a water-binder ratio of 0.56 and slag content of 70 %. The samples were wet-cured for 3 months and thereafter carbonated in a 3% CO_2 flux at RH 70% for 6 months. She found that accelerated carbonation does not coarsen the pore structure of GBFS mortar but in fact creates a slightly denser pore structure in both OPC and GBFS mortar samples (HÄKKINEN 1993, pp. 43 and 87). However, the careful analysis of the results shows the pore structure in OPC mortar to have clearly coarsened and the total porosity to have slightly increased. The pore structure of GBFS mortar has become denser and the pore volume has decreased. Samples measuring 850 mm^3 were studied by the MIP apparatus in which the maximum intrusion volume is 1500 mm^3. The maximum intruded volume of mercury observed in the tests was roughly 70 mm^3/g, corresponding to 7-8% of the capacity of the measuring cell. Operating at such a low measuring level affects the accuracy of the test results, possibly explaining the discrepancy with OPC mortar. HÄKKINEN has also studied the effect of carbonation on the pore size distribution of slag paste with a water-binder ratio of 0.30. In these tests she used a different MIP apparatus and the same size of sample as before. Total porosities of OPC and GBFS pastes were found to have decreased by 24% and 41% respectively. Volumes of pores in GBFS paste in the ranges, 10-50, 50-100 and 100-10000 nm had decreased, whereas in OPC paste those in the coarsest and finest pore ranges had increased (HÄKKINEN 1993, p. 61).

Increased permeability of carbonated GBFS concretes have been reported by DE CEUKELAIRE AND VAN NIEUWENBURG (1992). DISTLER ET AL. (1992, p. 434) reported similar results after studying the surface permeability and water absorption of carbonated and non-carbonated concrete samples. Carbonation increased permeability and water absorption in GBFS concrete with 60% slag replacement, contrary to concretes without slag replacement.

HO ET AL. (1986, pp. 1471-1472) studied the effect of slag content on water sorptivity when concretes were aged by wetting and drying treatment after initial curing. Drying time of samples in the laboratory atmosphere was 18 days after each wetting period of 3 days. The results showed that a slag content of 36% of the binder increased the first-stage water penetration due to aging, when the effect of increased degree of hydration in cycled specimens was taken into account.

Accelerated carbonation

HÄKKINEN (1993, p. 45) states that carbonation in normal and accelerated conditions creates a slightly denser pore structure in OPC and GBFS mortars, which is in sharp contrast to the results reported by BIER ET AL. (1987, p. 930). According to the latter, accelerated carbonation, especially with GBFS concrete, coarsens the pore structure more than does atmospheric carbonation. Increased CO_2 concentrations in the carbonation tests affected the coarsening of the pore structure, also in the inner hydration product, and large areas of SH gel formed on the boundary of the inner and outer hydration products in OPC paste, in the same way as observed in GBFS pastes carbonated at atmospheric CO_2 concentration. On the other hand, subjecting GBFS pastes to increased CO_2 concentration changed the originally dense structure of the inner hydration product, which remained unaffected in tests at atmospheric CO_2 concentration (BIER 1988). This finding suggests that the conclusions drawn from pore structural changes observed in accelerated carbonation tests are questionable in general, and that comparison of pore structures between carbonated OPC and GBFS concretes is misleading.

In summary it can be concluded that the majority of published literature presents findings according to which carbonation causes particular redistribution in the pore structure of GBFS concrete, and that this coarsening may be associated with the carbonation of CSH gel. The only reported explanation for this phenomenon is the formation of a porous silica gel. Thus the effect of severe carbonation on the pore structure of OPC concretes should be somewhat similar although delayed due to the CH phase. The literature does not give specific values as to the extent of redistribution, over all pore size ranges, through the gel and capillary pores.

3.2.7 Calcium carbonates and their identification

Calcium carbonates

Calcium carbonates exist in concrete in three mineralogical forms. Calcite and aragonite occur in nature as well-defined minerals, the former being more stable (RICHARDSON 1988, p. 13). The third form, vaterite, is observed to be fairly stable and transforms to calcite in a moist environment. Calcite has a rhombohedral symmetry with a bimodal unit cell of constants a=6.3748 Å, α =46.08°. Aragonite is orthorhombic with unit cell parameters a=7.6791 Å, b=5.7404 Å and c=4.9614 Å. Vaterite has a hexagonal symmetry with parameters a=7.15 Å, c=16.94 Å and γ =120°. Solubility of calcium carbonate polymorphs is in the order calcite, aragonite and vaterite, of which the latter has the highest solubility (VERDOES 1991, p. 6). The densities for calcite, aragonite and vaterite are 2.71, 2.93 and 2.65 g cm^{-1} respectively (CRC 1990).

The metastable phases vaterite and aragonite are formed first, followed by transformation into the stable polyform calcite. This is supported by the generally accepted explanation according to which the metastable phases have relatively higher rates of nucleation and growth than the thermodynamically stable polyform (VERDOES 1991, p. 21). The presence of impurities, e.g. ions of deviating radius, is observed to affect the precipitation of carbonates. SAWADA ET AL. (1990, p. 397) reported that the Mg^{2+} ion retards the transformation of vaterite into calcite. OGINO ET AL. (1990, p. 166) have explained the strong inhibition of calcite growth with Mg^{2+} to be caused by strain of the crystal surface due to the incorporation of this ion or the very large energy required for the dehydration of Mg^{2+}. This observation is very interesting with regard to GBFS blends with a high MgO content and with regard to the enrichment of Mg^{2+} ions in the skeleton hydrate of GBFS pastes, as discussed in Chapter 3.1.

Identification of carbonates

The methods mostly used to identify carbonates in cement paste are XRD, DTA, TG, EGA and IR. NMR is also utilized in the study of phases after carbonation (e.g. IKEDA ET AL. 1992).

LACH AND SAUMAN (1976) have presented a DTA/TG method by which the decomposition of vaterite and calcite can be determined. They found that vaterite that transforms at atmospheric temperature slowly to calcite I decomposes at the ordinary decarbonation temperatures of 750-900° C. On the other hand, vaterite that transforms fast at 490-530° C to calcite II decomposes at lower temperatures of 600-750° C. This enables the separation of vaterite from calcite with particular precision by the TG test. According to FORRESTER (1976), transformation from vaterite to calcite may take place at a lower temperature, and this poorly crystallized calcite decomposes between 500° C and 750° C and the well-crystallized calcite correspondingly between 710° C and 850° C. KOJIMA ET AL. (1992, p. 1134) stabilized flat hexagonal vaterite crystals by heating and found by XRD that the transformation of vaterite to calcite begins under 500° C and all vaterite fully converted into calcite at 600° C. Temperatures between 600° C and 800° C were not studied but some calcite transformed from vaterite was detected at 800° C. Thus the identification of calcite II on the basis of decomposition temperature may not necessarily be all that accurate. In any case, calcite II did not have the conventional rhombohedral crystal shape of calcite I but instead a flat hexagonal crystal shape resembling that of vaterite. The limits reported in the literature must be considered carefully since they are clearly dependent on the crystal size of carbonate and on the test procedure itself. In our test procedure the lowest decomposition limit of calcite was roughly 690-730° C and the end of the decomposition at 800° C. The limits were determined by pure calcite.

Goto and Ikeda (1992, p. 308) have reported two clearly separated decomposition areas of carbonates at temperature ranges 450-600° C and 600-650° C in DTA. The former peak was attributed to the decarbonation of vaterite and the latter to that of calcite. Both carbonates were also identified by XRD. The findings were drawn from a study in which synthesized 11Å tobermorite was carbonated in an atmosphere of 5% CO_2. The carbonation products were vaterite and silica gel in the early stages and later calcite.

The use of TG alone cannot be regarded as sufficiently accurate. The decomposition range of carbonates is so broad that some loss of water occurs in the same range, and the separation of CO_2 and H_2O gases from each other should be done e.g. by gas analyzer. Nilsson (1980) has presented that several percent of the non-evaporable water may be liberated above 600^{o} C, i.e. at the decomposition temperatures of carbonates. Quantitative determination of evolved CO_2 gases during the TG run enables accurate measurements of the total amount of carbonates, and the separation of vaterite from calcite is possible with a certain degree of accuracy using the decomposition limits presented above. The dehydration of carboaluminate can be recorded by TG, at least with some precision. Dehydration of $C_4A\overline{C}H_{12}$ is observed to take place in two stages during the TG run. The first decomposition area in the temperature range 120-180°C represents the loss of interlayer water. In the second stage, from 240 to 280° C dehydration of the hydroxide ion in the interlayer region is observed (Nishikawa et al. 1992 p. 440). The first decomposition area coincides with that of tri- and monosulfates. The reported peaks for carboaluminates in DTA are at 155° C, 165° C and 260 ° C (Negro et al. 1976). However, it should be remembered that in the TG run the loss of interlayer water and strongly chemically bound water of the CSH liberates simultaneously with aluminate phases (e.g. Nilsson 1980, p. 13, Taylor 1990, p. 220). Furthermore, hydrotalcite-type phases are reported to decompose also in the same temperature ranges.

XRD is a powerful method for the qualitative and quantitative determination of different morphologies of calcium carbonates and carboaluminates. The main diffraction patterns for calcite are at 3.86 Å, 1.93 Å, 1.91 Å, for vaterite at 3.57 Å and 2.06 Å, and for aragonite at 3.4 Å and 1.98 Å, and are clearly distinguishable from the patterns produced by cement minerals. The 1.93 Å line coincides with CH (Forrester 1976). The peaks for carboaluminates are at 3.77 Å, 7.51 Å, and 7.59 Å (Negro et al. 1976).

Different morphologies of calcium carbonates and carboaluminates can be defined qualitatively and possibly also quantitatively using IR spectroscopy. Very strong absorbance bands for calcite, aragonite and vaterite are at 1425 cm^{-1}, 1500 cm^{-1} and 1450 cm^{-1}. Strong bands are also found at 712 cm^{-1} and at 875 cm^{-1} for calcite, at 855 cm^{-1} for aragonite, and at 875 cm^{-1} for vaterite. Carboaluminate shows a very strong band at 1420 cm^{-1} and at 1370 cm^{-1}, the latter differing from that of calcite. Formation of SH due to the carbonation of CSH gel can be identified reliably by IR. CSH gives the absorbance band at 970 cm^{-1} and SH at 1040-1080 cm^{-1}.

Of the methods discussed above XRD, TG, EGA and FTIR were selected to identify the carbonates and to measure their amounts in the paste and mortar test samples in this study.

4 METHODS FOR THE CHARACTERIZATION OF PORE STRUCTURE

4.1 REVIEW OF THE METHODS

Characterization of porosity in pastes, mortars, and concretes made of OPC/GBFS blends is highly problematic. The pore space is bound together by a variety of particle morphologies that change with time and atmospheric conditions. SEM micrographs show an irregular pore shape for pores spanning hundreds of nanometers. The same irregularity is obvious, not only among small pores, but also in the connecting cavities between them. Pore sizes vary from micropores of approximately 1 nm through coarse capillaries of several micrometers to air pores measuring hundreds of micrometers. Water plays an essential role in hardened paste, being the bridging component in the gel structure, existing as an adsorbed layer on pore walls, and condensing in pores at various levels of relative humidity. All these features demand exceptional requirements for the measuring technique used in the characterization of pore structure.

PARROT (1987, p. 91) has underlined two topics in the characterization of pore structure. The first is the serious difficulties encountered in pore structure characterization associated with sample preparation, the wide range of pore sizes and geometries to be measured, and the choice of experimental method. The second is deciding what pore structure characteristics are required to reliably describe the properties and performance of cement paste and concrete. The prediction of diffusion and permeability properties requires some measure of pore connectivity, while the pore size distribution may be an important property in frost resistance.

The measuring techniques most used in the characterization of pore structure are:

- Gravimetric methods by which the fractional state of the pore structure can be measured,
- Mercury intrusion porosimetry (MIP) making it possible to measure pores from 2 nm to tens of micrometers,
- Adsorption methods with water, nitrogen, methanol, and isopropanol for measuring the specific surface area and pore volume fractions at specified relative humidities,
- Differential thermal analysis (DTA) and thermogravimetric analysis (TGA) for differentiation of interlayer and adsorbed water,
- Pycnometric measurements, e.g. by helium, for differentiation of interlayer and adsorbed water,
- Small-angle X-ray scattering (SAXS) for determination of specific surface area,
- Neutron scattering for differentiation of chemically bound and free water,
- Nuclear magnetic resonance (NMR) for differentiation of interlayer, physically adsorbed and free water,
- Conductometric and dilatometric phase transition porosimetries,
- Thermoporometry based on low-temperature calorimetry or differential scanning calorimetry,
- Optical and electron microscopy.

SCRIVENER ET AL. (1987, p. 61) divide the techniques for studying the microstructure of cement based materials into three categories. The first group provides information about the average fractional state of phases or pores. Such techniques include e.g. TGA, quantitative X-ray diffraction (QXRD), IR spectrometry, etc. The second group includes techniques such as MIP, adsorption methods and low temperature calorimetry (LTC) by which the distribution of sizes in a component can be measured. The third category includes a wide range of optical and electron microscopical techniques allowing measurements of porosity on the macroscopic scale. BSE image analysis has proven efficiency for analyzing coarse pore structures. The resolution in this technique with available microscopes makes it possible to measure porosities over 500 nm.

The property of pore structure under consideration resolves the selection problem. If changes in pore structure are considered, as in this study, the method must give information about pore volumes within particular pore ranges, i.e. pore size distribution, total porosity, and some knowledge of pore connectivity. The studies referred to in Chapter 3 show that the method of choice for characterization of pore structure is MIP, along with different adsorption methods. The other methods are seldom used, probably due to the high running costs and/or difficulties in interpretation of the results.

MIP method

Initial pore structure may be changed during the drying pretreatment of MIP specimens before testing. Vacuum drying, drying in elevated temperatures up to 105° C, D-drying, solvent replacement by methanol or isopropanol or a combination of these are generally used as pretreatment. Changes in the pore structure of cement paste due to pretreatment were studied e.g. by FELDMAN (1986) and FELDMAN AND BEAUDOIN (1991). The latter study recommended the use of isopropanol replacement and immediate evacuation, and heating to 100° C for 20 hours as a drying technique before Hg intrusion. Methanol should not be used as it increases the threshold pore diameter. FELDMAN AND BEAUDOIN (1991) also pointed out that actual pore size distributions of hardened cement paste cannot be obtained by MIP due to sensitivity of the material to stress. Relative changes in pore structure may, however, be monitored.

Some reservation has been expressed concerning the use of different solvents in sample preparation due to their possible reaction with cement paste. However, using both XRD and IR techniques THOMAS (1989) found no evidence of a reaction product due to interaction of methanol with either CH or cement paste. He further states that the mercury pore size distribution was unaffected by soaking vacuum-dried samples in methanol for up to 90 days. The third important finding in his study was that solvents such as methanol, propan-2-ol or ethanol should be used with caution for thermal analysis studies. He adds, however, that techniques using solvents are suitable for pore structure characterization. Drying treatment at elevated temperatures has been observed to change pore structure. According to e.g. TAYLOR (1990, p. 176), some of the water is held by tri- and monosulfate dehydrates below 100° C. COSTA AND MASSAZZA (1987, p. 165) consider drying at 70° C under vacuum too rough, as it leads to partial decomposition of the hydrated phases.

Other precautions should also be considered when using MIP. For example, sample size has been observed to affect the total porosity detected. HEARN AND HOOTON (1992, p. 972) varied the volume of samples from 20 to 80% of the maximum of sample cell capacity of 0.5 cm$^{3.}$ They found that total intruded porosity with the smallest sample size was only 78% of the volume of the largest sample size, the intermediate sizes giving porosities in between. No size effects on pore size distribution or effects of pressure rate on total porosity were observed, but the latter affected pore size distribution. SELLEVOLD (1974) has also reported that sample dimensions may influence the test results, especially pore size distribution.

In the MIP test the volume readings must be corrected at least by the following correction values: The blank run correction takes into account the machine expansion and the compressibility of the mercury volume needed to fill the empty cell. Differences in the compressibility of mercury and the tested sample should also be considered. The values for surface tension and contact angle of mercury are traditionally kept constant using the Washburn equation. Changes in both of these factors shifting the intrusion curve horizontally. Values for the contact angle of 117° to 142° are reported in the literature. The lower values are used for oven-dried materials and the higher values for samples dried by other means. Commonly used surface tension values are 0.473 to 0.484 N/m, the effect of pore radius on these values being negligible. A circular cross-section is traditionally assumed in calculations. The correction factor for a lattice pore structure is 0.5 and for an irregular shape 0.75 (COOK AND HOVER 1993, p. 235-236).

Despite the uncertainties listed above, MIP is a useful and rapid tool for measuring total porosity in the capillary area and also its continuity. Naturally, closed pores are excluded. Therefore a fully accurate pore size distribution is not obtained, as the measured pore sizes correspond to the neck dimensions between pores. Nonetheless the method allows comparison of relative changes in pore size distribution between different mix compositions. Sample preparation and its effects on pore structure should be considered when drawing conclusions on pore structure from MIP test results. MIP was selected as one of the main methods in this study for characterization of pore structure.

Other methods

Samples for testing by N_2 gas adsorption method must also be predried. This obviously affects the specific surface areas and pore volumes. E.g. ODLER AND KÖSTER (1991) gave clearly lower surface areas of 5 to 20 m^2/g with N_2 gas as absorbance compared with 100-115 m^2/g obtained with water. The difference in results is also affected by the lower accessibility of N_2 to the gel surfaces. The results of N_2 gas adsorption and those calculated from the MIP results were found to correlate well. The same conclusion can be drawn from the results reported by OLEK ET AL. (1990). Pore sizes, from the gel pore range to small capillaries, can be measured by adsorption methods. The method appears sensitive to the pretreatment of samples. Sensitivity to vacuum drying of the gel pore volume of high strength pastes measured by N_2 gas adsorption has been reported by MATALA (1995). Pore sizes in the gel pore range were in good agreement with the results obtained by thermoporometry, but the gel pore volume was underestimated, probably due to changes in the gel pore structure during vacuum drying.

A recent method for measuring the pore size distribution has been presented by GUNNINK (1991). In this method, referred to as conductometric phase transition porosimetry, the changes in electrical conductance and temperature of saturated porous materials subjected to capillary freezing and melting are measured and used to calculate pore size distribution. The method has two advantages - minimal sample preparation before testing and the ability to measure the pore size distribution of large samples. Phase transition porosimetry, in which phase changes are observed through dilatometric measurements, has been proposed by ECKRICH ET AL. (1986). SAXS and NMR have also been used to study the pore structure of saturated materials. Recently ALLEN AND AL. (1988, p.119), presented the use of small-angle neutron scattering to characterize the gel and pore structure also in cement based materials. The method belongs to the group of non-destructive test methods where no sample preparation is needed.

The advantages of low temperature calorimetry and differential scanning calorimetry lie in the minimal sample preparation before testing. This was the main reason for selecting low temperature calorimetry to use in this study. This method is considered in greater detail below.

4.2 THERMOPOROMETRIC APPROACH

4.2.1 Background

Each method used in the characterization of pore structure has its limitations. Conventional MIP makes it possible to detect pore radius sizes over 2-4 nm, but is fairly sensitive to the preparation of samples. As discussed above the need for predrying alters the pore structure of the finest pore range. To counteract this problem a seldom-used test method, thermoporometry, was chosen to confirm the MIP results. During the last 20 years this method has been used in the characterization of pore structure of cement based materials by e.g. FAGERLUND (1973), SELLEVOLD with his coworkers (1980), BAGER (1984), BAGER AND SELLEVOLD (1986a and 1986b), ZECH AND SETZER (1989), BAHTIA ET AL. (1989), BEDDOE AND SETZER (1990) AND SETZER (1990). BRUN's calculation method using water and benzene as absorbances was presented in 1977 (BRUN ET AL. 1977).

The principle behind low temperature calorimetry and differential scanning calorimetry is very simple: The phase transformation energy evolved during freezing or thawing of the condensate in pores between the specified temperatures is measured calorimetrically, and corresponds to the pore volume in the pore ranges which relate to the solidification or fusion temperature of the condensate.

Although the principle is simple, there are many approximations in the theory on which the method is based. The energy evolved during phase transformation can be measured with high accuracy, but the correct evolution of entropy of the applied condensate before, during and after solidification and fusion is more difficult to calculate. Entropy changes in the adsorbed water layer, in the ice sphere, and in the interphases must be known. Supercooling of water lowers its freezing temperature and these thermodynamic properties are not well known.

The second difficulty lies in the phase state of the pore water. Pure pore water in cement paste is generally assumed in this context, but various impurities are known to exist. The effect of these substances on the entropy of water and ice, and on the entropy due to curvature of the water-ice interphase, are usually neglected, as is the case in this study. The values of surface tension for the solid-gas interphase, solid-liquid interphase and/or liquid-gas interphase must be known. One of these can be expressed as a function of the others, but in a case of incomplete saturation two of these must be formulated, and the surface tension of solid-liquid interface must be known in a state of full saturation. Unfortunately the reported values in the literature are mostly based on calculations using homogeneous nucleation theory or on the tests with samples having large pore diameters.

The third category of uncertainties lies in the freezing phenomenon in the porous system. The volume change during solidification affects the changes in the strain state of the matrix if the developed pressure cannot be released through the non-frozen pore space. If the matrix is unable to resist these strains it breaks down, and the calorimetric readings may include part of the fracture energy. How significant for analysis of the fusion thermogram are the changes in pore structure due to freezing pressure? In other words, what then is the validity of the fusion thermogram to represent the pore size distribution of the original structure? Further, if the matrix is strong enough and transport through the pore space is prevented, what really occurs in the pores? Is solidification possible at all? These phenomena may play a certain role especially in the gel pore range.

Of course there are also some experimental problems. Sample used for low temperature calorimetry are quite large. This, and although a temperature rate is slow, causes a delay in temperature over the sample. In addition, the pore space is measurable only within the limits of its saturation. If total porosity is of interest, there must be some certainty of water saturation in the sample. The aforementioned theoretical and experimental uncertainties should be taken into account as limiting factors when analyzing the results of thermoporometric measurements and when drawing conclusions about pore structure on the basis of any thermoporometric approach.

The following sections describe the method used to calculate the pore volume and pore size distribution from calorimetric measurements made in the experimental part of this study. The method is based on the pioneering work in the application of thermoporometry on cement based materials done by the researchers listed at the start of this section.

Section 4.2.2 highlights the theoretical basis derived from elementary thermodynamics. The framework of this study focuses on porosity and its changes during aging, which definitely requires total porosity determination. This, on the other hand, demands full saturation of test samples. This enabled to consider the basic Equation 18 in the special case, in which the solid-gas interphase is plane, as occurs at full saturation, and hence the radius of the ice nucleus is expressed as a function of surface extension energy of the water-ice interphase. If a state of under-saturation prevails, differential Equation 18, or the corresponding analogous formulation between other phases, should be solved in its complete form.

In section 4.2.3, the change of entropy due to phase transformations is formulated according to the method proposed by BRUN. Traditionally, the effect of compression heat of phases caused by the pressure change on the entropy is neglected in thermoporometric considerations of cement based materials. Although this effect is minor (roughly 3% at 30^{o} C depression), it is included in the numeric formulation of solidification entropy in Equation 24. Another feature of the following presentation, in which it differs from conventional approaches, is the included effect of superficial phase transformations on entropy, i.e. during solidification of ice changes occur in the interphase between layers that do not freeze and the adjacent phase (water before solidification and ice afterwards). Since this additional entropy is dependent on the pore geometry, the author has used in its formulation a hypothetical pore size distribution typical of the finest pore structure in cement based materials.

The ice sphere radius can be dimensioned theoretically as a function of temperature depression. Therefore in thermoporometric pore size characterization the thickness of the non-freezable water layer must be added to the ice dimensions. This has been done in section 4.2.4 after FAGERLUND (1973). Also discussed in this section is the effect of the interphase between water and ice, the so-called liquid-like layer, on total entropy of the pore system. The author has formulated an expression for the surface tension of the liquid-solid interphase (Equation 33) for use in the Laplace equation with the semi-empirical and theoretical data published in the literature. Pore size as a function of temperature depression in solidification and in fusion is given separately by equations 35 and 36.

Finally, section 4.2.5 gives the calculation procedures by which total freezable water and its distribution can be calculated. The main points of the procedure proposed by SELLEVOLD, BAGER AND LE FONTENAY are presented first, and followed by the author's proposal.

4.2.2 Theoretical basis

BRUN ET AL. (1977, p. 61) have derived a differential equation for the triple point temperature dependent on the entropies and volumes of three phases (liquid, solid and gaseous) and on the free surface extension energies and curvatures of two interphases (solid-gas and solid-liquid) as follows:

$$\left(\frac{S_s - S_g}{V_s - V_g} - \frac{S_l - S_s}{V_l - V_s}\right) dT = \frac{V_g}{V_g - V_s} d\left(\gamma_{sg} \frac{dA_{sg}}{\mathrm{d}V_g}\right) - \frac{V_l}{V_l - V_s} d\left(\gamma_{sl} \frac{dA_{sl}}{\mathrm{d}V_l}\right) \tag{18}$$

where S and V are the specific entropy and the volume of phases, subscripts l, s and g denote the phases liquid, solid and gas, γ is surface tension and dA/dV is the curvature of the interphase. From Equation 18 it can be seen that the curvatures of two of the three interphases should be known in order to calculate the triple point temperature in a general case. In the special case where the solid-gas interphase is plane and its curvature is zero, as in the case of full saturation, the equation 18 can be presented in the form:

$$\Delta S_f \, dT + V_l \, d\left(\gamma_{sl} \frac{dA_{sl}}{\mathrm{d}V_l}\right) = 0 \tag{19}$$

where ΔS_f is the solidification entropy of the condensate. Assuming that solidification takes place by nucleation in a porous saturated material the curvature of the nucleus equals that of the pore radius subtracted by the thickness of the layer where phase transformation cannot take place. If the interphase has a spherical shape, the curvature dA_{sl}/dV_l equals $-2/R_n$, where R_n denotes the radius of the nucleus and from Equation 19 can be expressed as:

$$R_n = \frac{2 \cdot \gamma_{sl}}{\int_T^{T_0} \frac{\Delta S_f}{V_l} dT} \tag{20}$$

4.2.3 Numeric formulation of the solidification energy

The measurable solidification energy of pore water can be evaluated theoretically if the change of entropy during phase transformation can be formulated. In a fully water saturated porous system the solid-gas interface is plane, and the change in entropy of the water-ice system of pores for temperature change $T_0 \rightarrow T$ and for the corresponding changes in pressure of liquid phase $P_0 \rightarrow P_l$ and solid phase $P_0 \rightarrow P_s$ can be expressed by the equation:

$$\Delta S_f = \Delta S_{f0} + \int_{P_l}^{P_0} \left(-\frac{\partial v_l}{\partial T}\right)_P dP + \int_T^{T_0} \frac{c_l}{T} dT + \int_{T_0}^{T} \frac{c_s}{T} dT + \int_{P_0}^{P_s} \left(-\frac{\partial v_s}{\partial T}\right)_P dP \tag{21}$$

where the first term is the basic entropy and the second and the fifth terms represent the effects of compression heat of phases due to the change in pressure, assuming that the phases are incompressible. The third and the fourth terms take into account changes in the specific heat of liquid and solid due to the depression of temperature. BRUN has rearranged Equation 21 as follows:

$$\Delta S_f = \Delta S_{f0} + \int_{T_0}^{T} \left(\frac{c_s - c_l}{T}\right) dT + \left[\left(\frac{\partial v_l}{\partial T}\right)_P - \left(\frac{\partial v_s}{\partial T}\right)_P\right]_T (P_s - P_0) + \left[\left(\frac{\partial v_l}{\partial T}\right)_P\right]_T (P_l - P_s) \tag{22}$$

where P_s is the vapor pressure of ice at temperature T, and P_l-P_s can be expressed by Laplace's equation:

$$P_l - P_s = -\frac{\gamma_{sl}}{R_n} = -\int_{T_0}^{T} \frac{\Delta S_f}{V_l}\, dT$$

(23)

BRUN ET AL. have presented the numeric formulation for Equation 22 in the form:

$$\Delta S_f = \frac{-1{,}2227 - 4{,}889 \cdot ln\left(1 + \frac{\theta}{T_0}\right) + 10{,}124 \cdot 10^{-3} \cdot \theta + 1{,}265 \cdot 10^{-5} \cdot \theta^2}{1 - 4{,}556 \cdot 10^{-5}(\theta - 0{,}227 \cdot \theta^2)}$$

(24)

where θ is the freezing point temperature in °C. The numeric values for the variables in Equation 22 are given in Appendix A. In the numerator of Equation 24 the first term represents the normal entropy. The second and major part (99%) of the third term represent the entropy variation of the freezing temperature, and the last term the curvature of the water-ice interphase. The denominator of the equation is the correction factor; it is of minor significance and is due to assumptions made in integration of Laplace's equation. As is seen above, the third term $\left[\left(\frac{\partial v_l}{\partial T}\right)_P - \left(\frac{\partial v_s}{\partial T}\right)_P\right]_T (P_s - P_0)$ of Equation 22 is neglected in Equation 24. The magnitude and significance of this term by comparison with other terms is considered in Appendix A and is shown to be minor.

Equation 22 is not fully accurate when considering the solidification of ice, as it does not take into account the effect of entropy of superficial phases. During solidification of ice, changes occur in the interphase between layers that do not freeze and the adjacent phase (water before solidification and ice afterwards). BRUN derived the correction factor of entropy due to this additional entropy variation, considering the equality of chemical potentials and the equilibrium of three interphases at a triple point (BRUN ET AL. 1977 p. 65). BRUN's correcting factor is as follows:

$$\eta_{e_{sup}} = 1 - \frac{d\gamma_{ls}}{dT} \cdot \frac{\theta}{\gamma_{ls}}$$

(25)

It is a function of surface tension of liquid-solid interface and temperature depression. The change of entropy of superficial phases is also presented in the form $\Delta S_{f_{sup}} = -0.78/R_n$, where R_n is the radius of the ice sphere at the nucleation point (BRUN ET AL. 1977, p. 73). Using BRUN's expression for the relationship between the pore radius and temperature depression, the correction factor $\eta_{e_{sup}}$ can be expressed in the form:

$$\eta_{e_{sup}} = 1 + \frac{0.78}{64.67/\theta + 0.23}$$

(26)

Correction factor $\eta_{e_{sup}}$ gives a very high increase in the total entropy change of the pore system, especially in small pore sizes as Table 2 shows.

Table 2. Effect of superficial phase transformations on the total entropy of a pore system calculated from Equation 26.

Temperature depression [°C]	1	2	5	10	20	30	40	50
$\eta_{e_{sup}}$	0.988	0.976	0.939	0.875	0.740	0.595	0.438	0.267

Closer examination of Equation 25 shows that the correction factor in BRUN's expression is connected with the temperature depression and surface tension at the nucleation point. According to the author this means that the proposed relationship can be applied only in special cases where pore sizes have a narrow distribution, and if the surface tension of the liquid-solid interphase is independent of temperature depression. Otherwise the effect of superficial phase transformations of large pores at lower temperatures is overestimated.

In order to have an estimate of the effect of superficial phase transformations on total entropy in typical cement based materials, the basic Equation 21 was considered in different thermodynamic states of a pore system with a hypothetical pore size distribution. This is described in Appendix A. This effect was found to be for a pore system, having a typical pore size distribution of cement paste or mortar, much less than suggested by Equation 26, as seen in Figure 1.

Figure 1 shows that BRUN's equation overestimates $\Delta S_{f_{sup}}$ for the pore structure normally observed in cement pastes. Obviously Brun's equation gives correct values for the pore structure near the nucleation point. The hypothetical pore structures used in testing Brun's equation are much finer than observed in ordinary cement pastes and mortars with different testing methods. This is also true of pore structures termed "coarse". The "coarse" curve gives an increase of 20% at -50° C for the entropy at the nucleation point, and the curve is roughly linear. Hence linearization of the curve between -50° C and 0° C gives a rough estimate which is on the safe side for the effect of $\Delta S_{f_{sup}}$. The linearized expression as a function of temperature depression enables the effect of superficial phase transformations to be taken into account when deriving the equation for the entropy of the pore system. Of course, theoretically this is not absolutely correct, since $\Delta S_{f_{sup}}$ is a function of the pore size.

However, in practical calculations this approximation must be accepted, otherwise the calculation procedure leads to a highly complex iterative process whereby the correct pore size distribution is determined step by step and the entropy of the previous pore system is used as a starting value for the next calculation step. Another argument for accepting the approximation is that, in any case, enthalpy is the thermodynamic state property, allowing estimation of the total amount of freezable water without making any assumptions of the temperature dependence of solidification or fusion energy as proposed by SELLEVOLD AND BAGER (1980) (see 4.2.5). Approximated entropy change due to superficial phase transformations is used only to distribute the total freezable water over different pore sizes.

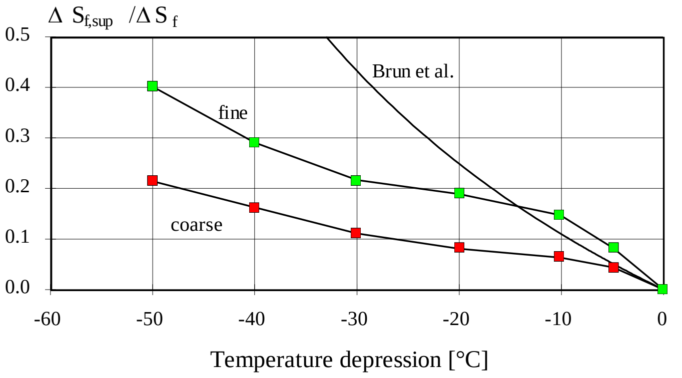

Figure 1. Ratio $\Delta S_{f_{sup}} / \Delta S_f$ as a function of temperature depression for hypothetical fine and coarse pore systems.

Using the linearized correction factor for entropy changes of superficial phase transformations, and multiplying this by Equation 24, the numerical expression for the entropy at the nucleation point is:

$$\Delta S_f = \frac{(1+0{,}004\cdot\theta)\cdot\left[-1{,}2227-4{,}889\cdot ln\left(1+\frac{\theta}{T_0}\right)+10{,}124\cdot 10^{-3}\cdot\theta+1{,}265\cdot 10^{-5}\cdot\theta^2\right]}{1-4{,}556\cdot 10^{-5}(\theta-0{,}227\cdot\theta^2)} \qquad 27)$$

where θ is the freezing point temperature in °C. The enthalpy at the nucleation point can be calculated from the equation:

$$W_{th} = (273{,}15+\theta)\cdot \Delta S_{f_{np}} \qquad (28)$$

Equation 28 is illustrated in Figure 2, together with the enthalpy values proposed by other researchers. Numerically the solidification energy W_a based on Equation 28 can be expressed within the temperature range 0 > T > -60° C by the quadratic equation:

$$W_a = 334 + 4.83\cdot\theta + 0.0125\cdot\theta^2 \qquad (29)$$

where W_a is expressed in J/g and θ in °C. Linear correlation analysis between Equations 28 and 29 gives a determination factor of 0.999985 (R-squared) within the temperature range 0° C > T > -60° C .

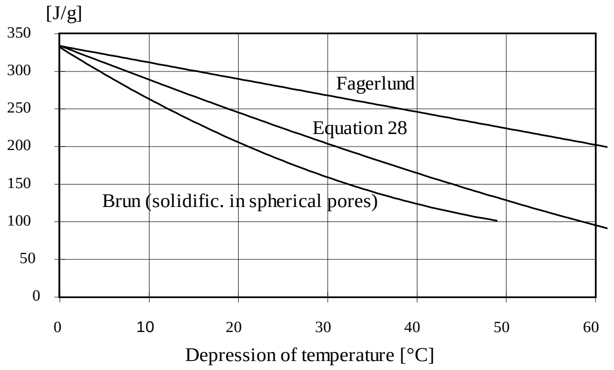

Figure 2. Enthalpy at nucleation point for a spherical pore structure.

4.2.4 Pore radius as a function of temperature depression

<u>Phases in the pore after nucleation</u>

The ice sphere in a saturated porous medium can be schematically represented as in Figure 3. After nucleation water is in three different phases, each of which has different thermodynamic properties. The entropy of ice at lower temperatures is the best known of these. Different and somewhat controversial assumptions concerning the entropy of the water phase have been presented in the literature. Mostly, however, it is assumed to be linear between 0 and 10° C, where it becomes measurable. Also very high values have been reported but there is little evidence to support this assumption.

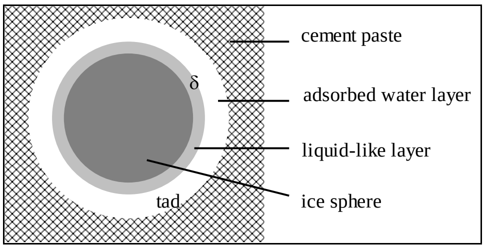

Figure 3. Schematic representation of the ice sphere in saturated porous medium.

Perhaps the most unknown parameter among these water phases is the liquid-like layer on the ice sphere. Evidence of the existence of this water-ice film may now be considered established (TAKAGI 1990, p. 446). The thermodynamic properties of this layer are somewhere between those of supercooled water and well-crystallized ice. The thickness of the liquid like-layer varies from 0.1 Å to tens of Å within the pore range of cement paste. Variations in thickness of the liquid-like layer as a function of pore size and temperature depression are shown in Figure 4. The curves are calculated using the equations derived by TAKAGI (1990, p. 448). The figure shows that the thickness of the layer on an ice sphere of over 10 nm is roughly half the thickness of the adsorbed non-freezable water layer calculated according to Fagerlund (1973). Brun has measured the thickness of the adsorbed water layer and found it to be 9.5 to 11.5 Å at pore range 1.5-9.5 nm. This value fits quite well to those calculated by Fagerlund's method. On the other hand it is known from the literature that the thickness of the liquid-like layer of bulk ice from -1° C to -4° C varies from 30-40 Å to 15-20 Å (Hobbs 1974). These temperature depressions correspond to the pore ranges 70 to 16 nm. Again these values fit well the sum of values calculated using Fagerlund's equation for adsorbed water and Takagi's method for a liquid-like layer in porous media. It can be assumed that in a porous system the total thickness of adsorbed water and the liquid-like layer of the ice sphere can be calculated by the equation:

$$t_{tot} = t_{ad} + \delta \tag{30}$$

where $t_{ad} = 1.97 \cdot \sqrt[3]{1/(\theta)}$ [nm] as evaluated by Fagerlund (1973), and δ can be taken from Takagi's quintic equation (31)

$$\rho_w \cdot S_w \cdot \theta + \frac{2\gamma_{vw}}{r+\delta} - \frac{2A^2(\gamma_{vi}-\gamma_{vw})(r-A)}{(r+\delta)(A+\delta)^3} + \frac{2A^2r^2\gamma_{vi}}{(r+\delta)^2(A+\delta)^3} = 0 \tag{31}$$

where A is the radius of the ice molecule and can be approximated at 2 Å. Assuming the values for other parameters to be those proposed by Takagi, the thickness of the liquid-like layer δ can be solved as a function of the ice radius r_{ice} by iteration. The dependence of the liquid-like layer on the ice sphere radius as a function of temperature depression is presented in Figure 4.

A rather good general approximation for the thickness of the liquid-like layer (δ [nm]) as a function of the radius of the ice sphere (r_{ice} [nm]) and the temperature depression (θ [°C]) is:

$$\delta = \frac{0{,}9+0{,}1\cdot\log r_{\text{ice}}}{\frac{3}{(\log r_{\text{ice}})^{0{,}938}}+\theta\cdot\left(0{,}07\cdot\log r_{\text{ice}}-0{,}0365+\ln\sqrt[3]{\frac{\log r_{\text{ice}}+0{,}12}{\log r_{\text{ice}}-0{,}12}}\right)} \tag{32}$$

Equation 32 is fitted using the curves of ice sphere radius 1.4-60 nm in Figure 4 and temperatures between the nucleation point and -50° C. The maximum absolute errors between the calculated values from Equations 31 and 32 are presented in Table 3 for specific ice sphere radii.

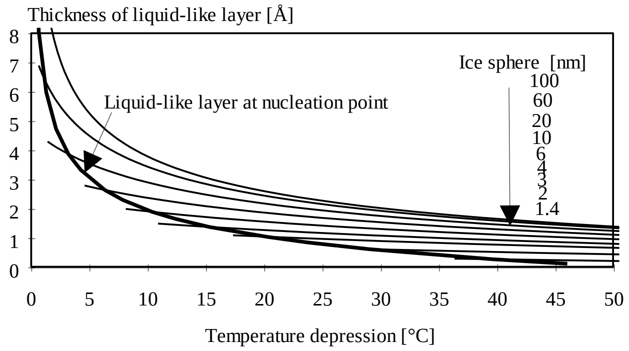

Figure 4. Variation in thickness of the liquid-like layer as a function of pore size and temperature depression.

Table 3. Maximum absolute errors of calculated values for δ.

Ice sphere radius [nm]	Absolute error δ(31)-δ(32) [Å]
60	0.10
20	0.08
10	0.04
6	0.03
4	-0.02
3	-0.06
2	-0.07

In Figure 5 the thickness of the liquid-like layer at the nucleation point and that added by the adsorbed water layer calculated from Equation 30 are presented as a function of the ice sphere radius. The figure shows that at ice sphere radii of 100, 10, 4 and 2 nm the ratio t/δ is 3.3, 4.0, 5.6 and 11.3 respectively.

Figure 6 shows the relative volumes of the aforementioned water phases nucleation point. The volume fractions are corrected on the basis of the entropies of each component. The entropy value for the liquid-like layer has been assumed to be the average of ice and water (dashed line). The ice phase and the adsorbed water phase are marked by continuous and dotted lines. The effect of the liquid-like layer on the total entropy of the pore is roughly 2 to 3%, being maximum at a pore size of 9 nm. The entropy of the liquid-like layer has been assumed in this case to correspond to the average entropy of ice and water, and the effects of changes in surface energies at the interfaces on the total entropy of the pore are assumed negligible. Investigation shows that the effect of the liquid-like layer vanishes in the gel pore space, where the adsorbed water phase determines the entropy changes of the pore system. In coarse capillaries over 100 nm the ice phase is the determinant factor.

The effect of the liquid-like layer on pore size was estimated by calculations in which the thickness of the liquid-like layer was taken from Equation 32 and that of the adsorbed water layer from Equation 30. In addition, the entire liquid like-layer was assumed to correspond to ice in terms of thermodynamic properties. Calculations showed that neglecting the liquid-like layer as a whole underestimates the pore size only by a few percent, namely 3.8, 3.1, 3.0, 1.5 and 0.7% at pore ranges of 3, 5, 9, 30 and 100 nm respectively. In fact the real underestimation of pore size is even lower, since the entropy of the liquid-like layer obviously differs from that of well-crystallized ice.

Although the significance of this interphase is of minor importance it is included in the calculation method presented in Section 4.2.5

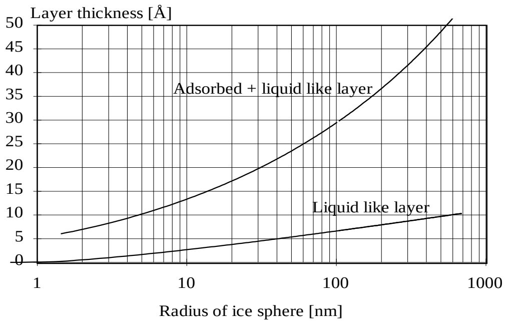

Figure 5. Thicknesses of liquid-like and adsorbed layers at nucleation point as a function of ice sphere radius.

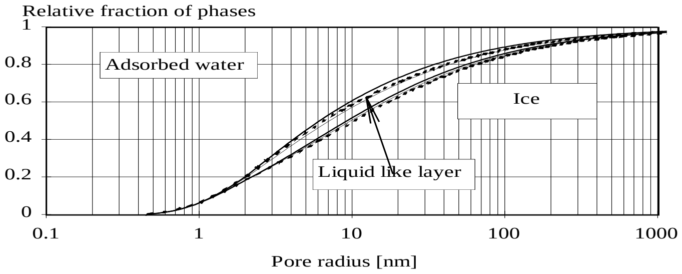

Figure 6. Volume fractions of adsorbed water, water-ice of the liquid-like layer, and ice phases as a function of pore radius after nucleation.

Surface tension of the water-ice interphase

In the literature many suggestions have been made in concerning the surface extension energy, i.e. surface tension, of the water-ice interphase. Most of the values are theoretical and based on the homogeneous nucleation theory (HOBBS 1974, p. 434, BRUN, 1977 p. 69). The surface tension of the water-ice interphase is possible to determine semi-empirically using material with known porosity and applying Laplace's equation (23) for a spherical pore shape. BRUN measured surface tension by using six different materials with pore radii of 2.4-10.5 nm. These results are plotted in Figure 7 together with values reported by other researchers. All values at -40° C are based on theoretical calculations. Assuming γ_{ls} to vary linearly with temperature, and taking in account the experimental values from 0 to -30° C, the temperature dependence of surface tension can be expressed as:

$$\gamma_{ls} = (36 + 0{,}25 \cdot \theta)10^{-3} \tag{33}$$

where γ_{ls} is expressed in N/m and θ in °C.

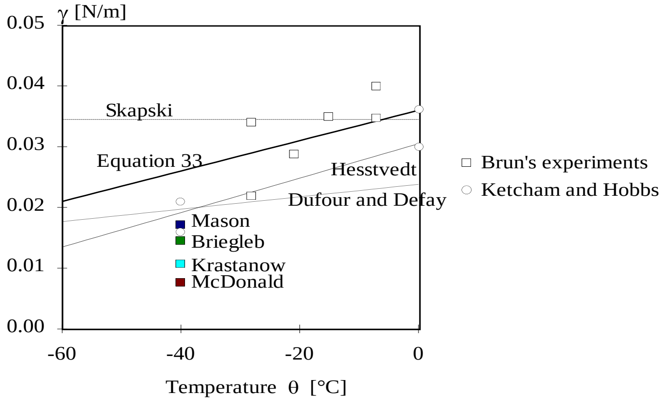

Figure 7. Values of surface tension of the water-ice interphase presented in the literature.

The relationship between ice sphere radius R_n and freezing point temperature θ can be calculated directly by insertion of Equation 33 (γ_{ls}), Equation 27 ($\Delta S_{f,np}$) and v_l from Appendix A into Equation 20. Now all variables in Equation 20 can be expressed as a function of temperature, and numerical integration is possible. The relationship between the ice sphere radius and temperature according to Equation 20 can be expressed by the following quadratic equation with good accuracy:

$$R_n = \frac{2 \cdot (36 + 0{,}25 \cdot \theta)}{1{,}222 \cdot \theta + 0{,}0068 \cdot \theta^2 - 8{,}67 \cdot 10^{-7} \cdot \theta^3} \tag{34}$$

The ice sphere radius as a function of nucleation temperature is strongly dependent on the assumptions made in the evaluation of surface tension of the water-ice interphase. Equation 34 gives clearly smaller values than do equations based on surface tension of the liquid-vapor interphase, e.g. FAGERLUND's expression (FAGERLUND 1973). Figure 8 compares the ice sphere radius from Equation 34 with those found in the literature. It shows that the curves calculated from Equation 34 differ only slightly from that calculated according to BRUN. This is because, although the entropy in BRUN's presentation differs markedly from the value used in Equation 34, its effect is compensated by the higher surface tension.

When the ice sphere radius R_n is expressed as a function of temperature depression, the pore size R_p can be expressed by adding the values of the adsorbed water layer and the liquid-like layer from Equation 30 to the value of the ice sphere radius. For a spherical pore shape and generally always during nucleation, R_n is taken directly from Equation 34. In the case of fusion, for the cylindrical pore model the multiplier 2 in the numerator of Equation 20 vanishes according to Laplace's equation. The curves for the spherical and cylindrical pore radii in the case of nucleation, and for the cylindrical pore radius in the case of fusion, are presented in Figure 9. Since summing Equation 30 into Equation 20 gives a very complex formula, the direct relationship between temperature depression and pore radius during nucleation and fusion are given by Equations 35 and 36 respectively.

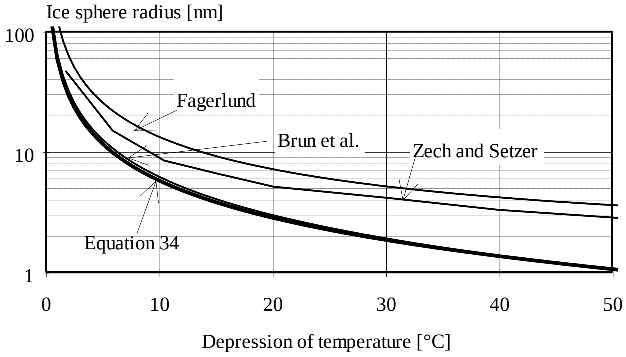

Figure 8. Comparison of the ice sphere radius calculated from Equation 34 with those presented in the literature.

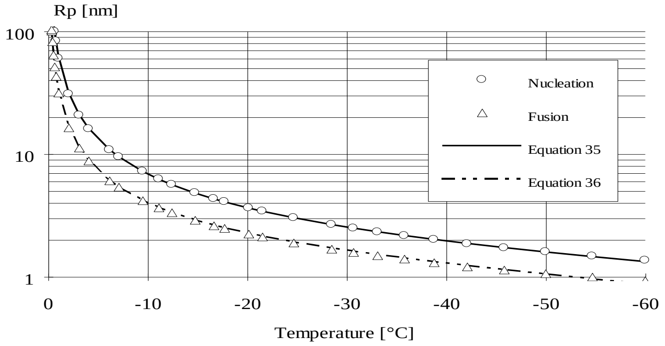

Figure 9. Pore radius R_p at nucleation and fusion for a cylindrical pore.

$$R_{p_n} = 0.584 + 0.0052 \cdot \theta - \frac{63.46}{\theta} \qquad (35)$$

$$R_{p_f} = 0.757 + 0.0074 \cdot \theta - \frac{33.45}{\theta} \qquad (36)$$

In Equations 35 and 36 $R_{p,n}$ and $R_{p,f}$ are the values of the pore radius for nucleation and fusion in nm, and θ is the temperature in °C.

4.2.5 Calculation procedures

The heat flow thermogram measured calorimetrically can be converted to the apparent heat capacity by the following equation:

$$c_p^s = \frac{H_f}{\dot{T} \cdot g_{ssd}}$$

(37)

where c_p^s is the apparent heat capacity of the specimen [J/°C/g], H_f is the heat flow [mW], $\dot{T}$ is the rate of block temperature change [°C/sec] and g_{ssd} is the weight of the saturated surface dry specimen [mg].

Procedures presented in the literature

Sellevold, Bager and le Fonteney have developed a set of methods to calculate the amount of total freezable water and the water content freezable at specified temperatures. The method involves two different principles called "The increment method" and "The total method" (Sellevold and Bager 1980, le Fontenay and Sellevold 1980, Bager 1984, and Hammer and Sellevold 1990). These methods assume that there is no freezable water in the porous cement paste below -55° C. In the "Increment method" the baseline between the first freezing point and -55° C is formulated using linear temperature dependence of the heat of fusion as follows:

$$W_a^f(\theta) = 79{,}3 + 0{,}53 \cdot \theta$$

(38)

where $W_a^f(\theta)$ is the heat of fusion at temperature θ (cal/g) and is the temperature in °C. In the "Increment method" the baseline is obtained after iteration, and the total amount of ice formed during freezing and the distribution of ice over the temperature range can be calculated. In the "Total method" the total amount of ice formed between 0° C and -55° C can be calculated without making any assumptions regarding the temperature dependence of solidification or fusion energies, assuming that all ice is formed at 0° C. Then the heat capacity of the specimen decreases by the magnitude of the difference between the heat capacities of water and ice at 0° C (Bager 1984, p. 11). The baseline can now be formulated by a straight line between the apparent heat capacity of the specimen at - 55° C and the decreased heat capacity at 0° C, and the total amount of heat evolved during freezing is the difference of the integrals between the curves of specific heat capacity of the specimen and the baseline from -55° C to 0° C. The amount of ice can now be calculated by dividing the total heat capacity by the heat of fusion of ice at 0° C. In the "Total method" the first estimate for the amount of ice is the value found by the "Increment method". A couple of iteration cycles are needed to get the final value for freezable water.

Proposed method

Tada (1987, p. 88) studied phase transformations with variable adsorbed film thicknesses and found that no phase transformation occurs up to the second water layer at temperatures down to -190° C but that third to sixth layers are able to change their thermodynamic state already at around -

40° C. ZECH AND SETZER (1989, p. 128) noted during DSC measurements down to -60° C that all the gel water except for one or two molecular layers on internal solid surfaces was freezable. These findings are in accordance with the film thicknesses proposed by FAGERLUND and with the values measured by BRUN. Thus there is the strong evidence that all phase transformations have occurred at above -50° C. This can also be seen from Figure 10, in which the heat capacity curve is linear under the aforementioned temperature.

The linear decrease in specific heat of the specimen at low temperatures is due to changes in the entropy of bulk ice, and to entropy changes in the surface energy between ice and the non-freezable water layer of the pore wall. Also entropy changes in non-freezable water and in the solid components of the specimen affect this decrease in specific heat of the specimen. However, from the literature it can be assumed that the change in entropy of all these parameters behaves linearly along the linear part of the heat capacity curve. Now, if a straight line a-b (Figure 10) is extended up to the higher temperatures, this line crosses the y-axis at point c. If the assumptions taken above are correct, the straight line a-b-c represents the lower limit of the specific heat of the specimen, and the real specific heat capacity curve must lie above this line at all temperatures during the phase transformations.

The upper limit for the heat capacity curve can be constructed in the same way. However, a rough approximation must be made of the change in entropy of supercooled water $d\left(c_p^w\right)/dT$. In the temperature range where this is measurable, it is reported to be linear. CRC (1987, p. D-150) gives the values -0.0018 to -0.0021 J/g/°C^2 in the temperature range -4 to 0° C . In fact, this quantity was measured every time during tests in which no nucleation agent was used. E.g. in Figure 10, $d\left(c_p^w\right)/dT$ is -0.0025 J/g/°C^2 measured by regression analysis over the temperature range -4 to -8° C. In the literature the suspicion has been voiced that the change in entropy of supercooled water at low temperatures is not linear. ANGELL has found very high values of c_p for supercooled water at -38° C (BAGER 1974, p. 12). BAHTIA, PIGEON AND LACHANCE have also reported 25% to 30% higher values for the specific heat of water at -40° C than at 0° C (BAHTIA ET AL. 1989, p. 944). In their tests $d\left(c_p^w\right)/dT$ was constant down to -15° C and thereafter the c_p value of supercooled water increased gradually achieving a value of 5 to 5.5 J/g/°C at -40° C. However, the measuring techniques used in BAHTIA's tests may affect the results. OPC pastes were used, and the linear part between the two clear transition parts of the thermogram was assumed to represent changes in entropies of the paste itself, supercooled water and ice. However, in OPC pastes, it is extremely unusual for the pore structure to separate into two well-defined parts, and no freezing occurs between these areas. Thus the latter results do not give clear evidence of the high specific heat values for supercooled water.

In this study it is assumed that in construction of the upper limit for the specific heat of the specimen, the change in the specific heat of supercooled water is linear also at low temperatures, and the line f-e-d represents the linear regression line determined by the experimental values within the temperature range e-d.

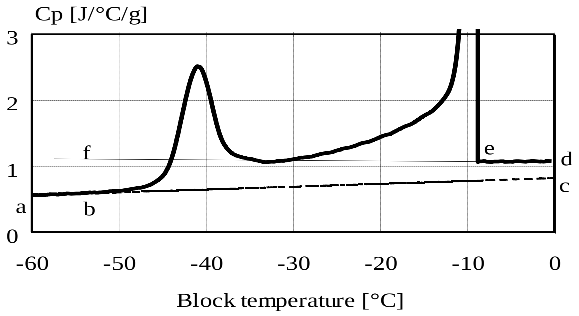

Figure 10. Definitions for baselines in the freezing thermogram

In Figure 10, point c represents the heat capacity of the frozen sample, and point d the heat capacity of the sample before freezing at 0° C. The difference Δc_p^0 in heat capacities from d to c is the amount of ice w_{ice}^0 multiplied by the heat capacity of ice $c_{p_{ice}}^0$ at 0° C. Since the two quantities $c_{p_{ice}}^0$ and Δc_p^0 are known, the total amount of ice formed during the freezing process can be calculated directly. In fact the only condition is that the stability of the thermogram is perfect for fitting of the regression line to c_p-values down from -55° C and in the vicinity of point d. If there is doubt concerning the stability of the curve, the correctness of w_{ice} can be ascertained from the equation:

$$w_{ice} = \frac{\int \left(c_p - c_p^{bl}\right) dT}{W_0} \tag{39}$$

where c_p^{bl} is the specific heat of the baseline bc and W_0 is the heat of fusion of ice at 0° C. If w_{ice} differs from the previous value w_{ice}^0, the stability of the thermogram is not good enough, and a new position must be formulated for the baseline. This can be done simply by calculating the new estimate for Δc_p^0 at 0° C from the equation:

$$\Delta c_{p_1}^0 = w_{ice}^0 \cdot c_{p_{ice}}^0 \tag{40}$$

and correcting the position of point c accordingly. Now the c_p^{bl} values in Equation 39 are replaced by the new $c_{p_2}^{bl}$ values of the new corrected baseline cb, and Equation 39 gives a new estimate for w_{ice} by numeric integration. Only a few iteration steps are needed for 1‰ accuracy in the total amount of ice. SELLEVOLD, BAGER AND LE FONTENAY used the same type of iteration in their investigations. They determined the first estimate of total amount of ice by the so-called increment method described by BAGER (1984).

When the total amount of freezable water was calculated by the method described above, no assumptions regarding temperature dependence of the heat of solidification of water or of the heat of fusion of ice were needed. However, when the evolution of ice during continuous phase transformation over the temperature range 0 to -55° C must be known, the heat of solidification of pore water must be formulated. FAGERLUND has proposed the following linear function:

$$W_a^f(\theta) = 333{,}7 + 2{,}19 \cdot \theta \tag{41}$$

where θ is temperature in °C and $W_a^f(\theta)$ is the fusion heat of ice [J/g]. Formula 41 is used widely. BRUN (1977) has proposed a quadratic equation:

$$W_a^s(\theta) = 332 + 7{,}43 \cdot \theta + 0{,}0556 \cdot \theta^2 \tag{42}$$

that is valid down to -40° C. Equations 41 and 42 differ markedly from each other at low nucleation temperatures under -20° C. Naturally this difference affects also the distribution of freezable water at lower temperatures. The heats of fusion determined from Equations 41 and 42 are compared with the values calculated from Equation 29 (Section 4.2.3) in Figure 2. The effect of entropy changes due to superficial phase transformations is included in Equations 29 and 42. This is why use of these expressions gives lower enthalpy values than FAGERLUND's expression. Since the entropy of superficial phase transformation is a function of pore shape, Equation 29 is valid only in nucleation and for a spherical pore shape in fusion due to the assumptions made in the evaluation of equations. BRUN has also derived a fusion enthalpy (43) for a cylindrical pore shape valid down to -25° C.

$$W_a^f(\theta) = 332 - 11{,}39 \cdot \theta + 0{,}155 \cdot \theta^2 \tag{43}$$

In this study, neglecting the effect of pore geometry, the enthalpy has been calculated in solidification and in fusion using Equation 29'

$$W_a^s(\theta) = 334 + 3{,}49 \cdot \theta - 0{,}0015 \cdot \theta^2 \tag{29'}$$

which is derived from Equation 29 by subtracting the effect of superficial phase transformations on enthalpy. This has been done due to the unpredictability of uncertainties concerning entropy changes caused by superficial phase transformations in fusion, and because the temperature dependence of enthalpy has been applied only to calculations of the distribution of freezable water, not to calculations of total freezable water.

Earlier it was concluded that all freezable pore water freezes between points e and b (Figures 10 and 11). Thus lines bc and ef are the upper and lower bounds between which the zero line (baseline) for the freezing thermogram lies. The baseline between points e and b can be evaluated by iteration. The difference between the ordinates of lines bc and ef represents the total amount of freezable water at a specified temperature. This is illustrated in Figure 11, where w_i is the amount of ice formed during the temperature decrease from point A to point b. The line AC represents the total amount of freezable water w_{tot} and parts AB and BC the freezable water between the temperature ranges A to b (w_i) and e to A (w_{tot}-w_i). When point B has been measured at each measuring point of the heat flow thermogram by iteration, the difference between curve bBe and line bc represents the distribution of freezable water over the block temperature of the calorimeter.

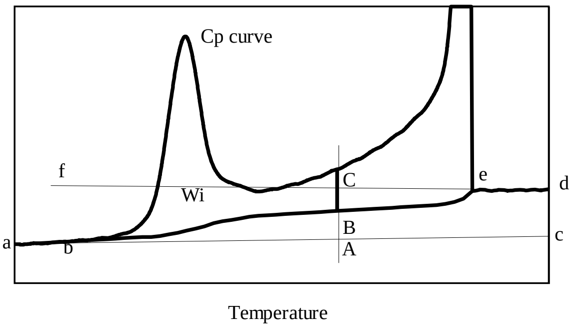

Figure 11. Notation for the calculation procedure in the freezing thermogram.

Freezable water between points A and b in Figure 11 is described as:

$$w = \int_{T_b}^{T_A} \frac{c_p(T)-c_p^{bl}(T)}{W_a(T)}\, dT \tag{44}$$

Since the upper and lower baselines in Figure 11 represent thermodynamic states in which no solidification (line ef) and no fusion (line bc) occur, line AC corresponds to the total freezable water w_{tot}^{LM} measured by the linear method described earlier, and line AB corresponds to the freezable water between points A and b. The ordinate of the baseline (point B) can be determined by the equation:

$$c_p^{bl}(T_A) = \frac{c_p^{ubl}(T_A)-c_p^{lbl}(T_A)}{w_{tot}^{LM}} \cdot \int_{T_b}^{T_A} \frac{c_p(T)-c_p^{bl}(T)}{W_a(T)}\, dT + c_p^{lbl}(T_A) \tag{45}$$

Equation 45 can be solved by numeric integration if $c_p^{bl}(T)$ inside the integral is replaced by the estimate based on linearization of the baseline through the previous incremental points. Using the notation in Figure 12, the freezable water between temperatures T_{i+1} and T_i can be expressed by the equation:

$$w_\mathrm{i} = \frac{\left[c_{p_i} - \left(2 + {}^{\Delta T_i}/_{\Delta T_{i-1}}\right) \cdot c_{p_i}^{bl} + c_{p_{i+1}} + \left({}^{\Delta T_i}/_{\Delta T_{i-1}}\right) \cdot c_{p_{i-1}}^{bl}\right] \Delta T_i}{W_\mathrm{a}(T_i) + W_\mathrm{a}(T_{i+1})} \quad (46)$$

where $\mathrm{c}_{\mathrm{p}_\mathrm{i}}$ and $\mathrm{c}_{\mathrm{p}_\mathrm{i}}^{\mathrm{bl}}$ are the specific heat capacities of the sample and the baseline at point i. $\Delta \mathrm{T}_\mathrm{i} = \Delta \mathrm{T}_{\mathrm{i}+1} - \Delta \mathrm{T}_\mathrm{i}$ and $W_\mathrm{a}(T_i)$ is taken from Equation 29' from which the effect of superficial phase transformations included in Equation 29 was subtracted. Now Equation 44 can be expressed as a sum:

$$w_\mathrm{i} = \sum_{i=0}^{i+1} \frac{\left[c_{p_i} - \left(2 + {}^{\Delta T_i}/_{\Delta T_{i-1}}\right) \cdot c_{p_i}^{bl} + c_{p_{i+1}} + \left({}^{\Delta T_i}/_{\Delta T_{i-1}}\right) \cdot c_{p_{i-1}}^{bl}\right] \Delta T_i}{W_\mathrm{a}(T_i) + W_\mathrm{a}(T_{i+1})} \quad (47)$$

Inserting this into Equation 45 gives the baseline position at point i+1 as follows:

$$c_p^{bl}(T_{i+1}) = \frac{c_p^{ubl}(T_{i+1}) - c_p^{lbl}(T_{i+1})}{w_{tot}^{LM}} \cdot \mathrm{w} + c_p^{lbl}(T_{i+1}) \quad (48)$$

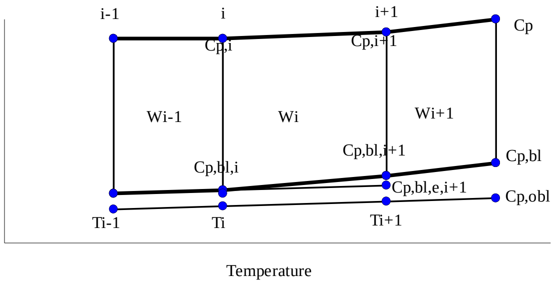

Figure 12. Notation used in Equations 45 to 49.

For the first iteration cycle, $\mathrm{w}_{\mathrm{tot}}^{\mathrm{LM}}$ measured by the linear method is used. For subsequent iteration cycles $\mathrm{w}_{\mathrm{tot}}^{\mathrm{LM}}$ is replaced by $\mathrm{w}_{\mathrm{tot}}^{\mathrm{IM}}$, calculated using the baseline of the former iteration cycle and Equation 44 with integration limits b and e. A few cycles are needed to obtain a stable baseline. Normally five cycles gives an accuracy of 1°/oo for $\mathrm{w}_{\mathrm{tot}}^{\mathrm{IM}}$. The baseline is then corrected by the ratio $\mathrm{w}_{\mathrm{tot}}^{\mathrm{LM}} / \mathrm{w}_{\mathrm{tot}}^{\mathrm{IM}}$. This is necessary since the sample temperature is higher than the detected block temperature. Also, supercooling of pore water lowers the nucleation temperature. Both these factors affect the increase in value of $\mathrm{w}_{\mathrm{tot}}^{\mathrm{IM}}$.

The above calculation method for the distribution of freezable water can be applied directly also for calculations of melting ice using the fusion thermogram.

4.2.6 Discussion of the method

The main differences between the method presented in this study and those described in the literature are as follows:

- The change in entropy due to superficial phase transformations has been included in the total entropy. There is evidence that this can be omitted in calculations of total freezable water by calorimetric measurement (e.g. FAGERLUND 1973, SELLEVOLD AND BAGER 1980), as enthalpy can be regarded as a thermodynamic state property. However, when the pore size distribution is of interest this is no longer feasible. The increasing effect of this additional entropy on the total entropy of the pore system at lower temperatures can be as much as 20%. Because this additional entropy depends on pore geometry, its accurate determination requires a highly complex iterative calculation process. Thus in this study a rough approximation for the superficial entropy increase has been developed using a hypothetical pore size distribution typical of the finest capillary pore structure of cement pastes and mortars.

- The thickness of the liquid-like layer on the ice sphere has been added to the non-freezable adsorbed water layer in the proposed method, although its significance is minor (a few percent in the case of small capillary pores up to tens of nanometers wide, non-existent for coarse capillary pores and gel pores).

- In previous studies (FAGERLUND, SELLEVOLD, etc.), the analysis of pore size distribution was based on surface extension energy due to curvature of the liquid-vapor interphase. In this study the surface tension of the liquid-solid interphase, derived from previously published research data, is used in Laplace's equation. According to the author, this approach is more practical when analyzing fully saturated samples; it affects pore size dimensioning, giving a finer pore structure than the earlier proposals.

The method enables calculation of the freezable water in porous material at different temperatures from the data collected in calorimetric measurements. The pore size distribution can also be calculated with a certain amount of accuracy. The proposed thermoporometric approach is based on the work done by other researchers in the field over the last 20 years, and should be seen only as one application of these, developed for comparative analysis of the porosity of fully saturated samples. The background of the method is very theoretical that arises some drawbacks. Some suspicions whether the Laplace's equation applies on the scale of small gel pores are presented in the literature. Laplace's equation in such applications is not placed on suspicion in this study and its validity is discussed in Section 5.4.3.6. Laplace's equation is used to derive equations of entropy, and later when deriving the relationship between pore size and temperature depression. Furthermore, the values of surface tension for the water-ice interphase are only semi-empirical, and the entropy variation of supercooled water at lower temperatures is somewhat inaccurate.

5 EXPERIMENTS WITH CONCRETES, MORTARS AND PASTES

5.1 EXPERIMENTAL PROGRAM

The effect of aging on the pore structure of concrete was studied by means of tests with concrete, mortar, and paste samples.

The methods used for characterization of the pore structure of concrete were MIP and water immersion tests. Thin section analysis of concrete samples was also performed. Frost-salt tests were performed to investigate the effect of aging on the surface layer of concrete. In addition, compressive strength tests and carbonation tests in different climatic conditions were done to collect data for further service life modeling.

Changes in the composition of aged pastes and mortars were analyzed using TG+EGA, IR, and XRD. Low-temperature calorimetry (LTC) and MIP were used throughout in the studies of pore structure and pore structure changes in pastes and mortars.

Mixes for concretes were designed to give GBFS contents of 0, 50 and 70% of the binder. The water-binder ratio in both air-entrained and non air-entrained concretes varied from 0.35 to 0.75. Mortar mixes were designed so that the aggregate binder ratio corresponded to the fine aggregate (<2 mm) binder ratio of non air-entrained concrete mixes. Mixes for pastes and mortars were cast with water-binder ratios of 0.35, 0.45 and 0.60 and GBFS contents of 0, 50 and 70% of the binder.

The experimental program also included concrete, mortar and paste tests with silica fume additions of 5 and 10%. The results and analysis of these tests are not presented here, nor those of the carbonation rate tests and critical degree of saturation tests of concrete samples.

5.2 CURING PROCEDURES

After demolding at an age of 24 hours, the concrete, mortar and paste samples were exposed for 6 days in a curing chamber at 20 °C and >95% RH. Subsequently the specimens were prepared for different tests and exposed to three different curing procedures.

In curing procedure "Curing 1", also termed "non-aged" or "28 days", the specimens were stored for 21 days at 45% RH before testing. "Curing 2" or "cycled" involved precuring for 21 days at 45% RH, followed by six drying and wetting cycles, each with wetting in water for 1 week and drying at 45% RH for 6 weeks, and thereafter storage at 45% RH until the start of tests at an age of 1 year. The third curing procedure, "Curing 3" or "carbonated" involved storage at 45% RH and atmospheric CO_2 concentration until age 13 months for concretes and 15 months for pastes and mortars. The temperature in all curing procedures was 20° C.

5.3 CONCRETE TESTS

5.3.1 Mixes and properties of fresh and hardened concrete

The mixes used in the tests are shown in Appendix B. The binders for concretes were GBFS and OPC with a prism compressive strength of 16, 34, 43 and 51 MPa at ages 1, 3, 7 and 28 days, respectively. The specific surface area of both binders was 400 m^2/kg (Blaine). The chemical composition of the binders and mineralogical composition of the cement are presented in Appendix B.

The properties of fresh concrete are shown in Appendix B. Air content in air-entrained mixes varied from 2.7% to 6.7% (8.7%) and slump values from 4 to 16 cm. Strength results for different curing procedures and for standard curing are presented in Appendix B. Compressive strength at 28 days varied from 22 to 74 MPa and at age 1 year after repeated wetting and drying cycles from 33 to 92 MPa. Carbonation for 1 year at 45% RH did not visibly increase the strength values of OPC concretes, but the increase in strength of GBFS concretes was remarkable, averaging 16 and 23% for slag contents of 50 and 70%, respectively.

5.3.2 Frost-salt tests

Three series of 100 mm^3 cube specimens were prepared in order to study the effect of carbonation on the frost resistance of concrete. The specimens were prepared from the same mix as specimens for the compressive strength test, capillary suction test, carbonation tests, critical degree of saturation tests and thin section analysis. The curing procedures are presented above (5.2) and the mix compositions in Appendix B.

Selection of a test procedure able to detect changes in the frost resistance of aged concrete is problematic. In ordinary tests for frost resistance, the sample size is too large to obtain a representative aged specimen in reasonable time without the use of accelerated tests. Thus the Finnish frost-salt scaling test was chosen. A series of nine different concretes were also tested using the Swedish scaling test SS 13 72 44. Comparison of the results showed the order of superiority of the concretes to be the same for both scaling tests. The frost-salt scaling test does not directly measure the frost resistance but in this case gives valuable information about the behavior of the surface layer of concrete cured in different ways.

The frost-salt tests were performed according to the Finnish standard SFS 5449. It included freezing in saturated NaCl solution at -15^{o} C and thawing in pure water at $+20^{o}$ C. The saturation time in water at the start of the test was 3 weeks instead of 1 week in the standardized method. Each cycle took 24 hours. Volume and weight changes were measured frequently at intervals of five to 25 cycles to detect changes in scaling as accurately as possible. Tests were started for all mixes at age 28 days (series "28"), and after aging by wetting and drying (series "cy") or by carbonation at RH 45% (series "ca") at age 13 months. Carbonation levels in the specimens were measured by the phenolphthalein method at the start of the frost-salt scaling test using a parallel sample series.

The results of the frost-salt tests for all OPC and GBFS mixes, with or without air-entrainment, are presented graphically as mean values of three test results in Figures 13 to 15, using appropriate scales, and fully in Appendix D. The notation in the figures refers to the mixes presented in

Appendix B. Carbonated volumes of specimens measured from parallel samples are presented in Table 5 of Appendix D.

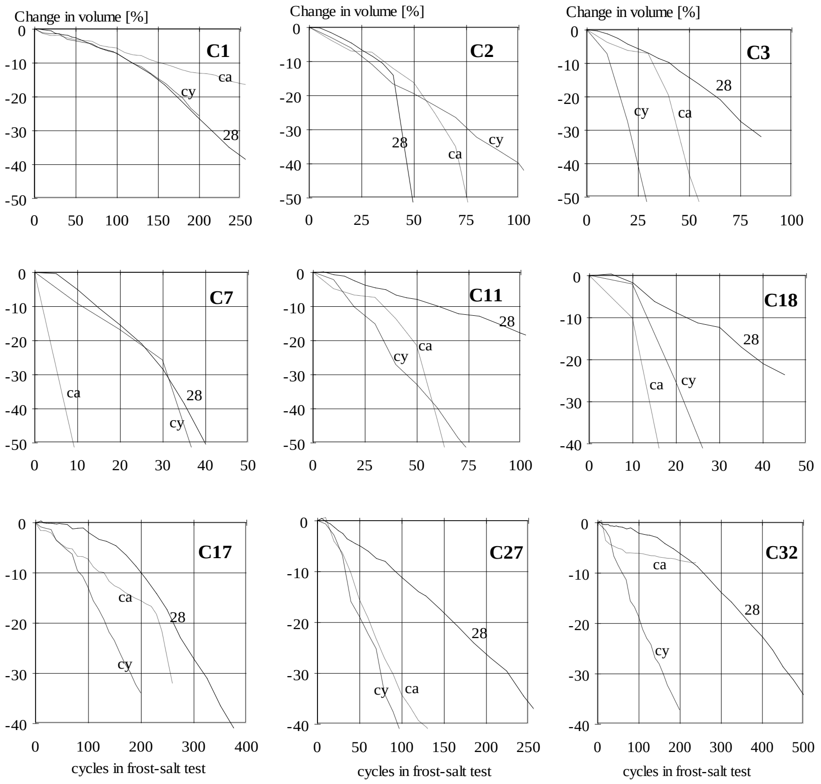

Figure 13. Scaling curves for OPC concretes in the frost-salt test.

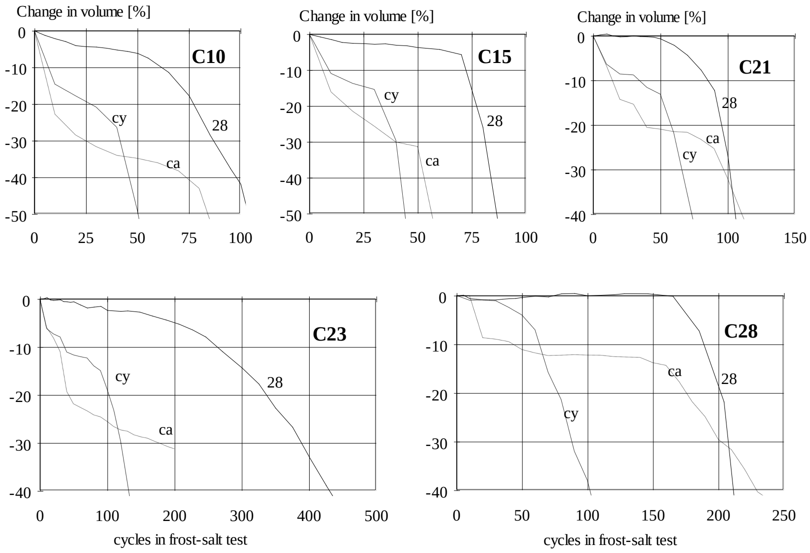

Figure 14. Scaling curves for concretes with 50% GBFS in the frost-salt test.

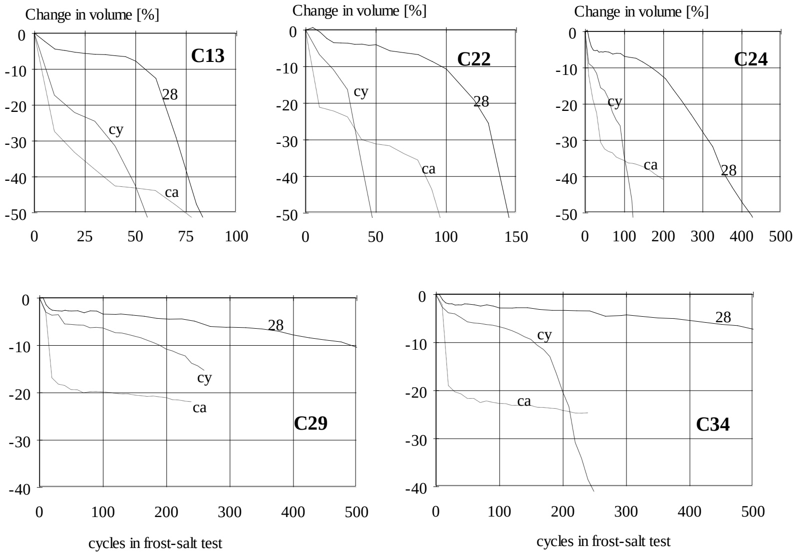

Figure 15. Scaling curves for concretes with 70% GBFS in the frost-salt test.

5.3.3 Water suction tests

The water suction tests were performed on concrete slices 100 • 100 • 25 mm cut from beams 100 • 100 • 500 mm which had been stored after demolding at 95% RH for 7 days. Three slices of each mix were subjected to the three curing conditions described earlier. At the start of the test the samples were dried at 50° C until the daily weight change was less than $5 \cdot 10^{-6}$ times the initial weight of the sample. The limit was achieved for ordinary strength concretes in 7 to 12 days and for high strength concretes within 4 weeks. The slices were totally immersed in distilled water to allow water absorption across the whole surface area of the specimen. This differs from the traditional capillary suction test in which the specimen absorbs water from one side only. The methods were compared with in a series of six different mixes. No deviation in the degree of capillary saturation (S_{cap} in Appendix E) was found between them, and the "capillary" suction time in the traditional test method was fourfold compared with the method used in this study (KALLIO AND MIKKONEN 1992). Thus the edge effect does not seem to play a significant role with the sample size used here. The weight of the specimen was measured after immersion times of 1, 7, 13, 20, 40 minutes, 1, 2, 4 and 8 hours and thereafter frequently up to 4 weeks. Afterwards the specimens were completely saturated at a water pressure of 15 MPa for 1 day and thereafter weighed immediately, followed by drying at 105° C for the determination of total porosity. The carbonated volume and depth of carbonation of carbonated and cycled specimens were subsequently measured by the phenolphthalein method.

The results of the water suction test are presented in the tables of Appendix E. The straight lines (Lines 1 and 2) in the figure of Appendix E were calculated by fitting regression lines to the linear parts of the plots of degree of saturation as a function of the square root time, before and after the nick point. The coordinates of the intersection point of the regression lines were assumed to represent the degree of capillary saturation (S_{cap}) and the time of capillary saturation (t_{cap}).

5.3.4 Mercury porosimetry tests

Samples for mercury porosimetry tests were drilled from concrete beams 100 • 100 • 500 mm stored after demolding at 95% RH for 7 days. The sample diameter was 24 mm and height 20-32 mm depending on the water-binder ratio and air-entrainment. Three samples were prepared for each curing procedure and for each mix. After curing the samples were vacuum-dried for 6 weeks and tested in a porosimeter with maximum pressure 200 MPa. The assumed contact angle was 141.2º and surface tension 0.48 N/m. The minimum measurable pore radius was 3.74 nm.

Pore size distributions of concretes are presented in Figures 17-20 in section 5.4.2 together with the results for paste and mortar samples. Each graph represents the mean of two tests. The porosity of the capillary pore range and the mesopore range, and the total porosity measured in MIP tests are presented for each concrete mix and for each curing procedure in the tables of Appendix F. The capillary and the mesopore ranges are defined in Figure 37.

5.3.5 Thin section analysis

Thin section analysis of concrete samples was performed to study the effect of aging procedures on crack formation, and also to determine the air pore volume of hardened concrete. Thin sections were prepared and the air pore analysis was done at the Building Material Laboratory of the Technical Research Centre of Finland. The crack analysis was performed at the Concrete Laboratory of Helsinki University of Technology.

Specimens for thin section analysis dimensioning 25 • 30 • 50 mm were cut from concrete beams 100 • 100 • 500 mm stored at 95% RH for 7 days. The specimens were exposed at an age of 7 days to the three curing procedures described earlier. Thereafter the specimens were vacuum-treated and impregnated with a fluorescent epoxy. The samples for curing procedures "28 days" and "cycled" were cut from the center line of the sample to exclude the carbonated area. The samples for the "carbonated" curing procedure were cut from the surface part of the specimen. Specimens were polished to a thickness of 25 μm and fixed between glass plates. Thin sections were analyzed by fluorescent and polarizing microscopes.

Crack analysis was done manually by calculating the number of cracks in 150 areas of radius 530 μm. The area was accepted if the aggregate portion was less than 50% of the total area. The highest total number of cracks in 150 areas was given cracking index of 10. The results are presented in Figure 16. One sample with an average number of cracks was analyzed for eight times to study variations in counting. The average cracking index was 4.22, standard deviation 6.6% of the average and the 95% confidence interval 3.99-4.45, showing acceptable repeatability of the method.

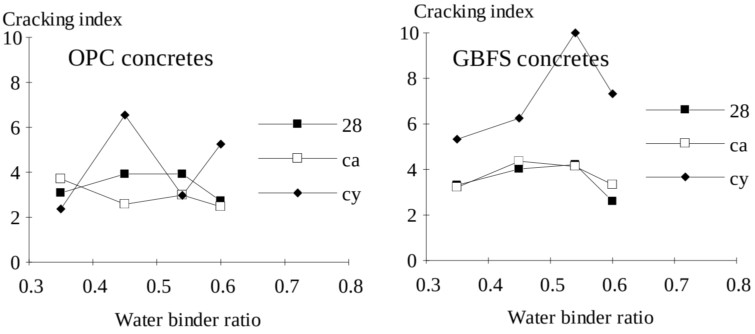

Figure 16. Effect of curing methods on the cracking of OPC and GBFS concretes observed in thin section analysis.

5.4 PASTE AND MORTAR TESTS

5.4.1 Mixes

Paste and mortar mixes were prepared for tests with TG+EGA, IR, XRD, LTC and MIP using the mix proportions presented in Appendix G. Total mixing time was 4.5 minutes and admixture was added after mixing for 1 minute. The pastes were then poured into plastic bottles and rotated for 8 hours to avoid segregation. At age 24 hours the bottles were demolded and the samples exposed in a curing chamber at 20° C and >95% RH for 6 days. Mortar samples were prepared according to the Finnish standard SFS-EN196-1 using 40 • 40 • 160 mm prism molds. Demolding time and precuring conditions up to 7 days as the paste samples.

5.4.2 Mercury porosimetry tests

Samples for MIP tests dimensioning 12 • 12 • 35 mm were cut from the center part of paste cylinders and from mortar prisms stored at 95% RH for 7 days. Three samples for each curing procedure and for each mix were prepared and exposed to the three curing conditions described earlier. After curing the samples were pretreated and tested as for the concrete samples.

Pore size distributions of pastes, mortars and concretes are presented in Figures 17-20. Each graph represents the mean of two tests. The porosity of the capillary pore range and the mesopore range, and the total porosity measured in MIP tests are presented for each paste and mortar mix and for each curing procedure in the tables of Appendix F.

5.4.3 Low-temperature calorimetry tests

5.4.3.1 Preparation of samples

At age 7 days octahedral specimens were cut from the center line of paste cylinders and mortar prisms. This was necessary especially with mortars to avoid segregation and to ensure a homogeneous specimen with regard to the paste content. The specimen size was 12 • 12 • 70 mm with cut-off corners of 1.5 mm. Specimens were exposed to the three different curing procedures described earlier. Specimens for LTC were then weighed and vacuum-treated for 2 days prior to saturation with distilled water. The immersion time in water was 5 days. Thereafter the samples were weighed in water and in the saturated surface dry state in air.

Full saturation of a sample is an essential demand in order to measure total porosity reliably by the LTC method. The validity of the used procedure was tested by MIP. The results showed that no mercury intruded into the sample at a pressure level up to 200 MPa giving an evidence that at least the pores larger than 4 nm by radii are in a state of full saturation.

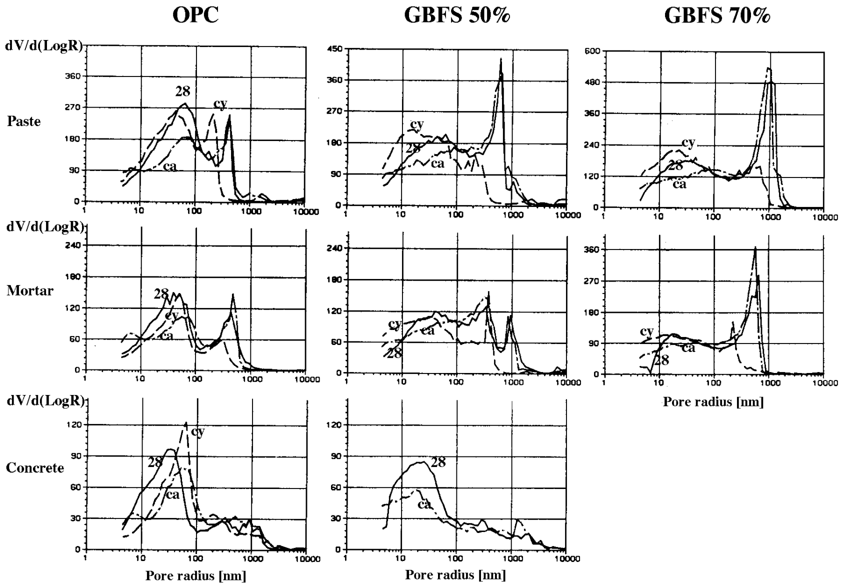

Figure 17. Pore size distribution of pastes, mortars and concretes with a water-binder ratio of 0.60. (Notation: "28" = 28 days curing", "ca" = curing with carbonation", and "cy" = curing with drying and wetting cycles).

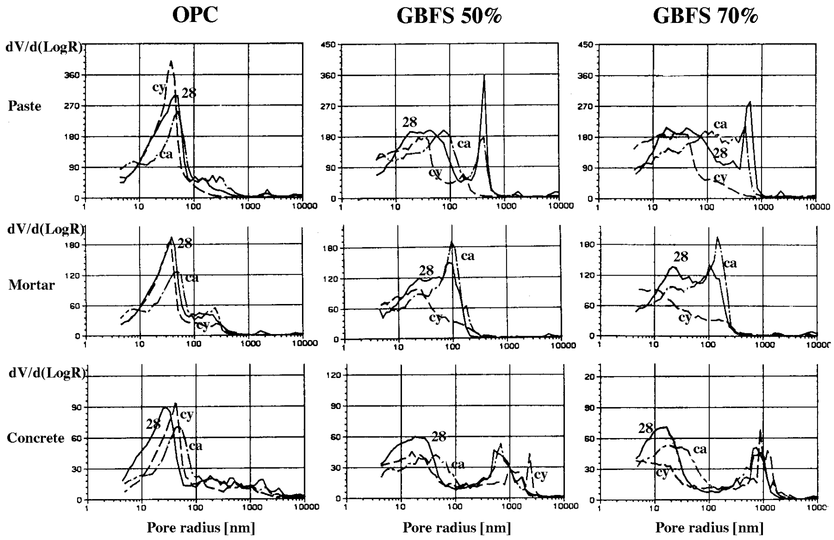

Figure 18. Pore size distribution of pastes, mortars and concretes with a water-binder ratio of 0.45. (Notation as in Figure 17)

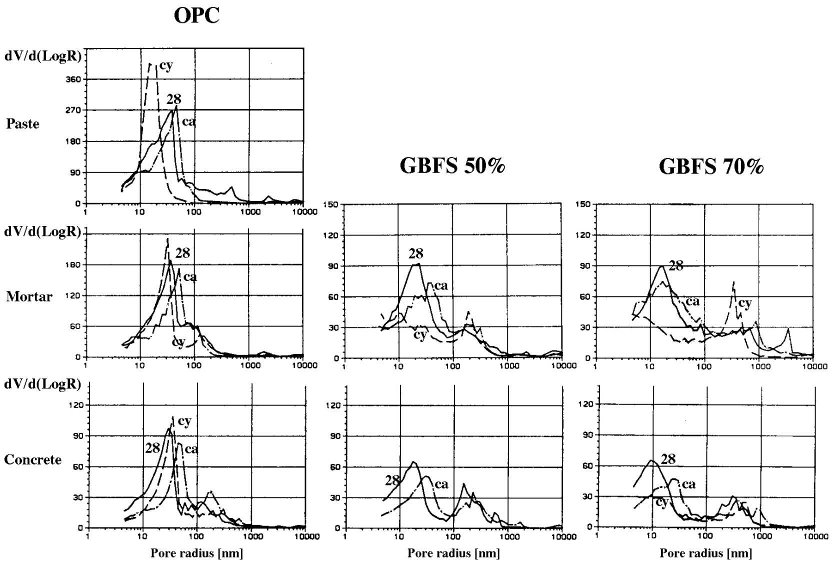

Figure 19. Pore size distribution of pastes, mortars and concretes with a water-binder ratio of 0.35. (Notation as in Figure 17)

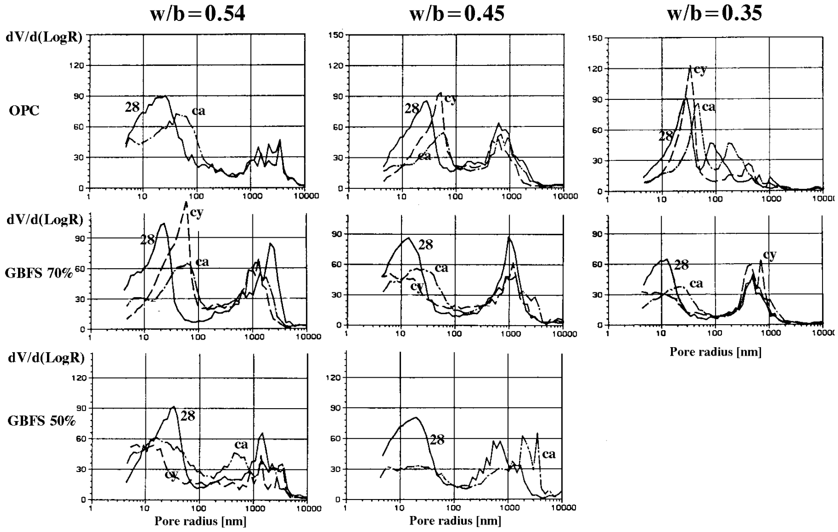

Figure 20. Pore size distribution of air-entrained concretes. (Notation as in Figure 17)

For each mix proportion of the pastes and mortars, one sample was tested in the calorimeter. Some mixes were tested using two parallel samples. The results show good repeatability of the method with both paste and mortar samples.

5.4.3.2 Test equipment and procedure

A microcalorimeter of model CALVET BT 2.15D was used in calorimetric measurements. Facilities included a calorimeter with a liquid nitrogen cooling system and gas circuit equipment, a computerized version of the microprocessor-operated controller (model G11), and a microcomputer to pilot the instruments. A number of computer programs were designed made to transform the output data of the calorimeter into numeric mode and for handling of the results by microcomputer.

Before use the calorimeter was calibrated in isothermal mode at temperatures of 150, 100, 50, 25, 0, -25, -50, -80, -100, -120, -145 and -170° C, and in scanning mode from 20° C to -60° C. To ensure the most accurate calibration, the scanning rate and gas circuit of the sample and reference cells were similar to those used in tests later. Calibration was carried out by a Joule effect calibration device with an applied pulse power of 0.1, 1, 10 and 100 mW into the sample cell. The differential thermopile signal was registered before, during and after a pulse input of 60 minutes at each temperature. The sensitivity of the calorimeter at each temperature is the ratio between the output potential, obtained by integration of the thermopile signal curve, and the input pulse power. A fourth order regression equation for the calorimeter software was evaluated to formulate sensitivity as a function of temperature. The results fitted to this equation well, a determination factor of 0.9993 (R-squared).

A vessel containing the saturated surface dry sample was introduced into the sample cell once the block temperature of the calorimeter exceeded 14° C. Powdered aluminium oxide was used throughout the test series of this study as a reference sample, primarily to compensate for the thermal effect due to the specific heat of the sample. After introducing the sample into the calorimeter, the cell pits were vacuum- treated for 5 minutes. Thereafter nitrogen gas was allowed to sweep the cell pits with a flow rate of 4 l/hour to avoid condensation in the cells during the temperature decrease. Gas flow was constant throughout the test and the same as used for calibration.

At the start of the test the block temperature was kept at 14° C for 1 hour. This time was necessary to stabilize the output signal. The temperature was then lowered at a rate of 3.0° C/hour to -63° C, where it was maintained for 1.5 hours. Thereafter the block temperature was increased at a rate of 4.2° C/hour to 14° C. Using this procedure one test took 47 hours. The procedure was selected for its convenience, as the tests could proceed uninterrupted for periods of 3 weeks. The same type of procedure has also been used, with good results, by other researchers (SELLEVOLD AND BAGER 1980, LE FONTENAY AND SELLEVOLD 1980, BAGER 1984 and HAMMER AND SELLEVOLD 1990).

The heat flow (mW) is the ratio between the output signal of the calorimeter (mV) and its sensitivity (mV/mW). It was registered at a sampling rate of 30 seconds starting from a block temperature of 2° C and ending at 10° C.

After the test the sample was weighed and cut into halves. One was ground immediately for the tests in TG+EGA and IR. The other was dried in a ventilated oven at 105° C to constant weight to measure the rough total porosity of the sample, and thereafter ignited at 1000° C for 2 hours to determine the total amount of non-evaporable water and gases evolved during ignition.

5.4.3.3 Test results

The results of the calorimetry tests are presented in the figures of Appendix H. The graphs involve the baseline corrected values for specific heat capacity as a function of calorimetry block temperature calculated from solidification and fusion thermograms. Solidification thermograms are presented in two parts of representative scaling. In each figure the results of three different curing procedures are shown for the pastes and mortar specimens. Figure 21 is an example of a measured solidification thermogram, with below it the baseline determined by the method presented in Chapter 4. Figures 22 and 23 show the baseline corrected solidification and fusion thermograms of GBFS mortar with a water-binder ratio of 0.35 and slag content 70%, for each curing procedure.

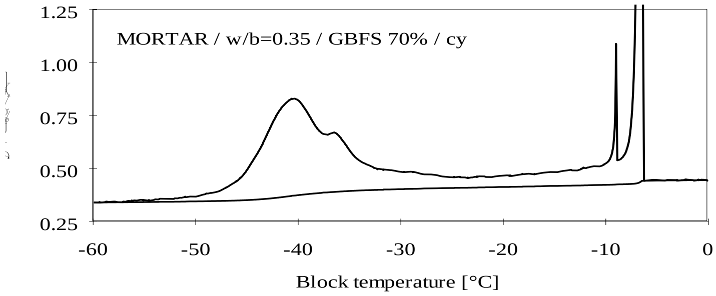

Figure 21. Solidification thermogram with its baseline.

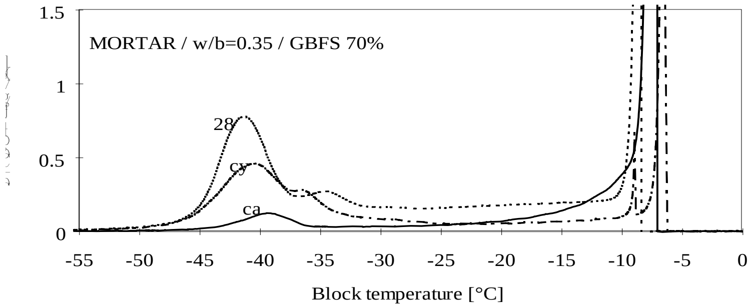

Figure 22. Baseline-corrected solidification thermograms.

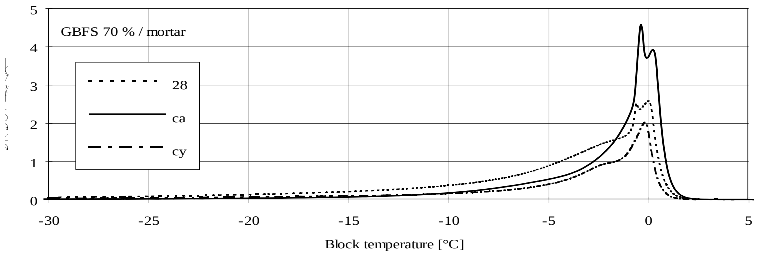

Figure 23. Baseline-corrected fusion thermograms.

5.4.3.4 Porosity and pore size distribution

Freezable water and its distribution over the different pore sizes were calculated using the method presented in chapter 4. The plots of cumulative freezable water as a function of pore radius are presented in Appendix I (example in Figure 24). The derivative pore size distribution is shown in Figure 25, where the amount of non-freezable water is included in the pore volume assuming a cylindrical pore model. The amount of total water content measured by drying at 105° C, total freezable water, and freezable water above -20° C calculated by the developed method are given in Table 4.

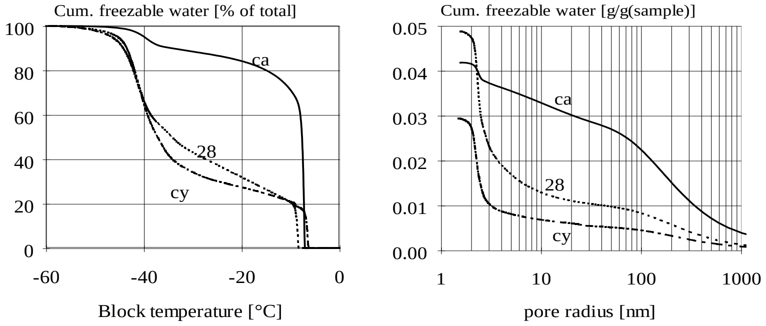

Figure 24. Relative and total cumulative freezable water as a function of calorimetry block temperature and pore radius for mortar with w/b=0.35 and GBFS 70%.

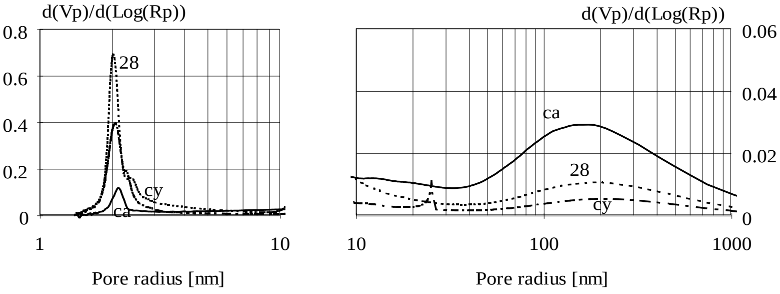

Figure 25. Derivative pore size distribution for mortar with w/b=0.35 and GBFS 70%.

The total water content of LTC samples was also estimated from fusion thermograms. In Table 5 both values are listed for each curing procedure and plotted in Figure 26. Regression lines in Figure

26 and the values in Table 5 show that the calculation method gives slightly higher values for the total freezable water calculated from solidification thermogram. The standard deviation of the difference for the "28 days" curing procedure was 0.002 g/g_{ssd}, giving variation limits +0.002 g/g_{ssd} ...-0.004 g/g_{ssd} at a significance level of 90 %. The total difference at the lowest porosity of 0.05 g/g_{ssd} may vary within the limits +4%... -8% of the value calculated from the solidification thermogram. At highest porosity the variation limits are +1%...-2%. The corresponding variation limits for the curing procedures "carbonated" and "cycled" were higher, being +0.008 g/g_{ssd} ...-0.011 g/g_{ssd} and +0.003 g/g_{ssd} ...-0.010 g/g_{ssd}. One explanation for the smaller values detected by the fusion thermogram is the difference between the block temperature and the sample temperature at the measuring point. The mercury sample nucleated at -41.9° C, giving the difference of 3.0° C between the block and sample temperatures. Fusion took place in a fusion temperature of -38.9° C. In fusion, thawing of the frozen distilled water started at a block temperature of -1.6° C, meaning that the calculation method without any temperature correction must give somewhat higher values for the total freezable water obtained from the solidification thermogram. No specific reason could be found for the higher variation or for the larger difference between the total freezable water detected by fusion and solidification thermograms for the aged samples.

Table 4. Total porosity and freezable water of LTC samples in grams per gram of saturated surface dry sample.

Mix	w/b	Total porosity (w_{105}/g_{ssd})			Total freezable water T>-55° C (g/g_{ssd})			Freezable water T>-20° C (g/g_{ssd})		
		28 days	carb.	cycled	28 days	carb.	cycled	28 days	carb.	cycled
Paste										
OPC	0.60	0.281	0.223	0.253	0.175	0.181	0.163	0.125	0.162	0.138
GBFS 50%	0.60	0.291	0.258	0.246	0.217	0.233	0.198	0.142	0.220	0.170
GBFS 70%	0.60	0.304	0.281	0.271	0.247	0.241	0.225	0.170	0.230	0.200
OPC	0.45	0.223	0.167	0.200	0.117	0.124	0.103	0.070	0.101	0.080
GBFS 50%	0.45	0.240	0.192	0.204	0.157	0.161	0.132	0.085	0.146	0.084
GBFS 70%	0.45	0.248	0.217	0.208	0.185	0.179	0.165	0.113	0.167	0.119
OPC	0.35	0.177	0.139	0.168	0.080	0.078	0.067	0.044	0.056	0.049
Mortar										
OPC	0.60	0.142	0.106	0.119	0.087	0.085	0.071	0.061	0.073	0.057
GBFS 50%	0.60	0.148	0.127	0.128	0.104	0.105	0.091	0.063	0.098	0.062
GBFS 70%	0.60	0.163	0.136	0.123	0.129	0.117	0.100	0.085	0.110	0.082
OPC	0.45	0.108	0.074	0.099	0.053	0.060	0.052	0.031	0.048	0.040
GBFS 50%	0.45	0.116	0.085	0.106	0.070	0.064	0.055	0.035	0.054	0.027
GBFS 70%	0.45	0.122	0.100	0.107	0.089	0.081	0.068	0.052	0.074	0.027
OPC	0.35	0.093	0.072	0.083	0.047	0.041	0.040	0.026	0.030	0.030
GBFS 50%	0.35	0.082	0.055	0.066	0.046	0.034	0.039	0.019	0.024	0.017
GBFS 70%	0.35	0.084	0.054	0.053	0.049	0.042	0.029	0.017	0.036	0.009

Table 5. Amount of freezable water calculated from solidification and fusion thermograms.

Mix	w/b	Curing 28 days		Carbonated		Cycled	
		Sol.therm/ w_{tot}	Fus.therm./ w_{tot}	Sol.therm/ w_{tot}	Fus.therm./ w_{tot}	Sol.therm/ w_{tot}	Fus.therm./ w_{tot}
Paste							
OPC	0.60	0.175	0.179	0.181	0.177	0.163	0.159
GBFS 50%	0.60	0.217	0.217	0.233	0.224	0.198	0.192
GBFS 70%	0.60	0.247	0.247	0.241	0.256	0.225	0.229
OPC	0.45	0.117	0.114	0.124	0.108	0.103	0.097
GBFS 50%	0.45	0.157	0.156	0.161	0.153	0.132	0.132
GBFS 70%	0.45	0.185	0.181	0.179	0.189	0.165	0.153
OPC	0.35	0.080	0.081	0.078	0.076	0.067	0.064
Mortar							
OPC	0.60	0.087	0.085	0.085	0.081	0.071	0.068
GBFS 50%	0.60	0.104	0.099	0.105	0.108	0.091	0.089
GBFS 70%	0.60	0.129	0.129	0.117	0.120	0.100	0.089
OPC	0.45	0.053	0.052	0.060	0.049	0.052	0.049
GBFS 50%	0.45	0.070	0.070	0.064	0.067	0.055	0.060
GBFS 70%	0.45	0.089	0.088	0.081	0.083	0.068	0.067
OPC	0.35	0.047	0.046	0.041	0.040	0.040	0.037
GBFS 50%	0.35	0.046	0.042	0.034	0.033	0.039	0.029
GBFS 70%	0.35	0.049	0.049	0.042	0.041	0.029	0.027

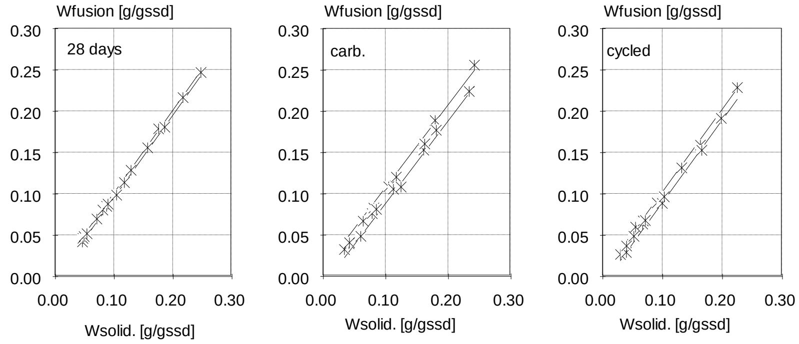

$W_{fusion}^{28days} = 1.008 \cdot W_{solid.}^{28days} - 0.002$ $W_{fusion}^{carb} = 1.022 \cdot W_{solid.}^{carb.} - 0.004$ $W_{fusion}^{cycled} = 0.996 \cdot W_{solid.}^{cycled} - 0.003$

Figure 26. Freezable water contents calculated from fusion and solidification thermograms for different curing procedures with 90% confidence limits.

5.4.3.5 Hysteresis between solidification and fusion thermograms

As a phenomenon, hysteresis is known to exhibit in the imperfectly elastic material systems, in which the reaction of the system to changes is dependent upon its past reactions to change. The phenomenon is clearly noticeable in the characterization of porous systems, especially, by the sorption and capillary methods; e.g. the adsorption-desorption and MIP tests. The facts causing hysteresis in porous cementitious materials are not comprehensively explained, but generally they are associated with the pore geometry and pore continuity. Obviously, the inelasticity and viscoelasticity of concrete have influence on this behavior.

The Equations 35 and 36 and Figure 9 in Chapter 4 bring to light the existence of a strong hysteresis between the solidification and fusion thermograms seen in Figures 22 and 23. If the pore shape is strictly spherical the curvature of ice sphere remains the same when fusion takes place as it was when solidification took place, and the fusion and solidification temperatures are the same (BRUN ET AL. 1977, p.76). On the other hand, if the pore shape is cylindrical the curvature of ice-water interface becomes equal to the inverse of radius in fusion, but in solidification the spherical nucleus grows spontaneously through the cylindrical pore hence the curvature of ice-water interface is two times the inverse of radius. E.g. Equations 34 gives the radius of 1.37 nm for the nucleating ice at -40° C. In fusion, the same ice in cylindrical pore melts at -20.8° C. Obviously, the irregularity of pore system; likely layered than cylindrical shape, may give even higher hysteresis. Another feature in pore geometry which causes hysteresis can be derived from the differences in solidification and fusion energies. Solidification enthalpy (Equation 29) is dependent on the enthalpy caused by the entropy changes due to the superficial phase transformations. This, on the other hand, is strongly dependent on the pore geometry, as discussed in Chapter 4. If this effect is included in the consideration above, the ice formed in cylindrical pore at -40° C melts at -17° C.

Hysteresis between the solidification and fusion thermograms was considered above starting from the irregularities of the pore geometry only. Although the pore shape explains a quite representative part of hysteresis there exist possibly also other facts. ENÜSTÜN ET AL. (1978, p. 514) are proposed that melting is controlled by the radii of cavities and the freezing by the radii of openings between the cavities. They state that since, by geometric necessity, the latter radii are on the whole smaller than the former, the model may form a basis for a theory to explain the observed freezing-melting hysteresis. In terms of this plastic ice theory, capillary freezing and melting take place by virtual movement of the ice-water interface along the capillary channels (ENÜSTÜN ET AL. 1978, p. 510). The same type of hypothesis for the freezing-melting hysteresis is proposed later by SELLEVOLD AND BAGER (1980, p. 395). They present that the spreading of the ice front through a pore system with variable cross sections would be controlled by the pore necks and the melting by the sizes of pores rather than of the necks, and hence, the hysteresis gives information about the continuity of the pore system.

Whatever the reasons for the hysteresis are; the pore shape, the pore continuity or some other reasons, the fact is that the direct calculation of pore size distribution from the fusion thermogram is unrealistic. This can be seen from Figure 27. There the freezable water and melting ice are shown as a function of pore radius calculated by Equations 35 and 36 assuming the spherical and cylindrical pore shape. Equation 35 was used in the solidification thermogram for both pore models and in fusion for the spherical model. Equation 36 was used in fusion for the cylindrical pore model. Hysteresis is very strong with the non-aged OPC and GBFS 70% pastes in spite of the pore model. Aging, here the carbonation treatment seems to reduce the hysteresis reflecting the changes in pore structure; the diminishing of the finest pores and/or the increased pore continuity in terms of the elimination of the pore necks.

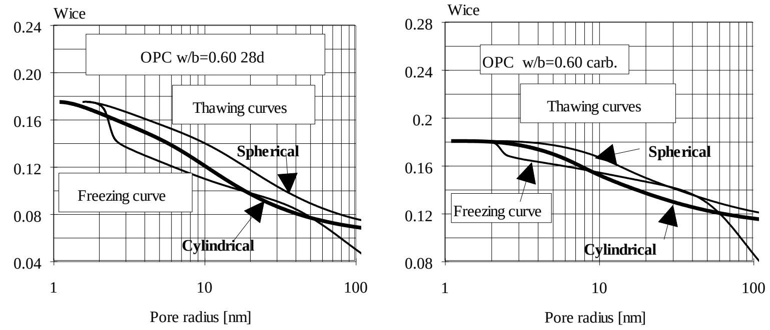

a) OPC paste, non-aged and carbonated

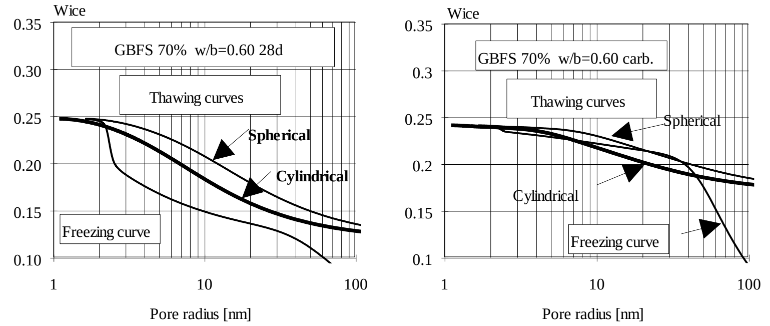

b) Paste GBFS 70%, non-aged and carbonated

Figure 27. Hysteresis in pore size distribution curves derived from the solidification and fusion thermograms of the non-aged and carbonated pastes. Pore radius in fusion for the spherical pore shape is calculated from Equation 35 and for the cylindrical shape from Equation 36.

It is interesting to compare the hysteresis observed in the LTC runs to the hysteresis found in the MIP results of the same mixes. Of course, the MIP results in Figure 28 represent only the pores wider than 4 nm when the suggested smallest pore radii detected by the LTC runs were in the range from 1.5 to 2 nm. Two very clear differences in the hysteresis loops between the two methods can be found. Firstly, the loops with the MIP method are much wider than the estimated loops for the same pore range in the LTC method. Secondly, the aging treatment does not seem to affect on hysteresis with the GBFS paste at all and with the OPC paste only slightly. This reflects the possibility that the pretreatment of the non-aged MIP samples is caused some changes in pore structure.

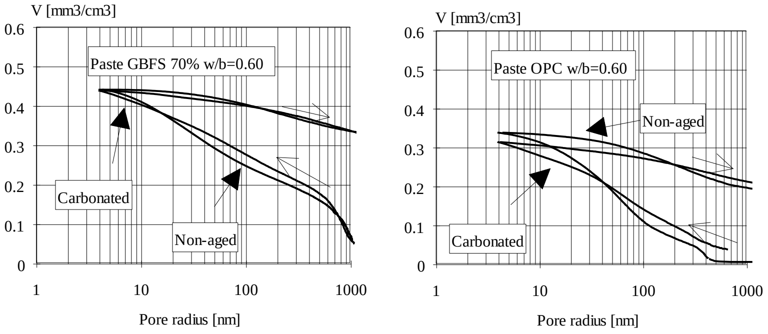

Figure 28. Cumulative pore size distribution curves of the non-aged and carbonated OPC and GBFS 70% pastes and the corresponding return curves in the MIP test.

The results and discussion above shows that the analysis of pore size distribution on the basis of fusion thermograms is not possible using the single fusion thermogram. SETZER has recently presented a cyclic scanning method for DSC to analyze the fusion thermograms. In the procedure cooling and heating cycles were measured between 20° C and a lower reversal temperature. The reversal temperature was increased with every time from - 70° C to 0° C in steps of 2° C. The difference curves were obtained by subtracting two adjacent fusion thermograms; in the plot of Figure 29 they are characterized by the two reversal points (SETZER 1990, p. 423).

In Figure 29 SETZER gives the fusion thermograms determined by four different reversal temperatures. Figure shows that ice, formed in freezing from -40° C to -55° C, melts in a very large temperature range giving a detected fusion heat at -35° C to -5° C in the DSC run (the shaded area in Figure 29). Further, the subtraction of the curves -40/30° C and -30/20° C gives the difference curves between the temperatures -20° C to 0° C and -10° C to 0° C, respectively. Further, the difference of the fusion thermograms with the reversal temperatures of -40° C and -38° C (marked -40/38° C in Figure 29) has a distribution between the temperatures from -25° C to -3° C and a peak at - 10° C. Evidently, the distribution of the difference curves is dependent on the experimental conditions, especially on the size effect of the sample and on the rate of temperature change in the run. Figure 29 gives some evidence of the effect of pore shape on hysteresis discussed above. There it was calculated according to the theory of Chapter 4 that the ice formed in cylindrical pore at -40° C melts at -17° C. In Figure 29 the mean of the shaded area coincides to the latter temperature giving a slight strengthening for the theory used in Chapter 4.

The above consideration shows that in theory the fusion thermogram can be analyzed also with respect to the pore sizes. Hence, the effect of supercooling of pore water being evident in solidification could be eliminated. However, the use of SETZER's cyclic scanning method in the LTC method used in this study was impossible. One test with a single run from 14° C to -63° C and backwards to 14° C took 2 days. A cyclic scanning method would take 2 months per each sample in practice meaning the uninterrupted testing time of more than 10 years for the reported LTC results of this study. These were the reasons why the pore size analysis was done by the solidification thermogram, although also there exist various limitations for the reliable interpretation of the thermogram. Fusion thermograms were used only to certify the total freezable water calculated from the solidification thermogram by the calculation procedures presented in Chapter 4.

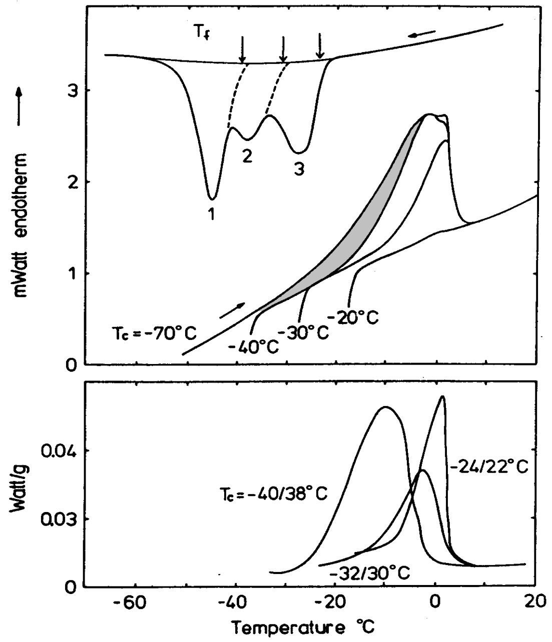

Figure 29. DSC plots of the scanning cycles with different reversal temperatures of -70, -40, -30 and -20° C and three difference plots of fusion curves. OPC paste, w/b=0.50, stored at 96% RH. Replotted from SETZER 1990, p. 424.

5.4.3.6 Pore size distribution by the solidification thermogram

In the determination of the pore sizes according to Equation 35 it was assumed that the Laplace's equation is valid also at small pore sizes. The solidification thermograms in Appendix H show that the secondary peak exists at -40° C if the lag between the block and sample temperatures is considered (see Section 5.4.3.4). This peak denotes the pore radius of 2 nm and the radius of nucleating ice about 1.4 nm.

In the literature, e.g. SELLEVOLD AND BAGER (1980) and SIDEBOTTOM AND LITVAN (1971, p.2735), it is discussed that application of the capillary theory in small pore sizes may be questionable. These suspicions are based on the theories to explain the freezing phenomenon in porous saturated material. The former is presumably derived from Everett's theory which explains the solidification process by the progressive penetration of the solid phase as discussed in the context of hysteresis, and the latter is based on Litvan's theory which explains the solidification to take place always at 0° C and the observed melting below 0° C to be due to anomaly (Litvan 1972b, p. 40). The both theories explain the freezing phenomenon without any dependence between the temperature depression and pore size. In Everett's theory ice tend to form simultaneously in all pore sizes in the same temperature. BRUN ET AL. (1977, p.63) have criticized the theory since it does not account by itself for the solidification observed in an unsaturated material in which only the smaller pores are filled with water; neither does it apply to a material with ink-bottle shaped pores. On the other hand, ENÜSTÜN ET AL. (1978) have proved by calculations that Litvan's theory cannot be true in saturated material. Furthermore, Litvan's theory explains that solidification occurs through evaporation of water followed by condensation into ice outside the material and inside the larger pores. Possibly, the process occurs if the vapor phase exists, but again, in the saturated state this phase does not exist.

Two strong evidences of the solidification by nucleation and of the relationship between the temperature depression and pore size can be found in the literature. First, it is widely accepted that all the gel water except for a couple molecular layers on internal solid surfaces is freezable in temperatures used in this study (Litvan 1972a, Tada 1987, Zech and Setzer 1989 and Setzer 1990). Tada's finding that third to sixth layers are able to change their thermodynamic state already at around -40° C fits nicely on the estimated gel pore radius of 2 nm presented above. Further it is stated that an *in situ* freezing in gel pores is possible since there is an unfrozen adsorbed layer between the surface of the matrix and the pore ice which reduces the change in surface energy on freezing (Setzer 1990, p.417). Some evidence of the freezing of gel pore water can be found from the study where the gel pore volume of high strength pastes were determined by the LTC method and by the N_2-gas adsorption method. Both methods gave the same pore range for gel porosity as Figure 30 shows (Matala 1995).

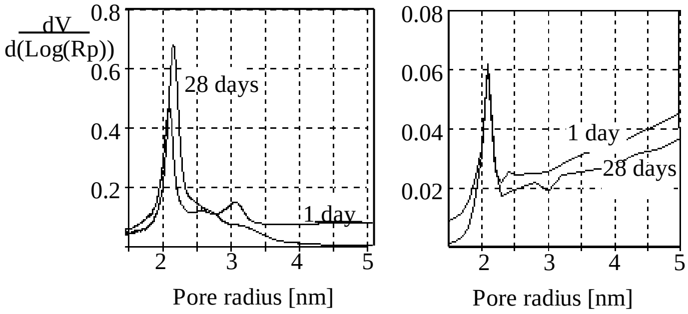

a) Low-temperature calorimetry b) Nitrogen gas adsorption

Figure 30. Derivative pore size distribution by two different test methods for high strength pastes after 1 and 28 days water curing (Matala 1995).

Perhaps the strongest evidence of the applicability of the Laplace's equation also at gel pore range can be found from the investigation in which the solidification is studied with materials of the known pore sizes; Vycor glass of 2.4 nm pore radius and five alumina porous plugs with the pore radii of 3.2, 3.4, 5.0, 9.5 and 10.5 nm (Brun et al. 1977). When water was used as condensate the temperature depressions given by the peak of the solidification thermogram were -28, -28, -21, -15, -7 and -7.1° C, respectively. The results show that the phase transformation occurs in the smaller pores, the higher the temperature depression is, and that the correlation between these parameters is very strong. Equation 35 derived in Chapter 4 gives the pore radii of 2.7, 3.5, 4.7 and 9.6 nm in the solidification temperatures of -28, -21, -15 and -7° C being extremely well in accordance with the experimental values.

Consideration above shows the validity of Equation 35 in the calculations of pore size distribution by solidification thermograms and that the gel porosity is possible to estimate by the LTC method. However, it should be remembered that the whole solidification heat observed at -40° C does not consist of the heat caused by the nucleation of gel pore water as discussed in Chapter 4. It comprises also the heat output of the superficial phases; i.e., the adsorbed water layer of larger capillary pores, the thickness of which decreases in temperatures below the pore nucleation temperature.

5.4.4 Thermogravimetry tests and evolved gas analysis

5.4.4.1 Sample preparation and test procedure

TG+EGA were used to determine the degree of hydration and the degree of carbonation in non-aged and aged paste and mortar samples. Since the porosity was studied with MIP and LTC, the TG+EGA tests were performed with parallel samples for both porosity tests. The first series comprised samples of the same size and cured in the same way as those tested by the MIP method. The second series was prepared from the pastes and mortar samples used in the LTC test by grinding half of the sample and subjecting directly to TG+EGA. These two series involved paste and mortar samples with three different water binder ratios of 0.35, 0.45 and 0.60 and GBFS contents of 0, 50 and 70%, cured with the three different procedures described in section 5.2. The third series was prepared for measurement of the degree of hydration at 28 days. The samples for this series were cured for 28 days at 95% RH, ground to powder and subjected to TG+EGA. The precuring, preparation, and the notation of samples for the TG+EGA test are shown in Table 6.

The evolved gases H_2O, CO_2 and SO_2 were analyzed and measured simultaneously with the TG run by a Fourier transmission infrared spectrometer. The powdered 120 mg sample was first dried in the TG for 20 minutes at 50° C. Thereafter the temperature was increased linearly at a rate of 20° C/minute to 110° C followed by a 5 minute pause before increasing the temperature to 1100° C at a rate of 20° C/min. Helium was used as a protective gas in the TG+EGA test. The collection of IR scans during the TG run, transforming and converting the scans into an absorbance spectrum, and handling the spectrum are described in detail by PENTTALA (1992 p. 90). The detection limits for H_2O and CO_2 were 0.2-0.4 µg/s and 0.04 µg/s, respectively.

Table 6. Preparation of samples for TG+EGA, and corresponding MIP and LTC porosity tests

Series	Notation	Curing combination	Size of sample mm^3	Corresponding porosity tests
Series 1	28 days / dry	C1+C2	12·12·35	MIP
	ca / dry	C1+C4+T2	12·12·35	MIP
	cy / dry	C1+C3+T2	12·12·35	MIP
Series 2	28 days / wet	C1+C2+T1+LTC test	12·12·70	LTC
	ca / wet	C1+C4+T1+LTC test	12·12·70	LTC
	cy / wet	C1+C3+T1+LTC test	12·12·70	LTC
Series 3	28 days / std	C5+T2	12·12·70	

Curing	Curing conditions
C1	7 days at RH>95%, T=20° C
C2	21 days at RH=45%, T=20° C
C3	six cycles, each 7 days in water and 42 days at RH=45%, T=20° C
C4	15 months at RH=45%, T=20° C, CO_2=0.03%
C5	28 days at RH >95%, T=20° C
T1	Vacuum treatment for 2 days and, water intrusion and storage in water for 5 days T=20° C
T2	Vacuum treatment for 14 days, T=20° C

5.4.4.2 Calibration of IR curves

The results of the IR test can not be used directly in calculations of the degree of hydration or the degree of carbonation. The method gives the weights of each gas as relative values within the specified gas and not within all evolved gases. For this reason the evolved gases in the IR test must be calibrated against the weight losses detected in the simultaneous TG run. Calibration was done within the domain of evolved gases H_2O, CO_2 and SO_2. The combination of test methods enables separation of weight losses due to the gel water from those of carbonates which decompose simultaneously in the same temperature range above 450° C. Furthermore, the calibrated weight curves of CO_2 gas as a function of temperature make it possible to differentiate carbonates obtained with different GBFS contents.

The calibration coefficients for the gases η_H, η_C, and η_S were determined in the three temperature ranges, 110-500° C, 500-800° C and 800-1100° C, respectively. In these ranges the domain gases are H_2O, CO_2 and SO_2, respectively. The correction coefficient of each gas was obtained by solving the compatibility matrix of gases

$$\begin{vmatrix} \eta_H \\ \eta_C \\ \eta_S \end{vmatrix} \cdot \begin{vmatrix} H_2 - H_1 & C_2 - C_1 & S_2 - S_1 \\ H_3 - H_2 & C_3 - C_2 & S_3 - S_2 \\ H_4 - H_3 & C_4 - C_3 & S_4 - S_3 \end{vmatrix} = \begin{vmatrix} w_2 - w_1 \\ w_3 - w_2 \\ w_4 - w_3 \end{vmatrix} \qquad (49)$$

where notation H, C and S corresponds to the values read from the weight curves of the H_2O-, CO_2- and SO_2-gases in the IR test respectively, subscripts 1, 2, 3 and 4 signify temperatures of 110° C, 500° C, 800° C and 1100° C respectively, and *w* is the value of the weight curve at the corresponding temperature in the TG test, according to the schematic representation in Figure 31. In the second step the weight curves of gases in the IR test were multiplied by the correction coefficients to get the corrected gas curves. The sum of corrected gas curves was compared with the weight loss curve observed in the TG test within the entire temperature range 110-1100°C. The calibration was accepted if the sum of corrected gas curves deviated less than 3% from the weight loss in the TG test. The values in the TG tests were calculated as percentages of the ignited weight of the sample.

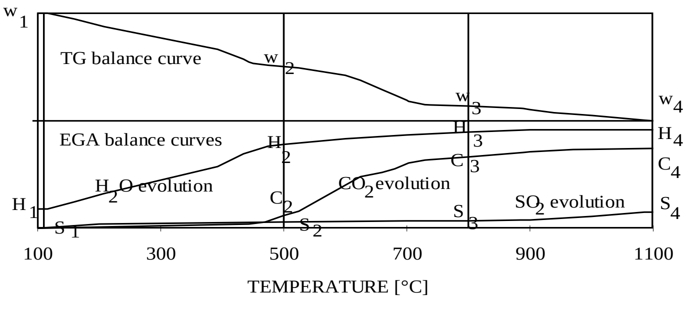

Figure 31. Schematic representation of the TG balance curve and gas evolution curves, and notation for the compatibility matrix of gases.

5.4.4.3 Degree of hydration

Degree of hydration refers to the fraction of cementitous material reacted at a given time. In the literature, several methods to quantify this fraction, directly or indirectly, have been proposed; QXRD, TG, DTG, EGA, DTA, DSC, IR, BSE, NMR and extraction methods (e.g. TAYLOR 1990 and SCRIVENER 1989). QXRD is reported to be the most accurate method, 1 to 3%, to quantify the fraction of the individual, hydrated clinker phases (TAYLOR 1990, p. 204). However, the precision of the technique is much worse when the degree of reaction of the OPC or OPC/GBFS pastes is considered. In this study, TG+EGA were selected to determine the degree of hydration on the basis of non-evaporable water described in the following paragraphs. The method is widely used, despite of its limitations, and the same method was used in the determination of the degree of carbonation in the same non-aged and aged paste and mortar samples.

In principle there are three possible procedures by which the degree of hydration of pastes cured by different methods can be determined with TG. The first is direct measurement of CH by TG. This procedure is useful when no carbonation takes place. In this study this could be applied directly only to OPC pastes and mortars cured for 28 days at RH >95%, since in all other curing procedures the carbonation of samples is possible. Degree of hydration can also be determined by measuring the chemically bound water or non-evaporable water. Chemically bound water has been defined here as a ratio of the loss of water from 110°C to 1000°C to the residue at a later temperature. This definition is sensitive to the delay in the TG run at 110° C. Due to this fact and the knowledge that not all interlayer water is necessarily released at this temperature (e.g. NILSSON 1980, p. 13), a more practical and reliable method is to consider the non-evaporable water content, defined here as the amount of water retained at 160° C. The choice of 160° C as the differentiating limit was based on the fact that all interlayer water and water combined in the AFt phase, and most of the water of the AFm phase, is lost at this temperature (TAYLOR 1990). These two latter definitions for the degree of hydration are not directly applicable to carbonated samples, since carbonation of the CSH gel releases chemically bound and non-evaporable water that evaporates or takes part in further hydration.

Another problem in measuring the degree of hydration is to define the non-evaporable water at full hydration, especially when GBFS is used as a binder. In this study the values presented in the literature were used. First, the non-evaporable water for full hydration of OPC $w_{cb_\infty}^{Bogue}$ was calculated from the Bogue equation (LEA 1980, p. 114). Thereafter the values for GBFS were obtained by the ratio $w_{cb}^{GBFS} / w_{cb}^{OPC}$ calculated using the experimental values published in the literature (HINRICHS AND ODLER 1989, p. 9). HINRICHS AND ODLER have done extensive research on the hydration kinetics of slag pastes. The oxide compositions of binders and GBFS contents in their work were well in line with those used in this study. Since the fineness of cement and GBFS was 400 m^2/kg (Blaine) in this study, the values were interpolated between the finenesses of 300 and 500 m^2/kg used by HINRICHS AND ODLER. The relationship between the chemically bound water of GBFS and OPC at full hydration was 0.900 and 0.755 for slag contents of 50% and 70 %, respectively (Table 7). The same relationships were applied to the mortars.

Table 7. Calculation of chemically bound water at full hydration.

Mix	Fraction of hydrated compounds and chemically bound water at 28 days, after HINRICHS & ODLER						
	Alite [%]	GBFS [%]	α_{28}	w_{cb28}	$\frac{w_{cb_{28}} / \alpha_{28}}{w_{cb_{28}}^{OPC} / \alpha_{28}^{OPC}}$	$w_{cb_\infty}^{Bogue}$ 1)	w_{cb_∞}
OPC	79	0	0.790	0.246	1	0.177	0.177

GBFS 50%	89	54	0.715	0.201	0.900		0.159
GBFS 70%	91	57	0.672	0.156	0.755		0.134

1) Chemically bound water for OPC used in this study includes all except the water of CH

To determine the degree of hydration at a specified age, the chemically bound water and non-evaporable water at 28 days were determined by the TG+EGA method for pastes and mortars cured at RH > 95%. These values were divided by the values of full hydration to obtain the degree of hydration at 28 days α_{28}. The course of hydration with regard to age 28 days was investigated by the ignition method. The paste and mortar samples were cured for 7, 14, 28, 49 and 90 days at RH >95% before testing. Two separate samples were tested at each age. The total loss of ignition at the specified age in relation to the total loss of ignition at 28 days was assumed to represent the course of hydration from 7 to 90 days. This relation α_t/α_{28} has been presented for all compositions in Appendix K. The values of α_7, α_{28} and α_{49} are presented for pastes and mortars in Figure 32.

Variations in the aggregate-binder ratio in mortar samples, and the preparation of samples, cause deviations in the degree of hydration. This deviation was studied by preparing samples from six different mixes. The mix composition represented the lowest consistency observed in the preparation of mortars and pastes with a GBFS content of 50% and water-binder ratio of 0.35. The testing age of these series was 7 days, at which the variation in the degree of hydration was presumed to be highest. The results show that the variation limits for pastes were only ±0.1% of the mean at a confidence level of 90%. The variation limits between mortar samples were clearly higher, as expected, being ±5.01% of the mean. These variation limits are used throughout Figure 32.

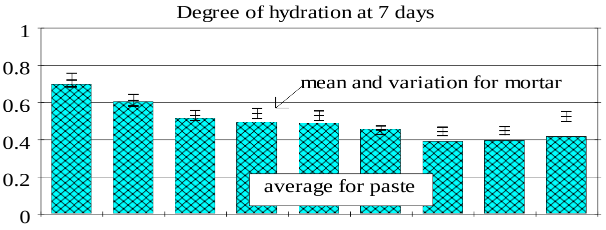

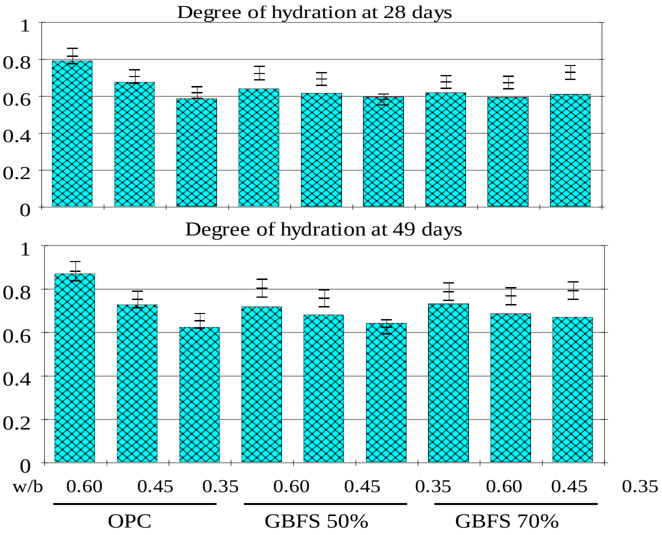

Figure 28. Degree of hydration at 7, 28 and 49 days of paste and mortar samples.

5.4.4.4 Estimation of degree of hydration in aged samples

The degree of hydration of aged samples was estimated in order to calculate the volumetric distribution of different phases, and to determine the degree of carbonation of aged samples. Determination of the degree of hydration in carbonated samples by TG+EGA is possible with a high degree of accuracy if all existing carbonates originate merely from the carbonation of calcium hydroxide. However, when a binder with high contents of GBFS is used carbonation of the CSH gel is evident, and accurate direct determination of the degree of hydration is no longer possible.

In the estimation of degree of hydration in aged compositions, a rough assumption was made that one mole of H_2O is released for each mole of bound CO_2 during the carbonation of CSH gel. If all carbonated hydrates originate from CSH this value should be somewhat lower, at roughly 0.85 as estimated in Chapter 3. Another assumption must be made when considering which part of CO_2 originates from the carbonation of CH and which part from other hydrates. The evolution curves of CO_2 showed that the higher the OPC content, the higher was the CO_2 evolution in the temperature range from 650-800° C, which is the typical decomposition range for well-crystallized calcite. Moreover, calcite is assumed to be the most evident polyform of carbonates originating from CH, which led us to presume that part of the evolution of CO_2 gas in this range is due to decomposition of carbonates originating from CH. Roughly half of CO_2 gases evolved between 650^{o} C and 800^{o} C and all evolving below 650^{o} C, were assumed to originate from the decomposition of carbonated hydrates. Using the aforementioned assumptions, the water of hydrates and that lost due to carbonation can be calculated for each curing procedure by the equation:

$$w_{tot} = [H_2O]_{160\ ^oC<T<1000\ ^oC} - [H_2O]_{CH} + {}^{18}/_{44} \cdot \left([CO_2]_{T<650\ ^oC} + 0{,}5 \cdot [CO_2]_{650\ ^oC<T<800\ ^oC}\right) \qquad (50)$$

where the subscripts denote the temperature ranges of the TG+EGA test. The degree of hydration for the "28 days" curing procedure was taken directly as a value of 7 days of hydration, and for the curing procedures "cycled" and "carbonated" it was calculated from the equations

$\alpha^{ca} = \left(w_{tot}^{ca}/w_{tot}^{28\,days}\right)\cdot\,\alpha^{28days}$ and $\alpha^{cy} = \left(w_{tot}^{cy}/w_{tot}^{28\,days}\right)\cdot\,\alpha^{28days}$. The values of the degree of hydration for each curing procedure are given in Figure 33.

Comparison of values for the degree of hydration between non-aged and cycled-cured specimens leads us to suspect that the applied method slightly underestimates the development of hydration in OPC mixes, and perhaps overestimates that in GBFS mixes. The most probable reason is the assumption regarding the carbonates precipitated from the CH phase. Possibly the 50% fraction of carbonates decomposed in the temperature range typical for calcite is too high for GBFS binder and correspondingly too low for OPC. Hence, the approximation given by this method is more on the safe side concerning fractional phase calculations in which values of the degree of hydration are needed (see Section below).

5.4.4.5 Degree of carbonation of aged samples

The degree of carbonation of samples tested with LTC was defined as the ratio of the total amount of CO_2 gases evolved in the TG/EGA test to the maximum CO_2 content possible to combine with the oxides of Ca, Mg and alkalis of the binders. The oxide content able to carbonate was assumed to be directly related to the degree of hydration. The results are shown in Appendix M, together with the calculated volume fractions of unhydrated material, carbonates (ρ=2.73 g/cm^3), calcium hydroxide

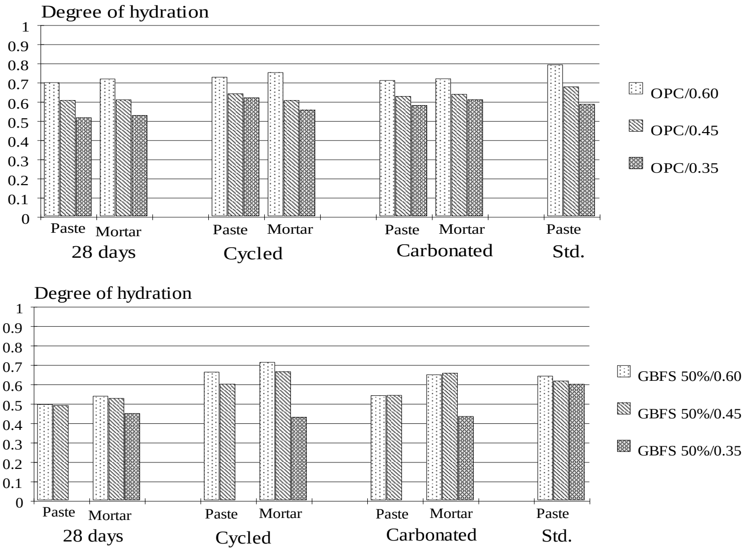

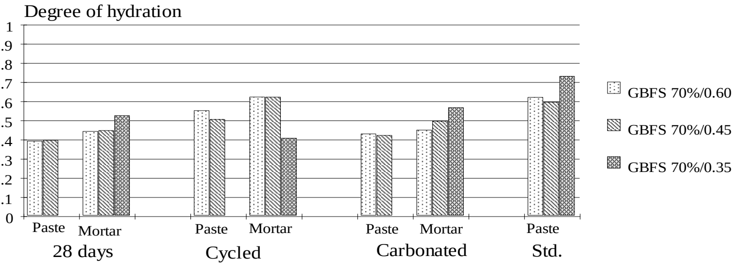

Figure 33. Degree of hydration of aged samples with OPC, GBFS 50% and GBFS 70% binders.

(ρ=2.24 g/cm3) and hydrates. Volumetric calculations have been done only in order to determine the volume fraction of carbonates in a specified tested sample. Thus the results should not be generalized as a reliable description of the distribution of different phases in OPC and GBFS pastes and mortars. The level of carbonation in samples carbonated at RH 45% for 15 months in a laboratory atmosphere appears surprisingly high. This is due to the small sample size of 12 mm by side. This also caused other problems: The degree of carbonation in samples cured only for 3 weeks in the above mentioned circumstances was also unexpectedly high, especially at high water-binder ratios. Thus the state of these "non-aged" samples also included certain carbonation and drying in the gel structure as discussed in Chapter 6.

Total carbonate content of samples

Carbonates expressed as weight percents of $CaCO_3$ of the ignited weight of the paste fraction in samples are presented in Figure 34. The values do not include carbonates in unhydrated binders, since CO_2 evolution from blank TG+EGA runs with unhydrated binders was subtracted from the results of the hydrated sample tests.

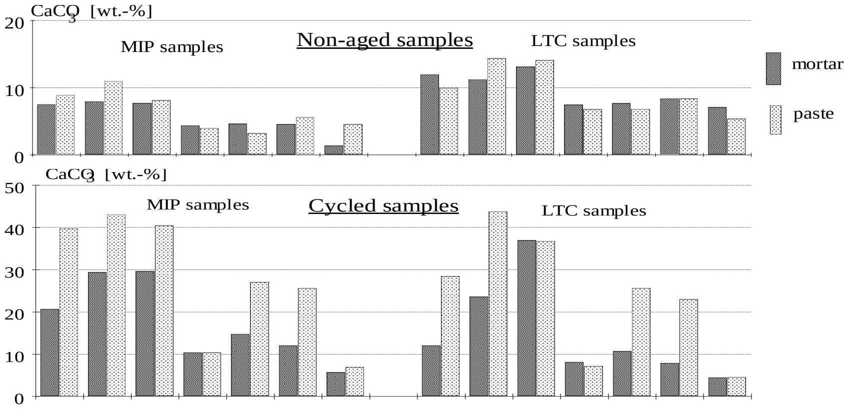

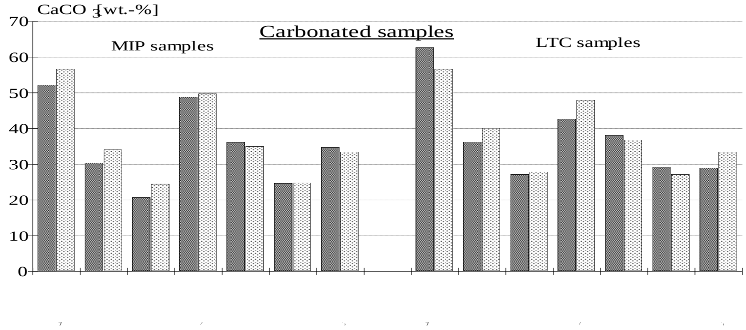

Figure 34. $CaCO_3$ contents for paste and mortar samples cured by different methods.

Figure 34 shows that the level of carbonation in LTC samples differs from that in reference samples for the MIP test, even though the specimens were prepared from the same mix and the curing conditions were identical. The differences between the means of ratios of the amounts of carbonates in LTC samples to those in MIP samples were studied statistically. In the calculations the populations of mortars and pastes, both cycled and carbonated, were compared using the t-test. The results in Table 8 show that the curing procedure has a significant effect on the ratio of $CaCO_3^{LTC} / CaCO_3^{MIP}$. In cycled specimens the mean of the ratios was 0.82, denoting a higher carbonate content of MIP samples and in carbonated samples 1.12, indicating lower content. The only explanation for this lies in the differences in precuring of samples before testing: MIP samples were vacuum-dried for 2 weeks before the TG+EGA test. It is very possible that cycled samples, having a higher chemically bound water content than carbonated samples, lose the relatively higher part of water calculated as a part of that in vacuum drying. This explanation is reasonable if the amount of carbonates is calculated from the initial weight, but not when all values are calculated on the basis of ignited weight, when the effect of water loss on carbon loss is eliminated. Also, it is possible that during the prolonged hydration some portion of the carbonates have transformed to a form which does not decompose totally below 1100° C in LTC samples ground in a wet condition, but which can decompose in MIP samples ground in the dry state after vacuum treatment for 2 weeks. Some evidence of this is found in the greater loss above 800° C. The total loss between 800° C and 1100° C was about 15% lower for LTC samples than for MIP samples, and for CO_2 gases 13%, by comparison with 2% below 800° C. Penttala has observed a shift of carbonate evolution to higher temperatures during extended hydration (PENTTALA, 1992 p. 105). This does not, however, cause as large a difference as observed in these tests.

When the samples were cycled, the absolute carbonate contents in the paste samples were clearly higher than in mortar samples. This is clear from the statistical data of the one-way analysis of variance for the ratio $CaCO_3^{MORTAR} / CaCO_3^{PASTE}$, shown in Table 9. The results show with strong significance, that cycled paste samples had carbonated to a far greater extent than cycled mortar samples. The other curing procedures show only slightly higher carbonation levels for pastes. This is due to the weak resistance of paste samples to repeated wetting and drying. Permeability of samples increases and carbonation is stronger than in corresponding mortar samples. Also noticeable was the fact that there were no significant differences between results for different binder types, although consideration of average values shows the slag binder to have had a 16% higher carbonate content in paste than in mortar. Correspondingly the increase with OPC was 8%.

Table 8. Significance level in t-test for hypothesis concerning differences between the two means of ratio $CaCO_3^{LTC}/CaCO_3^{MIP}$.

Populations	Significance level of difference between means	Significance of differences between the two means
Carbonated/cycled	0.0008	Very significant
Paste-cycled/paste-carb	0.0030	Very significant
Mortar-cycled/mortar-carb	0.0197	Significant
Mortar/paste	0.6665	Not significant
Mortar-carb/paste-carb	0.3522	Not significant
Mortar-cycled/paste-cycled	0.8942	Not significant

Table 9. Results from one-way analysis of variance of the ratio $CaCO_3^{MORTAR}/CaCO_3^{PASTE}$.

Curing	No. of samples	Average	Std. error	95% confidence intervals of mean
28 days	14	0.971	0.076	0.85...1.09
Carbonated	14	0.968	0.022	0.85...1.09
Cycled	14	0.658	0.069	0.56...0.81
Total	42	0.875	0.035	0.80...0.95
F-ratio=7.363 Sig. lev.=0.0019				
Binder	No. of samples	Average	Std. error	95% confidence intervals of mean
OPC	18	0.917	0.063	0.79...1.04
Slag 50%	12	0.842	0.083	0.69...1.00
Slag 70%	12	0.844	0.065	0.69...1.00
Total	42	0.875	0.041	0.79...0.96

F-rato=0.441 Sig. lev.=0.6661

Decomposition rate of carbonates

According to the results of the TG tests the decomposition of carbonates depends on the binder type. The graphs in Figure 35 and in Appendix K/5 show the absolute and relative decomposition. The relative decomposition in GBFS mixes below 650° C was 45%, 50% and 67% of the total at water-binder ratios of 0.60, 0.45 and 0.35 after carbonation treatment. The corresponding percentages for OPC mixes were 32%, 40% and 38%. This reflects the different crystalline structure of carbonates in OPC and GBFS mixes. Vaterite has been observed to form calcite II and decompose in the TG test below 650° C, i.e. clearly earlier than calcite I, which decomposes between 690° C and 800° C. The phenomenon is not distinctly noticeable in the absolute curves of Figure 35, since the total carbonate content in OPC mixes is higher than in GBFS mixes. However, in Figure 35, especially in mixes with a low water-binder ratio, also absolute values of calcite II were higher with GBFS blends. If the limit of 650° C is accepted as a differentiating point between vaterite and calcite plus aragonite, it can be stated that in OPC mixes at high levels of carbonation roughly 30-40% of carbonates exist in the form of vaterite and 65-55% as calcite and aragonite, and less than 5% in other forms of carbonates, e.g. carboaluminates that obviously decompose at higher temperatures. The corresponding approximate percentages in GBFS mixes of 50-70% slag content are 50-65% as vaterite and 45-30% as calcite and aragonite, and the rest in other forms such as hydrotalcite, carboaluminates, and similar phases.

Experimental conditions affect variation in the results of the TG test in general. Higher total amounts of decomposing carbonates may cause a delay in recorded results. This is not, however, relevant to our tests. A test with a pure calcite sample of 50 mg showed no delay over the reported decomposition limit in the used test procedure. The amount of sample corresponded to the maximum $CaCO_3$ content observed in the tests. Comparing the results, which gave roughly the same total amounts. also proves that there are differences in the decomposition rate of carbonates depending on the binder. E.g. OPC paste with a water-binder ratio of 0.60 gave a total content of 33%, with only 4% of carbonates decomposed below 650° C. GBFS paste with a water-binder ratio of 0.45 gave the same total content, but 15% of carbonates decomposed under the limit. The second experimental factor that may effect the decomposition rate can be seen in Figure 36 and in the figures of Appendices K/2 and K/4, which show that decomposition in mortar samples begins earlier than in paste samples. This is obviously due to the higher grindability of mortar samples caused by aggregates. The third affecting factor may be differences in the moisture content of LTC and MIP samples, which may also have an effect on grindability.

Changes in gel composition

Compositional changes in gel structure were estimated by considering the mole ratios of C/S and H/S on the basis of the TG+EGA results. In the calculations it was assumed that the degree of hydration defines the CaO and SiO_2 contents available in the gel. Thereafter CaO existing in the structure of the CSH gel was determined by deducting CaO combined with carbonates, CH and monosulfates from the CaO

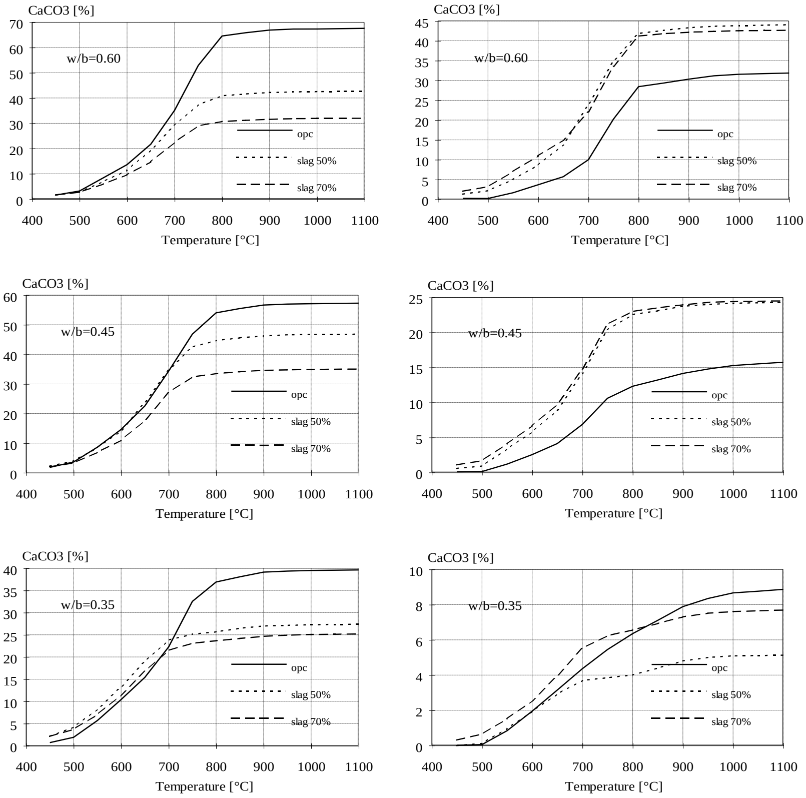

Carbonated samples Cycled samples

Figure 35. Evolution of CO_2 gases in the TG+EGA tests, expressed as $CaCO_3$ for different water-binder ratios and GBFS contents. Curves are averages of MIP and LTC samples for pastes and mortars.

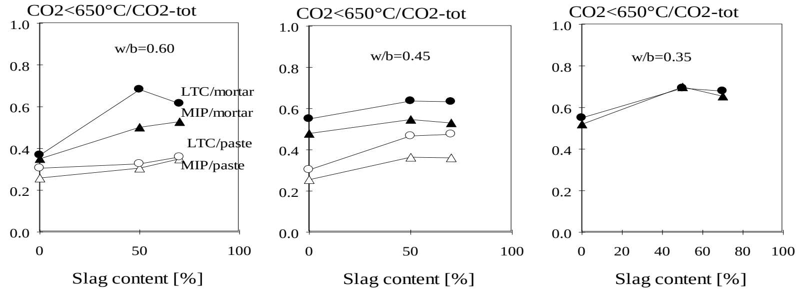

Figure 36. Evolution of CO_2 gases below 650° C in carbonated samples.

content liberated into the matrix depending on the degree of hydration. CaO from the AFm phase was calculated assuming that all gypsum in the binder is consumed. Another assumption that all water liberated between 110° C and 160° C represents 8 moles of water in the AFm phase, results in the same C/S mole ratio. H_2O was calculated by subtracting the water combined with CH from that liberated between 160° C and 1100° C. This is a rather rough assumption since it is known that CSH gel loses some of its water under 160° C and that there exist sulfate and hydrotalcite compounds which decompose above 160° C. However, the procedure is accurate enough to compare H/S ratios. Tabulated values for C/S and H/S mole ratios are given in Table 10.

Table 10. Calculated C/S and H/S mole ratios of CSH gel in different curing procedures.

Binder	w/b ratio	C/S mole ratio				H/S mole ratio			
		28d	cy	ca	28d-std	28d	cy	ca	28d-std
Pastes									
OPC	0.60	1.83	1.28	0.34	2.17	2.20	1.78	1.10	2.09
OPC	0.45	1.99	1.81	0.32	2.16	2.23	2.15	0.96	2.12
OPC	0.35	2.05	2.15	1.07	2.32	2.14	2.26	1.45	2.16
Slag 50%	0.60	0.91	0.11	0.06	1.46	1.38	0.99	0.90	1.40
Slag 50%	0.45	1.07	0.58	0.00	1.50	1.56	1.21	0.81	1.54
Slag 50%	0.35				1.47				1.50
Slag 70%	0.60	0.53	0.00	0.00	1.22	1.15	0.91	0.89	1.00
Slag 70%	0.45	0.74	0.19	0.00	1.22	1.30	1.03	0.83	1.08
Mortars									
OPC	0.60	1.96	1.72	0.23		2.16	2.07	0.88	
OPC	0.45	1.91	1.74	0.44		2.29	2.28	1.07	
OPC	0.35	2.12	2.02	1.12		2.49	2.50	1.57	
Slag 50%	0.60	1.05	0.68	0.47		1.38	1.05	0.86	
Slag 50%	0.45	1.14	1.21	0.24		1.58	1.66	0.88	
Slag 50%	0.35	1.29	1.46	0.46		1.61	1.69	0.89	
Slag 70%	0.60	0.58	0.27	0.23		1.17	1.00	0.95	
Slag 70%	0.45	0.80	0.87	0.13		1.17	1.18	0.66	
Slag 70%	0.35	1.08	1.03	0.62		1.05	0.98	0.66	
OPC	average	1.98	1.79	0.59	2.22	2.25	2.17	1.17	2.12
Slag 50%	average	1.10	0.81	0.25	1.48	1.50	1.32	0.87	1.48
Slag 70%	average	0.75	0.47	0.19	1.22	1.17	1.02	0.80	1.04

Average values of the C/S ratio in standard cured samples were 2.22, 1.48 and 1.22 for slag contents of 0%, 50% and 70%, respectively. The corresponding average values for the H/S ratio in tested samples were 2.12, 1.48 and 1.04. In the literature, C/S values for GBFS blends were reported to be within the limits 1.2-2.0, the lowest value belonging to pure GBFS and the highest for OPC. The calculation procedure seems to overestimate the C/S ratio with OPC blends, whereas it underestimates it with GBFS blends. The same is true of the H/S ratio.

After carbonation, in samples with the highest degree of carbonation the H/S ratios reached the theoretical minimum, which is 0.83 with pure silica gel. At the same time the C/S ratio decreased correspondingly to 0, representing the transformation of CSH gel to pure silica gel. Comparison of the mole ratios makes it possible to estimate the degree to which the CSH gel transformed to SH gel. The results of this comparison for paste and mortar samples are presented in Table 11. It can be concluded that the higher the slag content, the higher is the degree to which SH gel is formed during carbonation treatment. Naturally, mortar samples give lower SH fractions. This is in line with the lower degree of carbonation.

Table 11. Calculated fractions of SH gel of the total hydrated gel amount after different curing procedures.

Binder	w/b ratio	Percentage of SH gel in pastes			Percentage of SH gel in mortars		
		28d	cy	ca	28d	cy	ca
OPC	0.60	14.3	41.3	85.0	9.3	21.0	90.0
OPC	0.45	5.0	13.4	85.3	5.4	15.0	79.5
OPC	0.35	6.3	2.9	53.9	4.5	8.1	50.6
Slag 50%	0.60	33.8	92.7	95.8	26.6	53.1	69.5
Slag 50%	0.45	20.6	60.3	99.8	18.9	17.8	83.8
Slag 50%	0.35				12.3	10.2	69.8
Slag 70%	0.60	53.8	100.0	100.0	49.6	78.1	81.9
Slag 70%	0.45	33.8	84.0	100.0	31.5	24.8	89.7
Slag 70%	0.35				12.7	16.3	51.2

5.4.5 X-ray diffraction tests

The XRD tests were performed for paste and mortar samples after "28 days" and "carbonated" curing procedures. A Philips PW1710 diffractometer and CuKα radiation were used with voltage 40 kV and current 40 mA. The results are presented in Appendix N.

All mineralogical forms of calcium carbonate: calcite, vaterite and aragonite were present in the OPC and GBFS compositions after the samples were carbonated for 15 months at RH 45%. Although the tests were not performed quantitatively, the main peak comparison between different types of carbonates in Figures 37 and 38 shows that the ratio of intensities of vaterite and calcite is only 0.22 and 0.27 for OPC pastes with a water-binder ratio of 0.45 and 0.60, but as high as 0.45 and 0.44 for corresponding GBFS pastes of 70% slag content. The ratio of aragonite to calcite peaks is of same magnitude for both types of binders, being 0.17 to 0.20 for OPC and 0.22 to 0.23 for GBFS 70% (Table 12). The higher proportion of vaterite with GBFS binder observed with XRD is consistent with the results of TG+EGA, where evolution of CO_2 gas from GBFS samples occurred at lower temperatures than with OPC samples, reflecting the higher vaterite content.

An interesting finding in the results was the disappearance of tri- and monosulfate phases and also carboaluminate phases in carbonated samples. This reflects the possibility that also these compounds carbonate. The X-ray patterns for GBFS binder showed that also hydrotalcite may carbonate.

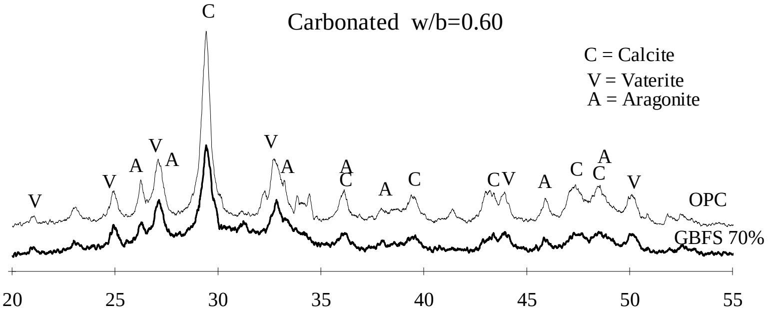

Figure 37. X-ray patterns for carbonated paste samples of w/b ratio 0.60.

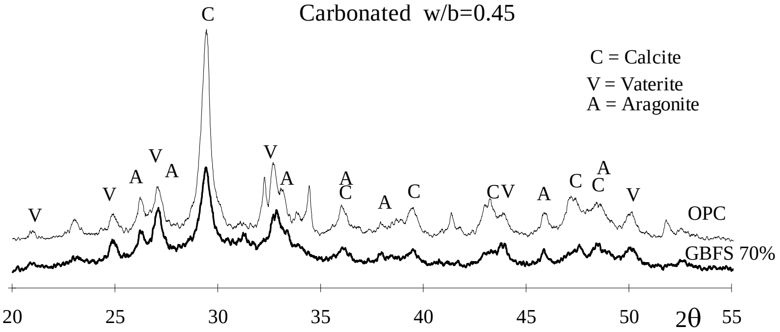

Figure 38. X-ray patterns for carbonated paste samples of w/b ratio 0.45.

Table 12. Relative fractions of calcium carbonate according to XRD main peak intensities.

Binder	Aragonite	Vaterite	Calcite
OPC	0.12	0.18	0.70
Slag 70%	0.14	0.28	0.58

5.4.6 Infra-red spectroscopy analysis

Infra-red spectroscopy was used to certify qualitatively the changes in the CSH phase during carbonation. The diffusion reflectance test by IR spectroscopy was done using powdered samples with water binder ratios of 0.60 and 0.45 and slag contents 0 and 70%. Figure 39 shows absorbance bands in the range of wavenumber 800-1600 1/cm for the samples. The results show that CSH gel (band at 970 1/cm) transforms to SH gel (band between 1040 1/cm and 1090 1/cm) during carbonation. This is true of both binder types. A strong shift at high water-binder ratios is additional evidence for the low C/S ratios reported in Section 5.4.4.

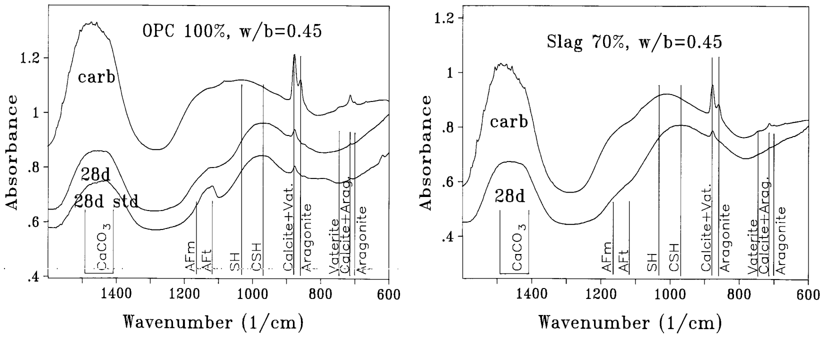

a) Pastes of water-binder ratio of 0.45

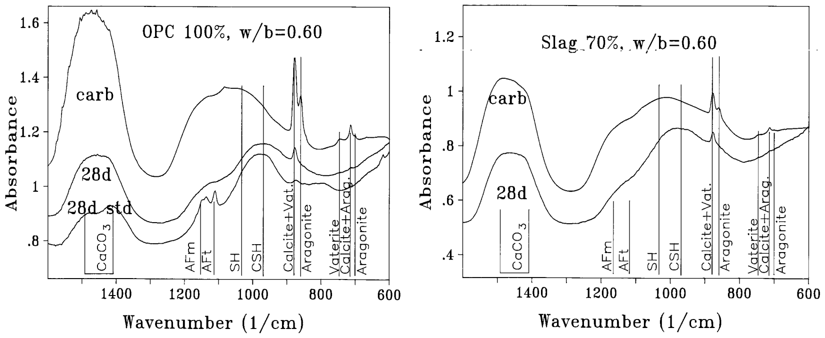

b) Pastes of water-binder ratio of 0.60

Figure 39. FTIR spectra of pastes having water-binder ratios of 0.45 and 0.6.

The bands certify the results of the XRD tests, namely that all mineralogigal forms of carbonates, vaterite, aragonite and calcite are present after carbonation. With slag binder the relative proportion of aragonite is lower and that of vaterite higher than with OPC pastes. The same conclusion could be drawn from the relative proportions of carbonates in the XRD and TG+EGA results. From the intensities in the main band of carbonates at 1400-1500 1/cm and in the secondary band at 870 1/cm, it can be concluded that the total amounts of carbonates among the pastes in Figure 39 are in the same order of superiority as observed in the TG+EGA test. Although FTIR analysis is used mostly as a qualitative measure only, Figure 40 shows that a rather good correlation is obtained between the integrated absorbance band area 830-880 1/cm and the evolved CO_2 gases in the TG+EGA test.

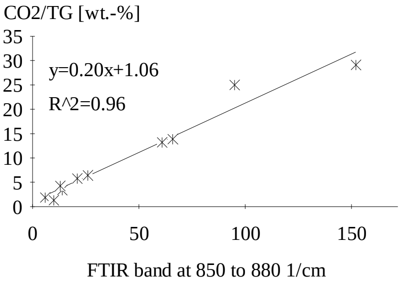

Figure 40. Integrated absorbance band areas between 830 1/cm and 880 1/cm related to the evolved CO$_2$ gases in the TG+EGA test. (Areas for FTIR bands are only relative).

5.4.7 EDX phase map analysis

In order to estimate the distribution of Mg-containing phases in the skeleton, inner and outer slag hydrates, a mortar sample of 70% slag content was studied by EDX phase map analysis. SEM images were gathered by an environmental scanning electron microscope, and phase maps were produced from EDX element maps of micrographs using statistical principal component analysis. The size of each EDX micrograph was 256 • 256 pixels. The analysis was done by Penttala, and the description of method is given in the reference PENTTALA AND MATALA (1995). The results showed that the skeleton and inner hydrates are enriched by magnesium supporting the phase compositions of these hydrates presented in the literature.

6 ANALYSIS OF THE TEST RESULTS

The results presented in the previous chapter were also analysed there with respect to parameters such as degree of hydration, degree of carbonation and gel compositions, which are used in the characterization of pore structure and its changes due to carbonation in this chapter.

Section 6.1 comprises the analysis of concrete test results with respect to total porosity (water immersion test) and to capillary porosity in the capillary and mesopore ranges (MIP test). Effects of aging on durability aspects is considered in the sections 6.1.3 and 6.1.4.

Section 6.2 deals with pore structure changes as seen in the results of MIP and LTC for paste and mortar samples. Here the gel porosity, namely pores finer than 4 nm radius, is separated into micropores and microcapillaries. The third category of pores is defined as macropores larger than 4 nm, in which the pore water is freezable at the minimum temperature of the frost salt test according to the theory presented in section 4.2. The comprehensive definition of these pore ranges is given in Chapter 6.2.1. Consideration is bipartite. First, in sections 6.2.2 to 6.2.4, gel porosity is analyzed on the basis of freezable water within specified pore ranges. Thereafter, in sections 6.2.5 and 6.2.6 the analysis is expanded to include the adsorbed water, so that total porosities within different pore ranges become comparable, and so that comparison between MIP and LTC test results is possible. The effect of carbonation on the redistribution of porosity and on the total porosity is studied in section 6.2.6.

Porosity as function of the degree of hydration, water-binder ratio, slag content and degree of carbonation is studied using statistically-evaluated models to clarify the significance of different variables for both the porosity and the pore structural changes.

In the analysis, the paste and mortar samples have not been separated to the different populations. Paste samples gave slightly higher porosity values measured by the MIP and LTC tests if considered on the basis of the average paste porosity values. However, the statistical analysis done at a risk level of 0.01 did not support the differentiation of the paste and mortar populations. Non-freezable water contents with all curing procedures and freezable water contents in the "non-aged" and "cycled" curing methods measured in the paste and mortar tests by the LTC method did not differ significantly from each other. The comparison of the total porosity values by the MIP method resulted to the same conclusion. The only exception was the freezable water content in the carbonated paste and mortar samples measured by the LTC test. There the difference between the paste porosities of the paste and mortar samples was statistically significant. But, since the degree of hydration in mortar samples was slightly higher (Section 5.4.4.4) which cause a decrease in the paste porosity of mortars, the aforementioned significance diminishes. The deviation due to the sample preparation was exceptional low in paste samples as considered in Section 5.4.4.4. In mortars, the deviation was greater (confidence limits of ± 5.0% of the mean at a risk level of 0.05), being evidently due to variations in the paste-aggregate ratio. This reason causes also variation in the porosities between the paste and mortar samples. On the above grounds, the handling of the porosity results obtained in the paste and mortar tests in one statistical population has its justification.

Mostly the models, presented in this chapter, have been evaluated by the multiple linear regression analysis in which the degree of hydration, water-binder ratio, slag content and degree of carbonation were as predictor variables each of the first degree and the linear combination of these as a random response variable that was compared to the experimental values. Hence the model expresses the mean value of this random variable as a function of predictor variables. In analysis the method of least squares was applied to estimate the coefficient parameters for each predictor variable. The adequacy of the least squares fit was examined by the residual analysis in which a plot of residuals versus fitted values and versus each included and omitted variables were studied. If the residuals correlated with fitted values or with variables, the model was not accepted. Further, the lack of fit was examined by testing the significance of regression using the analysis of variance. F-ratio, meaning the ratio between the mean squares of the model and residuals, is given in Figures together with the coefficient of determination and with the standard error of the model. The variables of the model were selected by the stepwise variable selection procedure which considers properly also the possible interrelationships of the variables. The variable were included in the model if its significance level was smaller than 0.05.

The statistical models have been evaluated to contribute the interpretation of the effects of carbonation on the pore structure within the OPC and GBFS mixes cured by particular procedures. Therefore those models should not be seen as accurate expressions covering the effects of studied variables in general. For that, probably a much more extensive experimental program should have been carried out.

It should be emphasized that, although carbonation has been regarded as an aging process in the following interpretation of the test result, the used procedure comprises also the effects of the changed moisture state in which carbonation has taken place. As stated in Chapter 2, carbonation was studied simultaneously with drying as a single aging process in experimental conditions of controlled moderate relative humidity and ordinary climatic CO_2 concentration. Drying, as very well known, changes the pore structure of cementituous materials (see e.g., BAGER AND SELLEVOLD 1986b and PIHLAJAVAARA 1982). In order to minimize the effect of varying moisture history on the results, the specimens were designed so that all curing conditions comprised at least a short drying period at 45% RH. The non-aged curing consisted of the moist curing of 7 days followed by the storage of 3 weeks at 45% RH before the porosity tests by the MIP and LTC methods. A small sample size of 12• 12• 70 mm enabled a very rapid drying, Calculations with the sample size corrections, based on the experimental values published by PIHLAJAVAARA (1982), showed that a short storage of 3 weeks at 45% RH gave the moisture state corresponding an equilibrium state at 58 to 63% RH. Hence, the tested samples even in the non-aged state have endured noticeable drying and the pore structural changes caused by that. Then the changes in pore structure between the "non-aged" and "carbonated" states can be primarily interpreted to be caused by carbonation giving an evidence to consider the changes with respect to this aging phenomenon.

6.1 CONCRETE TESTS

6.1.1 Changes in total porosity

The results of the water suction tests confirm that carbonation caused a clear decrease in the porosity of OPC concretes (Figure 41). In the results of Figure 41 the porosity is obtained by subtracting the air porosity from the total porosity. The values are the means for non air-entrained and air-entrained concretes at each water-binder ratio. Reduction in porosity is greatest the higher the water-binder ratio, as was the carbonated volume of samples (Table 13). The same, however, is not true for GBFS concretes. At high water-binder ratios a weak reduction in porosity was observed, but at low water-binder ratios the porosity was roughly the same or a little higher. The results for GBFS concretes are the means for both slag contents of 50% and 70%. Another aging procedure, in which specimens were subjected to repeated wetting and drying cycles, reduced the porosity with both binders, obviously due to the higher degree of hydration.

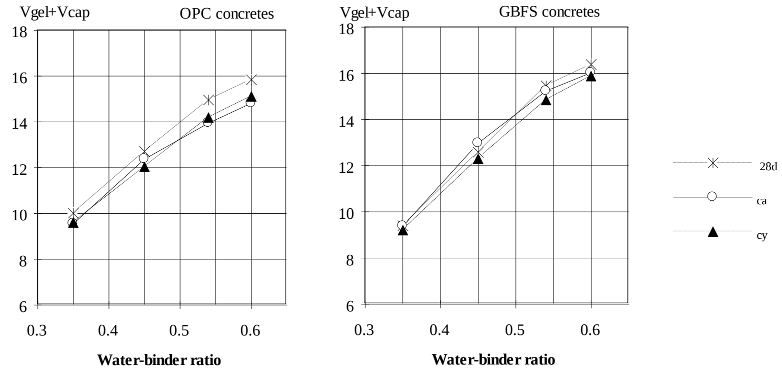

Figure 41. Total porosity minus air porosity in concrete samples, as a function of water-binder ratio.

Table 13. Carbonated volume as % of total volume in water suction specimens.

Water-binder	Cycled samples		Carbonated samples		Decrease in porosity at full carbonation [%]	
ratio	OPC	GBFS	OPC	GBFS	OPC	GBFS
0.60	27	31	55	74	11.7	2.9
0.54	24	45	53	74	12.7	2.0
0.45	14	25	47	51	5.5	-6.2
0.35	3	11	28	43	16.4	0.5

Assuming that the degree of hydration within carbonated and non-aged samples is approximately the same, i.e. the whole change in porosity is due to carbonation, the effect of full carbonation on the porosity of the gel and capillary pore ranges can be estimated by correcting the decrease in total porosity by the fraction of the carbonated volume. The values listed in Table 13 show clearly the stronger ability of OPC binder to decrease gel and capillary pore volumes during carbonation. Average reduction in porosity with OPC and GBFS binders was 14% and 2% respectively, which corresponds to the different amounts of carbonable material in the binders.

6.1.2 Changes in capillary porosity

Pore structure changes of concretes due to carbonation were studied by comparing the peak movement in the derivative pore size distributions of MIP test results. Appendix F shows the pore volumes, the location of peaks, and the boundaries of the capillary and mesopore ranges. The capillary and mesopore ranges are defined in Figure 42. The shift of the capillary pore range towards the coarser pore range was studied by comparing the onset pore radius at the range boundaries both before and after carbonation. Figure 43 shows the ratio of the extracting pore radius Rca/R28. As can be seen, the whole capillary pore range has shifted towards larger pore radii with all binder types. The same conclusion can be drawn from the position of the main peak of this area (Appendix E). When coarsening is expressed as average values, the higher slag content gives only slightly higher values, although the relative fraction of capillary pore volume to total pore volume seems clearly higher with the higher slag content, as shown in Figure 44. Capillary pore volume in terms of average values decreases by 6% and 2% for OPC and GBFS 50% concretes, but increases by 2% in GBFS 70% concretes. The high values > 1.2 in Figure 44 were excluded from population in this context.

The shift of the capillary pore range towards coarser pore sizes is also seen in cycled samples, but clearly to a lesser extent. Here the capillary pore volume decreases due to cycling, the decrease being greatest for the highest slag content concretes and thus reflecting the more efficient extended degree of hydration in GBFS mixes.

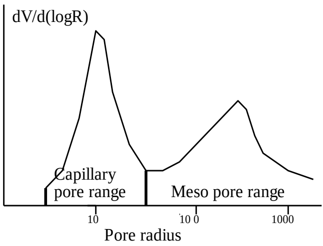

Figure 42. Definition of capillary and mesopore ranges.

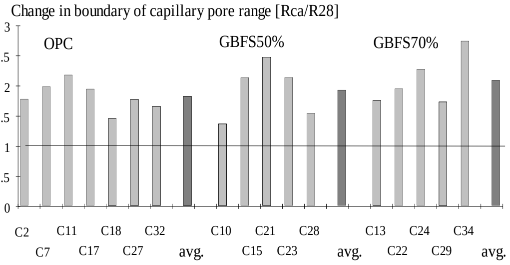

Figure 43. Shift in extracting pore radius towards larger pore sizes.

Coarsening of the pore structure in the capillary pore range, i.e. from 4 nm to tens of nanometers, due to carbonation seems to be obvious with both binder types. The shift towards larger pores in GBFS binders is only slightly stronger than with OPC binder. Since the pore volume in the capillary pore range seems to decrease more in OPC concretes than in GBFS concretes, the net effect of carbonation on coarsening is stronger in GBFS concretes. In the mesopore range the pore volume decreased after carbonation by 15% and 12% for OPC and GBFS 50% concretes respectively, and increased by 2% for GBFS 70% concrete (Figure 46). When total porosities measured by MIP are considered, carbonation seems to decrease porosity by 7% on average in OPC concretes and by 2% in GBFS concretes (Figure 47). The trend in both pore ranges is the same.

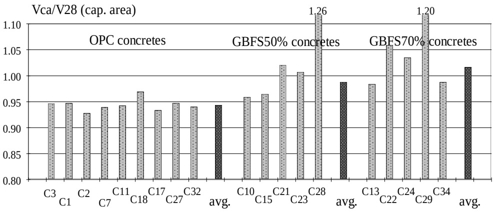

Figure 44. Change in capillary pore volume due to carbonation in MIP tests.

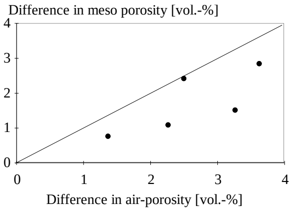

Figure 45. Change in mesoporosity in MIP test in relation to that of air porosity in thin sections.

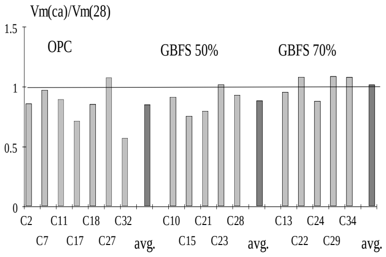

Figure 46. Effect of carbonation on change in mesoporosity in MIP tests.

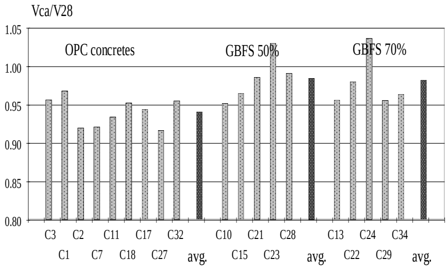

Figure 47. Effect of carbonation on change in total porosity in MIP tests.

Among the concretes, five mix compositions differed only in terms of air-entrainment. Plotting the difference in air porosity of the corresponding mixes measured by thin section analysis against the difference of mesoporosities determined by MIP shows a clear correlation (Figure 45). This demonstrates that isolated air pores dimensioning tens of micrometers are at least partly intruded through smaller mesopores dimensioning of hundreds of nanometers. The same phenomenon may also be true of the smaller capillary range.

The coarsening phenomenon observed in MIP tests is in agreement with the results for carbonated GBFS concretes reported e.g. by Bier et al. (1987) and Litvan and Meyer (1986). However, the observed coarsening of concretes with OPC binder, and only slight increasing effect of GBFS on coarsening are somewhat conflicting with regard to the literature, possibly due to different experimental conditions. In our test procedure, vacuum drying was used in the pretreatment of samples, which might affect the pore structure of OPC concretes more strongly and cause certain coarsening already in the non-aged state. This subject is discussed more closely in the analysis of paste and mortar tests in section 6.2, which compares the results of the MIP and LTC methods.

6.1.3 Water permeability

Changes in water permeability due to carbonation can be studied by comparing the coefficients of water absorption curves obtained from the water suction test. Kcap, here called the capillary index, defines the change in the degree of saturation as a function of the square root of time before the nick point. It is equal to the coefficient k1 in Appendix E. The values for Kcap before and after carbonation are given in Figure 48. It shows that in OPC concretes the capillary index is generally higher than in GBFS concretes, indicating higher capillarity in the form of pore continuity. After carbonation at high water-binder ratios, the pore continuity is diminished in OPC concretes but increased in GBFS concretes. At low water-binder ratios the change is the opposite. In OPC concretes the capillary index is slightly increased but in GBFS concretes it is decreased.

The changes observed in the capillary suction test do not correlate with the results concerning the pore structure obtained from MIP tests or with those based on thin section analysis. For the highest cracking index in thin sections, the capillary index should be highest. However, as can be seen in Figure 49, the increase in capillary

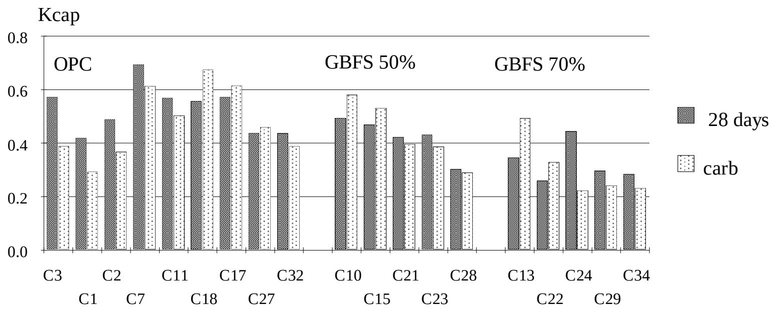

Figure 48. Capillary indices for concretes before and after carbonation.

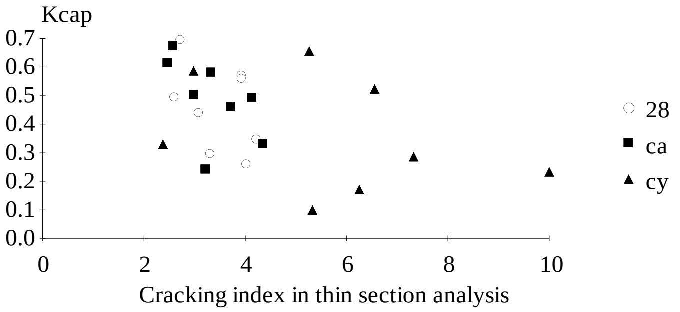

Figure 49. Capillary indices related to cracking indices from thin section analysis.

index does not correlate with that in the cracking index. It can be concluded that randomly distributed cracks several micrometers wide do not affect the capillarity observed in the water immersion test. Further, the MIP test detected a shift towards larger pore necks after carbonation. This and the fact that the porosity in the capillary and mesopore ranges did not change with GBFS concretes, should provoke an increase in capillarity. Concrete C34 (w/b=0.35; GBFS 70%), in which coarsening due to carbonation observed in the MIP test was highest, showed a clear decrease in capillary index (Appendix E/3). In contrast, concrete C13 (w/b=0.54; GBFS 70%) gave the same relative change in porosity as C34, the lowest coarsening among all GBFS 70% concretes, but clearly the highest increase in capillary index.

The findings of the water immersion tests indicate an increase in continuity of pores after carbonation in GBFS concretes with high water-binder ratios (w/b>0.50), but a decrease at lower ones. The pore structure at high water-binder ratios is so open, and the precipitation of carbonates in GBFS concrete so insignificant in the capillary pore range, that the net effect is increased water permeability. In contrast, in OPC concretes, even at high water-binder ratios, carbonates formed from CH are able to block the capillary pore space and decrease permeability. The differences in capillary indices between OPC and GBFS concretes indicate differences in overall pore structure. No profitable influence of air-entrainment on water permeability could be found.

6.1.4 Changes in frost-salt resistance

Comparison of the deterioration curves shows that in all cases, including different levels of air-entrainment, water-binder ratio, type of binder and strength, the deterioration of concretes increased with aging. Aging seems to affect the shape of the deterioration curve differently depending on the type of binder. With OPC concretes the curve is smooth or the slope rises gradually. This is also the case with GBFS concretes in non-aged tests. The most significant difference in the scaling curves for OPC and GBFS concretes can be seen with carbonated samples. In GBFS concretes, especially in those tested after carbonation at RH 45%, a very rapid period of deterioration was observed at the start of the test, as the scaling curves in Figures 14 and 15 show. This is indicated by the arrows in Figure 50 for air-entrained GBFS 70% concrete C34.

The relationship between the volume of rapid deterioration observed in the frost-salt test (crossing point of arrow and ordinate at 0 cycles in Figure 50) and the level of carbonation of samples was studied by linear regression analysis. Figure 51 shows a highly significant correlation (probability level above 99.9%) between the carbonated volume and the volume of rapid deterioration for all GBFS concretes cured in the carbonation procedure at RH 45% for 13 months. Also the curing procedure of repeated wetting and drying cycles ("cy") shows significant correlation (99%< P < 99.9%) between these two variables for GBFS concretes. No correlation could be found for OPC concretes (Table 5 in Appendix D).

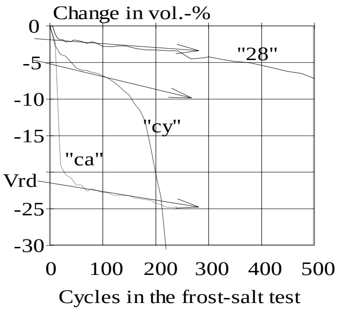

Figure 50. Shapes of deterioration curves for different the aging procedures.

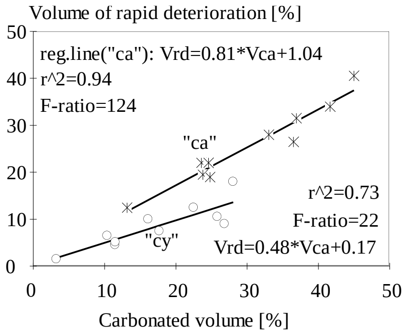

Figure 51. Relationship between volume of rapid deterioration (Vrd) in frost-salt test and carbonated volume of specimens (Vca) of GBFS concretes.

The difference in the results of the two curing procedures can be explained by the higher degree of hydration in tests done with cycled samples, affecting the lower values of carbonation. The strong relationship between deterioration and carbonation may be due to the changes in the pore structure in the carbonated and non-carbonated concrete. This is also supported by the fact that following the rapid phase in degradation the slope of the deterioration curve is very close to that of the non-carbonated curve. This means that the pore structure under the carbonated zone is probably very similar to that of non-aged concrete. It also means that drying in itself cannot be the primary reason for increased deterioration.

Comparing the results from curing procedures "cy" and "28" shows that the shapes of the deterioration curves are alike after the rapid phase of deterioration, and that the final deterioration took place clearly earlier in the aged concretes than in non-aged concretes. This reflects the possibility that aging without carbonation, in addition to extended hydration, also changes the pore structure and that as a result the critical degree of saturation may be decreased.

From the results it can be concluded that carbonation of the surfaces seems to accelerate the deterioration of concrete early in the frost-salt scaling tests, and that the phenomenon is especially clear with all GBFS concretes. After rapid scaling in the carbonated zone, deterioration seems to follow the curves for non-carbonated concretes. This presumably reflects the notable modifications in the pore structure of GBFS concretes and the differences in the overall pore structure of OPC and GBFS concretes. Increased frost susceptibility due to aging is in accordance with the results of laboratory tests and those obtained in the Canadian studies on structures or specimens exposed to natural climatic conditions.

6.2 PASTE AND MORTAR TESTS

6.2.1 Definition of pore ranges

The conventional definitions of pores; the gel and capillary pores, have separated in this study at an extracting pore radius of 4 nm by radius. The smaller pores are defined as gel pores divided into micropores and microcapillaries which can be measured by the LTC method as discussed in Section 5.4.3.6. The capillary pores are called here as macrocapillaries or macropores ranging from 4 nm to a few microns. Capillary pores are detectable in the MIP and LTC method.

The effect of carbonation on porosity is considered in the following for the three different pore ranges. Micropores are defined here as representing the pore range radius < 1.5 nm. The micropore volume was measured by assuming, according to the method presented in Chapter 4, that no freezing occurs in pores under 1.5 nm in the LTC test, where the minimum temperature was -63° C. The nucleating pore at -63° C is according to Equation 35, exactly 1.26 nm in radius, but as the freezing thermograms in Appendix H show, the minimum phase transformation temperature is roughly -53° C corresponding to a pore radius of 1.5 nm and the major part of the smallest pores is concentrated above -45° C where the pore radius is 1.76 nm. The micropore range could not be confirmed by any other test method used in this study.

Microcapillaries are defined here as representing the pore range 1.5 to 4 nm. The range is determined by practicality, as the lowest limit meets the smallest pore size able to freeze in the LTC test. It also corresponds to the saturated pore size at RH 45% during carbonation treatment. The upper limit of 4 nm is the lowest limit detectable by the MIP test and corresponds to the freezing temperature of -18° C according to the theory presented earlier. This limit also corresponds to the minimum temperature used in frost-salt tests of concrete.

6.2.2 Micropores

The micropore volume was measured as the non-freezable pore volume (V_{pnf}) in the LTC test for paste and mortar samples cured by three different methods. Thus it does not include the adsorbed water content in microcapillaries and macropores, hence the value is somewhat higher than the actual volume of pores smaller than 1.5 nm. The effect of adsorbed water on the pore volume range is considered later in section 6.2.5.

The dependence of micropore volume on the mix characteristics in the non-aged state was studied by correlation analysis. The best correlation between the measured micropore volume and the three mix variables - degree of hydration (α), water binder ratio (w/b) and slag weight fraction of the binder content (s) - was obtained using Equation 51. The expression gives the non-freezable water as vol.-% of the paste volume, with a low standard error of estimate and a rather good factor of determination of 0.97 (Figure 52). This should not be seen as a generalized expression for the non-freezable water content but as the relationship between the binders used in this study. In OPC blends it results in roughly 30% (α=1) to 40% (α=0.4) higher values at a low water-binder ratio of 0.40 compared with conventional expressions for the gel pore volume. At a water-binder ratio of 0.85 the values are practically equal for OPC independently of α. The 70% slag incorporation seems to decrease the finest gel pore range by 17%, according to Equation 51, at equal degrees of hydration and at the same water-binder ratios. The absolute values given in Figure 53 show clearly lower micropore volumes for GBFS mixes. This is naturally caused by the lower degree of hydration with GBFS binder. A strong correlation with GBFS content is evidence of the different gel and pore structural states of these binders in the non-aged state.

$$V_{nf} = (2{,}7 + 37{,}2\alpha) \cdot (1{,}27 - \mathrm{w/b}) \cdot \left(1 - 0{,}5s^3\right) \quad (51)$$

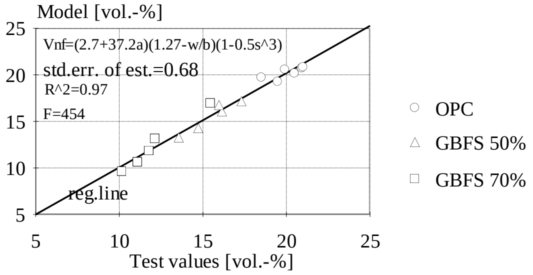

Figure 52. Correlation between tested and modeled non-freezable water contents according to LTC tests of non-aged samples at 28 days.

Figure 53 shows the absolute volume fractions of micropores smaller than 1.5 nm in relation to the paste volume for paste and mortar samples cured by different methods. The absolute pore volumes in non-aged samples are strongly dependent on the slag content but correspond to the degree of hydration as expected. E.g. at the high water-binder ratio of 0.60, pore volumes from the highest to the lowest slag content were related to each other in terms of ratios 0.56:0.74:1 and the corresponding degrees of hydration as 0.57:0.79:1. The correlation at higher water-binder ratios was not as clear. Carbonation decreases the micropore volume, giving roughly similar absolute values independently of the binder type. This phenomenon is very clear with high water-binder ratios, having very high degrees of carbonation, and leads to the assumption that gel structure becomes increasingly alike in the course of carbonation, regardless of the binder type.

The effect of carbonation on micropore volume was studied by means of the so-called carbonation factor, or degree of carbonation (CaF), defined in section 5.4.4.4. V_{pnf} was determined by drying one half of the LTC sample at 105° C and subtracting from this value the amount of total freezable water in the LTC test. Obviously the micropore volume is slightly overestimated, as some hydrated water is lost at 105° C and non-freezable adsorbed water becomes included in V_{pnf}. The other half of the sample was ground and tested by TG+EGA to determine the carbonation factor and the gel water. Micropore volume and the ratio of this to the total porosity (V_{pnf}/V_{ptot}) as a function of the carbonation factor are considered in the following.

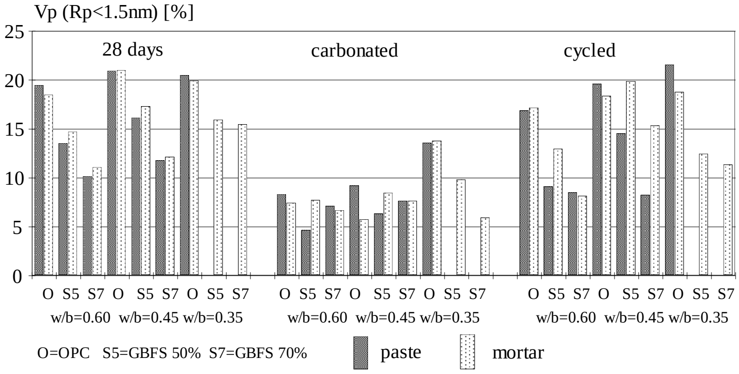

Figure 53. Absolute volumes of micropores smaller than 1.5 nm after different curing procedures. Results are volume fractions of the paste volume.

Non-freezable water in relation to the total porosity was modeled as a function of the carbonation factor. In Figure 54 the ratio V_{Pnf}/V_{Ptot} has been plotted against the carbonation factor for pastes and mortars of different mix compositions. Variance analysis showed that separation between groups representing pastes and mortars and different water binder ratios was not feasible. The regression lines of the linear model $V_{p_{nf}} / V_{p_{tot}} = a + b \cdot CaF$ (Table 14) show that with all mix compositions carbonation decreases the relative volume of micropores as expected. The same conclusion was drawn from the absolute volumes in Figure 55. The absolute volumes between different mix compositions were closer to each other than relative volumes at high degrees of carbonation.

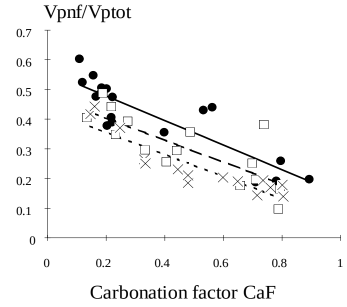

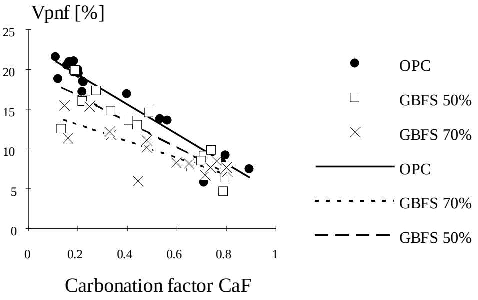

Figure 54. Effect of carbonation on the relative volume of micropores.

Figure 55. Effect of carbonation on the absolute volume of micropores.

Figure 56 shows the micropore volume as a function of the volume of carbonates, both as absolute values. The volume of carbonates has been calculated assuming that all of the CO_2 evolved in the TG/EGA test originates from calcite of density 2.710 g/cm^3. This is because it is not feasible to distinguish all possible mineralogical

Table 14. Statistical data of the regression lines in Figure 49.

		OPC	GBFS 50%	GBFS 70%
Estimates	a/b	0.561/-0.414	0.476/-0.370	0.430/-0.372
Std. error of estimates	s_a/s_b	0.0259/0.0573	0.0426/0.0808	0.0282/0.0505
t-values	T_a/T_b	21.656/-7.231	11.201/-4.581	15.242/-7.371
Prob. levels	a/b	0.00000/0.00000	0.00000/0.00052	0.00000/0.00001
Model :	F-ratio	52.282	20.986	54.336
	Prob. level	0.00000	0.00052	0.00001
	Deg. of freedom	17	14	14
	R-squared	0.766	0.618	0.807

compositions of calcium-, magnesium- and alkali carbonates, possible hydrocarbonates, and different forms of carboaluminates. If the volume of carbonates is broken down into volumes of Ca-, Mg- and alkali carbonates on the basis of oxide composition, the total volume of carbonates in any case only 0.5, 2.9 and 4.1% less for samples of OPC, GBFS 50% and GBFS 70 %, respectively, than if the above assumption is made. Therefore the error due to the approximation is negligible and it does not effect markedly on the plots in the presented figures. The non- freezable water content is seen to decrease almost linearly with increasing carbonate volume. This is not, however, due to precipitation of carbonates in the smallest gel pore space, as the pore dimensions do not allow it. Presumably the strong correlation is indicative of declining adsorbed water content and clear structural changes in the smallest gel porosity caused by carbonation.

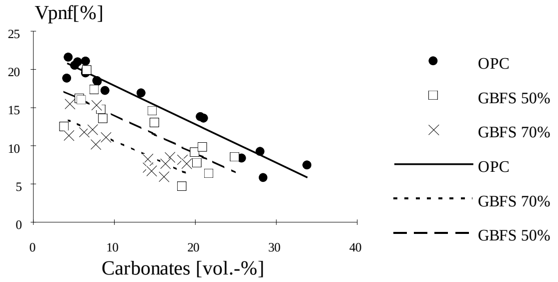

Figure 56. Effect of volume of carbonates on absolute volume of micropores.

The results show that carbonation decreases the relative and absolute pore volume of micropores. This is the case with all mix compositions regardless of GBFS content. The higher the slag content, the smaller is the volume of micropores before and after carbonation when this is regarded as a function of absolute volume of carbonates (Figure 56). This observation is, however, somewhat misleading since the amount of carbonatable compounds is clearly smaller with GBFS binder than with OPC binder. Therefore the more realistic assumption is to consider the volume of micropores as a function of the carbonation factor (Figure 55). This shows that at a high degree of carbonation the volume of micropores is roughly independent of the type of binder. It can be concluded that carbonation decreases micropores more strongly with OPC binder than with GBFS binder. This finding also reflects the possibility that the structural state of micropores in OPC mixes approaches that of GBFS in the course of carbonation. The strong decrease with OPC blends cannot be explained by the closing effect of carbonates precipitation in the pore space as discussed earlier.

The following explanations are more evident. First, the more powerful decrease in micropore volume of OPC mixes compared with that of GBFS mixes could be explained by changes in pore geometry. In the non-aged state, the pore shape of OPC compositions resembling cylindrical or even spherical geometry has shifted toward a more layered or slit-like shape. This is supported by the greater decrease in specific surface area of gel with OPC than with GBFS (Appendix J). In the carbonated state, the layered pore model is possible with both binders but in the non-aged state only OPC mixes, as the calculations later in Section 6.2.5 show. The second explanation can be drawn from the particular redistribution of porosity over the pore ranges. Carbonation has attacked the structure of the CSH gel and affected the formation of porous silica hydrate gel, which has a coarser pore structure than unaltered CSH gel. This phenomenon is discussed in greater detail later in connection with the mathematical modeling of gel porosity in the carbonated state.

Experimental conditions may also affect the smaller detected micropore volume, defined as the amount of non-freezable water. This amount may decrease during extended hydration in the vicinity of isolated pores. Such self-desiccation is possible with cement pastes having a fine and isolated pore structure, especially those of low water-binder ratio. However, this is impossible to take into account in the test methods used in this study, although it can be estimated to a certain accuracy. Extended hydration gives a higher content of non-evaporable and chemically bound water which, on contrast, decreases due to carbonation. Thus detection of these changes is problematic with the TG+EGA tests used in this study. In order to separate these two effects, the amount of chemically bound water released from CSH gel during carbonation should be known. In the literature it is presented that fully carbonated CSH gel loses roughly one water molecule per molecule of CO_2 (ATLASSI 1993). This was taken into account when measuring the degree of hydration for cycled and carbonated specimens. The maximum loss of water in micropores due to self-desiccation can be estimated from the differences in degrees of hydration. This calculation presumes that not all the water released during carbonation takes part in hydration, but simply exists as evaporable water. Figure 57 shows the volume of micropores measured by LTC, added to the calculated maximum volume of the non-evaporable water lost due to self-desiccation, $V_{P_{nf}} + w_{sd}$, as a function of the carbonation factor. Comparison of the regression lines in Figures 55 and 57 (plotted in Figure 58) shows that self-desiccation during carbonation does not affect the micropore volume of OPC samples, whereas with GBFS samples a certain effect is noticeable: the correlation between decrease in micropore volume and carbonation becomes slightly weaker. It should be pointed out that the lines which include the effect of extended hydration are very much on the safe side, as it is very possible that at least part of the water released due to carbonation can take part in hydration.

Another experimental factor that could affect the volume of micropores observed in the LTC test is the different amounts of dehydrated compounds below the drying temperature of 105° C. V_{Pnf} was measured here as the content of water retained at

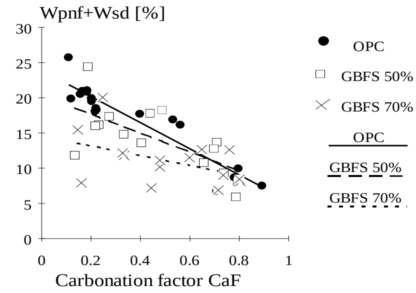

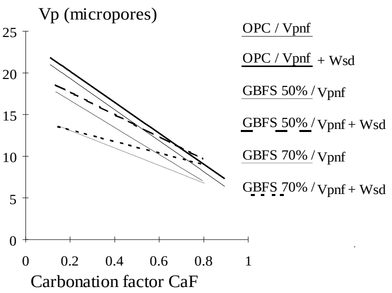

Figure 57. Effect of carbonation on the absolute micropore volume defined by the sum $V_{Pnf}+w_{sd}$.

Figure 58. Regression lines for the micropore volume measured by LTC tests V_{Pnf}, and for V_{Pnf} added to the amount of self-desiccated water w_{sd} as a function of the carbonation factor.

105° C minus the amount of freezable water down to -63° C. According to TAYLOR, trisulfates start to dehydrate already at 70° C to 80° C. Also other compounds, such as monosulfates, may dehydrate below the drying temperature of 105° C. Therefore, changes in these compounds during carbonation also affect V_{Pnf}. It can be assumed that most of sulfate compounds are in the form of monosulfates or carbonated monosulfates (testing age over 28 days). TAYLOR (1990, p 220) has proposed that monosulfate $C_4A\bar{S}H_{12}$ loses 2 to 3 moles of water at 100° C. Its carbonated form $C_4A\bar{C}H_{11}$ dehydrates at 200° C (RAMACHANDRAN 1969). The measuring technique involving drying treatment at 105° C gives too high micropore volume, being 1 to 2 moles of water (per mole of gypsum) higher than that of the state where monosulfate is totally carbonated. This was taken into consideration and the difference in volumes of evaporable water between $C_4A\bar{S}H_{12}$ and $C_4A\bar{C}H_{11}$ was calculated for all mix compositions as a function of the carbonation factor. In the calculations it was assumed that the amount of monosulfate formed before carbonation follows the general degree of hydration. The results for different mix compositions are presented in Figure 59.

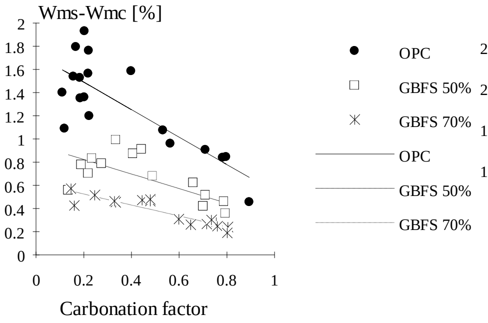

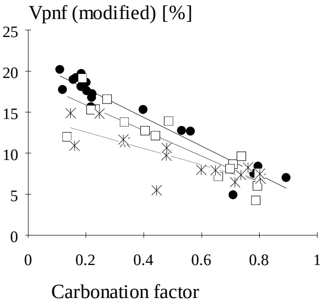

Figure 59. Effect of carbonation of the monosulfate phase on water content retained during drying treatment at 105° C.

Figure 60. Corrected micropore volume as a function of carbonation factor; notation as in Figure 59.

Figure 59 shows that the loss of chemically bound water in the monosulfate phase causes an approximate error of 1.7 and 0.8 vol.-% in V_{Pnf} in non-aged and carbonated states, respectively, for OPC mixes. Naturally, errors with GBFS pastes are smaller due to the lower gypsum content. The regression lines do not meet the zero value when the carbonation factor is 1. This is obviously due to the higher degree of hydration in carbonated samples than in non-carbonated samples. The effect of different dehydration of monosulfates and carboaluminates on micropore volume is subtracted from the values in Figure 59, and the differences are plotted in Figure 60 as a function of the carbonation factor. The results show a slightly stronger equality of micropore volumes of different binders after carbonation, giving additional evidence of the similar gel structure in aged compositions.

The third uncertainty concerns the preparation of samples subjected to vacuum water saturation before testing. If the pore structure is severely isolated it is possible that saturation does not reach all pores, causing underestimation of the micropore volume. This uncertainty is impossible to avoid with the test method used. The results should be considered against this background.

The non-freezable water content in the non aged state is expressed in Equation 51. The dependent variables are the degree of hydration, water-binder ratio and slag fraction. In order to formulate an expression for the effect of carbonation on the non-freezable water content, the basic value for the non-aged and carbonated test results was calculated by Equation 51 and thereafter the non-freezable water content of carbonated samples was subtracted from the aforementioned value. Then this difference was modeled as a function of significant variables using the multiple regression analysis to find out the factor η_{carb} (Equation 52) by which the non-freezable water content in the non aged state is corrected. Stepwise variable selection shows that all of the above variables and the carbonation factor are significant in the linear combination evaluated for the correction factor ### $_{carb}$ (Table 15). In the modeling, micropore volumes of samples cured with the "28 days" and "carbonated" procedures were used. The correction factor for the effect of carbonation on micropore volume is:

$$\eta_{carb} = 1.87 - 1.85 \cdot \alpha + 1.03 \cdot w/b - 0.29 \cdot s - 1.03 \cdot CaF \qquad (52)$$

Table 15. Statistical data for coefficients in Equation 52.

Variable	Coefficient	Standard error	t-value
Constant	1.87	0.155	11.06
Degree of hydration α	-1.85	0.260	-6.48
Water-binder ratio w/b	1.03	0.171	6.24
GBFS content s	-0.29	0.083	-3.31
Degree of carbonation CaF	-1.03	0.067	-14.24

Due to the procedure used in the evaluation of Equation 52, it cannot be used independently but together with Equation 51. Hence the volume of micropores after carbonation can be estimated from the equation:

$$W_{nf}^{carb} = \eta_{carb} \cdot (2,7 + 37,2\alpha) \cdot (1,27 - \mathrm{w/b}) \cdot (1 - 0,5s^3) \qquad (52)$$

The predicted values from Equation 53 are compared in Figure 61 with the experimental values, both for the whole set of experiments and for the population used in fitting Equation 53. The respective coefficients of determination are 0.86 (F-ratio=285) and 0.92 (F-ratio=336) and the standard errors for the estimates 2.1 and 1.5.

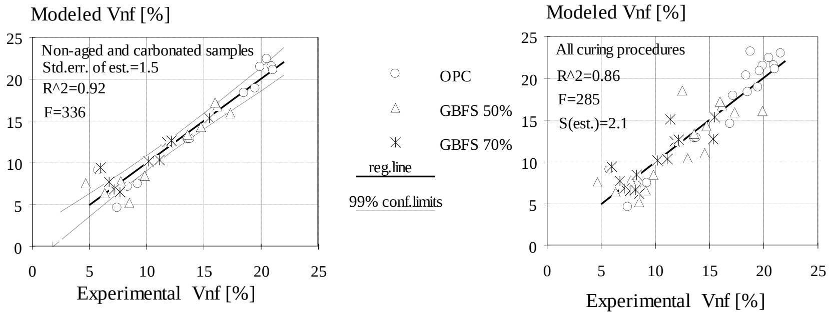

Figure 61. Correlation between modeled and experimental micropore volumes.

The following conclusions can be drawn concerning the effect of carbonation on the microporosity in OPC and GBFS concretes.

- Carbonation reduces the volume of micropores smaller than 1.5 nm in all mix compositions. The decrease is strongest with pure OPC compositions, lowering the pore volume by 12 vol.-% at a carbonation factor of 0.8 compared with the non-carbonated state. With a slag content of 50% and 70% the micropore volume decreased by 9 and 6 vol.-% respectively. The correlation between micropore volume and carbonation seems to be linear, although the variation of results is especially clear at high slag contents.

- The evaluated equations should not be regarded as an accurate relationship between mix characteristics, degree of carbonation and micropore volume, but rather as approximations showing the direction of effects of GBFS content and carbonation on the smallest pore structure of the cement paste. The variation in the results is due mainly to uncertainties in the volume ratios of mortar samples. A more precise relationship would require accurate determination of the paste volume in mortar samples or the use of mere paste samples.

- Carbonation decreases the micropore volume in OPC binder more than in GBFS binder. This reflects the possibility that the pore structural state of OPC in the micropore range approaches that of GBFS binder. At high levels of carbonation the modification of CSH gel toward porous SH gel explains primarily the declined micropore volume. Transformations in gel structure affect pore size redistribution at the expense of microporosity. The phenomenon is exacerbated by drying at low relative humidities.

6.2.3 Microcapillaries

Changes in the pore volume of microcapillaries are considered in the following on the basis of results of LTC tests. Total volumes of microcapillaries for different mix compositions, curing procedures and separately for samples of pastes and mortars are presented in Figure 62. The figure shows that the effect of water-binder ratio on pore range volume is not distinguishable in samples tested at 28 days. Some separation could be made between carbonated samples and cycled samples of the OPC binder. It is also evident that samples with pastes and mortar give roughly the same microcapillary volume calculated in relation to the paste volume. Comparison of the curing procedures "28 days" and "carbonated" (notation 28 and ca in Figure 62) shows that the microcapillary volume decreased drastically after 15 months of carbonation treatment at RH45 %.

The average reduction in this pore range volume due to carbonation treatment was 47, 75 and 83% of the original value with GBFS contents of 0, 50 and 70%, respectively. The highest slag content showed the highest total volume of 14.0% before carbonation, and lowest value of 2.4% after carbonation treatment. The corresponding average volumes with GBFS contents of 50 and 0% were 13.3 to 3.3% and 8.7 to 4.6%, respectively.

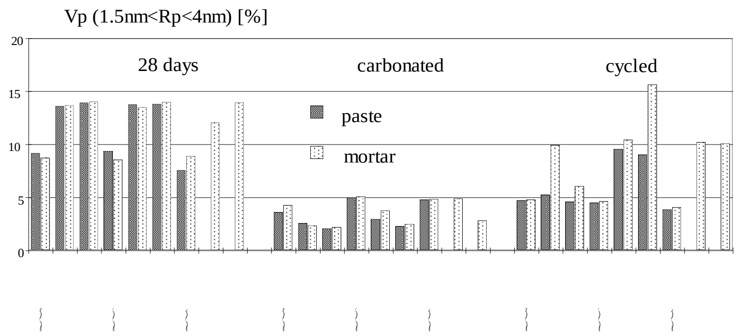

Figure 62. Pore volume of microcapillaries (1.5 nm to 4.0 nm) according to the LTC test.

The reasons for the decreased pore volume in this pore range are at least partly the same as in the micropore range. Figure 63 shows the microcapillary volume as a function of the carbonation factor. The figure separates the results for non-aged samples (notation "28") from those for aged samples (carbonated and cycled). The carbonation factor for non-aged OPC samples is seen to be around 0.2. The factor is same for samples aged by cycling, and the microcapillary volume is only half of the former. This may be explained by two facts. First, the degree of hydration is higher in aged samples and therefore the pore volume of small capillaries may be decreased. Another reason may be drying during the aging process. The same conclusion may also be drawn regarding mixes with a GBFS content of 50%. In this case the decreased volume is roughly 4 vol.-% and the degree of carbonation is of the same magnitude. However, the increase in the degree of hydration with GBFS was 34% compared with non-aged samples, which is clearly higher than with OPC.

An expression was formulated for the microcapillary volume as a function of the carbonation factor. In multiple regression analysis the pore volume in this pore range was significantly dependent only on the slag fraction and on the carbonation factor. Analysis showed no significance with respect to the degree of hydration or water-binder ratio. This is also observed in the absolute values given in Figure 62. In the modeling, microcapillary volumes of test samples subjected to "28 days" and "carbonated" curing were used, as in the case of micropore volume. The best fit for microcapillary volume due to carbonation was:

$$W_{mc}^{carb} = 4{,}9 - (10 + 26{,}3\,s) \cdot (\mathrm{CaF} - 0{,}66) \tag{54}$$

Predicted values from Equation 54 are compared with the experimental values in Figure 60 for the whole set of experiments and for the population used in fitting. The coefficient of determination was 0.85 (F-ratio=163) and standard error for the estimate 2.0. Figure 64 shows the average microcapillary volume for cycled specimens to be roughly 3 vol.-% higher than for non-aged and carbonated samples independently of the carbonation factor. This is due to the higher degree of carbonation, which increases gel porosity.

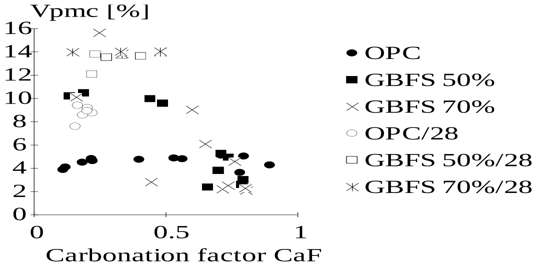

Figure 63. Effect of carbonation factor on the microcapillary volume.

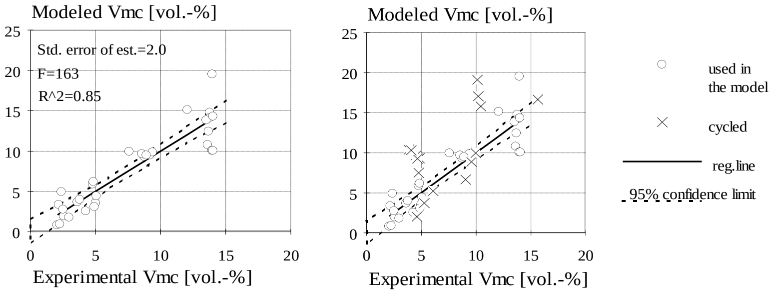

Figure 64. Correlation between experimental and modeled microcapillary volumes.

In summary it can be concluded that the microcapillary volume decreases with aging. Drying of cement gel during carbonation at low relative humidities, and the transformation of CSH gel to SH gel, lead to redistribution of pore sizes. Differences in overall gel structure between OPC and GBFS mixes explain the stronger effect in GBFS compositions. The modifications in the gel structure of the inner slag hydrate at high level of carbonation are evident. The formation of carbonation products in situ may not explain the decreased porosity in the studied pore range, since there is no evidence that calcite or even vaterite could precipitate in pores smaller than 4 nm. Vaterite may be formed at later ages in this pore range if the gel space has opened enough in the course of carbonation and the drying process.

Extended hydration may increase or decrease this pore volume, depending on whether hydration products form in a coarser pore range or whether hydration products form in the pore range under consideration. These contradictory effects may explain the discrepancy observed in the formulation of Equation 54, where no correlation between porosity and degree of hydration could be found. The higher degree of hydration explains some of the decreased pore volume in this range for GBFS samples, but not to the same extent for OPC samples, where the increase in degree of hydration is not as strong. In any case, comparison of corresponding degrees of hydration and carbonation with porosities of non-aged and cycled samples in Figure 62 shows that carbonation and its induced drying are primary factors in the reduction of microcapillary porosity.

6.2.4. Gel pores

The gel pore range was defined as representing pores smaller than 4 nm in radius, and comprises both pore ranges considered above. In Figure 65 the total pore volume of this pore range is plotted against the carbonation factor. The gain in pore volumes differs clearly between each of the two pore ranges within the gel porosity range. The decrease in micropore volume was greatest with OPC compositions, and that in microcapillary volume greatest with the highest GBFS content. Hence in the sum of these two converse variables the effect of the binder type is not of such major importance. This can be seen from the regression lines in Figure 66. The OPC samples show the smallest volume of gel pores with non-aged samples and the highest value when the degree of carbonation is high.

The effect of carbonation on gel pore volume can be estimated by summing Equations 53 and 54. When the sum function is expressed as a linear combination of variables α, w/b, s and CaF, the significance of the coefficients for parameters w/b and s is minor (Table 16). This is due to the two converse effects, whereby increased slag content clearly reduce the micropore volume while increasing the microcapillary volume, and increase water-binder ratio decreases the micropore volume in the non-aged state but increases it during carbonation. The net effect is that the significance of these variables on gel pore volume vanishes. Gel pore volume can be estimated by Equation 55.

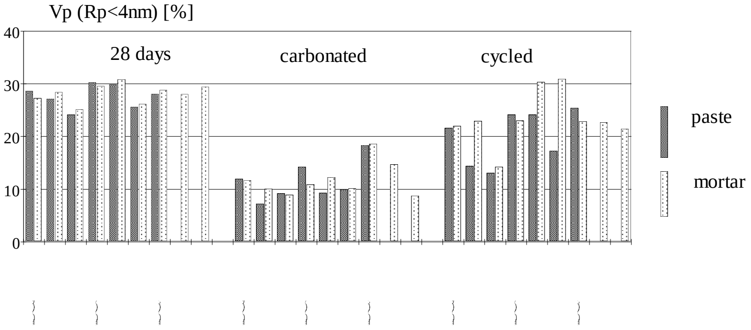

Figure 65. Absolute volume of pores smaller than 4 nm.

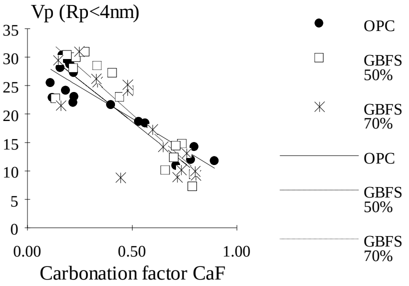

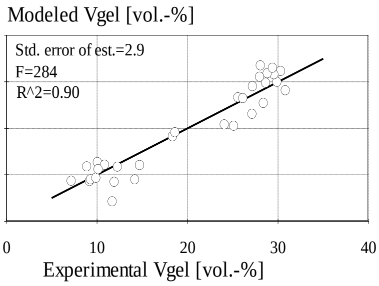

Figure 66. Effect of carbonation on the volume of pores smaller than 4 nm.

Figure 67. Correlation between experimental and modeled gel pore volumes.

$$V_{gel}^{carb} = 43.9 - 6.7 \cdot \alpha - 3.5 \cdot w/b - 1.3 \cdot s - 36.7 \cdot CaF \quad (55)$$

Table 16. Statistical data of coefficients in Equation 55.

Variable	Coefficient	Standard error	t-value	Sig.level
Constant	43.944	1.604	27.40	0.0000
Degree of hydration α	-6.693	2.793	-2.396	0.0210
Water-binder ratio w/b	-3.483	2.350	-1.482	0.1457
GBFS content s	-1.333	0.900	-1.481	0.1460
Degree of carbonation CaF	-36.665	0.866	-42.33	0.0000

F-ratio=591.98, DF=47, R-squared=0.982, Std. error of estimate=1.33

Predicted values from Equation 55 are compared with the experimental values in Figure 67 for the population used in fitting the basic equations 53 and 54. Coefficients of determination were 0.90 (F-ratio=284) and the standard error of estimate 2.9. Equation 55 is valid within the approximate limits $0.2<CaF<0.8$, $0.4<\alpha<0.9$, $0.3<w/b<0.8$ and $s<0.8$. Within these limits the gel pore volume of the non-aged paste volume is about 27% to 33%, the lower value belonging to GBFS paste with high α and high water-binder ratio, and the higher value to OPC paste with low α and low water-binder ratio. The corresponding percentages after carbonation are 5% to 11%, respectively. At full hydration the non-aged OPC paste porosity from Equation 55 at low water-binder ratios is 29±1.3 vol.-%, which is surprisingly close to the conventionally proposed gel porosity value of 28 vol.-%.

Gel porosity and the effect on it of carbonation was considered earlier on the basis of freezable water in pores smaller than 4 nm. This did not include adsorbed water on the pore walls, causes underestimation of the gel pore fraction, as the specific surface area of capillary pores is smaller than that of the excluded microcapillary range. The incorporation of adsorbed water into the pore volume presumes a knowledge of pore geometry. This consideration in the gel pore and capillary pore ranges is the subject of the following section.

6.2.5. Macropores

In this study the macropore area is defined to be the pore range in which water is freezable above -20° C. According to the theory presented in section 4.2 this corresponds to a pore radius of 4 to 8 nm. The smaller value corresponds to the equation derived in this study, and the higher is valid according to the theory presented by Fagerlund. 4 nm is also the lowest limit detectable in the MIP method. Consideration of the changes in this pore range are based on the results obtained from MIP and LTC tests. The changes in pore size distribution are discussed in section 6.2.8.

MIP tests

The graphs in Figure 68 show that total porosity detected by MIP is slightly reduced or stays the same when samples are aged by carbonation. Naturally the cycled aging procedure gives lower porosity in all cases due to the clearly higher degree of hydration. It is also noticeable that the results with pastes, mortars and concretes (Figure 47) deviate from each other, which is indicative of the variation in paste volume of mortars and concrete samples. The results listed in Table 17 show that with the highest GBFS content there is in fact no reduction in total porosity measured by MIP. With a GBFS content of 50% the reduction is from 7 to 12% and with OPC from 7 to 16%. There are probably several reasons for these differences. The amount of carbonates formed in OPC mixes is clearly higher, hence the most reasonable explanation lies in a blocking effect of carbonates. According to the differences between mix compositions it can be presumed that the origin of these carbonates is CH or sulfate compounds or both. Naturally, the carbonates formed from the CSH gel may also precipitate in the coarse pores and affect blocking of the pores. The average increases in the volumes of carbonates from non-aged to carbonated specimens in the TG tests were 20%, 14% and 10% of the paste volume for OPC, GBFS 50% and GBFS 70%, respectively. Thus a certain surplus in the porosity of this pore range must have occurred with GBFS binder during sample preparation or during carbonation treatment. Samples were vacuum-dried for 6 weeks which may have a coarsening effect, changing the pore structure of non-aged samples probably more than that of carbonated or cycled samples.

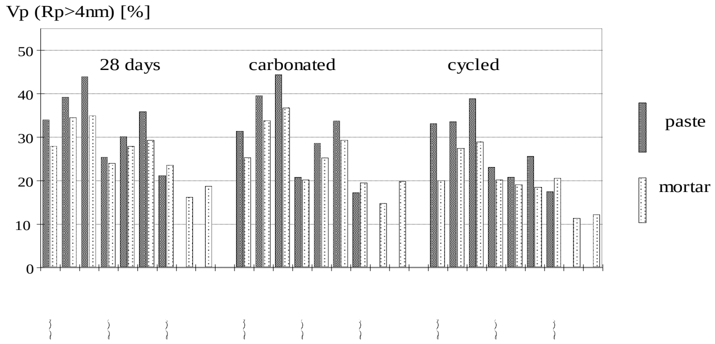

Figure 68. Pore volumes of macrocapillaries wider than 4 nm according to the MIP tests.

Table 17. Average of V_P^{carb} / V_P^{28} ratios of concretes, mortars and pastes in MIP tests for different water-binder ratios and GBFS contents.

w/b	GBFS content		
	0%	50%	70%
0.6	0.93	0.93	1.03
0.45	0.83	0.90	1.00
0.35	0.84	0.88	1.00
average	0.87	0.90	1.01

LTC test

The absolute volume fractions of macropores wider than 4 nm related to the paste volume for paste and mortar samples cured by different methods are given in Figure 69 for specimens tested with LTC. This pore volume does not include the adsorbed, non-freezable water layer on pore walls. In order to take this into account the thickness of this layer and its area should be known, both of which are dependent on pore size. The method presented in section 4.2 makes this possible, and is considered later. However, the comparison of pore volumes in Figure 69 is not questionable, since the average effect of the pore model on results, assuming a safe side approximation of cylindrical pore model for non-aged samples and the layered model for aged samples, is only 5.1, 2.0 and 1,7 vol.-%, giving the average pore volumes of 22.7%, 28.4% and 20.0% in the "28 days", "carbonated" and "cycled" curing procedures, respectively (Table 18).

On the basis of the LTC results, carbonation has significantly increased the coarse capillary pore volume, i.e. the result conflicts strongly with the MIP results, in which the mix composition was the affecting factor. Here the effect of mix composition is more clear. Carbonation treatment increased freezable water by 40%, 55% and 71% on average at slag contents of 0%, 50% and 70%, respectively. Closer examination of pore volume changes due to carbonation and of the role of the binder is presented later.

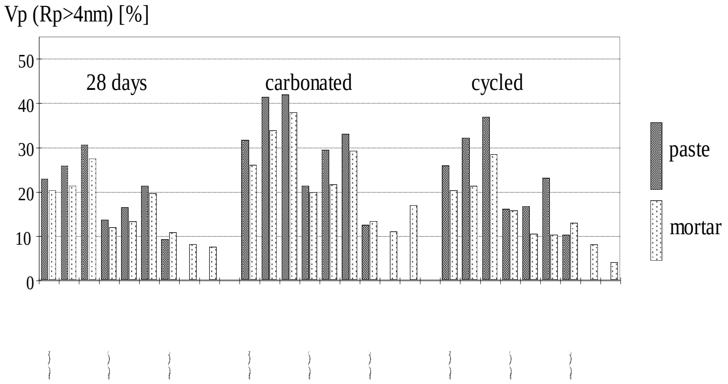

Figure 69. Freezable water in macrocapillaries wider than 4 nm according to the LTC test.

Table 18. Averages of freezable the adsorbed water volumes V_f and V_{ads} in pore range R_p >4 nm in different curing procedures.

Curing	V_f (R_p >4nm) [vol.-%]	V_{ads} (R_p >4nm) [vol.-%] according to the pore models		$V_{p(tot)}=V_f+V_{ads}$ [vol.-%]	
		cylindrical	layered	min.	max.
28 days	17.6	5.1	2.7	20.3	22.7
carbonated	26.4	4.7	2.0	28.4	31.1
cycled	18.4	3.7	1.7	20.0	22.1

LTC/MIP

The conflicting results obtained by MIP and LTC regarding the pore volume above 4 nm are considered in the following. As stated earlier the pore model affects the detected pore volume in the LTC test. The effect of the reduced specific surface area neglected in the calculations of LTC results cannot explain this differences, as a rough consideration above proves. The reason must lie elsewhere. The correctness of the lower limit of 4 nm based on the theory used in the analysis of LTC results may be questionable or perhaps there is an overall underestimation in the phase transformation enthalpy. The latter, however, is impossible: Following the Joule calibration of the calorimeter, a test with distilled bulk water was performed and the measured total enthalpy at 6° C supercooling was 314.2 J/g, which is well in line with the theoretical value of 313.8 J/g calculated from Equations A1, A2 and A5 in Appendix A. The correctness of the extracting pore radius of 4 nm can be studied by comparing the total freezable water amounts in the LTC test, added to the approximate adsorbed water of two molecular layers with the pore volume determined by MIP. According to the literature, it is generally accepted that two to three molecular layers of water remain in liquid phase at the temperatures used in the calorimetric measurements of this study (FAGERLUND 1973, BRUN 1977, STOCKHAUSEN ET AL. 1979, TADA 1987, ZECH AND SETZER 1989, SETZER 1990) .

Figure 70 shows that in all curing procedures the total water content in pores wider than 1.5 nm observed by LTC is clearly higher than the MIP volume. This supports the correctness of the extracting pore radius of 4 nm. The same conclusion can be drawn from the literature referred to Section 5.4.3.6.

The validity of pore radius 1.5 nm can be further examined by comparing the freezable water with the immersed water in carbonated specimens stored at RH 45%. This relative humidity corresponds roughly to the Kelvin radius of 1.5 nm. Figure 71 shows these ratios to correlate quite nicely, giving additional evidence of the size of the smallest freezable pore radius.

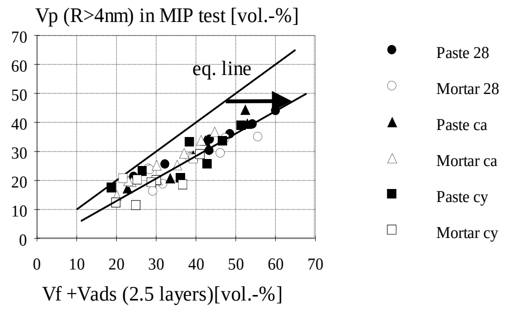

Figure 70. Freezable water in pores wider than 1.5 nm added to adsorbed water, in relation to the pore volume detected by MIP .

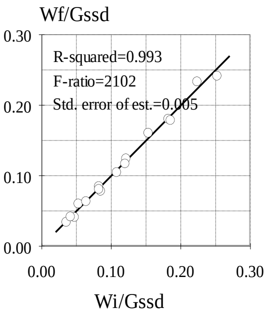

Figure 71. Total freezable water related to immersed water after carbonation at RH 45% for 15 months.

As stated earlier in the comparison of MIP results with those of LTC, an approximation of the pore model was presumed. Calculations with spherical, cylindrical and layered pore models were performed to determine the total pore volumes in the micropore (R_p<1.5nm), microcapillary (1.5nm<R_p<4nm) and macropore (R_p>4nm) ranges. Adsorbed water and specific surface areas for different pore models are presented in the tables of Appendix J. In the calculations the freezing thermogram was sifted, assuming the first freezing to take place at 0°C. This means that when supercooling was approximately 5.3° C, 3.7° C and 4.0° C in the curing procedures "28 days", "carbonated" and "cycled" respectively, the extracting pore radius of 4 nm corresponds to the freezing temperature of -24° C. Freezable water above 4 nm was calculated so that it corresponds to the temperature of -20° C. Examination of the freezing thermograms in Appendix H shows, however, that this shift has no effect on the freezable water above 4 nm, but naturally has a certain increasing effect on the adsorbed water content, since the specific surface area is calculated from slightly finer pore spaces. The case is as described if we accept the assumption that supercooling is of the same magnitude throughout the temperature range. If supercooling exists only at high temperatures, i.e. above -15° C, the shift of the thermogram should not be accepted at lower temperatures (columns entitled "Layered model/fine" in Appendix J). Then the adsorbed water content for microcapillaries increases remarkably, causing an average increase of 15.3, 14.3 and 9.9% in micropore volumes of specimens cured by the procedures "28 days", "carbonated" and "cycled", respectively, when the layered pore model is applied. Correspondingly, the changes in macropore volumes are -4.7%, 1.6% and 0.5%, which is not necessarily correct. The acceptable pore model in each case can be estimated from the tables in Appendix J, where the measured freezable water contents and calculated adsorbed water contents of the different pore models are subtracted from the total porosity. The shaded columns giving negative values show unacceptable pore models. The results show that the spherical pore model is impossible for any mix composition used in this study. Theoretically only OPC mixes subjected to curing procedures "28 days" and "cycled" fulfill the condition $V_{micropore}$>0, but the pore volume is too low to be realistic. The cylindrical pore model can be accepted for OPC mixes subjected to the above curing procedures, but with the "carbonated" procedure a layered model is most probable, as with all curing procedures for GBFS mixes. The aforementioned pore models were used to compare the pore volumes of macropores detected by LTC and MIP (Figure 72).

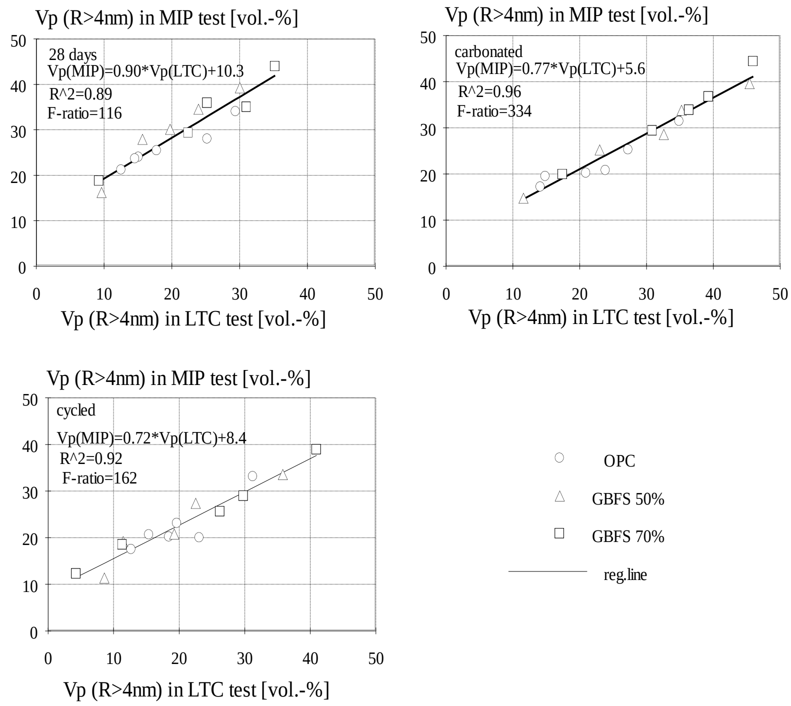

Figure 72. Correlation between macropore volumes measured by LTC and MIP.

Examination of the graphs in Figure 72 shows that the higher the degree of carbonation, the better is the fit between the results of MIP and LTC. In the non-aged state MIP gives clearly higher values than LTC. In the carbonated state the values are approximately equal, and after the "cycled" curing procedure the results lie in between. These facts lead to the conclusion that drying in a vacuum for 6 weeks at room temperature has coarsened MIP samples drastically in the non-aged state, and also in the aged state when carbonation has been minimal. Naturally, in the carbonated state the same phenomenon is possible, but in this case the changes will already have opened the pore structure due to the formation of silica gel and carbonation induced drying. With GBFS compositions the phenomenon seems to be more obvious, reflecting the differences in gel structure of this binder. Vacuum- drying makes the inner slag hydrate within the boundaries of the original slag grain more porous and more permeable, and the porous skeleton structure within this hydrate becomes measurable by MIP. Before vacuum drying or carbonation, the pore sizes in dense ISH layer are typically smaller than 4 nm and afterwards wider.

Carbonation related to porosity

In Figure 73 the freezable water contents V_f and the total water contents V_p in the macropore range obtained by LTC have been plotted as a function of the carbonation factor. The figure shows considerable scatter of the results. This is to be expected as the population includes samples of different water-binder ratios and varying degrees of hydration, which markedly affects the coarse capillary porosity. However, the figure shows a higher pore volume, due to the increased carbonation factor, with all mix compositions. When the pore model assumption is included, the differences in behavior according to binder type become visible.

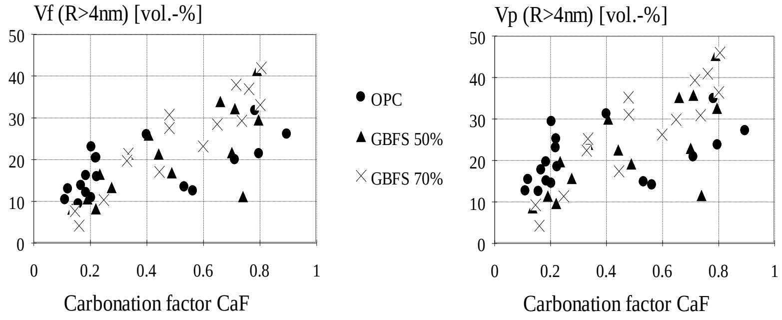

Figure 73. Effect of carbonation factor on macropore volume.

The effect of carbonation and cycling on the changes in macroporosity is given as average volumes of mortar and paste samples in Figure 74. With GBFS binders the increase in macroporosity after carbonation is three-fold compared with OPC. If a rough approximation is made according to which two thirds of carbonates precipitate in these pores, the net effect of carbonation can be estimated. Calculations show that the average increase in macroporosity after carbonation treatment was 9.3 vol.-% in OPC blends, and 18.0 and 18.7 vol.-% in GBFS 50% and GBFS 70%, respectively. The percentages after cycling were 3.3, 7.2 and 7.6, respectively. If all carbonates are assumed to precipitate in the coarse pores, the above values increase only by 2-3 vol.-% in carbonated samples and by 1-2 vol.-% in cycled ones.

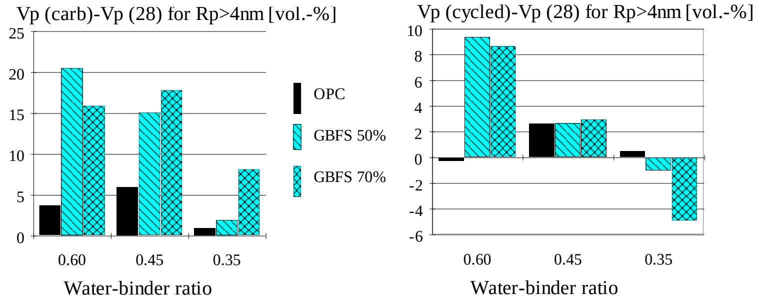

Figure 74. Difference in macroporosity values after carbonation and cycled treatments.

In order to investigate the effects of different parameters on macroporosity, multiple regression analysis was used to formulate a linear combination that gave the best fit in the population formed from the results with the "non-aged" and "carbonated" curing procedures (Figure 75). The analysis gave Equation 56, which includes the new variable SHP as the fraction of SH gel of the total gel volume calculated on the basis of the C/S ratio in section 5.4.4.4.

$$V_{MCap}^{carb} = 9 - 30 \cdot \alpha + 76 \cdot w/b - 8 \cdot s - 72 \cdot CaF + 67 \cdot SHP \qquad (56)$$

SHP is strongly dependent on the carbonation factor and also on the type of binder as follows:

$$SHP \cong (0{,}7 + s/5) \cdot {}^{(CaF - 0{,}1)}\!/_{0{,}6} \ \leq 1 \qquad (57)$$

Insertion of CaF from Equation 57 into Equation 56 gives a rough approximation for the volumes of macrocapillaries as a function of α, w/b, slag content and silica hydrate content (Equation 58).

$$W_{Mcap}^{carb} = 2 - 30\,\alpha + 76\,\frac{w}{b} - 8\,s + (5.3 + 15\,s) \cdot \mathrm{SHP} \qquad (58)$$

Equation 58 gives an increase of 3.5 and 7.9 vol.-% in macroporosity of OPC and GBFS 70% blends, respectively, due to the transformation of CSH gel to SH gel to an extent typical of non-aged and carbonated states in this study. No changes are supposed to occur in the degree of hydration. The above values are in a rather good agreement with the average values in Figure 74. This leads to the conclusion that the grater part of the increase in macroporosity can be attributed to the formation of hydrous silica gel, and that this increase is roughly two-fold in GBFS blends compared with OPC blends.

6.2.6 Total porosity and its redistribution

Increased macroporosity due to carbonation of CSH gel should be in line with the decrease in gel porosity. Gel porosity was expressed earlier as a function of α, w/b, slag content, and carbonation factor in Equation 55, evaluated by the assumption that gel porosity equals the freezable water amount in pores smaller than 4 nm. Here the adsorbed water content is excluded. Now, if the gel porosity is formulated again assuming the pore models described earlier, it can be expressed as a function of slag content and SHP only (Figure 76). This gives:

$$W_{gel}^{carb} = (29.3 + 20\ \mathrm{SHP}) \cdot\ [1 + 0{,}4\,s\,(1 - \mathrm{SHP})\,] - 3{,}2 \qquad (59)$$

This shows that the gel porosity after carbonation is roughly 13.3 and 12.9 vol.-% in OPC and GBFS 70% binders, respectively, when SHP values typical of non-aged and carbonated states are used. These values are in good agreement with the changes in macroporosity (+3.5 and +7.9 vol.-%) and with those in total porosity (-9.3 and -3.3 vol.-%) calculated from Equation 60.

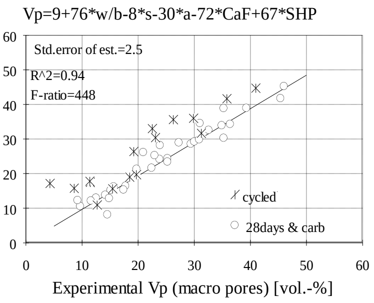

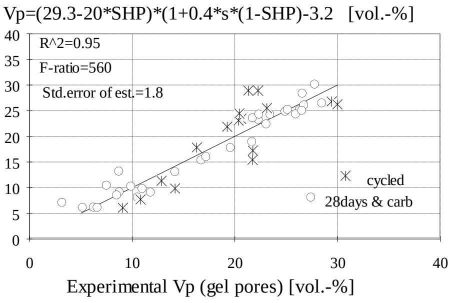

Figure 75. Modeled macroporosity in relation to measured porosity.

Figure 76. Modeled gel porosity in relation to measured porosity.

The derived equations are only estimates describing the effect of different variables on pore fractions. Standard errors of these estimates are within the limits 1.8 to 2.5 vol.-%, meaning that the effect of carbonation on coarsening of the macropore range wider than 4 nm differs significantly in OPC and GBFS compositions. It can be further concluded that changes in the CSH gel during carbonation explain the greater part of this behavior.

Differences in the macroscopic gel structure between OPC and GBFS compositions can be observed in the redistribution of porosity inside the gel pore range. Figure 77 shows that in OPC mixes most of the overall coarsening has taken place at the expense of the finest gel porosity smaller than 1.5 nm. In GBFS blends, however, microcapillaries from 1.5 to 4 nm have diminished more than in OPC blends. This reflects the changes in pore structure of the dense inner slag hydrate (ISH). Initially the dominant pore dimensions in this part of gel represented those typical of the gel pore range, i.e. smaller than 4 nm. During carbonation the lack of open pore space in the ISH gel prevents precipitation of carbonates in this part of gel, which remains permanently in its coarse state if there is no possibility for further hydration. This same behavior also explains the discrepancies between the results obtained by MIP and LTC, as discussed earlier.

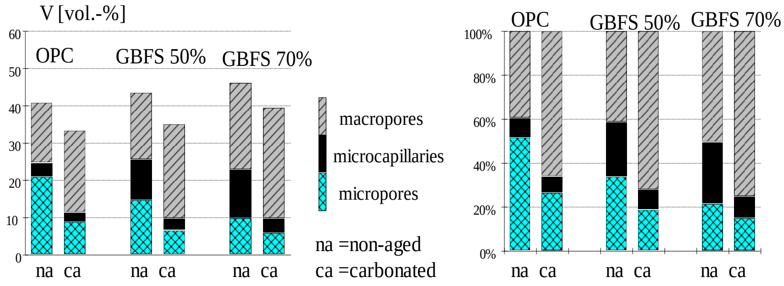

igure 77. Absolute and relative redistributions in pore ranges of different binder compositions due to carbonation.

Aging treatments decrease the total porosity in all mix compositions, as shown in Figure 78. The effect is strongest with OPC samples, but also GBFS samples show noticeable changes in total porosity. The average decreases in pore volumes due to carbonation are related to the volumes of carbonation products, which are highest with OPC binder (Figure 79). The decreases were 21%, 18% and 13% of the pore volume before carbonation for OPC, GBFS 50% and GBFS 70% compositions, respectively.

The reduction in total porosity caused by aging treatment occurs in OPC compositions at the expense of micropores and in GBFS blends due to the reduction in microcapillaries, as can be seen in Figure 77. The high decrease in microcapillaries was linked to the ISH gel of GBFS blends. Outer slag hydrate in GBFS blends obviously resembles the gel structure in OPC blends. On the other hand, the skeleton structure between the ISH and unhydrated slag is reported to be the most porous part of the slag hydrates (FENG ET AL. 1989). The coarsening of ISH due to carbonation opens the dense barrier between the closed skeleton porosity and the rather open outer porosity. As a result the permeability of the system increases. However, since total porosity decreases also in GBFS blends, spaces where the formed carbonates can precipitate are of interest. The pore diameters of the microcapillary range prevent precipitation as calcite and probably also as vaterite. Thus, the only place for carbonates to precipitate in the first stage is the outer slag hydrate and the transition zones. Although there would be enough space in skeleton structure, the ingress of CO_3^{2-} ions through the ISH barrier is slow or wholly prevented. As the formation of carbonates in the outer slag hydrate proceeds, more Ca^{2+} ions are needed to buffer the pore solution. This accelerates the formation of the SH gel, first in outer slag hydrate and finally in the ISH gel. As a result, the gel shrinks due to loss of interlayer water between the gel sheets and due to the escape of calcium ions from the CSH structure. Silica polymerization starts in the gel, and as a result of further carbonation the volume of solid gel decreases and porosity in the vicinity increases. In the GBFS gel, permeability increases and the ingress of CO_2 through the ISH hydrate enables precipitation of carbonates also into the skeleton space, and later also into the ISH gel.

Changes in the total pore volume can be estimated from Equation 59 derived by the same procedure as for earlier relationships.

$$V_{tot}^{carb} = 40 - 41 \cdot \alpha + 76 \cdot w/b - 8 \cdot s - 50 \cdot CaF + 29 \cdot SHP \qquad (60)$$

The standard error of the estimate for total porosity from Equation 60 is 1.9 vol.-%. Equation 60 describes poorly the changes in total pore volumes of cycled samples, as shown in Figure 80. This is due to the clearly higher degrees of hydration that Equation 60 does not take into account properly. Since the main purpose was to investigate pore structural changes due to carbonation, in the evaluation of Equation 60, as also in the equations before, the carbonated and non-aged samples were included in the test population.

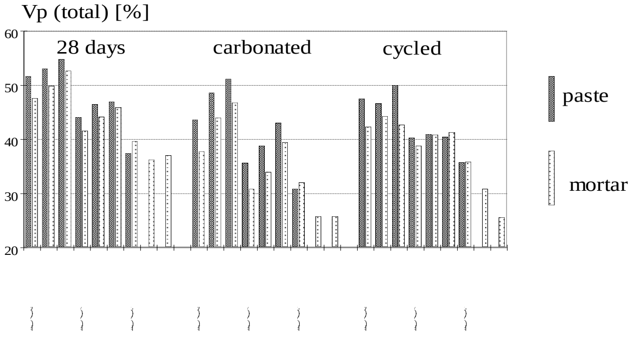

Figure 78. Effects of aging procedures on total porosity in paste and mortar samples.

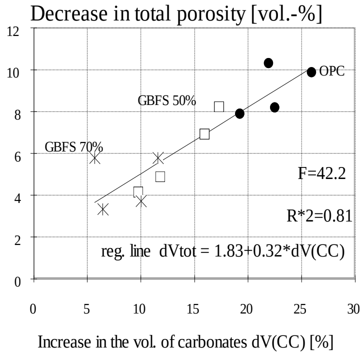

Figure 79. Relation between changes in total porosity and volume of carbonates, w/b-ratios 0.45 and 0.60.

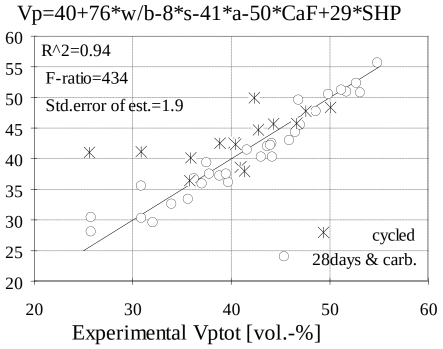

Figure 80. Modeled total porosity in relation to test results.

6.2.7 Coarsening of the pore structure during carbonation

The effect of aging on coarsening of pore structure was studied by comparing the ratios of freezable water at -20° C to the total porosity measured by LTC at different degrees of carbonation. This ratio is termed the "coarsening factor" (CoF). It describes the degree of "harmful" changes in the pore structure with respect to freezable water content in conditions typical of ordinary climatic exposure and generally used in laboratory tests. In fact, it could be regarded as the ability of mix composition to withstand freezing. Furthermore, this ratio corresponds approximately to the ratio of the volume of pores larger than 4 nm to the total pore volume.

Figure 81 shows the coarsening factor CoF as a function of the carbonation factor for the whole set of specimens studied by LTC. As can be seen from Figure 81 and Table 19, this relationship is strongest in compositions having the highest slag content. The effect of carbonation on coarsening of the pore structure was investigated by linear regression analysis between these two factors. The regression lines in Figure 81 include all mix compositions of each binder type, which explains the deviation in results. The regression lines fitted to the test results are presented in Table 19 for mix compositions of different binder types and in Table 20 for different water-binder ratios of each binder type. On the basis of the analysis of variance the results with pastes and mortars were included into the same population. Furthermore, the analysis proved that it is possible to separate the groups on the basis of binder type and water-binder ratio.

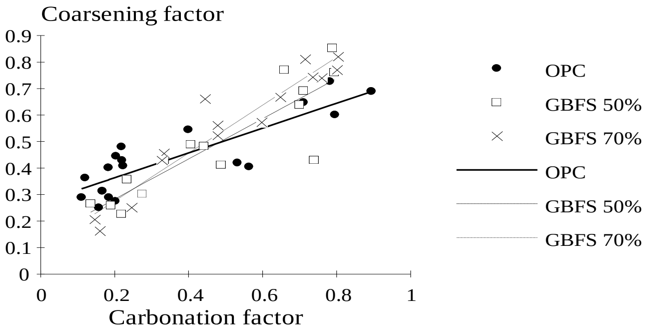

Figure 81. Relation between coarsening factor and carbonation factor for different binder types.

Consideration of the estimates for parameters A and B in the linear model $\mathrm{CoF} = \mathrm{A} + \mathrm{B} \cdot \mathrm{CaF}$ shows that the estimate for parameter B, describing the effect of change in the carbonation factor on coarsening, gives an acceptable probability level of <0.05 in the t-test for water-binder ratios of 0.60 and 0.45. Clearly there are not enough test results for concretes with a water-binder ratio of 0.35. It is also possible that carbonation in the paste and mortar samples of a low water-binder ratio 0.35 has not been enough extensive to provide the measurable changes.

The analysis demonstrates a significant correlation between coarsening of the pore structure and level of carbonation, and that coarsening of GBFS samples is roughly two-fold compared with OPC samples. The reasons for coarsening due to a decrease of the smallest pore range, namely micropores and microcapillaries, were considered earlier.

The increased coarsening supports the behavior observed in the frost-salt tests, which showed frost susceptibility of aged GBFS concrete in particular. In OPC compositions with typical carbonation factors, in both the non-aged and aged states the average coarsening factor increased from 0.41 to

0.64, an increase of 56%. Correspondingly, with GBFS 70% compositions, the comparable coarsening factors were 0.36 and 0.83, which as an increase of 220%. There is therefore no doubt that pore structural changes at this level are responsible for the reduced frost resistance of concrete.

Table 19. Statistical data of regression lines in Figure 81.

		OPC	GBFS 50%	GBFS 70 %
Estimates	a/b	0.270 / 0.468	0.131 / 0.758	0.095 / 0.904
t-values	T_a/ T_b	8.49 / 6.67	2.23 / 6.82	2.21/ 11.80
Prob. levels	a	0.00000	0.04346	0.04584
	b	0.00001	0.00001	0.00000
Model				
F-ratio		44.49	46.48	139.2
Prob. level		0.00001	0.00001	0.00000
Deg. of freedom		17	14	14
R-squared		0.736	0.781	0.915

Table 20. The statistics of the coarsening model CoF=a+b*CaF for different w/b-ratios.

		OPC			GBFS 50%			GBFS 70%		
	w/b	0.60	0.45	0.35	0.60	0.45	0.35	0.60	0.45	0.35
Estimates	a	0.372	0.263	0.257	0.111	0.115	0.193	0.136	0.121	-0.06
	b	0.400	0.477	0.272	0.912	0.759	0.313	0.850	0.818	1.63
t-values	T_a	13.55	6.62	7.27	1.62	2.40	4.31	1.51	2.08	-1.13
	T_b	7.79	5.56	2.61	7.75	7.97	3.61	6.21	7.74	8.19
Prob. levels	a	0.0001	0.0027	0.0019	0.1805	0.0749	0.1453	0.2064	0.1055	0.4606
	b	0.0015	0.0051	0.0593	0.0015	0.0013	0.1951	0.0034	0.0015	0.0774
Model:										
F-ratio		60.61	30.97	6.82	60.09	63.54	9.99	38.54	59.94	67.05
Prob. levels		0.0015	0.0051	0.0593	0.0015	0.0013	0.1951	0.0034	0.0015	0.0774
R-squared		0.94	0.89	0.63	0.94	0.94	0.91	0.91	0.94	0.99

6.2.8 Changes in pore size distribution

The effect of carbonation on the pore size distribution of concrete samples was considered in Section 6.1. MIP gave slight coarsening with all binder types. The same conclusion can be drawn from paste and mortar tests. The results show a slight decrease in the finest detectable pore range and correspondingly a small increase in the mesopore range. The results between paste, mortar and concrete specimens do not deviate markedly from each other. Differences between aggregate contents could not be registered.

Analysis of pore size distribution in the gel pore and macropore ranges is possible using the LTC results. Cumulative pore volumes or freezable water amounts related to pore sizes in the macropore range is, however, very obscure. In the graphs of Appendix I, carbonation seems to increase pore volumes from tens of nanometers to about 200 nm in the macropore range. With GBFS binders the phenomenon is clearer than with OPC binders. The position of the main peak in the macropore range should be regarded with great care due to the uncertainties caused by supercooling and delays in freezing over the specimen.

As stated above, the LTC method is very difficult to use reliably in dimensioning of coarse pore structure from the solidification thermogram. Perhaps extending the analysis to the fusion thermogram offers a more realistic manner to obtain a more reliable description of pore size distribution of coarse capillary pores. This can be done by a step-by-step method proposed by SETZER (1990) as discussed in Chapter 5. However, the method, based on several runs performed in different temperature ranges, was not used in this study due to the long testing time by LTC.

7 CARBONATION MODEL FOR GBFS CONCRETE

Carbonation was defined as an aging process where dissolved CO_2 in the pore solution or free CO_2 in the pores attack unhydrated or hydrated binder products by a through-solution process or by a topochemical process changing the chemical, mineralogical, microstructural and pore structure characteristics of the binding component of concrete in its environment. This report concentrates on the pore structural changes in OPC and GBFS concretes exposed to environments where severe carbonation is possible. Due to these facts the model to be presented is only a contribution toward explain this feature of the carbonation phenomenon.

Drying is an essential element in the aging process of concrete. It is closely associated with the carbonation process, and it is difficult or impossible to separate from the rest of the carbonation process. In any case, any attempts to take this into consideration would have increased the test program considerably. Therefore drying was not differentiated from carbonation, and the volumetric changes observed in the experiments also include the effect of irreversible shrinkage at RH 45%. In fact, a certain proportion of the drying-induced shrinkage will be considered, as the test procedure used in calorimetric measurements enables account to be taken of the effect of reversible shrinkage occurring in small samples during a water immersion time of 5 days.

The main differences in the hydration kinetics of GBFS and OPC pastes lie in their *in-situ* products. According to the literature, the outer CSH formed is alike. Naturally OPC pastes comprise more portlandite and sulfate phases, which play an important role during carbonation in the most porous spaces of the cement matrix, in large capillaries and in porous transition zone areas. In GBFS pastes the dense inner slag hydrate layer (ISH) separates the two areas of the most porous hydrates, the outer slag hydrate (OSH) and the skeleton hydrate (SKH), as shown in Figure 82. In OPC pastes the inner hydration product is more porous but the connection of its homogeneous structure to the unhydrated material is more uninterrupted than with GBFS pastes (Figure 83).

Carbonation begins with the attack of dissolved carbon dioxide in the OSH gel. In this phase available calcium hydroxide is consumed and tri- and monosulfates begin transforming to their carbonated forms. Carbonation resembles that of OPC, with the exception that more Ca^{2+}ions must dissolve from CSH than in OPC to maintain the alkalinity in the pore solution. Carbonates precipitate as calcite or as vaterite in the open capillaries in the transition zones between the aggregate particles and binder paste and the OSH gel (stages 1 and 2, Figures 82 and 83). Due to the lower lime content in GBFS paste, simultaneous carbonation of the CH and CSH gel is more likely in GBFS. When the most easily available CaO is consumed, the CSH gel starts losing its Ca^{2+} and OH^- ions present in the interlayer regions of the tobermorite-like gel or mixed tobermorite-jennite like gel.

When more CO_2 penetrates the binder matrix and dissolves in the pore water, and when the availability of buffering Ca^{2+} ions from the OSH gel becomes abundant, the ISH gel serves as a buffering reserve for the pore solution with increased CO_3^{2-} concentration in the OSH gel space. Interlayer water in the gel, adsorbed water on gel surfaces and on pore walls, and water released during carbonation guarantee the mobility of Ca^{2+} ions by diffusion to the species of the OSH gel large enough for precipitation of carbonates (stages 2 and 3, Figure 82). Overall porosity in the ISH increases as a consequence of the net loss of calcium and water from the gel matrix. It is possible that Ca^{2+} ions from the ISH framework may be partly replaced by Mg^{2+} ions enriched in the ISH gel. In any case, the net effect is increased porosity. Once the porosity in this pore space has increased enough, the penetration of CO_2 into the ISH and through it into the SKH gel is eventual (stage 4, Figure 82). More Ca^{2+} ions are released and carbonation may proceed as precipitation of the finest morphologies, i.e. vaterite in SKH gel and partly also in the most porous spaces of the ISH gel (stage 5, Figure 82).

In OPC pastes the dissolution of Ca^{2+} ions from the outer and inner CSH gel is slower than in GBFS pastes, since the lime from CH enables longer buffering of the pore solution. Consequently the transformations of the CSH gel structure take longer throughout the cement matrix, in the inner and outer hydrates, and also in the transition zones (stages 2 to 4, Figure 83).

The morphology of calcium carbonates inside the borders of the initial slag particle, i.e. in the spaces of ISH and SKH, is vaterite and its further crystallization into calcite is probably impossible or very slow. Two facts supports this polyform. First, there is insufficient space in these gels for the formation of well-crystallized calcite. Second, the enrichment of Mg^{2+} ions in the gel space (section 5.4.7) inhibits vaterite from transforming into calcite, as discussed in section 3.2.7. Calcium carbonates formed in the inner CSH of OPC blends clearly also have the metastable polyform of vaterite, but only due to lack of precipitation space rather than the incorporation of foreign ions. The more open structure of OPC compositions in this gel space may also enable precipitation of more crystallized polyforms. The morphologies of calcium carbonates in the OSH gel are vaterite, aragonite and calcite for both binders. The metastable phases vaterite and aragonite are formed first, followed by transformation into calcite to an extent determined by the dimensions of the open porosity. Well-crystallized calcite is observed to form in large pores over 50 nm in radius, and poorly crystallized vaterite in smaller pores of 5 nm. This provides evidences of the existence of calcite in the relatively open structure of transition zones.

When modeling the carbonation process in GBFS concrete with high slag content, the role of MgO should not be neglected. Mg^{2+} ions in the ISH and SKH gels have deviating ionic radii that retard or totally inhibit crystallization of calcite in these gel areas. Evidently then these ions form part of the mixed vaterite phase. There are, however, at least in principle two ways in which carbonates involving MgO compounds can form. The first is the formation of magnesium carbonate from the brucite phase. Although the solubility of this phase in water is low, it is possible that at a low pH level of high CO_3^{2-} concentration in the pore solution it dissolves, and that subsequent formation of $MgCO_3$ is possible. This presumes that the brucite phase is first formed through the hydrolysis of MgO. Possibly this kind of direct carbonation seldom occurs in extreme conditions of well-saturated pastes with high CO_3^{2-} concentrations in the

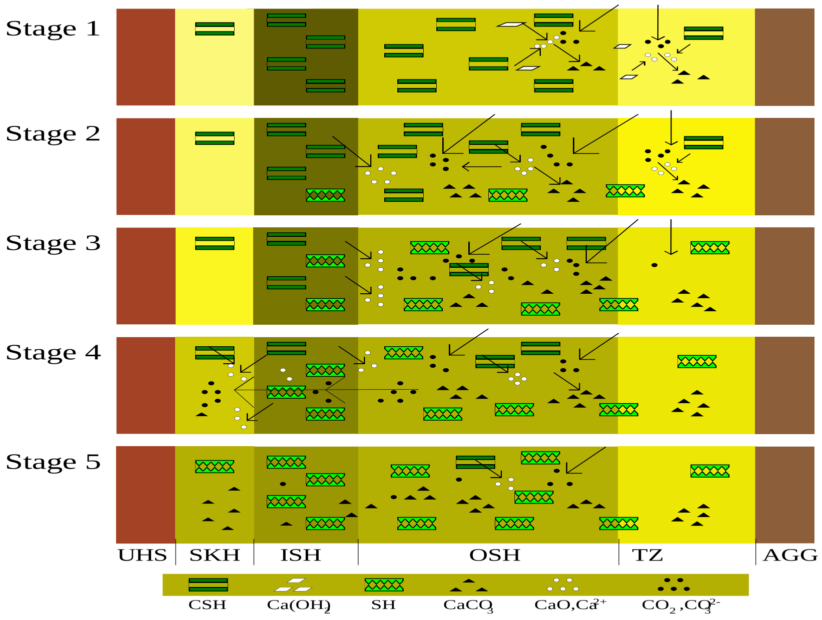

Figure 82. Schematic representation of the proposed carbonation model for GBFS concrete.

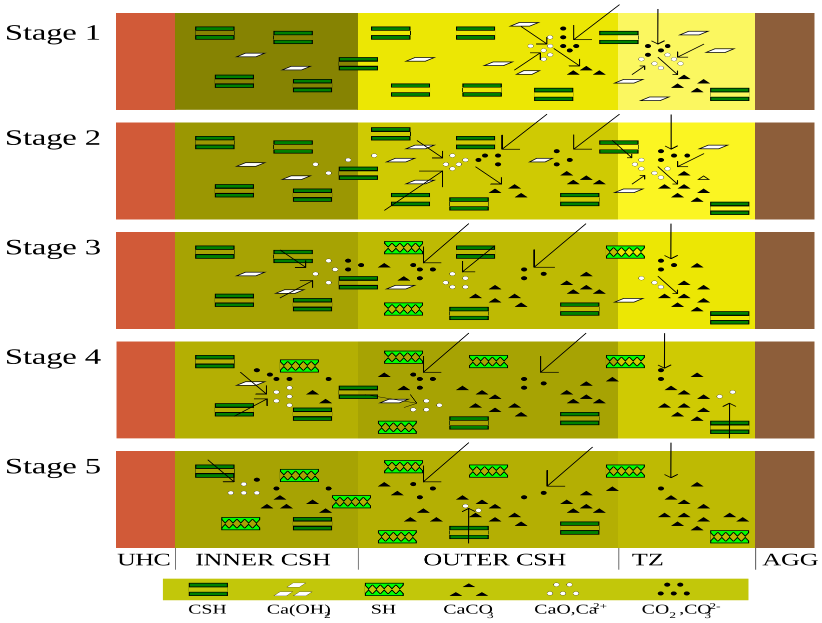

Figure 83. Schematically presented progress of carbonation in OPC concretes.

pore solution. The second is the existence of hydrotalcite $M_6A\overline{C}H_{12}$ by itself in GBFS concrete. What the chances are of this compound forming during carbonation is not clear. Perhaps its appearance is merely associated with the hydration process as a result of the direct reaction of cement containing carbonates with magnesium aluminate hydrates, being analogous to the direct formation of carboaluminates. Its separation from monosulfate and carboaluminate phases by XRD is obscure, and at least the results of XRD tests in this study do not support the formation of hydrotalcite during carbonation at relatively low RH.

Redistribution of pore sizes during carbonation is explained by the changes in interlayer regions of the tobermorite-like gel or of the mixed tobermorite-jennite-like gel, by the silicon polymerization that results, and by the loss of interlayer water of the gel. Calculations of C/S and H/S ratios in section 5.4.4.5 showed that CSH gel in GBFS mixes loses roughly 75% of its CaO and about 40% of its H_2O during carbonation. The corresponding losses with OPC mixes were 70% and 50%. The rearrangement of silicon tetrahedra after the escape of Ca^{2+} and OH^- ions causes a certain volumetric decrease in the remaining gel. A rough estimate for the volumetric decrease due to the 75% loss of Ca^{2+} ions from the CSH network could be as high as 40%. One dimensional change is about 20%. Assuming that the CSH gel is composed of two of the three 14 Å tobermorite layers, with one adsorbed water layer between and along the sheets, one dimensional decrease of 20% in the thickness of the initial gel is enough to double an average gel pore radius of 1.5 nm. Negative pressure in the gel at low RH assists the rearrangement of silicon tetrahedra in the remaining SH gel into more ordered position. Of course, this contributes to the increase in gel pore space.

Carbonation at low RH accelerates modification of the pore structure in the ISH gel and, possibly due to the parallel effects of carbonation and drying, the changes are greatest at the lower level of intermediate humidities, i.e. 45% to 50% RH. When carbonation occurs at higher RH the coarsening process differs from the described one. Ingress of CO_2 into the pore system of the OSH gel and the transition zone is slower but the effect is the same as described in stages 1 and 2 above. Differences exist with regard to the transformation of the ISH gel and to the changes in the SKH gel. The higher degree of saturation in the pores enables the dissolution of Ca^{2+} ions from unhydrated slag and Ca^{2+} ion diffusion occurs through the ISH gel to the OSH gels. This may take place by direct diffusion or by a restoring process in which lost Ca^{2+} ions from the tobermorite-jennite-like gel of the ISH needed to buffer the pore solution in the OSH gel are replaced by the Ca^{2+} ions dissolved in the SKH gel. This leads to a net increase in the porosity of the SKH gel, the porosity of the ISH gel remains unchanged, and the barrier between the more open gel structures of the SKH and OSH gels may densify even further. The open porosity of the SKH gel remains isolated from the rest of the paste as long as the ISH preserves its density. If carbonation proceeds at lower RH or drying-induced coarsening of the ISH gel begins, the density of the isolating barrier diminishes and the gel structure becomes more permeable. The porous SKH gel then comes within the field of activity of the penetrated substances.

As a consequence of both the above hypotheses, the gel structure coarsens. The more homogeneous structure of the inner hydrate in OPC compositions gives a relatively smaller redistribution in overall porosity of the binder matrix than is a case in GBFS mixes. At what rate coarsening occurs depends naturally on the predominant RH. At high RH, carbonation is slow and carbonation-induced coarsening is at least partly compensated for by further hydration. However, as the results with samples cured by repeated wetting and drying treatment show, a certain amount of coarsening takes place anyway.

8 DISCUSSION

8.1 TEST METHODS FOR POROSITY MEASUREMENTS

The methodology used in measuring porosity is of great importance. Most test methods presume certain preparation processes able to change or even to destroy the original pore structure. The observations based on the results of this study confirm the difficulties to characterize reliably and unambiguously the pore structure of cement based materials. In this study porosity was studied by thermoporometry and MIP for pastes and mortars, and by water suction and MIP for concretes.

Thermoporometry

The basis of thermoporometry is very theoretical. The absolute value of freezable water at specified temperature is highly dependent on the transition enthalpy of the pore water itself. Values ranging from 80 J/g (SETZER 1990 p. 423) to 126 J/g (T=253° K), 172 J/g (T=233° K) and 208 J/g (T=213° K) (BRUN ET AL. 1977) are presented in the literature. The equation proposed in this investigation gives the values 92, 134 and 170 J/g, respectively, at the above temperatures. The enthalpy of pore water can only be estimated, and the entropy of the pore system at specified temperature is dependent on the overall pore geometry due to the effect of superficial phase transformations. Due to the uncertainties associated with these facts, the evaluated relationship between the enthalpy and freezing point depression (Equation 28) was used only as a relative measure to distribute separately-calculated total freezable water among different pore sizes. Total freezable water content was calculated using the assumption that enthalpy is a thermodynamic state property, in which case approximations regarding the temperature dependence of enthalpy are not necessary.

The surface extension energy of the liquid-solid interface was used in Laplace's equation for pore size dimensioning. However, reported data in the literature on the magnitude of this quantity is scarce. Only estimates determined semi-empirically or solely theoretically were available for the formulation of surface tension as a function of temperature depression (Equation 33). The quantity is linearly proportional to the temperature, creating an evident uncertainty in thermoporometry. Some doubt also exists concerning the thickness of the adsorbed non-freezable water layer at larger pore sizes. In the gel pore range it seems established that the thickness is 2 to 3 molecular layers. This, coupled with the fact that third to sixth molecular layers are able to change their thermodynamic state at around -40° C is evidence of the correctness of the largest gel pore range of 2 nm in radius determined by Equation 35.

Despite some uncertainties, thermoporometry gives a highly accurate total porosity above 1.5 nm for fully saturated samples, and a rather accurate pore size distribution in the pore range 1.5-50 nm. LTC enables measurement of the gel porosity range, as stated above. Further confirmation could be drawn by comparing the obtained results with nitrogen gas adsorption results. Both methods gave peaks in the same pore range of radius 1.5-2.5 nm. This confirms that suspicions that a second peak at -40° C in freezing thermograms is caused by an anomaly in the specific heat of pore water, are not correct. This part of the freezing thermogram belongs to the entropy of phase transformation in gel pore water and partly to the entropy changes caused by superficial phases. The same conclusion can be drawn from the fusion thermograms, which showed that the higher the peak at -40° C in the freezing thermogram, the earlier and more powerful was the deviation of the fusion thermogram from its baseline.

When considering pore volumes on the basis of the test method used, it should be borne in mind that there is a degree of uncertainty related to the test method itself. The used method involves vacuum saturation of samples with water before testing. If the pore structure is severely isolated, it is possible that saturation does not reach all of the pores and part of the cement paste remains under-saturated, giving an underestimation of the pore volume. This uncertainty is impossible to restrict with the test method used, and may cast a small shadow over the porosity values of very dense high-strength test samples. However, the results of the MIP run with the vacuum saturated sample did not show any intrusion of mercury giving evidence that at least the coarsest pore range is in a state of full saturation.

Although there are uncertainties in the thermoporometric characterization of the pore structure, the method is a useful tool for linking the gel and capillary porosities to each other, and gives a direct measure for the freezable water when frost resistance is of interest. In the latter consideration, distrust of the saturation degree in the tested sample is pointless.

MIP method

The great advantage of thermoporometric testing over conventional methods is that sample preparation is unnecessary. Water plays an essential role in hardened paste, being the bridging component in the gel structure, existing as an adsorbed layer on pore walls, and condensing in pores at various levels of relative humidity. This is why any sample preparation technique which alters the moisture state of the matrix causes serious difficulties in pore structure characterization. In MIP testing the samples were predried in a vacuum. Due to this the test results are more strongly dependent on the gel structure and pore geometry. The test results provided some evidences to the use of MIP with vacuum-dried samples as a measure for total porosity. For aged samples the pore structure has already changed so much that the effects of vacuum drying are not as pronounced and are partly compensated for by another error feature associated with underestimation of the non-measurable, isolated porosity in the pore space larger than the lower detectable pore radius. A relatively high portion of this porosity cannot be measured in aged, or possibly also in non-aged, samples due to the irregularity of the pore structure.

The MIP results for compositions differing in terms of air-entrainment showed that roughly half of the air pores in the range 10 - 850 μm become detectable in the mesopore range 50 nm to 1000 nm. Correspondingly this phenomenon causes underestimation of the porosity in the skeleton hydrate gel in GBFS concretes. Intrusion of mercury through the dense ISH layer into the porous skeleton hydrate space underestimates capillary porosity in GBFS compositions. Due to this, the comparison of OPC and GBFS compositions based on MIP tests alone leads undoubtedly to misleading conclusions regarding the effect of slag replacement on pore characteristics. This is the case regardless pretreatment methods or aging procedures, but with aged samples opening of the ISH gel decreases underestimation of the porosity in the SKH gel. Perhaps a reassessment of the current understanding concerning the pore structure of GBFS concretes based on MIP results would be timely.

Vacuum drying seems to be far too strong as a pretreatment method for MIP samples. It alters the porosity of non-aged samples to roughly the same extent as would carbonation at 45% RH for 15 months. This accounts fully for the contradictory results reported in the literature concerning the effect of carbonation on the coarsening of the pore structure of GBFS concretes. Perhaps a more gentle drying method, such as the solvent replacement method, should be used if the effect of aging on the pore structure is to be studied by MIP.

8.2 POROSITY OF AGED SLAG CONCRETE

8.2.1 Carbonation-induced changes in porosity

Porosity and its redistribution were studied using MIP and LTC in the macropore range and LTC in the gel pore range. Pores smaller than 4 nm were defined as representing the gel porosity, micopores and microcapillaries, denoting pore radii of <1.5 nm and 1.5 - 4 nm, respectively. Macropores or macrocapillaries were divided into capillary and mesopore ranges of 4 nm to tens of nanometers, and tens to hundreds of nanometers, respectively.

Micropores

The micropore volume was measured as non-freezable water (V_{pnf}) determined by drying the tested LTC sample at 105° C and subtracting from this the amount of total freezable water in the LTC test. This slightly overestimates the micropore volume as some hydrated water is lost under 105° C and non-freezable adsorbed water at -63° C becomes included in V_{pnf}. However, this approximation can be accepted in order to compare the effects of different binder types on the smallest porosity range during carbonation. Naturally some error arises from the fact that the pore geometry, especially in the microcapillary range, may be different in the gel structure of OPC and GBFS compositions. GBFS compositions, having a more layered pore structure in the non-aged state than in OPC compositions, has a smaller adsorbed water content which causes a lesser overestimation of micropore volume.

The results show that carbonation decreased the relative and absolute pore volume of micropores. This was the case with all mix compositions regardless of GBFS content. The higher the slag content, the smaller was the volume of micropores both before and after carbonation when taken as a function of absolute volume of carbonates. The amount of carbonable compounds with GBFS binder is clearly smaller that with OPC binder. Due to this the volume of micropores was considered as a function of the carbonation factor (i.e. the degree of carbonation), defined as the ratio of the total amount of CO_2 gases evolved in the TG+EGA test to the maximum CO_2 content able to combine with the oxides of Ca, Mg and alkalis of the binders. The oxide content able to carbonate was assumed to be related to the degree of hydration. The consideration showed that at a high degrees of carbonation the volume of micropores is roughly independent of the binder type. This led to the conclusion that carbonation reduces micropores more strongly with OPC binder than with GBFS binder, and further that the micropore structural state of OPC seems to approach that of GBFS during carbonation. The "collapse" of the layered structure of the cement gel is evident due to carbonation and/or to the simultaneous carbonation and drying of the cement gel. The transformation of the denser CSH gel toward a more porous SH gel also partly explains the decrease in micropore volume, as was also observed in the microcapillary volume.

The decrease in micropore volume was strongest with pure OPC compositions, lowering the pore volume by 12 vol.-% at a carbonation factor of 0.8 compared with the non-carbonated state. With slag contents of 50% and 70% the micropore volume decreased by 9 and 6 vol.-%, respectively. The correlation between micropore volume and carbonation seemed to be approximately linear, although variation of the results is obvious especially at high slag contents.

The relative micropore volume in the non-aged state can to be expressed as a function of the degree of hydration (α), water-binder ratio (w/b) and slag weight fraction of the binder content (s). A strong dependence of the micropore volume on the slag fraction (Equation 51) reflected the differences in overall non-aged gel structure between OPC and GBFS compositions. Statistical analysis showed that the same independent variables added to the carbonation factor (CaF) were significant in the formulation of the micro porevolume after carbonation.

Microcapillaries

The results obtained from the LTC test showed the microcapillary volume to have decreased remarkably due to carbonation treatment for 15 months at RH 45%. Average reductions were 47, 75 and 83% of the original value with the GBFS contents of 0, 50 and 70%, respectively. The highest slag content gave the highest total volume of 14.0% before carbonation and the lowest value of 2.4% after carbonation. The corresponding average volumes with GBFS 50% and with OPC binder were 13.3 - 3.3 vol.-% and 8.7 - 4.6 vol.-%, respectively.

The reasons for the decreased pore volume in this pore range are at least partly the same as for the micro pores. Differences between the OPC and GBFS binders indicate dissimilarities in the gel structure. GBFS concrete has a smaller lime content and is more strongly influenced by carbonation of the CSH gel. The formation of hydrous silica gel is more extensive in GBFS compositions. A very strong decrease in microcapillarity at high GBFS contents is powerful evidence as to the concentration of these changes in the ISH gel. The declined porosity in the ISH gel cannot be explained by the precipitation of carbonates, as the space is insufficient. The redistribution of porosity during carbonation is the most probable explanation. The initially relatively dense gel has become more porous, diminishing the microcapillarity due to changes in the outside and in the interlayer regions of the layered gel, to the resulting silicon polymerization, and to the loss of interlayer water of the gel. As a result, the average pore size in the ISH gel increases. Carbonation at low RH accelerates pore structural changes in the ISH gel, and possibly due to the parallel effects of carbonation and drying, the changes are very strong at the rather low RH (45%) used in the carbonation treatment in this study. Carbonation occurring at higher RH, as in the cycling treatment, also causes a reduction in microcapillary volume depending on the degree of carbonation. In this case, however, the pore volume was about 3 vol.-% higher than for non-aged and carbonated samples. This is due to the higher degree of hydration, which supposedly increases porosity in coarse gel pores.

In multiple regression analysis, the pore volume in this pore range was significantly dependent only on the slag fraction and on the carbonation factor. Analysis showed no significance with respect to the degree of hydration or water-binder ratio when the results of non-aged and carbonated treatments were included in the model. The most probable reason is the effect of extended hydration, which may increase or decrease this pore volume. The increase is caused due to formation of hydration products in the coarser pore range and the decrease due to hydration in the pore range considered. These contradictory effects may explain the discrepancy observed in the formulation of Equation 54, where no correlation could be found between porosity and degree of hydration. The higher degree of hydration explains to some extent the decreased pore volume in this range with GBFS samples, but less so for OPC compositions where the increase in the degree of hydration is not as strong.

The microcapillary volume was measured as freezable water between the temperatures of -20° C and -63° C in the LTC test. It does not include the adsorbed water content which causes underestimation of the microcapillary volume. Here the error due to possible changes in the pore geometry is naturally smaller with layered GBFS gel than with OPC blends having a more cylindrical pore shape.

Gel pore range

Transformation of CSH gel into SH gel causes a decrease in the gel pore volume. This phenomenon is enhanced by simultaneous drying of the gel structure. The transformation is stronger with GBFS compositions than with OPC blends. The gel pore volume of non-aged paste volume was about 27% to 33%, the lower value belonging to the slag paste with high degree of hydration and high water-binder ratio, and the higher value to the gel porosity in OPC paste with low degree of hydration and low water-binder ratio. The corresponding percentages after carbonation were 5% and 11%.

The effect of the fraction of SH gel on gel pore volume was confirmed by statistical analysis. An average SH gel fraction of the total gel volume (SHP) could be estimated on the basis of the CaO/SiO_2 ratio from the results of the TG+EGA test. This fraction correlated strongly with the slag content and, of course, with the degree of carbonation. The SHP value was roughly 40% higher in GBFS 70% blends than in OPC mixes. Using the most probable pore models in each curing state for different types of binder, the adsorbed water layer could be added to the freezable water in pores smaller than 4 nm in order to estimate gel porosity and to study its dependence on the degree of hydration, water-binder ratio, slag content, degree of carbonation and fraction of the SH gel. Multiple regression analysis showed that the gel porosity in non-aged and carbonated stages could be expressed as a function of the slag content and the SHP value only. Statistical analysis showed that 95% of the gel pore volume could be explained by these two variables only. Forcing the degree of hydration and the water-binder ratio into the model did not improve the correlation between the experimental and modeled values, due to the reversed effects of these variables discussed above in the context of microcapillarity.

In summary it can be concluded that during carbonation the initially higher gel porosity of GBFS compositions (around 20%) has become slightly lower (around 5 to 10%) than that of OPC compositions. Decreased gel porosity could not be explained by volumetric changes of precipitated carbonates. Transformation of the CSH gel into SH gel, and the redistribution of porosity due to carbonation and simultaneous drying, were the most comprehensive and probable explanations for the decreased gel porosity.

Macropore range

The effect of carbonation on the macropore volume can be studied using two different test methods. However, the results obtained by MIP and LTC differed markedly. Very clear coarsening of the pore structure in the form of decreased gel porosity and increased macroporosity during carbonation was observed with LTC, but this pore size redistribution was only slightly detectable with MIP. The reasons for this were discussed in Section 8.1.

According to the MIP tests, carbonation decreased the macroporosity by 7 to 16% in OPC mixes and by 7% to 12% with the GBFS 50% composition. With the highest GBFS content of 70% there was no reduction in macroporosity. The precipitation of carbonates takes place in this pore range. Average increases in volumes of carbonates from non-aged to carbonated specimens in the TG+EGA tests were higher than the decreased porosity values, being roughly 20%, 14% and 10% of the paste volumes for OPC, GBFS 50% and GBFS 70%, respectively. At least some of the increase in macro porosity in this pore range occurred with GBFS mixes during sample preparation or during carbonation, also according to the MIP results. It is most unlikely that these gel pore dimensions enable precipitation of carbonates.

According to the LTC results, carbonation increased significantly the coarse capillary pore volume, i.e. the result strongly contradicts the MIP results. Carbonation treatment increased freezable water above -20° C, i.e. the approximate volume of pores larger than 4 nm, by 40%, 55% and 71% on average with slag contents of 0%, 50% and 70%, respectively.

Comparison of the results of the two test methods shows that in the non-aged state MIP gives clearly higher values than LTC. In the carbonated state the values were roughly equal, and after cycling treatment somewhere in between. This provides strong evidence that the vacuum pretreatment of non-aged MIP samples causes marked coarsening. With GBFS compositions the phenomenon is even stronger. Vacuum drying makes the inner slag hydrate within the original slag boundary more porous and permeable, and the porous skeleton structure inside this hydrate becomes measurable by MIP. Before vacuum drying or carbonation, the dense ISH layer has a maximum pore radius typical of the microcapillary range smaller than 4 nm, whereas afterwards it is wider. This makes the MIP method combined with hard pretreatment somewhat unreliable. At least some precautions should be taken when comparing the results.

GBFS binder appears to be more inclined toward increased macroporosity due to carbonation. The increase was three-fold compared with that with OPC. If a rough and safe side approximation is made that two thirds of the carbonates precipitate in these pores, the average increase in macroporosity after carbonation was 9.3 vol.-% in OPC blends and 18.0 and 18.7 vol.-% in GBFS 50% and 70%, respectively. Correspondingly, the percentages after cycling were 3.3, 7.2 and 7.6.

Multiple regression analysis was used to formulate a mathematical expression for macroporosity. The following variables: degree of hydration, water-binder ratio, slag content, degree of carbonation, and SH gel fraction, were shown to be significant in the linear combination (Equation 56). Most of the increase in macroporosity could be explained by the formation of hydrous silica gel and this increase is roughly twofold in GBFS blends by comparison with OPC blends.

OPC and GBFS binders behaved differently in terms of redistribution of the pore structure. Results show that in OPC mixes most of overall coarsening occurs at the expense of the finest gel porosity smaller than 1.5 nm. In GBFS blends, however, microcapillaries from 1.5 to 4 nm diminish more than in OPC blends. This could be explained by changes in the pore structure of the dense inner slag hydrate (ISH). The initially dominant pore dimensions in this gel space are typical of the gel pore range, i.e. smaller than 4 nm. During carbonation, a shortage of open pore space in the ISH gel prevents precipitation of carbonates there, and the gel remains its coarse state as long as there is no further hydration. This same behavior also explains the discrepancies between the results obtained by MIP and LTC, as discussed earlier.

Pore structural changes within the macroporosity of concretes due to carbonation were studied by comparing peak shifts in the derivative pore size distributions obtained from MIP test results. The results showed a shift of the whole capillary pore area towards larger pore sizes with all binder types. The same conclusion could be drawn from the position of the peak. Capillary pore volume was decreased on average by 6% and 2% for OPC and GBFS 50% concretes but increased by 2% for GBFS 70% concretes. The cycled curing method caused a shift of the capillary pore area towards larger pore sizes too, but clearly to a lower extent. In this case the capillary pore volume decreased due to cycling, the decrease being greater for the highest slag content. In the mesopore range the pore volume decreased after carbonation by 15% and 12% for OPC and GBFS 50% concretes, respectively, and increased by 2% for GBFS 70% concrete. Despite the uncertainties associated with MIP, this method also does give evidence for coarsening due to carbonation in general, and for the stronger effect of the GBFS binder in particular.

The results obtained concerning pore structural changes in the capillary porosity of carbonated GBFS concretes in this investigation are in very good agreement with the results published by LITVAN AND MEYER (1986), BIER ET AL. (1987). BIER (1988), MATALA (1988), DISTLER ET AL. (1992), DE CEUKELAIRE AND VAN NIEUWENBURG (1992), and PARROT (1992). The only conflicting result is obtained by HÄKKINEN (1993).

8.2.2 Total porosity and its redistribution

Total porosity decreased in all mix compositions due to aging treatments in all tests with pastes, mortars and concretes. This was confirmed for concretes by the water suction test and for pastes and mortars by the LTC test. The reductions in pore volumes due to carbonation relate to volumes of carbonation products, which were naturally highest in OPC test samples. The average decreases in porosity with OPC and GBFS concretes for fully carbonated specimens were 14 and 2 vol.-%, respectively. The latter represents the average for both slag contents of 50% and 70%. In paste and mortar specimens the decrease was strongest in OPC samples but GBFS samples also showed noticeable changes. The decreases were 21%, 18% and 13% of the pore volume before carbonation for OPC, GBFS 50% and GBFS 70% compositions, respectively. The porosity reductions are related to paste volumes.

Decreased total porosity is caused by the precipitation of carbonates into the most porous spaces of the gel structure, such as transition zones between the aggregates and binder paste and outer hydrates in both binder types. Small pore diameters in the microcapillary range prevent precipitation of calcite and probably also of vaterite. Hence, the only place where carbonates can form in the first stage is the outer slag hydrate and the transition zones. It is also possible that at later stages of carbonation precipitation may also take place in the skeleton structure of GBFS gel enriched with Mg^{2+} ions. A relatively higher portion of vaterite among the calcium carbonates in carbonated GBFS mixes supports this concept. It is also possible that the existence of more poorly crystallized carbonates, such as vaterite, are more common in GBFS mixes which are more liable to carbonation of the CSH gel. Obviously carbonates will attempt to precipitate at the closest site where space allows. In GBFS mixes this as outside the ISH gel in the smallest range of macrocapillarity, where space does not allow the precipitation of calcite. Carbonation at low relative humidity also contributes to the formation of vaterite in small macrocapillaries due to the lower mobility of Ca^{2+} ions in the gel structure.

The results showed that there are clear differences in the redistribution of porosity between the OPC and GBFS binders during carbonation. Coarsening of the pore structure, i.e. the increase in the macroporosity and the corresponding decrease in gel porosity, takes place with both binder types but at the expense of different gel pore ranges. The reduction in total porosity and increased capillarity due to carbonation takes place with OPC blends at the expense of micropores and with GBFS blends due to the reduction in microcapillaries. This means that there are clear differences in the overall gel structure produced by these binders. The ISH gel is obviously the most probable site for the large amount of microcapillaries in GBFS blends. The outer slag hydrate in GBFS clearly resembles obviously the gel structure in OPC blends. The skeleton structure between the ISH and the unhydrated slag is the most porous part among the slag hydrates within the initial border of the slag particle. Now, coarsening of the ISH gel during carbonation opens the dense barrier between the closed skeleton porosity and the relatively open outer porosity. As a result redistribution of the porosity in GBFS compositions causes a certain increase in permeability of the matrix, enabling the ingress of CO_2 through the ISH hydrate and the precipitation of carbonates also in the skeleton space and, to a certain extent, also in the coarsened ISH gel.

The effect of carbonation on the total porosity of the OPC and GBFS concretes observed in this study is in line with the results published in the literature. The higher the GBFS content, the lower is the decrease in total porosity, due naturally to the lower amount of carbonable compounds in GBFS mixes. Few reports in the literature deal with the redistribution of porosity over its whole range. Instead, it is mainly considered within the capillary pore range, where it is measurable by MIP. Bier's results from measurements of the specific surface area in carbonated pastes by SAXS, and from the determination of the smallest capillary porosity (i.e. microcapillaries) by high pressure porosimetry, support the findings concerning changes in the gel pore structure determined by LTC in this research. These results confirm that the main reason for coarsening of the pore structure in GBFS concrete, i.e. the increase in capillary porosity at the expense of diminution in gel porosity, is due to transformation of the CSH gel into porous SH gel during carbonation.

According to Bier's carbonation model, the main part of the SH gel formed in GBFS concretes is situated in the outer CSH, right on the border between the inner and outer CSH. In the proposed carbonation model presented in Chapter 7, it was concluded that also the ISH has a tendency to carbonate and that this is one reason for the increased permeability in GBFS pastes. This conclusion, the inclination of the ISH gel to carbonate, was drawn from the very high degree of carbonation at high slag contents. The results with the TG+EGA tests showed that almost all carbonatable CaO was consumed, demonstrating that changes must also have occurred in the ISH gel. The models in this respect are not necessarily contradictory. The ISH and SKH gels in this study represent the hydrates within the borders of the initial unhydrated slag particle, corresponding to the inner CSH in Bier's model, and the inner slag hydrate here corresponds to the border zone between the inner and outer CSH.

Pure OPC and two GBFS contents comprising 50% and 70% of the binder were used throughout the tests in this study. Based on the calculated fraction of SH gel with different slag contents, no threshold value was found below which detrimental transformation of CSH into SH in the dense ISH gel does not occur. The C/S mole ratios of the CSH gel showed that in some mixes of both slag contents changes occurred in the ISH structure also after carbonation at RH 45%, and even after cycled curing. No threshold slag content was found for tolerable coarsening of the pore structure. DISTLER ET AL. (1992) have reported coarsening already at 20% slag replacement, but according to BIER the amount of carbonates formed from the CSH is not necessarily linear. Slag contents of 50% and 75% gave clearly higher carbonate contents from CSH than 30% slag replacement (BIER 1988 p. 81).

8.3 CARBONATION AND DURABILITY ASPECTS

Pore structural changes during carbonation and the effect on them of GBFS were the main subjects of this study. However, some concrete tests were performed to study the effect of carbonation on the durability of OPC and GBFS concretes.

Water permeability

Changes in water permeability due to carbonation were studied by comparing the changes in capillary indices defined as the change in degree of saturation as a function of the square root of time before the nick point. The results showed that in OPC concretes the capillary index is generally higher than in GBFS concretes, meaning higher capillarity in the form of pore continuity. After carbonation at high water-binder ratios the pore continuity was diminished in OPC concretes but increased in GBFS concretes. At low water-binder ratios the opposite was true. The capillary index had slightly increased in OPC concretes but decreased in GBFS concretes. Increased water permeability of severely carbonated GBFS concretes of high water-binder ratio may be associated with coarsening of the ISH gel.

The shape in the vicinity of the nick point area for the saturation curves gives information concerning differences in the gel structures of OPC and GBFS concretes. In slag concretes the curve deviates smoothly from the capillary line before reaching the upper line. In contrast, in OPC concretes the crossing point of the lines is clear, giving a well-defined location for the nick point. This is probably due to the existence of the ISH gel layer which prevents rapid saturation of the porous SKH gel.

There was no correlation between the capillary index obtained from the water saturation test and the cracking index based on thin section analysis. The results showed that randomly distributed cracks several micrometers wide scale did not affect the capillarity observed in the water immersion test. No correlation could be found between changes observed in the capillary pore range in the MIP tests and changes in capillary indices. Both methods should indicate pore continuity. Perhaps in OPC concretes the blocking effect of carbonates originating from the CH phase in the coarsest capillary pores efficiently prevents capillary water suction and in GBFS concretes the OSH gel has a dominant role.

Increased water permeability at high water-binder ratios was detected for GBFS concretes. Similar results have been reported in the literature by DISTLER ET AL. (1992) and DE CEUKELAIRE AND VAN NIEUWENBURG (1992).

Frost-salt resistance

Results of the frost-salt tests showed that in all cases, including different levels of air-entrainment, water-binder ratio, type of binder and strength, the deterioration of concretes increased after carbonation or after curing by repeated wetting and drying. In OPC concretes scaling was smooth or increased gradually. This was also the case in non-aged GBFS concretes. The most significant difference between the curves for OPC and GBFS concretes was observed with carbonated concretes. In GBFS concretes a very rapid period of deterioration was observed at the start of the test.

The correlation between rapid deterioration in the frost-salt test and the carbonated volume of GBFS samples was studied by linear regression analysis. This gave a very good coefficient of correlation between these variables at a probability level of over 99.9%. Significant correlation was also observed in GBFS concretes cured by repeated wetting and drying. On the contrary there was no correlation between these variables in either carbonated or cycled OPC concretes. This remarkable difference in the behavior of OPC and GBFS concretes in the carbonated state could not be explained by overall coarsening of the pore structure, although this coarsening was clearly strongest with GBFS binder. Coarsening itself explains the smooth increase in deterioration clearly observed with OPC concretes. The rapid deterioration in the early stages of the frost-salt test in GBFS concretes can be attributed to gel and pore structural changes during carbonation. Since scaling follows the carbonation front, gel spaces where the increase in porosity is relatively highest are in a key position. The densest gel spaces in the GBFS mixes before carbonation was the ISH gel, which had a dominant gel porosity smaller than 4 nm. Carbonation coarsens the pore structure toward small macrocapillaries, where water becomes freezable at the temperatures of the frost-salt test, causing rapid scaling in frost salt test.

Another explanation could be the increased degree of saturation in the SKH gel after carbonation. In the non-aged state this part of the gel remains in a state of under-saturation and the dense ISH gel may inhibit its saturation during the frost-salt test. After carbonation it may saturate quickly due to increased permeability of the ISH layer, which strengthens the frost action inside the OSH gel, i.e. within the boundaries of slag particles in the unhydrated state. Rapid deterioration of carbonated GBFS concretes was also noticed in properly air-entrained compositions. This supports the above mentioned hypothesis concerning the significant role of the ISH and SKH gels in the phenomenon. Conventional air-entrainment, even with low spacing factors, acts on the spaces of the OSH gel, and possibly cannot prevent frost damage caused by freezing of the pore water in the ISH and SKH gels.

The described degradation process is reconstructed on the basis of pore structural changes in aged GBFS concretes. It does not, however, entirely exclude the possibilities of other degradation processes. Osmotic pressure may play a role in rapid deterioration. Furthermore, it is not a total impossibility that some chemical reactions occur in the SKH gel after carbonation, which could increase degradation due to crystallization pressures. According to the author such processes would occur in the spaces of the ISH and SKH gels in GBFS concretes.

Consideration of the scaling curves of non-aged and aged samples shows that, after the rapid phase of degradation, the slope of the deterioration curve is very close to that of the non-carbonated curve. This suggests that possibly the pore structure under the carbonated zone is very similar to that in non-aged concrete. This demonstrates that drying itself cannot be the main reason for increased deterioration.

The abnormal and rapid deterioration observed in the frost-salt tests of carbonated GBFS concretes have also been reported in the literature. MALHOTRA ET AL. (1987 and 1988) reported rapid deterioration of GBFS concretes with varying slag contents. These *in-situ* tests were performed in a marine environment representing exposure conditions in practice. Similar results from laboratory tests are reported by VESIKARI (1988) and MATALA (1988) for GBFS concretes of ordinary strength grades and by KUKKO AND MATALA (1991) for high strength GBFS concretes with moderate slag contents. LITVAN AND MEYER (1986) found greater freeze-thaw susceptibility in GBFS concretes than in OPC concretes after 20 years of carbonation in natural atmospheric conditions. Contradictory results on the frost-salt resistance of aged GBFS concrete have been presented by VIRTANEN, according to whom aging of concrete is not as dangerous a problem as has been claimed on the basis of laboratory tests. However, in spite of the encouraging results, VIRTANEN recommends that permitted amounts of GBFS in frost-resistant concrete should be limited to 50% of the binder weight (VIRTANEN 1990, p. 107).

GBFS used in this investigation was of ordinary quality with a rather low specific surface area of 400 m^2/kg. Grain size in these slag types is so large that the degree of hydration remains low after appropriate curing times. After carbonation large amounts of unhydrated material remain that may hydrate further and make the coarsened pore structure denser, either by restoration of Ca^{2+} ions into the porous SH gel structure or in the form of totally new hydration products. In fact, under favorable conditions the increased permeability of the carbonated GBFS structure enables and accelerates extended hydration. Due to this self-healing process, coarsening of the pore structure in carbonated GBFS concretes does not necessarily imply severe rapid deterioration of concrete structures when the field conditions are favorable.

The recent development of GBFS binders toward very fine grain sizes, i.e. slags with specific surface areas of 600 to 900 m^2/kg is, however, slightly questionable. In light of the pore structural changes of the ISH gel, the forecast for the frost resistance of GBFS concretes made with these extra fine slags is somewhat depressing. The degree of hydration automatically becomes high and the lack of unhydrated material leaves the ISH gel after carbonation permanently porous with pore radii above 4 nm. In this pore range water is freezable in moderate temperatures above -20° C. What then are the frost resistance properties of water-saturated, carbonated GBFS concretes? Perhaps some precautions should be taken by restricting the use of these slag concretes to environments where freezing of pore water is impossible. Conventional air-entrainment, acting in the space of the outer slag hydrate, does not necessarily guarantee frost resistance in these concretes.

9 CONCLUSIONS

The main objective of the research was to characterize the pore structures of OPC and GBFS concretes and the changes in them during different aging processes, of which carbonation in atmospheric conditions was the most important. The second target was to collect some research data to evaluate the effects of these binders, and the effects of pore structural changes of concretes with these binders, on durability.

Test methods

When characterizing the pore structure of a heterogeneous building material, selection of a reliable test method is of great importance. In this research, pore structure measurements were carried out primarily with two methods, the widely used mercury intrusion porosimetry (MIP) and a relatively new method of low temperature calorimetry (LTC). Use of the latter for the dimensioning of pore sizes required several approximations regarding parameters which are extremely difficult to determine experimentally. Despite uncertainties related to the theoretical background of the thermoporometric approach for characterization of the pore structure, the method proved to offer many advantages over conventional methods such as MIP.

The proposed thermoporometric approach for characterization of the pore structure is based on thermodynamics and on data published in the literature. The presentation should be considered as a synthesis of previous work done by Swedish, Norwegian, Danish, German and French researchers in the field. The approach definitely needs further development. Many factors of uncertainty remain to be solved before the pore characteristics of heterogeneous cementituous systems can be unambiguously described with this method. Obviously the composition of pore water affects the transition enthalpy. Superficial phase transformations affect the amount of freezable water at specified temperature and the approximate thickness of the adsorbed non-freezable water layer, and the semi-empirical value of surface tension on the liquid-solid interface has its own effect on pore size distribution. Supercooling and delays in heat transfer make the dimensioning of large pores somewhat obscure. Further research is needed to clarify the implication of such matters.

Since enthalpy can be regarded as a thermodynamic state property, the total freezable water content can be measured accurately by LTC. The total porosity above 1.5 nm for fully saturated samples can be estimated with high accuracy, and the pore size distribution with some certainty within the pore range 1.5 - 50 nm. The method is a useful tool for linking the gel and capillary porosities together and gives a direct measure of the freezable water when frost resistance is of interest.

Further, the analysis of hysteresis between solidification and fusion thermograms is a tool for pore shape determination.

Results of this study establish that the existence of a second peak at -40° C in the freezing thermograms is due not to an anomaly in the specific heat of pore water, but to phase transformation of the gel pore water. Three facts speak in favor of this: Nitrogen gas adsorption shows a peak in the derivative pore size distribution curve in the same position of 1.5 - 2.5 nm radius as the thermoporometric method used in this study. Secondly, it has been shown that the third to sixth molecular layers of the adsorbed water change their thermodynamic state already at around -40° C. The third evidence can be drawn from the hysteresis between the solidification and fusion thermograms. The higher the peak in freezing thermograms at -40° C, the earlier and more powerful was the deviation of the fusion thermogram from its baseline.

The superiority of the LTC method over MIP lies in the fact that no preparation of the sample which would change the original pore structure is needed. The preparation of samples for the MIP tests, which included drying in a vacuum, coarsened the pore structure of non-aged pastes, mortars and concretes to such an extent that the effect of carbonation on the structure became almost unmeasurable. Vacuum drying seems to be too strong a pretreatment method for MIP samples, causing changes in the porosity of non-aged samples roughly equivalent to carbonation at 45% RH for 15 months. This accounts fully for the contradictory results reported in the literature concerning the effect of carbonation on the pore structure in general and on GBFS concretes in particular. A more gentle drying method, such as the solvent replacement, should be used if the effect of aging on the pore structure is to be studied by MIP. Changes in pore structure were clearly noticeable in the LTC tests, where no sample preparation was required. This conclusion is based on comparison of more than 300 MIP test results with those of over 100 LTC runs.

<u>Carbonation, pore structure and durability aspects</u>

On the basis of the research, the following conclusions can be drawn concerning the compositional, microstructural and pore structural changes in OPC and GBFS concretes during carbonation, and on the effects of these changes on durability properties.

- Total porosity decreased as a result of precipitation of carbonates in the transition zones and outer hydrates in both binder types. The decrease was smaller the higher the slag content.

- Coarsening of the pore structure, i.e. increased macroporosity and the corresponding decrease in gel porosity, occurred with both binder types during carbonation. Coarsening was greater the higher the slag content, and there was no threshold value for the slag content in this respect. Reduction in total porosity and increased capillarity took place in OPC blends at the expense of micropores, and in GBFS blends due to the loss of microcapillaries. The loss of microcapillaries in GBFS concretes was associated with carbonation of the inner slag hydrate gel.

- Overall gel and pore structures of OPC and GBFS concretes differed from each other especially in the non-aged state, the latter being slit or layered already in the non-aged state. Carbonation changes the gel pore structure of OPC concretes toward that of GBFS concretes.

- Transformation of the CSH gel into porous SH gel is stronger in GBFS concretes. This is the main reason for the decreased gel porosity and for the increased macroporosity, both phenomena being stronger with GBFS concretes. The lack of carbonable calcium hydroxide in GBFS blends contributes to the increased macroporosity.

- The initially higher gel porosity of GBFS compositions (about 20%) became slightly lower (about 5 to 10%) than that of OPC compositions. This could not be explained by volumetric changes in precipitated carbonates. The transformation of CSH gel into SH gel, and the redistribution of porosity due to carbonation and simultaneous drying were the most comprehensive and likely explanations for the decreased gel porosity.

- Carbonation increased significantly the coarse capillary pore volume and freezable water above -20° C, i.e. the approximate volume of pores larger than 4 nm increased by 40%, 55% and 71% on average with slag contents of 0%, 50% and 70%, respectively. The shift of pore sizes in a coarser direction was also observed in the macroporosity range.

- GBFS binder seems more inclined than OPC to increase its macroporosity during carbonation. The increase was three-fold by comparison with OPC.

- Carbonation of CSH gel in the inner slag hydrate resulted in increased permeability of GBFS concretes with a high water-binder ratio.

- A clear difference in the morphologies of calcium carbonates formed in OPC and GBFS concretes was found to exist. GBFS concrete produced higher amounts of poorly crystallized vaterite, reflecting a denser gel structure before carbonation and the presence of foreign substances such as magnesium ions in the pore solution.

- Both CH and CSH phases, can carbonate simultaneously, and this is more probable in carbonation at moderate relative humidities where some precipitated CH can remain. The disappearance of AFt and AFm phases during carbonation is evidence of the susceptibility of these phases to attack by carbon dioxide.

- Aging seems to lower the frost-salt resistance in general. Increased scaling in carbonated concretes was observed in all mix compositions regardless of level of air-entrainment or binder type or strength grade. Decreased frost susceptibility can be associated with overall coarsening of the pore structure during carbonation.

- The shape of the scaling curve differed markedly between carbonated OPC and GBFS concretes. In GBFS concretes a period of very rapid deterioration was observed at the early stages of the test. The rapid volume loss of samples correlated strongly with their carbonated volume. No such correlation could be found in OPC concretes. The most probable explanation for the rapid deterioration of GBFS concretes at the start of the frost-salt test is gel and pore structural changes in the inner slag hydrate. Carbonation coarsens the densest part of the gel spaces in GBFS concretes, changing the gel porosity towards small macrocapillaries where water becomes freezable at moderate temperatures. Increased permeability in the ISH gel layer contributes to the higher degree of saturation in the more porous skeleton hydrate. The result is rapid scaling in the frost-salt test.

- Following the rapid degradation phase, scaling in carbonated GBFS concretes followed that of non-aged concretes, proving that drying is not a principal reason for increased deterioration in aged concretes.

Coarsening of the pore structure in aged carbonated concrete, especially in GBFS concrete, is an established fact, and lowered frost resistance may be associated with it. Both aging processes gave the same result but the phenomenon was not as marked when extended hydration took place. During aging the pore structure is in a continuous state of change, where parallel and alternate coarsening and densification processes change the durability parameters of concrete accordingly. For this reason the long-term evaluation of durability of concrete in the laboratory is not especially accurate, particularly when tests are performed in the green state. No single laboratory test exists that can simulate reliably and universally the changing temperature and moisture states of concrete in the prevailing climatic conditions, short- and long-term rates of changes, and the various simultaneous co-parameters. The final usability of material cannot be established until sufficient practical experience has been gained.

A high degree of hydration is traditionally regarded as a desirable property of concrete. However, a moderate degree of hydration guarantees a reserve of unhydrous material that can, in later favorable conditions, restore durability properties. Particularly in carbonated GBFS concretes this is of major importance, as increased porosity in the inner slag hydrate gel is the most evident reason for the inability of the binder matrix to endure frost action. Perhaps the development toward very fine binders is a somewhat dangerous trend in light of the durability aspects if an extremely high degree of hydration with a low amount of cementitous material is obtained. In this respect the forecast for high strength concretes in the preparation of durable concrete structures seems to be good. The degree of hydration is low, enabling healing of potential pore structural changes due to aging.

However, the somewhat alarming results concerning the behavior of carbonated GBFS concretes under frost action, and the carbonation-induced pore structural changes, do not necessarily constitute the demise of GBFS concrete. On the contrary, according to the author these results should be seen positively as a new beginning for developing concrete structures with a longer service life. There is also a special place for GBFS concretes, especially if all their properties, both favorable and hazardous, are objectively and exhaustively evaluated in the selection process of binding materials. A certain reassessment of the code of practice would be needed to guarantee service life costs within reasonable limits in the near future. This requires broad cooperation between all participants: researchers, the cement and concrete industry, slag producers, clients and users, and organizations active in standardization. How extensively the results of this report can be utilized to that end, or how directly they can be applied in practice remains open. The answer is left to the authorities responsible for the construction field, to the producers of binding materials, and, of course, to qualified scientists who have proven their expertise in applied research.

10 SUMMARY

The primary objective of the research was to characterize the pore structure and the aging-induced changes in ground granulated blast furnace slag (GBFS) concretes activated by ordinary Portland cements. The studied aging processes were non-accelerated carbonation in atmospheric conditions, and exposures to frequently changing moisture conditions. The GBFS composition was of typical quality with high magnesia, low aluminium and high glass content produced by the Finnish iron industry. This composition is widely used in the production of blended cements, and directly as a replacement binding material in concrete plants in Finland. Ordinary Portland cement (OPC) was used as an activator and as a reference binder throughout the investigation. The secondary objective was to clarify the effects of the aging-induced pore structural changes on a few durability properties of concrete, and especially to confirm the previous laboratory test results on the frost-salt resistance of aged GBFS concretes.

The effect of aging on the pore structure of concrete was studied with a program involving tests with concrete, mortar, and paste samples cured with three different procedures. GBFS content in the concrete mixes was from 0 to 70% of the binder, and the water-binder ratio in air-entrained and non-air-entrained concretes varied from 0.35 to 0.75. The level of air-entrainment varied from 2.7% to 6.7%, and the compressive strength 22 to 74 MPa in non-aged concretes and 33 to 92 MPa in aged concretes. Mixes for pastes and mortars were cast with water-binder ratios of 0.35, 0.45 and 0.60. Slag contents were 0, 50 and 70 % of the binder.

Mercury intrusion porosimetry, water immersion tests, and thin section analysis were used for characterization of the pore structure of concrete. Frost-salt tests were performed to investigate the effect of aging on the surface layer of concrete. Changes in the composition of aged pastes and mortars were analyzed with a thermogravimeter connected to a gas analyzer, and by infra red spectroscopy, and by X-ray diffractometry. Low-temperature calorimetry (LTC) and mercury intrusion porosimetry (MIP) were used throughout in the studies of pore structure and pore structure changes in pastes and mortars.

For analysis of the results by LTC a thermoporometric method was proposed. The method should be considered as one thermoporometric approach in the characterization of pore structure that enables accurate calculation of total porosity in porous materials. Pore size distribution is defined with good accuracy within the pore radius range of 1.5 to 50 nm. The method also gives information about the pore shape and specific surface area, and a direct measure for freezable water at temperatures of interest. The LTC method suffers from some uncertainties associated with its theoretical basis and semi-empirical determination of parameters needed for the calculation procedures. Further research is definitely needed to clarify the significant implications of these uncertainties. The clearest advantage of LTC as a pore probe lie in the unnecessity for sample pretreatment which affects the pore structure, and in the fact that concrete can be studied in its natural water containing state. Results showed that vacuum drying of specimens before testing drastically alters the pore structural state, particularly in the non-aged state. These changes, clearly visible in the LTC results, were only slightly detectable by the MIP method where vacuum drying was used as pretreatment. It could be concluded that vacuum drying coarsens the pore structure almost as efficiently as prolonged carbonation at RH 45%. A more gentle pretreatment method for MIP specimens should be used if a reliable pore analysis of concretes for comparison of binder types or curing procedures is of interest. Despite of these limitations MIP maintains its position in the characterization of pore structure. It is both cheap and rapid, and very useful as a comparative method, which offers significant advantages over LTC which is both time-consuming and relatively expensive to use and install.

Porosity and its redistribution were considered with respect to the following pore definitions: micropores, microcapillaries and macropores or macrocapillaries, denoting pore radii of <1.5 nm, 1.5-4 nm, and >4 nm, respectively. Gel porosity was defined as representing all pores smaller than 4 nm. Macropores or macrocapillaries fell into either the capillary or mesopore ranges of 4 nm to tens of nanometers or from tens to hundreds of nanometers, respectively.

Carbonation decreased the relative and absolute pore volume of micropores and microcapillaries, i.e. of the entire gel pore range. In the non-aged state GBFS binder gave lower microporosity and higher microcapillarity than OPC. At a high degree of carbonation the volume of micropores was approximately independent of the binder type. The highest slag contents gave the highest microcapillary volume before carbonation and the lowest value after carbonation treatment. With regard to the microcapillarity, the OPC binder behaved in the opposite manner.

The test results showed a strong redistribution of porosity during carbonation. When porosity values were considered on the basis of freezable water within particular pore ranges, it was found that the microcapillary volume decreased by 47%, 75% and 83% of the original values for average mix compositions of pure OPC binder and GBFS contents of 50% and 70%, respectively. In the macroporosity range, the corresponding increases were 40%, 55% and 71% on average. Coarsening within the macroporosity was also observed with all binder types, the trend being stronger with GBFS binders. Redistribution of the pore structure in OPC and GBFS concretes takes place at the expense of different gel pore ranges. In OPC mixes a relatively greater part of the overall coarsening occurs at the expense of the finest gel porosity smaller than 1.5 nm. On the contrary, microcapillaries from 1.5 to 4 nm diminished more strongly in GBFS blends than in OPC blends. Generally, it can be concluded that during carbonation the initially higher gel porosity of GBFS compositions (about 20%) becomes slightly lower (about 5 to 10%) than that of OPC compositions.

Gel structure and the greater liability of GBFS concretes for carbonation of the CSH gel, and the lack of calcium hydroxide in hydrated GBFS mixes, explains the more powerful coarsening phenomenon in GBFS concretes. Due to the lower amount of CH, GBFS compositions are more disposed to carbonation of the CSH gel, which transforms the initially relatively dense gel towards a more porous silica hydrate gel. Statistical analysis showed that the average SH gel fraction of the total gel volume correlated strongly with the slag content, being roughly 40% higher in GBFS 70% blends than in OPC mixes. In GBFS concrete, when the outer CSH gel loses its ability to buffer the pore solution, carbonation causes transformation of the CSH gel into SH gel in the inner slag hydrate. Initially the dominant pore dimensions in the ISH gel were typical of the gel pore range, i.e. smaller than 4 nm, but during carbonation the lack of open pore space in the ISH gel prevents precipitation of carbonates in this part of gel, which remains in its coarse state as long as further hydration does not occur. Evidence for the carbonation of the inner slag hydrate could be drawn from the IR spectra and from the CaO/SiO_2 ratios of hydrated and carbonated mixes calculated from the TG+EGA results. The results showed that at a high degree of carbonation almost all carbonable CaO in the hydrates is lost. This means that a drastic change in the inner slag hydrate has also taken place in carbonated GBFS compositions. Coarsening of the ISH gel causes an overall increase in porosity and for the continuity of pores in GBFS mixes, as the dense separative barrier is lost between the most porous parts of the GBFS matrix, the outer slag hydrate and the skeleton hydrate. As a result the permeability of GBFS concrete at high levels of carbonation also increases as observed in the tests with concrete. A few reports in the literature dealing with the redistribution of porosity over the whole porosity range confirm the changes observed in this report. Redistribution was mainly considered within the capillary pore range, where it is measurable by MIP. The results obtained in this study concerning the pore structural changes in the macroporosity of carbonated GBFS concretes are in a good agreement with the majority of results published in the literature.

Both primary phases CH and CSH may carbonate simultaneously, supporting recent results presented in the literature. Furthermore, the XRD results clearly indicate that carbon dioxide may also alter the compositions of tri- and monosulfate phases. Carbonation of these sulfate phases is probably partly responsible for the decreased permeability of carbonated OPC mixes, due to the closing effect in the porous transition zone together with carbonates precipitated from CH. All morphologies of calcium carbonates- vaterite, aragonite and calcite- are present in carbonated OPC and GBFS concretes, but in differing proportions. XRD, TG+EGA and FTIR tests showed that the relative proportion of vaterite in GBFS mixes was higher than in OPC mixes. Precipitation of carbonates is naturally a space-controlled process. In OPC concretes CH precipitates at the most porous sites in the gel structure, namely the transition zones and the outer CSH gel. In these regions the formation of well-crystallized calcite is evident. Calcite existing in GBFS mixes also precipitates in these spaces, since the pore diameters of microcapillarity in the ISH gel prevent precipitation as calcite and probably also as vaterite, and the space in the skeleton hydrate is unavailable behind the dense ISH barrier. It is possible that in GBFS mixes which are more susceptible to carbonation of the CSH gel, the existence of more poorly crystallized carbonates such as vaterite are more common. Carbonates precipitate at the closest site where space allows it. In GBFS mixes this is outside the ISH gel in the smallest range of macrocapillarity, where space does not allow precipitation as calcite. Carbonation at low relative humidity also contributes to the formation of vaterite in small macrocapillaries due to the lower mobility of Ca^{2+} ions in the gel structure. Formation of carbonates at later ages in the skeleton hydrate speaks in the favor of the higher vaterite amounts in GBFS compositions. Enriched Mg^{2+} ions in this pore space may act as incorporated impurities of deviating ionic radii which inhibit or totally prevent the precipitation of well-crystallized calcite.

Pure OPC and two GBFS contents, 50% and 70% of the binder, were used throughout the tests in this study. On the basis of the calculated fraction of the SH gel with different slag contents, no threshold value was found below which the detrimental transformation of CSH into SH in the dense ISH gel could occur. C/S mole ratios of the CSH gel showed that among both slag contents were mixes in which the changes had also occurred in the structure of the ISH after carbonation at RH 45%, and even after cycled curing. Nor was any slag content observed that would set a limit for tolerable coarsening of the pore structure. In the published literature, coarsening is reported to take place already at 20% slag replacement.

Aging generally lowers the frost-salt resistance of concretes regardless of the binder type. This trend could be associated with overall coarsening of the pore structure during carbonation. In GBFS concretes the rapid volume loss of samples in the early stages of the test correlated strongly with the carbonated volume. No correlation within OPC concretes could be found. According to the proposed carbonation model this phenomenon could be attributed to gel and pore structural changes in the inner slag hydrate. Carbonation coarsens the densest part of gel spaces in GBFS concretes, changing the gel porosity towards small macrocapillaries, where water becomes freezable at moderate temperatures. Prior to that the increased permeability of the ISH gel layer contributes to the higher degree of saturation in the more porous skeleton hydrate, further accelerating the rapid scaling early in the frost-salt test. Drying of the gel structure could not be regarded as a principal reason for rapid scaling, as scaling behind the carbonation front was similar to that of non-aged GBFS concretes. The observed abnormal and rapid deterioration in carbonated GBFS concretes is supported by the results reported by LITVAN AND MEYER (1986), MALHOTRA ET AL. (1987 and

1988), VESIKARI (1988), MATALA (1988) and KUKKO AND MATALA (1991). Contradictory results are given by VIRTANEN (1990).

The increased frost susceptibility of GBFS concretes due to carbonation of the CSH gel and its induced changes in the pore structure of the inner slag hydrate is very difficult, if not impossible, to compensate with conventional air-entrainment. This is clearly shown by the results obtained with properly air-entrained GBFS concretes. Obviously air-entrainment works as a precautionary action against coarsening of the gel structure in the outer slag hydrate, also in carbonated GBFS concretes as it does in OPC concretes. The significant correlation between carbonated and rapidly deteriorated volumes in the population comprising both slag contents of 50% and 70% led to the conclusion that there is no defined threshold value for the permitted slag content below which the phenomenon and coarsening of the inner slag hydrate cannot occur. The high degree of carbonation leads anyway to the transformations in the ISH gel, and if there are no qualifications for extended hydration following carbonation, the porous network of the gel structure will remain in the state in which the durability properties are diminished.

REFERENCES

ALLEN, A.J., BASTON, A.H. AND WILDING, C.R. 1988. Small angle neutron scattering studies of pore and gel structures, diffusivity, permeability and damage effects. In: Pore Structure and Permeability of Cementitious Materials, Ed. L.R. Roberts and J.P. Skalny. Materials Research Society. Vol. 137, pp. 119-125.

ASCHAN, N. 1963. Termogravimetrisk undersökning av karbonatiserings-fenomenet i betong. Nordisk Betong. Vol.7, No.3, pp. 275-284.

ATLASSI, E.H. 1993. A quantitative thermogravimetric study on the nonevaporable water in mature silica fume concrete. Chalmers University of Technology. Sweden. Publ. P-93:6. 169 p.

AUSTIN, S.A., ROBINS, P.J. AND ISSAAD, A. 1992. Influence of Curing Methods on the Strength and Permeability of GGBFS Concrete in a Simulated Arid Climate. Cement & Concrete Composites, Vol. 14, pp. 157-167.

BAGER D.H. 1984. Ice formation in hardened cement paste. Technical University of Denmark. Ph.D. Thesis. Technical Report 141/84. 66 p.

BAGER D.H. AND SELLEVOLD, E.J. 1978. Ice Formation in Hardened Cement Paste-II. Steam-Cured Pastes with Variable Moisture Contents. Durability of building Materials and Components. ASTM STP 691 (published 1980), pp. 439-454.

BAGER D.H. AND SELLEVOLD, E.J. 1986a. Ice formation in hardened cement paste, Part I - Room temperature cured pastes with variable moisture contents. Cement and Concrete Research. Vol 16. pp. 709-720.

BAGER D.H. AND SELLEVOLD, E.J. 1986b. Ice formation in hardened cement paste, Part II - Drying and resaturation on room temperature cured pastes. Cement and Concrete Research. Vol 16. pp. 835-844.

BAHTIA, N., PIGEON, M. AND LACHANCE, L. 1989. Calorimetric study of freezable water in cement paste. Cement and Concrete Research. Vol 19. pp. 939-950.

BEDDOE, R E. AND SETZER, M.J. 1990. Phase transformations of water in hardened cement paste, a low-temperature DSC investigation. Cement and Concrete Research. Vol 20. pp. 236-242.

BIER. T. A. 1988. Karbonatisierung und Realkalisierung von Zementstein und Beton. Massivbau, Baustofftechnologie, Karlsruhe. Heft 4. 170 p.+ Anhang 48 p.

BIER, T.A., KROPP, J. AND HILSDORF, H.K. 1987. Carbonation and realkalinization of concrete and hydrated cement paste. Proceedings of the First International RILEM Congress; Vol 3. Durability of Construction Materials. Versailles 1987. pp. 927-934.
BRUN, M., LALLEMAND, A., QUINSON. J-F. AND EURAUD. C. 1977. A new method for the simultaneous determination of the size and the shape of pores: The thermoporometry. Thermochimica Acta, 21. pp. 59-88.

CALLEJA, J. 1976. Topics on beneficial aspects of concrete carbonation. In: Rilem Symposium on Carbonation of Concrete. Fulmer Grange 1976. 11 p.

CALLEJA, J. 1980. Durability. Proceedings of the 7th International Congress on the Chemistry of Cement. Paris. Vol 3. pp. VII-2/1-48.

COOK, R.A. AND HOVER, K.C. 1993. Mercury porosimetry of cement-base materials and associated correction factors. Construction and Building Materials. Vol. 7, 4, pp. 231-239.

CRC 1990. Handbook of Chemistry and Physics. CRC Press, USA.

DIAMOND, M. 1987. Cement paste microstructure in concrete. In: Micostructural Development During Hydration of Cement. Boston, Materials Research Society, MRS Symp. Proc. Vol 85, pp. 21-31.

DE CEUKELAIRE, L. AND VAN NIEUWENBURG, D. 1992. Accelerated carbonation of a blast-furnace cement concrete. Cement and Concrete Research. Vol. 23, pp. 442-452.

DISTLER, P., KROPP, J., AND HILSDORF, H.K. 1992. Pore structure and transportation parameters of concretes containing blended cements. 9th International Congress on the Chemistry of Cement, New Delhi, India, Vol. V, pp. 431-437.

ECKRICH, J., ENÜSTÜN,, B. AND DEMIREL, T. 1986. Phase transition porosimeter. Am. Lab, 18(3), PP. 80-92.

ENÜSTÜN, B.V., SENTÜRK, H.S. AND YURDAKUL, O. 1978. Capillary Freezing and Melting. Journal of Colloid and Interface Science Vol. 65, No. 3. pp. 509-516.

ESSING, K., AND HILSDORF, H.K. 1976. Influence of Carbonation on Pore Structure of Hydrated Portland Cement Paste. in: Rilem Symposium on Carbonation of Concrete. Fulmer Grange 1976. 5 p.

FAGERLUND, G. 1973. Determination of pore-size distribution from freezing-point depression. Matériaux et Constructions Vol. 6, No. 33. pp. 215-225.

FELDMAN, R.F. 1983. Significance of Porosity Measurements on Blended Cement Performance. In: Fly Ash, Silica Fume, Slag & Other Mineral By-Products in Concrete. Ed. V. M. Malhotra. Detroit, American Concrete Institute, ACI Publ. SP-79. Vol I. pp. 415-433.

FELDMAN, R.F 1986. Pore structure, Permeability and diffusivity as related to durability. Proceedings of the 8th International Congress on the Chemistry of Cement. Rio de Janeiro. Vol 1. pp. 336-356.
FELDMAN, R. F. AND BEAUDOIN, J.J. 1991. Pretreatment of hardened hydrated cement pastes for mercury intrusion measurements. Cement and Concrete Research. Vol. 21, pp. 297-308.

FENG, Q.L., LACHOWSKI, E.E. AND GLASSER, F.P. 1989. Densification and Migration of Ions in Blast Furnace Slag-Portland Cement Pastes. In: Fly Ash and Coal Conversion By-Products: Characterization, Utilization and Disposal V. Ed. Hemmings, R.T., Berry, E.E., McCarthy, J.G. and Glasser, F.P. Boston, Materials Research Society, MRS Symp. Proc. Vol 136. pp. 263-272.

FLORIANO, M.A. AND ANGELL, C.A. 1990. Surface Tension and Molar Surface Energy and Entropy of Water to -27.2° C. The Journal of physical Chemistry. Vol. 94, No. 10. pp. 4199-4202.

DE FONTENAY, LE SAGE.C. AND SELLEVOLD, E.J. 1978. Ice Formation in Hardened Cement Paste-1-Mature Water-Saturated Pastes. Durability of building Materials and Components. ASTM STP 691(published 1980). pp. 425-438.

FORRESTER, J.A. 1976. Measurement of carbonation. In: Rilem Symposium on Carbonation of Concrete. Fulmer Grange 1976. 5 p.

GASPAR-TÉBAR, D., DEL OLMO-RODRIGUES, C. AND VÁZQUEZ-MORENO, T. 1976. Action du CO_2 sur le ciment portland anhydre. In: Rilem Symposium on Carbonation of Concrete. Fulmer Grange 1976. 7 p.

GLASSER, F.P., DIAMOND, S. AND ROY, D.M. 1987. Hydration reactions in cement pastes incorporating fly ash and other pozzolanic materials. In: Micostructural Development During Hydration of Cement. Boston, Materials research Society, MRS Symp. Proc. Vol 85. pp. 167-186.

GLASSER, F.P. 1989. Chemical, Mineralogical, and Microstructural Changes Occurring in Hydrated Slag-Cement Blends; In: Material Science of Concrete II, Ed. Jan Skalny and Sidney Mindess, pp. 41-82.

GOTO, S. AND IKEDA, S. 1992. Effects of carbonation on the thermal properties of tobermorite. 9th International Congress on the Chemistry of Cement, New Delhi, India, Vol. IV, pp. 304-309.

GRUBE, H. 1987. Measuring gas permeability of concrete for assessing factors of durability. Proceedings of the First International RILEM Congress; Vol 3. Durability of Construction Materials. Versailles 1987. pp. 1206-1213.

GUNNINK, B.W. 1991. New method for measuring pore size distribution in concrete. Journal of Materials in Civil Engineering, Vol. 3, No. 4. pp. 307-319.

HÄKKINEN, T. 1993. Influence of high slag content on the basic mechanical properties and carbonation of concrete. VTT Publications 141. Espoo. Finland. 98 p. + app. 45 p.
HAMMER, T. A. AND SELLEVOLD, E.J. 1990. Frost resistance of High Strength Concrete. In: Second Int. Symp. on Utilization of High Strength Concrete. Berkeley. 24 p.

HÄRDTL, R. 1992. Chemical binding of water during hydration of portland cements and blast-furnace slag cements blended with fly ash. 9th International Congress on the Chemistry of Cement, New Delhi, India, Vol. IV, pp. 678-683.

HARRISON, A.M., WINTER, N.B. AND TAYLOR, H.F.W. 1987. Microstructure and microchemistry of slag cement pastes. In: Micostructural Development During Hydration of Cement. Boston, Materials Research Society, MRS Symp. Proc. Vol 85. pp. 213-233.

HEARN, H. AND HOOTON, R.D. 1992. Sample mass and dimensions effects on mercury intrusion porosimetry results. Cement and Concrete Research. Vol. 22. pp. 970-980.

HINRICHS, W. AND ODLER, I. 1989. Hydration of Portland blast furnace slag cement: hydration kinetics. Advances in Cement Research Vol 2, 5, pp. 9-13.

Ho, D.W.S., Hinczak, I., Conroy, J.J. and Lewis, R.K. 1986. Influence of Slag Cement on the Water Sorptivity of Concrete. Fly Ash, Silica Fume, Slag and Natural Pozzolans in Concrete. Detroit, American Concrete Institute, ACI SP-91, Vol.II, pp. 1463-1473.

Hobbs, P.V. 1974. Ice Physics. Clarendon Press. Oxford. 745 p.

Hwang, C.L. and Lin, C.Y. 1986. Strength Development of Blended Blast Furnace Slag Cement Mortars. Fly Ash, Silica Fume, Slag and Natural Pozzolans in Concrete. Detroit, American Concrete Institute, ACI SP-91, Vol.II, pp. 1323-1340.

Ikeda, Y., Yasuike, Y., Kumagai, M., Park, Y., Harada, M., Tomiyasu, H. and Takashima, Y. 1992. ^{29}Si MAS NMR Study of Structural Change of Silicate Anions with Carbonation of Synthetic 11Å Tobermorite. Journal of the Ceramic Society of Japan, Int. Ed., Vol. 100, pp. 1083-1086.

Ikeda, Y., Yasuike, Y., Kumagai, M., Takahashi, K., Yamamoto, M. and Takashima, Y. 1993. A Study on Carbonation Reaction of Synthetic 11Å Tobermorite in Aqueous Solution. Journal of the Ceramic Society of Japan, Int. Ed., Vol. 101, pp. 140-143.

Jackson, P.J. and Brookbanks, P. 1989. Chloride Diffusion in Concretes Having Different Degrees of Curing and Made Using Portland Cements and Blended Cements Containing Portland Cement, Pulverized-Fuel Ash and Ground Granulated Blast Furnace Slag. Third CANMET/ACI International Conference on Fly Ash, Silica Fume, Slag & Natural Pozzolans In Concrete. Supplementary Papers. Norway 1989. pp. 641-655.

Johnston, J.R. and Glasser, F.P. 1992. Carbonation of portlandite single crystals and portlandite in cement paste. 9th International Congress on the Chemistry of Cement, New Delhi, India, Vol. V, pp. 370-376.

Kallio, L. and Mikkonen, V. 1992. Effect of chloride concentration on the capillary suction time and on the degree of saturation in silica- and GBFS concretes. Special assignment in concrete technology. Concrete Laboratory, HUT. 51 p. (in Finnish).

Kasai Y., Matsui I., Fukushima Y. and Kamohara H. 1983. Air Permeability and Carbonation of Blended Cement Mortars. Fly Ash, Silica Fume, Slag & Other Mineral by-Products in Concrete, 1983. Detroit, American Concrete Institute, ACI SP-79, Vol. I, s.435-451.

Kojima, Y., Sadotomo, A., Yasue, T. and Arai, Y. 1992. Control of Crystal Shape and Modification of Calcium Carbonate Prepared by Precipitation from Calcium Hydrogen Carbonate Solution. Journal of the Ceramic Society of Japan, Int. Ed., Vol. 100, pp. 1128-1135.

Kropp, J. 1983. Karbonatisierung und transportvorgänge in zementstein. Universität Karlsruhe. Dissertation. 161 p.

Kukko, H. and Matala, S. 1991. Effect of Composition and Aging on the Frost Resistance of High-Strength Concrete. In: Durability of Concrete. Second Int. Conf. Montreal, Canada. ACI SP-126. Ed. V.M. Malhotra. Vol. I, pp. 229-248.

Lach, V. and Sauman, Z. 1976. The determination of $CaCO_3$ modifications in the carbonated concrete. In: Rilem Symposium on Carbonation of Concrete. Fulmer Grange 1976. 5 p.

LEA, F.M. 1980. The Chemistry of Cement and Concrete. The Gresham Press, Surrey. 727p.

LITVAN G.G. 1972a. Phase Transitions of Adsorbates, III. Heat Effects and Dimensional Changes in Nonequilibrium Temperature Cycles. Journal of Colloid and Interface Science, Vol. 38, No. 1, pp. 75-83.

LITVAN G.G. 1972b. Phase Transitions of Adsorbates, IV. Mechanism of Frost Action in Hardened Cement Paste. Journal of the American ceramic Society, Vol. 55, No. 1, pp. 38-42.

LITVAN G.G. AND, MEYER A. 1986. Carbonation of Granulated Blast Furnace Slag Cement Concrete During Twenty Years of Field Exposure. Fly Ash, Silica Fume, Slag and Natural Pozzolans in Concrete. Detroit, American Concrete Institute, ACI SP-91, Vol.II, pp. 1445-1462.

MALEK, R.I.A., ROY, D.M. AND FANG,Y. 1989. Pore structure, permeability, and chloride diffusion in fly ash- and slag-containing pastes and mortars. In: Fly Ash and Coal Conversion By-Products: Characterization, Utilization and Disposal V. Ed. Hemmings, R.T., Berry, E.E., McCarthy, J.G. and Glasser, F.P. Boston, Materials Research Society, MRS Symp. Proc. Vol 136. pp. 255-262.

MALHOTRA V.M., CARETTE G.G. AND BREMNER T.W. 1987. Durability of Concrete Containing supplementary Cementing materials in Marine Environment. Silica Fume Slag and Natural Pozzolans in Concrete. Proc. Second Int. Conf. Madrid, Spain, ACI SP-91, Vol.II, pp. 1227-1258.

MALHOTRA V.M., CARETTE G.G., BREMNER T.W. 1988. Current status of CANMET's studies on the Durability of Concrete Containing supplementary Cementing materials in Marine Environment. Proc. Second Int. Conf. on Performance Concrete in Marine Environment. St. Andrews, Canada 1988. ACI SP-109. s.31-71.

MATALA, S. 1988. The Effect of Carbonation on Frost-Salt Resistance of Condensed Silica Fume-, Granulated Blast Furnace Slag-, Fly Ash- and OPC-Concretes. Karbonatisering av betong. Nordisk miniseminar, 15.11.1988, Trondheim. Forskningsinstituttet for Cement og Betong. STF65 A88085. pp. 67-80.

MATALA, S. 1995. Thermoporometric approach in characterization of pore structure in concrete. To be published in Proceedings of Int. Conf. on Concrete under Severe Conditions, CONSEC95. Sapporo. Japan. Aug 1995. 10 p.

MATSUSATO, H., OGAWA, M., FUNATO, M. AND SATO, T. 1992. Studies on the carbonation of hydrated cement and its effect on microstructure and strength. 9th International Congress on the Chemistry of Cement, New Delhi, India, Vol. V, pp. 363-369.

NEGRO, A., MURAT, M. AND CUSSINO, L. 1976. Nature et stabilite thermique des produits d'interaction entre les agrégats calcaires et certaines phases du ciment (C_3A et C_4AF). In: Rilem Symposium on Carbonation of Concrete. Fulmer Grange 1976. 5 p.

NILSSON, L. O. 1980. Hygroscopic Moisture in Concrete - Drying, Measurements & Related Material Properties. Lund Institute of Technology. Report TVBM 1003. 162 p.

NISHIKAWA, T., SUZUKI, K., ITO, S., SATO, K. AND TAKEBE, T. 1992a. Decomposition of synthesized ettringite by carbonation. Cement and Concrete Research. Vol. 22. pp. 6-14.

NISHIKAWA, T., SATO, K., ITO, S. AND SUZUKI, K. 1992 b. Thermal and chemical stability of AFm phase-isostructural group. 9th International Congress on the Chemistry of Cement, New Delhi, India, Vol. IV, pp. 437-442.

NUMATA, S., KOIDE, Y. AND SHIMOBAYASHI, S. 1986. Properties of Ultra-Highly Pulverized Granulated Blast Furnace Slag-Portland Cement Blends. Fly Ash, Silica Fume, Slag and Natural Pozzolans in Concrete. Detroit, American Concrete Institute, ACI SP-91, Vol.II, pp. 1341-1360.
Odler, I. and Hinrichs, W. 1989. Investigation of the hydration of Portland blast furnace slag cement: composition, structure and properties of the hydrated material. Advances in Cement Research Vol 2, 5, pp. 15-20.

ODLER, I. AND KÖSTER, H. 1991. Investigation on the structure of fully hydrated portland cement and tricalcium silicate pastes. III. Specific surface area and permeability. Cement and Concrete Research. Vol. 21, pp. 975-982.

OGINO, T., SUZUKI, T. AND SAWADA, K. 1990. The rate and mechanism of polymorphic transformation of calcium carbonate in water. Journal of Crystal Growth, Vol. 100, pp. 159-167.

OLEK, J., COHEN, M.D., AND LOBO, C. 1990. Determination of Surface Area of Portland Cement and Silica Fume by Mercury Intrusion Porosimetry. ACI Materials Journal, Vol. 87, pp. 473-478.

PARROT, L. 1987. Measurement and modeling of porosity in drying cement paste. In: Micostructural Development During Hydration of Cement. Boston, Materials research Society, MRS Symp. Proc. Vol 85. pp. 91-104.

PARROT, L. 1992. Carbonation, moisture and empty pores. Advances in Cement Research. 1991/92. Vol. 4. No. 15, pp. 111-118.

PENTTALA, V. 1992. Nature of compression strength in concrete. Magazine of Concrete Research, Vol. 44, No. 159. pp. 87-106.

PENTTALA. V. AND MATALA S. 1995. Strength and composition changes in carbonated GBFS and OPC mortars during extended water curing. To be published in Proceedings of Int. Conf. on Concrete under Severe Conditions, CONSEC95. Sapporo. Japan. Aug 1995. 12p.

PHILIPOSE, K.E., FELDMAN, R.F. AND BEAUDOIN J.J. 1991. Durability Predictions from Rate of Diffusion Testing of Normal Portland Cement, Fly Ash, and Slag Concrete. Second CANMET/ACI International Conference on Durability of Concrete. ACI SP-126. Montreal, Canada, 1991. Vol. I. pp. 335-344.

PIHLAJAVAARA, S. E. 1968. Some results of the effect of carbonation on the porosity and pore size distribution of cement paste. Matériaux et Constructions Vol. 1-No 6. pp. 521-526.

PIHLAJAVAARA, S. E 1976. On the effect of carbonation on shrinkage and weight change of concrete. In: Rilem Symposium on Carbonation of Concrete. Fulmer Grange 1976. 3 p.

PIHLAJAVAARA, S. E 1982. Estimation of drying of concrete at different relative humidities and temperatures of ambient air with special discussion about fundamental features of drying and shrinkage. In: Creep and shrinkage in concrete structures. Ed. by Z.P. Bazant & F.H. Wittmann. Chichester, John Wiley & Sons Ltd. pp. 87-108.

RAMACHANDRAN, V.S. 1977. Applications of Differential Thermal Analysis in Cement Chemistry. Chemical Publishing Company, Inc. New York. 308 p.

REGOURD, M., MORTUREUX, B. AND HORNAIN, H. 1983. Use of Condensed Silica Fume as Filler in Blended Cements. In: Fly ash, Silica fume, Slag & Other Mineral By-Products in Concrete. Ed. V. M. Malhotra. Detroit, American Concrete Institute, ACI Publ. SP-79. Vol II. pp. 847-865.

REGOURD, M. 1987. Microstructure of cement blends containing fly ash, silica fume, slag and fillers. In: Micostructural Development during hydration of Cement. Boston, Materials research Society, MRS Symp. Proc. Vol 85. pp. 187-200.

RICHARDSON, M. 1988. Carbonation of reinforced concrete, Its Causes and Management. Citis LTD. London. 205 p.

RICHARDSON, I.G., GROVES, G.W., BROUGH, A., AND DOBSON, C.M. 1992. Structural changes due to carbonation in hardened cement pastes. 9th International Congress on the Chemistry of Cement, New Delhi, India, Vol. IV, pp. 298-303.

RICHARDSON, I.G. AND GROVES, G.W. 1992. The composition and structure of C-S-H gels in cement pastes containing blast-furnace slags. 9th International Congress on the Chemistry of Cement, New Delhi, India, Vol. IV, pp. 350-356.

ROY, D.M. AND PARKER, K.M. 1983. Microstructures and Properties of Granulated Slag-Portland Cement Blends at Normal and Elevated Temperatures. In: Fly ash, Silica Fume, Slag & Other Mineral By-Products in Concrete. Ed. V. M. Malhotra. Detroit, American Concrete Institute, ACI Publ. SP-79. Vol I. pp. 397-414.

ROY, D.M., KUMAR, A. AND RHODES, J.P. 1986. Diffusion of Chloride and Cesium Ions in Portland Cement Pastes and Mortars Containing Blast Furnace Slag and Fly Ash. Fly Ash, Silica Fume, Slag and Natural Pozzolans in Concrete. Detroit, American Concrete Institute, ACI SP-91, Vol.II, pp. 1423-1444.

ROZENTAL, N.K. AND ALEKSEEV, S.N. 1976. Change in concrete porosity during carbonation. In: Rilem Symposium on Carbonation of Concrete. Fulmer Grange 1976. 10 p.

SAROTT, F. A., BRADBURY, M.H., PANDOLFO, P. AND SPIELER, P. 1992. Diffusion and adsorption studies on hardened cement paste and the effect of carbonation on diffusion rates. Cement and Concrete Research. Vol 22. pp. 439-444.

SAUMAN, Z. AND LACH, V. 1976. To the longterm carbonation of binding components in cellular concretes. In: Rilem Symposium on Carbonation of Concrete. Fulmer. 4 p. Grange 1976. 4 p.

SAWADA, K., OGINO, T. AND SUZUKI, T. 1990. The distribution coefficient of Mg^{2+} ion between $CaCO_3$ polymorphs and solution and the effects on the formation and transformation of $CaCO_3$ in water. Journal of Crystal Growth, Vol. 106, pp. 393-399.

SCRIVENER, K.L. 1989. The Microstructure of Concrete. In: Materials Science of Concrete. Ed. J.P. Skalny. The American Ceramic Society. Vol. I. pp. 127-161.

SCRIVENER, K.L. AND PRATT, P.L. 1987. The characterization and quantification of cement and concrete. Proceedings of the First International RILEM Congress; Vol 1. Pore Structure and Material Properties. Versailles 1987. pp. 61-68.

SELLEVOLD, E. I. 1974. Mercury Porosimetry of Hardened Cement Paste Cured or Stored at 97° C. Cement and Concrete Research. Vol. 4. pp. 399-404.

SELLEVOLD, E.J., AND BAGER D.H. 1980. Low temperature calorimetry as a pore structure probe. Proceedings of 7th Int. Cong. on the Chemistry of Cement. Vol. IV. Paris 1980. pp. 394-399.

SERSALE, R., MARCHESE, B. AND FRIGIONE, G. 1980. Microstructure of the reaction of hydrated cements with different slag content. Proceedings of the 7th International Congress on the Chemistry of Cement. Paris. Vol II. pp. III/63-68.

SETZER, M.J. 1990. Interaction of Water with Hardened Cement Paste. In: Ceramic Transactions, Advances in Cementitious Materials, Ed. S. Mindess. Gaithsburg. Vol. 16. pp. 415-439.

SIDEBOTTOM, E.W. AND LITVAN G.G. 1971. Phase Transitions of Adsorbates, Part 2. Vapor Pressure and Extension Isotherms of the Porous Glass+Water System Below 0° C. Transactions of the Farady Society. No. 585, Vol. 67, Part 9, pp. 2726-2736.

SMOLCZYK, H.G. 1976. Physical and chemical phenomena of carbonation. In: Rilem Symposium on Carbonation of Concrete. Fulmer Grange 1976. 10p.

STOCKHAUSEN, N., DORNER, H., ZECH, B. AND SETZER, M.J. 1979. Untersuchungen von Gefriervorgängen in Zementstein mit Hilfe der DTA. Cement and Concrete Research. Vol 9. pp. 783-794.

SUZUKI, K., NISHIKAWA, T. AND ITO, S. 1985. Formation and carbonation of C-S-H in water. Cement and Concrete Research. Vol 15. pp. 213-224.

TADA, S. 1987. Pore structure and moisture characteristics. Proceedings of the First International RILEM Congress; Vol 1. Pore Structure and Material Properties. Versailles 1987. pp. 85-91.

TAKAGI, S. 1990. Approximate Thermodynamics of the Liquid-like Layer on an Ice Sphere Based on an Interpretation of the Wetting Parameter. Journal of Colloid and Interface Science. Vol. 137, No. 2. pp. 446-455.

TANAKA, H., TOTANI, Y. AND SAITO, Y. 1983. Structure of hydrated slag in concrete. In: Fly Ash, Silica Fume, Slag & Other Mineral By-Products in Concrete. Ed. V. M. Malhotra. Detroit, American Concrete Institute, ACI Publ. SP-79. Vol II. pp. 963-977.

TAYLOR, H.F.W. 1990. Cement Chemistry. Academic Press. London. 473 p.

TENAOUTASSE, N. AND MARION, A.M. 1987. Influence of industrial by-products on the porosity of hydrated portland cement. Proceedings of the First International RILEM Congress; Vol 1. Pore Structure and Material Properties. Versailles 1987. pp. 33-40.

THOMAS, M. D. A. 1989. The suitability of solvent exchange techniques for studying the pore structure of hardened cement paste. Advances in Cement Research. Vol 2, 5, pp. 29-34.

UCHIKAWA, H., HANEHARA, S. AND SAWAKI, D. 1991. Influence of Water Cement Ratio on the Ionic Penetrability of Blended Cement Paste, Mortar and Concrete. Second CANMET/ACI International Conference on Durability of Concrete. Supplementary Papers. Montreal, Canada, 1991. pp. 525-543.

VERDOES, D. 1991. Calcium carbonate precipitation in relation to detergent performance. Delft University Press. 214p.

VESIKARI, E. 1988. The effect of ageing on the durability of concrete including by-products. In: Durable concrete with industrial by-products. Technical Research Centre of Finland. VTT Symposium 89. pp. 104...112..

VIRTANEN J. 1990. Effects of Mineral By-Products on the Frost-Resistance of Concrete. Licentiate's thesis. Helsinki University of Technology. Faculty of Civil Engineering and Surveying. 115 p.

ZECH, B. AND SETZER, M.J. 1989. The dynamic modulus of hardened cement paste. Part 2: Ice formation, drying and pore size distribution. Materials and Structures. 22., pp. 125-132.

APPENDICES

CONTENT:

Values used in the numeric evaluation of Equation 22

$$\Delta S_f = \Delta S_{f0} + \int_{T_0}^{T} \left(\frac{c_s - c_l}{T} \right) dT + \left[\left(\frac{\partial v_l}{\partial T} \right)_P - \left(\frac{\partial v_s}{\partial T} \right)_P \right]_T \cdot (P_s - P_0) + \left[\left(\frac{\partial v_l}{\partial T} \right)_P \right]_T \cdot (P_l - P_s)$$

$c_s = 2.114 \cdot (1 + 373.7 \cdot 10^{-5} \cdot \theta)$ [J/g] (A1)

$c_l = 4.222 \cdot (1 - 54 \cdot 10^{-5} \cdot \theta)$ [J/g] (A2)

$\left(\frac{\partial v_l}{\partial T} \right)_P = -9.11 \cdot 10^{-5} \cdot (1 - 0.227 \cdot \theta)$ [cm³/g/°K] (A3)

$\left(\frac{\partial v_s}{\partial T} \right)_P = 12.28 \cdot 10^{-5}$ [cm³/g/°K] (A4)

$\triangle S_{f0} = -1{,}2227$ [J/g/°K] (A5)

$P_0 = 4.58$ [mmHg] (A6)

$v_l = 1{,}000132 \cdot (1 - 9{,}1 \cdot 10^{-5} \cdot \theta + 1{,}035 \cdot 10^{-5} \cdot \theta^2)$ [cm³/g] (A7)

Examination of the significance of the third term in Equation 22

In the third term $\left[\left(\frac{\partial v_l}{\partial T} \right)_P - \left(\frac{\partial v_s}{\partial T} \right)_P \right]_T \cdot (P_s - P_0)$ the vapor pressure of ice is well known and the tabulated values (CRC 1990) can be expressed with quite good accuracy by the equation:

$P_s = 0.01333 \cdot e^{1.59 + 0.094 \cdot \theta}$ [N/cm²] (A8)

On the other hand, $\left[(\partial v_s / \partial T)_P \right]_T$ can be formulated using the tabulated values given by Eisenberg and Kauzmann (HOBBS 1974, p. 350). Linearization of the values in the temperature range -15° C to -50° C gives a rough relationship:

$\left(\frac{\partial v_s}{\partial T} \right)_P = (1.86 + 0.013 \cdot \theta) \cdot 10^{-4}$ [cm³/g/°K] (A9)

Insertion of Equations A8, A9 and A3 gives

$$\left[\left(\frac{\partial v_l}{\partial T}\right)_P - \left(\frac{\partial v_s}{\partial T}\right)_P\right]_T \cdot \left(P_s - P_0\right) \cong -1.881 \cdot 10^{-7} \cdot \left(1 - 0.0698 \cdot \theta\right) \cdot \left(e^{0.094 \cdot \theta} - 1\right)$$

in J/g/°K. Using this relationship and the variation of temperature from 0° C to -30° C, the change of entropy due to the third term of Equation 22 is only -0.357 $\cdot 10^{-6}$ J/g/°K. The corresponding effect of the second term at the same temperature range is 0.263 J/g/°K. The above consideration supports the omission of this term from the solidification entropy of freezable water.

Effect of superficial phase transformations on total entropy

The effect of superficial phase transformations on the total entropy of the pore system seems to be of great importance. Its magnitude is considered theoretically in the following.

During the solidification of ice, changes of interphase occur between layers which do not freeze and the adjacent phase (water before solidification and ice afterwards). In general the basic equation can be presented in the form:

$$S = A + B + C + D + E \qquad \text{(A10)}$$

where $A = \Delta S_{f0}$, $B = \int_{P_l}^{P_0} \left(-\frac{\partial v_l}{\partial T} \right)_P dP$, $C = \int_{T}^{T_0} \left(\frac{c_l}{T} \right) dT$, $D = \int_{T_0}^{T} \left(\frac{c_s}{T} \right) dT$ and $E = \int_{P_0}^{P_s} \left(-\frac{\partial v_s}{\partial T} \right)_P dP$.

The magnitude of the entropy change due to the transformation of thermodynamic states of interphases can be considered by studying the basic equation A10 in different thermodynamic states of the pore system. Hence, the equilibrium condition for the entropy of the pore system is not known, but rough estimates for the upper and lower bound entropies, between which the entropy of the equilibrium state must exist, can be formulated.

The change in energy state of a pore due to temperature depression can be described in three different stages. First, most of the energy state transformations are due to lowering of the entropy of the pore water during supercooling. At this stage, changes in the surface energy of the pore also take place. Before the nucleation point, the term A and integrals B and C of Equation A10 must be considered. At the nucleation point, the phase transformation from water to ice, and the surface energy of the ice-water interface change the energy state of the pore. Hence integrals D and E of Equation A10 must be included in the consideration of thermodynamic state. After nucleation, the energy of the pore decreases due to the changes in the entropies of all phases - namely crystallized ice, supercooled adsorbed water and the liquid-like layer - and their volume changes, and by the changes in surface tension of the interphases. The changes in the energy state of pores is illustrated in Figure A1 for different pore sizes. For numerical evaluation of the terms in Equation A10 the following expressions were used:

$$A = \Delta S_{f0} = 1.2227$$

$$B = \int_{P_l}^{P_0} \left(-\frac{\partial v_l}{\partial T} \right)_P dP = 18.22 \cdot 10^{-5} \cdot \frac{76 - 17.36 \cdot \theta + 0.0252 \cdot \theta^2}{R_p}$$

$$C = \int_{T}^{T_0} \left(\frac{c_l}{T} \right) dT = 4.845 \cdot \ln\left(1 + \frac{\theta}{T_0}\right) - 2.28 \cdot 10^{-3} \cdot \theta$$

$$D = \int_{T_0}^{T} \left(\frac{c_s}{T} \right) dT = 0.0439 \cdot \ln\left(1 + \frac{\theta}{T_0}\right) - 0.0079 \cdot \theta$$

$$E = \int_{P_0}^{P_s} \left(-\frac{\partial v_s}{\partial T} \right)_P dP = \frac{5.571 \cdot 10^{-5} \cdot \left(\theta + 0.227 \cdot \theta^2 \right)}{1 - 4.556 \cdot 10^{-5} \cdot \left(\theta + 0.227 \cdot \theta^2 \right)}$$

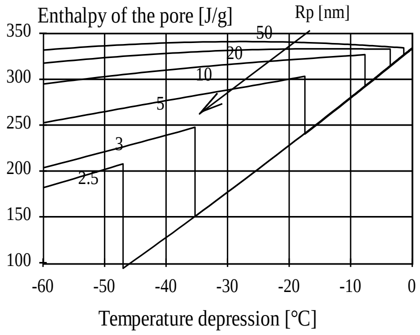

Figure A1. Changes in energy state of the pore system during temperature depression.

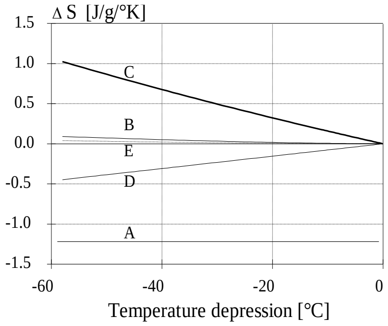

Figure A2. Entropy of parameters A-E.

In the evaluation of term B, a linear relationship was assumed between the surface tension of the liquid-gas interface and the temperature depression, and the values for surface tension were taken from the experimental results at -27 to 0° C presented by FLORIANO AND ANGELL (1990, p. 4200). In this context a rough approximation of liquid-gas surface tension is acceptable as its effect is of minor importance, and Floriano and Angell did not find a strong dependence of surface tension on capillary size at lower temperatures. The terms A, C, D and E were developed using the numeric values presented by Brun. In Figure A2 the values of parameters A to E are presented as a function of temperature depression. The effect on the total entropy for the surface tension values of the terms B and E is seen to be a minor one.

Using Equation A10 the course of enthalpy can be calculated for each pore size, as has been done in Figure A1. Furthermore, the enthalpy at each temperature depression can be presented as a function of pore size. This has been done at temperature -30° C in Figure A3. The curve over 3.4 nm represents the changes in enthalpy of pores already frozen over -30° C, and the curve under 3.4 nm the enthalpy of non-frozen pores. The drop in the curve illustrates the nucleation of a pore dimensioning 3.4 nm at -30° C.

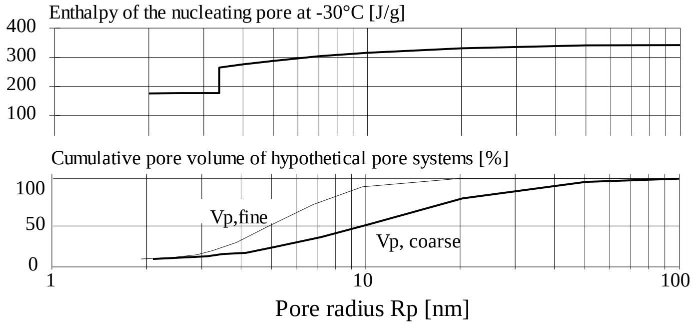

Figure A3. Enthalpy of superfacial phase transformations at -30° C for the pore range 2 to 100 nm.

Now, if the pore structure of the cement paste is known, the enthalpy change due to the superficial phases before and after the nucleation point at specified temperature can be calculated. For comparison purposes and to check the correctness of the values given by BRUN, the enthalpy changes due to the superficial phases were determined for two different pore size distributions. These pore size distributions are presented in Figure A3 as cumulative pore volume. Both of the pore systems are hypothetical and represent only the finest capillary area of ordinary cement paste. The coarser part of capillary pores are neglected as their effect on the enthalpy change is of minor importance, as can be seen from Figure A3. The enthalpies of the superficial phase transformations $\Delta S_{f,sup}$ were calculated for both pore size distributions at temperatures of -5, -10, -20, -30, -40 and -50° C. The ratio $\Delta S_{f,sup}/\Delta S_f$, where ΔS_f has been determined from Equation 24, is presented as a function of temperature depression in Figure A4. The same figure also shows the plotted values of $\Delta S_{f,sup}$ calculated by BRUN's equation.

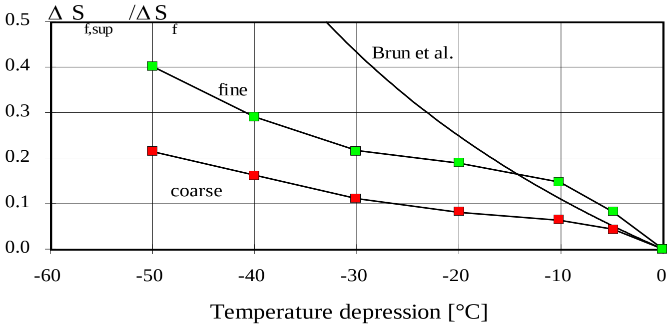

Figure A4. Ratio $\Delta S_{f,sup}/\Delta S_f$ as a function of temperature depression for hypothetical fine and coarse pore systems.

According to the examination, BRUN's equation overestimates $\Delta S_{f,sup}$ for the pore structure normally observed in cement pastes.

Mix composition of concretes and the properties of fresh concrete

Concrete	OPC [kg/m3]	Slag [kg/m3]	Water [kg/m3]	Aggregate [kg/m3]	Air-entr. % of binder	WR	Air [%]	Slump [cm]	SVB [sec]	W/B ratio
C03	252.2	-	188.8	1804.4	0.017	-	5.4	14.5		0.749
C01	248.2	-	147.7	1874.8	0.017	-	7.0	4.0	1.6	0.595
C02	251.2	-	151.0	2005.0	-	-	1.7	0.0	6.5	0.601
C07	405.5	-	243.3	1652.6	-	-	0.7	16.0		0.600
C10	201.4	201.4	241.7	1637.4	-	-	1.3	16.0		0.600
C11	411.8	-	222.2	1636.1	0.043	-	3.2	15.0		0.540
C15	206.8	206.8	223.2	1636.7	0.050	-	2.8	15.0		0.540
C13	124.2	289.9	223.5	1635.8	0.045	-	2.7	15.0		0.540
C18	405.6	-	179.4	1816.0	-	0.37	0.7	15.0		0.450
C17	380.9	-	171.4	1705.3	0.012	-	6.7	6.5	1.2	0.450
C16	388.6	-	174.7	1636.4	0.020	-	8.7	10.0	1.0	0.450
C21	202.0	202.0	181.2	1803.1	-	-	1.1	5.0	2.0	0.449
C23	196.9	196.9	177.8	1679.4	0.020	-	6.4	10.5	0.6	0.452
C22	122.0	282.7	181.5	1804.7	-	-	0.9	7.0	1.7	0.449
C24	120.1	280.3	180.2	1704.9	0.020	-	4.9	12.0	0.5	0.450
C27	401.2	-	136.4	1904.3	-	1.18	1.7	5.0	4.3	0.352
C28	202.1	202.1	137.4	1912.9	-	1.36	0.9	8.0	3.7	0.354
C29	121.4	283.3	137.6	1912.3	-	1.36	0.8	9.0	3.4	0.354
C32	402.3	-	135.8	1856.3	0.042	1.20	3.5	4.0	4.0	0.350
C34	120.8	281.8	135.4	1848.1	0.048	1.00	3.6	5.5	3.8	0.347

WR = water-reducer (SP62)
W/B = water-binder ratio

Chemical composition of binders
of cement

	Chemical composition %	
	Cement (OPC)	Granulated blast furnace slag
SiO2	20.4	36.1
Al2O3	4.7	9.9
Fe2O3	2.7	0.49
MgO	2.4	10.9
CaO	62.0	38.5
Na2O	0.77	0.4
K2O	0.99	0.5
SO3	2.7	-
Cl-		0.05
S		1.6
LOI	2.8	

Mineralogical composition

	% of cement
C3S	46.07
C2S	23.74
C3A	7.88
C4AF	8.21
H2O 1)	0.46
free CaO	0.50
CaCO3 2)	3.08
Alkalis	1.76
MgO	2.40
SO3	0.30
CaSO4.2H2O	5.07

1) water of hydrated alkalis and

free

CaO (measured by TG)

2)

measured on the basis of CO2 by

TG+EGA

Compressive strength of concretes

Concrete	Compressive strength (MPa)						
	Std. curing 28 d		Curing 1 28 d		Curing 2 1 year		Curing 3 1 year
	m 1)	s	m 1)	s	m 1)	s	m 2)
C01	30.4	0.2	30.4	1.3	40.3	0.3	31.3
C02	43.3	2.0	42.1	1.7	55.4	0.6	41.9
C03	22.2	1.0	23.2	0.8	32.6	1.1	23.0
C07	38.9	0.7	37.2	1.1	53.6	1.1	37.3
C10	28.1	1.0	26.0	0.4	45.2	2.0	29.4
C11	36.6	1.1	37.2	1.0	51.7	0.8	39.0
C13	26.2	1.2	25.3	1.0	45.7	0.3	29.4
C15	33.8	0.6	31.7	0.5	51.0	0.9	38.4
C17	41.2	1.4	41.0	1.6	57.0	0.9	41.8
C18	58.4	0.7	59.6	0.5	80.3	0.5	62.1
C21	47.6	0.1	49.8	0.7	71.3	1.0	57.5
C22	40.7	0.9	40.3	0.4	62.7	1.2	55.7
C23	33.8	1.4	33.1	1.4	53.2	0.3	37.1
C24	33.5	1.4	30.5	1.0	52.3	0.8	37.6
C27	73.7	1.3	71.8	0.2	89.8	5.0	76.1
C28	69.7	1.0	69.9	0.9	92.0	1.4	81.6
C29	60.5	0.4	57.6	0.8	85.0	1.9	68.1
C32	70.5	0.9	67.5	1.3	86.7	1.1	74.0
C34	54.8	1.1	50.5	2.1	77.5	1.6	59.9

Std. curing : 28 days at >95% RH
Curing 1 : 7 days at >95% RH + 21 days at 45% RH
Curing 2 : 7 days at >95% RH + 21 days at 45% RH + 6 wetting-drying cycles each with wetting in water for 1 week and drying at 45% RH for 6 weeks + storage at 45% RH until 1 year
Curing 3 : 7 days at >95% RH + storage at 45% RH until 13 months
m1) : mean of three results, 100 mm cubes
m2) : mean of two results, 100 mm cubes
s : standard deviation

Table 1. Results of frost-salt tests of non-aged concretes C1-C18

Change in vol-%													
Cycle	C1	C2	C3	C7	C10	Cycle	C11	C13	C15	C16	C17	C18
0	0.0	0.0	0.0	0.0	0.0	0	0.0	0.0	0.0	0.0	0.0	0.0
5	0.0	-0.1	-0.3	-0.4	-1.2	5	0.2	-2.2	-0.7	0.2	0.1	0.4
10	-0.2	-1.4	-1.2	-5.0	-2.1	10	-0.6	-4.4	-1.4	0.5	0.3	-1.7
15	-0.3	-2.9	-2.5	-10.5	-2.9	15	-1.1	-4.8	-2.2	-0.1	0.0	-6.1
20	-0.5	-4.5	-4.3	-15.4	-4.0	20	-2.5	-5.2	-2.5	-0.1	-0.1	-8.8
25	-1.2	-6.6	-5.6	-20.9	-4.2	25	-3.7	-5.6	-2.5	-0.1	-0.1	-11.2
30	-1.4	-8.4	-6.9	-28.4	-4.4	30	-4.5	-5.8	-2.7	0.0	-0.1	-12.3
35	-1.7	-10.5	-8.5	-38.6	-4.7	35	-5.0	-5.9	-2.6	-0.2	-0.2	-17.0
40	-1.8	-14.0	-9.7	-50.4	-5.2	40	-6.6	-6.2	-3.0	-0.2	-0.3	-20.9
45	-2.3	-33.9	-12.2		-5.6	45	-7.4	-6.5	-3.1	-0.1	-0.2	-23.6
50	-2.5	-53.5	-14.3		-6.1	50	-7.9	-7.7	-3.6	-0.1	-0.3	
55	-3.1		-16.4		-7.3	60	-9.9	-12.5	-4.2	-0.4	-0.4	
65	-4.1		-20.8		-11.3	70	-12.1	-29.1	-5.6	-1.0	-1.2	
75	-5.2		-27.4		-17.7	80	-12.8	-47.6	-25.9	-0.8	-1.1	
85	-6.0		-31.9		-28.3	90	-15.2	-59.2	-63.7	-0.6	-1.1	
95	-6.6				-37.5	100	-17.8	-71.1		-1.9	-1.9	
100	-7.2				-41.8	120	-22.3			-2.1	-3.3	
120	-10.2				-86.7	134	-24.5			-2.2	-3.7	
158	-16.5					171	-35.5			-3.7	-6.4	
197	-25.8					209				-6.6	-11.2	
216	-30.2					229				-8.2	-14.1	
236	-34.9					249				-10.5	-17.3	
281	-45.1					300				-16.7	-27.1	
300	-47.5					325				-19.6	-31.0	
325	-55.0					350				-23.6	-36.4	
350	-60.4					375				-26.7	-40.8	
375	-65.2					400				-30.8	-45.6	
400	-68.5					425				-34.5	-50.3	
425	-74.4					450				-39.1	-55.6	
450	-80.2					475				-43.2	-60.8	
475	-83.5					500				-48.2	-65.5	

Table 2. Results of frost-salt tests of non-aged concretes C21-C34

Change in vol-%												
Cycle	C21	C22	C23	Cycle	C24	Cycle	C27	C28	C29	Cycle	C32	C34
0	0.0	0.0	0.0	0	0.0	0	0.0	0.0	0.0	0	0.0	0.0
5	0.3	0.7	0.1	5	0.4	5	0.5	0.2	0.1	5	0.2	0.0
10	0.5	-0.5	0.3	10	-2.2	10	-0.2	-0.6	-1.4	10	-0.2	-1.1
15	0.0	-2.3	-0.1	15	-4.1	15	-0.6	-0.6	-2.2	15	-0.4	-1.7
20	-0.2	-3.5	-0.2	20	-5.1	20	-1.3	-0.8	-2.6	20	-0.4	-1.9
25	-0.1	-3.5	-0.2	25	-5.3	25	-2.0	-0.8	-2.6	25	-0.4	-1.9
30	0.0	-3.6	-0.1	30	-5.2	30	-2.5	-0.8	-2.7	30	-0.6	-2.2
35	-0.1	-3.9	-0.5	35	-5.7	35	-3.6	-0.7	-2.7	35	-0.6	-2.1
40	-0.1	-3.8	-0.5	40	-5.6	40	-4.0	-0.6	-2.6	40	-0.7	-2.2

Table 2. Results of frost-salt tests of non-aged concretes C21-C34 (continued)

Change in vol-%												
Cycle	C21	C22	C23	Cycle	C24	Cycle	C27	C28	C29	Cycle	C32	C34
45	-0.2	-4.2	-0.6	45	-5.6	45	-4.5	-0.5	-2.7	45	-0.6	-1.9
50	-0.6	-4.0	-0.5	50	-5.5	50	-4.9	-0.3	-2.7	50	-0.8	-2.0
60	-2.0	-5.7	-1.2	60	-5.6	60	-6.0	0.0	-2.7	60	-0.9	-2.1
70	-4.3	-6.2	-1.8	70	-6.2	70	-7.4	-0.2	-3.1	70	-1.2	-2.4
80	-7.6	-6.7	-1.6	80	-6.0	80	-8.0	0.5	-2.7	80	-1.0	-2.1
90	-12.2	-8.5	-1.5	90	-6.0	90	-9.6	0.5	-2.8	90	-1.6	-2.4
100	-27.0	-10.6	-2.3	100	-6.8	100	-11.2	0.1	-3.4	100	-2.1	-2.8
120	-75.1	-19.1	-2.5	120	-7.2	120	-14.0	0.3	-3.5	120	-2.4	-2.8
130		-25.4	-2.4	129	-7.3	128	-14.7	0.5	-3.4	126	-2.5	-2.7
148		-57.1	-2.7	147	-8.4	146	-17.5	0.4	-3.6	144	-2.9	-2.7
167		-59.7	-3.5	166	-9.7	165	-20.6	-0.1	-3.8	163	-4.2	-3.1
187		-66.7	-4.3	186	-11.3	185	-24.0	-7.2	-4.3	183	-5.1	-3.3
206		-91.1	-5.2	205	-13.0	204	-26.8	-21.8	-4.5	202	-6.3	-3.3
226			-6.3	225	-16.0	224	-29.5	-72.4	-4.4	222	-7.4	-3.4
246			-7.8	245	-18.9	244	-34.4	-79.5	-4.9	242	-8.7	-3.4
271			-10.9	270	-22.8	269	-39.6	-84.2	-6.0	267	-10.9	-4.5
300			-14.3	300	-27.7	294	-42.5	-86.7	-6.2	292	-13.1	-4.4
325			-17.7	325	-31.6	300	-43.8	-86.9	-6.2	300	-13.9	-4.2
350			-22.7	350	-38.5	325	-45.2	-89.3	-6.2	325	-15.8	-4.6
375			-26.7	375	-42.9	350	-48.7	-91.1	-6.5	350	-18.1	-4.9
400			-32.9	400	-47.0	375	-50.9	-93.3	-6.9	375	-20.5	-5.0
425			-38.8	425	-50.8	400	-52.6	-94.2	-7.8	400	-22.6	-5.4
450			-44.5	450	-56.7	425	-55.8		-8.4	425	-25.2	-5.8
475			-48.9	475	-59.7	450	-58.4		-8.9	450	-28.6	-6.2
500			-52.7	500	-68.3	475	-59.7		-9.2	475	-31.2	-6.5
						500	-62.5		-10.4	500	-34.1	-7.2

Table 3. Results of frost-salt tests of carbonated concretes

Change in vol.-%										
Cycle	C2	C3	C7	C10	C11	C13	C15	C18	C21	C22
0	0.0	0.0	0.0	0.0	0.0	0.0	0.0	0.0	0.0	0.0
10	-3.7	-3.8	-55.2	-22.8	-4.9	-27.4	-16.1	-10.2	-6.7	-21.2
20	-7.0	-6.2	-73.6	-28.5	-6.8	-33.3	-21.5	-60.5	-14.3	-22.2
30	-7.4	-7.1		-31.6	-7.4	-38.0	-25.7	-67.0	-15.4	-23.8
40	-12.0	-19.6		-34.0	-13.7	-42.6	-30.1		-20.6	-30.0
50	-16.3	-43.1		-34.8	-21.5	-43.2	-31.3		-21.0	-31.2
60	-25.2	-60.3		-36.1	-43.4	-43.9	-60.0		-21.5	-31.8
70	-35.1	-75.4		-38.3	-66.8	-48.0	-92.9		-21.7	-33.8
80	-63.0	-91.3		-43.0	-76.2	-52.4			-23.2	-35.6
90	-78.1			-59.7					-25.3	-43.6
100	-87.4								-32.0	-56.6
110	-95.0								-39.6	-66.4
120									-46.7	-77.4
130									-70.6	-88.6

Table 3. Results of frost-salt tests of carbonated concretes (continued)

	Change in vol.-%								
Cycle	C1	C17	C23	C24	C27	C28	C29	C32	C34
0	0.0	0.0	0.0	0.0	0.0	0.0	0.0	0.0	0.0
10	-1.4	-1.6	-5.9	-12.4	0.6	0.0	-2.8	0.4	-2.2
20	-2.0	-1.7	-8.1	-18.7	-4.1	-8.7	-16.9	-3.6	-19.0
30	-2.0	-2.1	-11.0	-22.6	-6.4	-9.0	-18.3	-4.4	-20.3
40	-2.7	-3.5	-19.3	-30.6	-10.4	-9.5	-18.6	-4.7	-20.8
50	-3.2	-4.4	-21.9	-32.5	-15.5	-11.1	-19.4	-5.2	-21.7
60	-3.4	-5.1	-22.6	-33.2	-19.1	-11.8	-19.5	-5.4	-21.7
70	-3.7	-5.3	-23.3	-33.5	-23.3	-12.3	-20.1	-6.1	-22.6
80	-4.9	-6.8	-24.2	-34.7	-27.2	-12.3	-19.9	-6.1	-22.2
90	-5.4	-6.8	-24.6	-35.2	-30.3	-12.1	-19.8	-6.2	-22.5
100	-5.7	-7.3	-25.6	-35.6	-34.2	-12.2	-19.9	-6.2	-22.8
110	-7.0	-8.9	-26.6	-36.3	-36.6	-12.3	-20.0	-6.2	-22.8
120	-7.7	-9.8	-27.3	-36.4	-39.4	-12.5	-20.2	-6.5	-23.2
130	-7.9	-10.0	-27.6	-36.7	-40.8	-12.6	-20.4	-6.6	-23.1
140	-9.1	-11.7	-28.4	-37.0	-43.5	-12.7	-20.3	-6.7	-23.1
150	-9.9	-12.6	-28.8	-37.5	-46.1	-13.8	-20.6	-6.9	-23.2
160	-10.5	-13.1	-29.0	-38.0	-47.9	-14.3	-20.7	-7.0	-23.5
170	-11.3	-14.0	-29.6	-38.7	-49.9	-17.7	-20.9	-7.2	-23.6
180	-12.2	-14.6	-30.2	-39.5	-51.5	-21.8	-20.8	-7.2	-23.7
190	-12.8	-15.2	-30.8	-40.2	-53.8	-24.9	-21.0	-7.3	-23.8
200	-13.1	-15.6	-31.3	-40.9	-55.5	-29.6	-21.1	-7.6	-24.2
210	-13.3	-16.2				-31.7	-21.6	-7.7	-24.4
220	-13.7	-16.7				-35.7	-21.6	-7.9	-24.8
230	-14.8	-18.3				-40.4	-21.9	-8.1	-24.8
240	-15.6	-21.6				-42.2	-22.0	-8.0	-24.7
250	-16.2	-26.9							
260	-16.6	-32.1							

Table 4. Results of frost-salt tests of cycled concretes

	Change in vol.-%								
Cycle	C3	C7	C10	C11	C13	C15	C18	C21	C22
0	0.0	0.0	0.0	0.0	0.0	0.0	0.0	0.0	0.0
10	-7.2	-18.3	-14.6	-2.2	-17.3	-11.0	-2.1	-6.4	-6.8
20	-27.5	-64.4	-17.8	-10.2	-22.2	-13.7	-25.3	-8.6	-10.9
30	-53.2	-78.6	-20.8	-15.2	-24.6	-15.4	-50.9	-8.8	-16.4
40	-56.5		-26.4	-27.1	-31.5	-29.6	-67.5	-11.6	-36.5
50			-49.0	-32.9	-42.5	-78.8		-13.1	-55.9
60			-77.9	-39.8	-57.3			-21.8	-100
70				-48.7	-68.9			-35.4	
80				-55.9				-49.0	
90				-73.1				-88.7	

Table 4. Results of frost-salt tests of cycled concretes (continued)

	Change in vol.-%									
Cycle	M01	M02	M17	M23	M24	M27	M28	M29	M32	M34
0	0.0	0.0	0.0	0.0	0.0	0.0	0.0	0.0	0.0	0.0
10	-1.2	-2.9	-0.9	-6.2	-9.0	-0.7	-1.0	-3.0	-0.8	-2.7
20	-1.5	-6.1	-1.2	-7.3	-9.8	-2.9	-0.9	-3.7	-1.6	-3.9
30	-1.5	-10.9	-1.4	-7.9	-11.7	-6.9	-1.1	-3.6	-3.0	-4.1
40	-3.1	-16.6	-3.6	-11.1	-15.6	-16.0	-2.4	-5.6	-6.7	-4.9
50	-3.6	-19.5	-4.5	-11.7	-16.4	-18.9	-4.0	-5.7	-8.5	-5.8
60	-4.1	-23.0	-5.5	-12.0	-18.5	-22.2	-7.0	-5.8	-10.0	-6.0
70	-4.4	-26.5	-6.3	-12.3	-22.3	-25.2	-15.8	-5.8	-11.5	-6.1
80	-5.8	-32.3	-9.6	-13.9	-24.5	-34.1	-21.4	-6.4	-15.6	-6.3
90	-6.6	-36.0	-10.8	-14.9	-26.1	-37.6	-32.0	-6.3	-16.8	-6.5
100	-7.2	-39.9	-12.9	-18.9	-34.3	-42.2	-38.0	-6.4	-18.6	-6.8
110	-8.8	-48.1	-15.6	-23.2	-40.1	-47.6	-48.6	-6.9	-21.3	-7.2
120	-10.3	-52.5	-17.3	-29.6	-46.6	-51.2	-75.0	-7.4	-23.0	-7.6
130	-11.2	-60.7	-19.3	-38.3	-63.4	-54.8	-90.1	-7.5	-24.2	-8.2
140	-12.9	-78.1	-21.9	-47.0	-78.9	-60.8		-7.8	-26.9	-8.9
150	-14.7	-80.3	-23.6	-49.8	-82.3	-63.2		-8.1	-28.1	-9.4
160	-16.2	-87.9	-25.9	-61.4	-90.9	-67.1		-8.5	-30.1	-10.7
170	-18.4		-28.1	-65.2		-69.8		-9.0	-32.3	-11.5
180	-20.4		-29.9	-70.3		-72.6		-9.5	-33.9	-13.0
190	-23.5		-32.3	-75.0		-76.9		-10.1	-35.6	-16.5
200	-25.7		-34.0	-85.0		-80.9		-10.9	-37.2	-20.3
220								-11.9		-30.9
240								-13.8		-38.6
250								-14.4		-41.3

Table 5. Volume of rapid deterioration in the frost-salt (FS) test, and carbonated volume of specimens before the frost-salt test.

Mix	Carbonated volume of specimen [%]		Volume of rapid deterioration in FS test [%]	
	carbonated	cycled	carbonated	cycled
C1	23.1	20.8	1.5	1.0
C2	20.0	16.9	0.0	0.0
C3	31.9	27.1	2.5	0.0
C7	27.5	17.9	0.0	0.0
C10	36.9	22.5	31.5	12.5
C11	24.3	15.8	3.6	0.0
C13	45.0	28.1	40.5	18.0
C15	36.5	25.9	26.5	10.5
C17	22.0	17.2	1.3	0.8
C18	15.8	10.1	0.0	0.0
C21	23.8	10.4	19.5	6.5
C22	33.0	17.7	28.0	7.5
C23	23.6	16.1	22.0	10.0
C24	41.6	26.8	34.0	9.0
C27	3.0	0.6	0.0	0.0
C28	13.2	3.3	12.5	1.5
C29	24.8	11.5	19.0	4.5
C32	5.6	3.0	4.3	0.0
C34	24.6	11.5	22.0	5.1

Results of the capillary suction test

Notations in Tables on the following pages are illustrated in Figures below

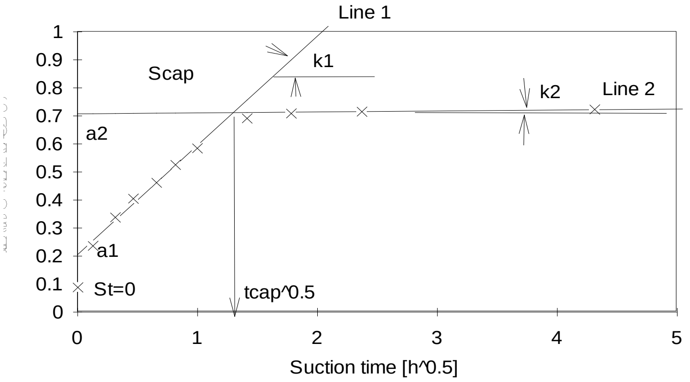

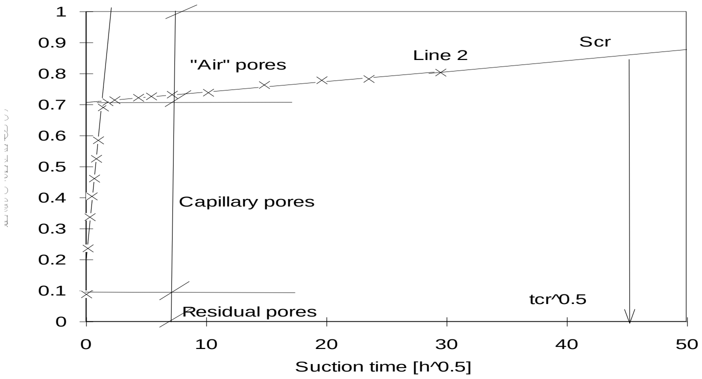

Specimen in the suction test 25*100*100 mm^3

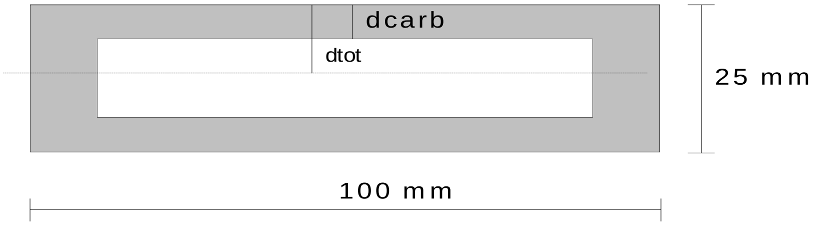

APPENDIX E/2

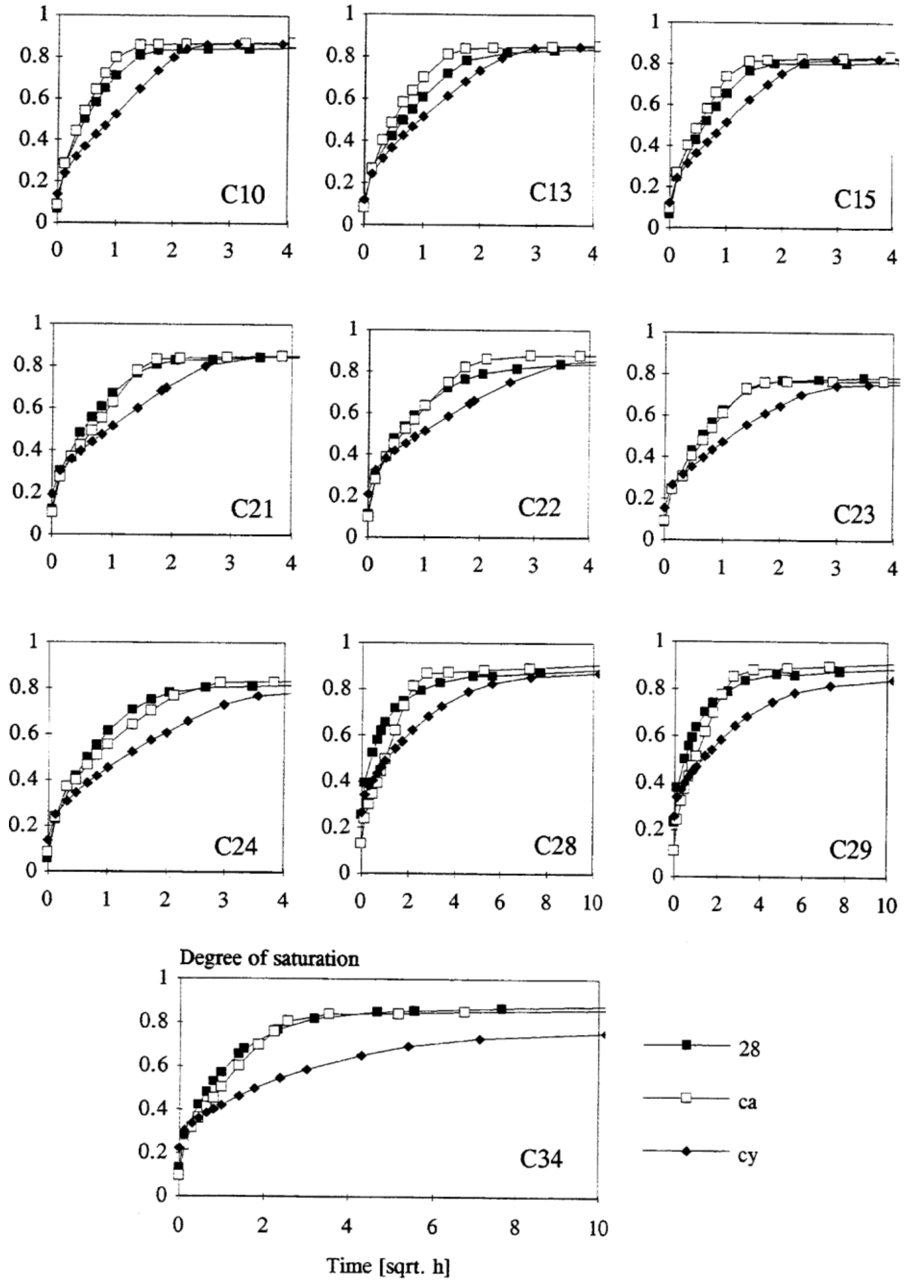

Figure E4. Degree of saturation as a function of capillary suction time for GBFS concretes.

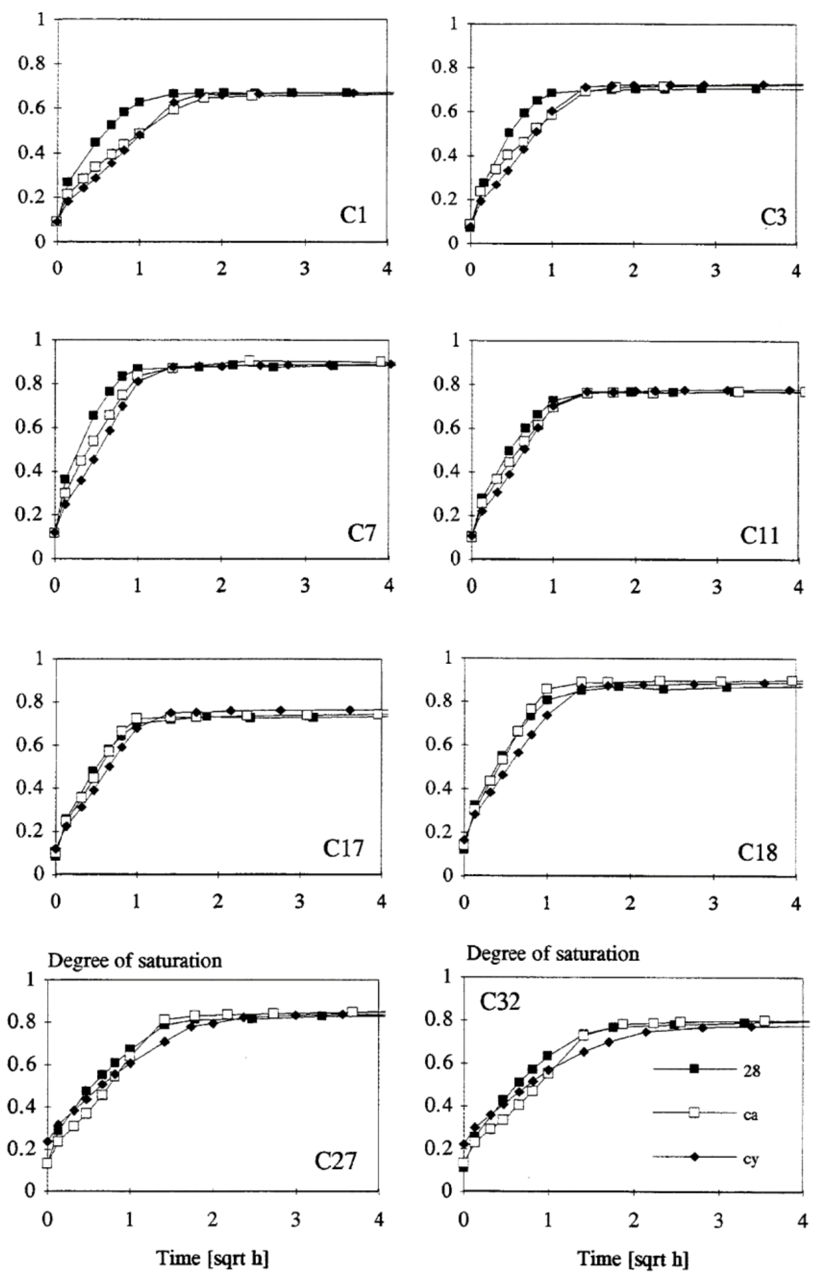

Figure E5. Degree of saturation as a function of capillary suction time for OPC concretes.

Table 1. Results of the capillary suction test

Mix/w/b/ GBFS %	curing	Line 1 k1	Line 2 k2	Line 1 a1	Line 2 a2	$S_{t=0}$	S_{ac}	S_{cap}	S_{cr}	t_{cap} [h]	t_{cr} [d]
C3/0.75/0	28	0.573	0.00202	0.198	0.698	0.070	0.627	0.700	0.845	0.8	218
	CYCLED	0.474	0.00218	0.122	0.718	0.078	0.220	0.720	0.853	1.6	162
	CARB.	0.390	0.00338	0.205	0.707	0.089	0.174	0.712	0.850	1.7	74
C1/0.60/0	28	0.420	0.00239	0.232	0.663	0.087	0.572	0.665	0.834	1.1	216
	CYCLED	0.348	0.00274	0.131	0.660	0.090	0.256	0.664	0.835	2.3	171
	CARB.	0.293	0.00363	0.192	0.650	0.091	0.195	0.656	0.832	2.5	104
C2/0.60/0	28	0.490	0.00263	0.281	0.753	0.099	0.674	0.756	0.870	0.9	83
	CYCLED	0.436	0.00220	0.149	0.792	0.105	0.326	0.796	0.887	2.2	77
	CARB.	0.367	0.00314	0.212	0.760	0.103	0.231	0.765	0.875	2.3	56
C7/0.60/0	28	0.694	0.00248	0.294	0.875	0.118	0.753	0.877	0.911	0.7	9
	CYCLED	0.656	0.00246	0.156	0.882	0.122	0.381	0.885	0.915	1.2	7
	CARB.	0.614	0.00217	0.241	0.888	0.117	0.263	0.890	0.917	1.1	8
C10/0.60/50	28	0.494	0.00269	0.241	0.838	0.069	0.724	0.841	0.897	1.5	20
	CYCLED	0.287	0.00299	0.236	0.855	0.137	0.439	0.861	0.905	4.8	12
	CARB.	0.580	0.00317	0.244	0.861	0.087	0.223	0.865	0.906	1.1	8
C11/0.54/0	28	0.570	0.00255	0.214	0.760	0.107	0.663	0.762	0.867	0.9	74
	CYCLED	0.587	0.00216	0.120	0.770	0.106	0.336	0.773	0.872	1.2	93
	CARB.	0.503	0.00298	0.203	0.758	0.100	0.235	0.761	0.868	1.2	57
C15/0.54/50	28	0.469	0.00395	0.202	0.791	0.067	0.692	0.796	0.880	1.6	21
	CYCLED	0.271	0.00323	0.232	0.812	0.124	0.409	0.819	0.890	4.7	24
	CARB.	0.532	0.00355	0.222	0.819	0.095	0.235	0.823	0.891	1.3	17
C13/0.54/70	28	0.346	0.00317	0.253	0.822	0.089	0.686	0.828	0.892	2.8	20
	CYCLED	0.233	0.00279	0.268	0.835	0.121	0.414	0.841	0.898	6.1	21
	CARB.	0.493	0.00315	0.234	0.838	0.082	0.217	0.842	0.898	1.5	15
C18/0.45/0	28	0.558	0.00349	0.273	0.856	0.118	0.799	0.859	0.908	1.1	10
	CYCLED	0.524	0.00246	0.219	0.879	0.164	0.482	0.882	0.919	1.6	11
	CARB.	0.675	0.00267	0.218	0.891	0.140	0.341	0.894	0.922	1.0	6
C21/0.45/50	28	0.423	0.00415	0.266	0.825	0.119	0.725	0.830	0.898	1.8	13
	CYCLED	0.201	0.00258	0.309	0.836	0.192	0.503	0.842	0.903	7.1	28
	CARB.	0.397	0.00328	0.232	0.835	0.104	0.318	0.840	0.902	2.3	17
C22/0.45/70	28	0.259	0.00374	0.367	0.824	0.111	0.721	0.831	0.898	3.2	16
	CYCLED	0.171	0.00215	0.332	0.859	0.209	0.493	0.866	0.912	9.7	25
	CARB.	0.329	0.00251	0.281	0.871	0.098	0.292	0.876	0.915	3.3	13
C17/0.45/0	28	0.573	0.00322	0.195	0.718	0.082	0.641	0.721	0.854	0.8	74
	CYCLED	0.545	0.00250	0.140	0.754	0.119	0.385	0.757	0.868	1.3	87
	CARB.	0.615	0.00323	0.163	0.728	0.100	0.250	0.731	0.858	0.9	68
C23/0.45/50	28	0.432	0.00455	0.209	0.765	0.085	0.674	0.771	0.874	1.7	24
	CYCLED	0.193	0.00349	0.264	0.739	0.156	0.426	0.747	0.865	6.2	55
	CARB.	0.387	0.00340	0.207	0.757	0.092	0.271	0.762	0.870	2.1	46
C24/0.45/70	28	0.444	0.00451	0.189	0.796	0.056	0.625	0.802	0.884	1.9	16
	CYCLED	0.166	0.00293	0.268	0.780	0.138	0.421	0.789	0.880	9.9	48
	CARB.	0.224	0.00311	0.313	0.821	0.083	0.271	0.828	0.893	5.3	22
C27/0.35/0	28	0.438	0.00389	0.249	0.816	0.136	0.712	0.821	0.899	1.7	19
	CYCLED	0.330	0.00240	0.283	0.830	0.236	0.564	0.834	0.906	2.8	41
	CARB.	0.460	0.00272	0.165	0.837	0.133	0.388	0.841	0.909	2.2	29
C28/0.35/50	28	0.303	0.00502	0.367	0.832	0.255	0.711	0.840	0.909	2.4	10
	CYCLED	0.114	0.00263	0.364	0.847	0.266	0.571	0.858	0.916	18.9	29
	CARB.	0.290	0.00346	0.205	0.864	0.129	0.409	0.872	0.921	5.3	11

Table 1. Results of the capillary suction test (continued)

Mix/w/b/ GBFS %	curing	Line 1 k1	Line 2 k2	Line 1 a1	Line 2 a2	$S_{t=0}$	S_{ac}	S_{cap}	S_{cr}	t_{cap} [h]	t_{cr} [d]
C29/0.35/70	28	0.296	0.00399	0.350	0.840	0.233	0.687	0.846	0.911	2.8	13
	CYCLED	0.100	0.00234	0.360	0.817	0.257	0.568	0.827	0.903	21.8	57
	CARB.	0.242	0.00288	0.263	0.873	0.111	0.372	0.881	0.925	6.5	13
C32/0.35/0	28	0.437	0.00406	0.212	0.776	0.111	0.661	0.781	0.882	1.7	28
	CYCLED	0.306	0.00208	0.265	0.768	0.223	0.507	0.772	0.879	2.7	118
	CARB.	0.388	0.00250	0.164	0.788	0.132	0.332	0.792	0.887	2.6	65
C34/0.35/70	28	0.284	0.00210	0.278	0.851	0.132	0.677	0.855	0.912	4.1	35
	CYCLED	0.093	0.00288	0.321	0.729	0.223	0.497	0.742	0.869	20.5	99
	CARB.	0.232	0.00303	0.258	0.830	0.097	0.321	0.837	0.906	6.2	26

S_{ac} = degree of saturation before the drying to the constant weight at 50 ^{o}C

Table 2. Results of the capillary suction test

Mix/ w/b/ GBFS %	curing	"Air" pores [%]	Capillary pores [%]	Residual pores [%]	Total porosity [%]	p_r	u (T=oo) [%]	Carb. vol. [%]	d_{carb}/ d_{tot} [%]	Specific gravity [kg/m^3]
C3/0.75/0	28	5.7	12.0	1.3	19.0	0.30	8.74			2175
	CYCLED	5.1	11.7	1.4	18.1	0.28	8.30	43	24	2196
	CARB.	5.2	11.3	1.6	18.2	0.29	8.23	66	49	2203
C1/0.60/0	28	5.5	9.5	1.4	16.4	0.34	7.28			2249
	CYCLED	5.2	8.9	1.4	15.5	0.34	6.87	36	24	2265
	CARB.	5.5	9.0	1.4	15.9	0.34	7.03	47	34	2258
C2/0.60/0	28	3.6	9.6	1.4	14.6	0.24	6.37			2293
	CYCLED	2.7	9.0	1.4	13.1	0.20	5.66	30	18	2333
	CARB.	3.2	8.9	1.4	13.4	0.24	5.78	57	43	2327
C7/0.60/0	28	2.2	13.7	2.1	18.1	0.12	8.18			2208
	CYCLED	2.0	13.0	2.1	17.1	0.12	7.64	27	15	2235
	CARB.	1.8	12.9	2.0	16.7	0.11	7.34	55	42	2255
C10/0.60/50	28	3.1	15.0	1.3	19.5	0.16	8.98			2169
	CYCLED	2.6	13.4	2.5	18.4	0.14	8.45	31	19	2194
	CARB.	2.5	14.4	1.6	18.5	0.14	8.43	74	60	2198
C11/0.54/0	28	4.7	12.9	2.1	19.6	0.24	9.09			2158
	CYCLED	4.2	12.2	2.0	18.4	0.23	8.40	24	15	2191
	CARB.	4.4	12.1	1.8	18.3	0.24	8.32	53	38	2199
C15/0.54/50	28	3.9	13.9	1.3	19.0	0.20	8.73			2177
	CYCLED	3.2	12.3	2.2	17.7	0.18	8.01	44	28	2212
	CARB.	3.2	13.4	1.7	18.4	0.18	8.33	73	58	2201
C13/0.54/70	28	3.3	14.1	1.7	19.1	0.17	8.77			2177
	CYCLED	2.9	13.0	2.2	18.1	0.16	8.22	46	31	2204
	CARB.	2.9	13.9	1.5	18.3	0.16	8.29	75	59	2204
C18/0.45/0	28	2.1	10.9	1.7	14.7	0.14	6.39			2296
	CYCLED	1.6	9.5	2.2	13.3	0.12	5.69	11	4	2338
	CARB.	1.5	10.5	2.0	14.0	0.11	6.04	43	31	2326
C21/0.45/50	28	2.5	10.5	1.8	14.7	0.17	6.43			2290
	CYCLED	2.2	9.2	2.7	14.2	0.16	6.09	20	8	2322
	CARB.	2.3	10.7	1.5	14.5	0.16	6.29	53	36	2308

Table 2. Results of the capillary suction test (continued)

Mix/ w/b/ GBFS %	curing	"Air" pores [%]	Capillary pores [%]	Residual pores [%]	Total porosity [%]	p_r	u (T=oo) [%]	Carb. vol. [%]	d_{carb}/d_{tot} [%]	Specific gravity [kg/m^3]
C22/0.45/70	28	2.4	10.4	1.6	14.5	0.17	6.26			2315
	CYCLED	1.9	9.3	3.0	14.2	0.13	6.07	22	12	2321
	CARB.	1.8	11.1	1.4	14.2	0.12	6.13	62	42	2326
C17/0.45/0	28	5.0	11.3	1.5	17.8	0.28	8.02			2215
	CYCLED	4.0	10.4	1.9	16.3	0.24	7.28	16	6	2247
	CARB.	4.5	10.6	1.7	16.8	0.27	7.53	51	37	2242
C23/0.45/50	28	3.6	10.8	1.3	15.7	0.23	7.01			2243
	CYCLED	4.0	9.4	2.5	15.9	0.25	6.94	23	13	2273
	CARB.	3.9	10.9	1.5	16.2	0.24	7.20	55	41	2250
C24/0.45/70	28	3.4	13.0	1.0	17.4	0.20	7.85			2214
	CYCLED	3.5	10.9	2.3	16.7	0.21	7.41	36	22	2250
	CARB.	3.1	13.4	1.5	18.0	0.17	8.19	65	49	2203
C27/0.35/0	28	2.1	8.2	1.6	11.9	0.18	4.97			2393
	CYCLED	1.9	6.7	2.7	11.2	0.17	4.66	4	2	2406
	CARB.	1.7	7.7	1.4	10.9	0.16	4.53	27	17	2416
C28/0.35/50	28	1.7	6.3	2.8	10.8	0.16	4.52			2389
	CYCLED	1.5	6.3	2.8	10.7	0.14	4.44	9	6	2404
	CARB.	1.4	8.0	1.4	10.7	0.13	4.46	33	19	2401
C29/0.35/70	28	1.7	6.7	2.5	10.9	0.15	4.59			2386
	CYCLED	1.9	6.4	2.9	11.3	0.17	4.73	15	10	2388
	CARB.	1.2	8.1	1.2	10.5	0.12	4.37	49	32	2403
C32/0.35/0	28	2.9	8.8	1.5	13.1	0.22	5.60			2346
	CYCLED	2.9	7.0	2.8	12.8	0.23	5.41	2	0	2352
	CARB.	2.6	8.3	1.7	12.5	0.21	5.34	28	17	2362
C34/0.35/70	28	1.7	8.6	1.6	11.9	0.14	5.08			2348
	CYCLED	3.2	6.4	2.7	12.3	0.26	5.17	10	5	2362
	CARB.	1.9	8.5	1.1	11.5	0.16	4.86	47	31	2369

p_r = Protective pore ratio (1-S_{cap})
u = Moisture content at full saturation

APPENDIX F/1

Results of the MIP-test of conretes

			Capillary pore area			Mesopore area			
Mix/ w/b/ GBFS %	curing	Vtot [%]	top of the peak [nm]	end of the area [nm]	Vcap [%]	top of the peak [nm]	end of the area [nm]	Vres [%]	Density [g/cm^3]
C3/0.75/0	28	12.5	30	59	5.8	1243	1632	6.7	2.25
C1/0.60/0	28	10.7	38	71	4.8	897	2521	6.0	2.30
C2/0.60/0	28	8.6	32	79	4.8	659	897	3.8	2.34
	CYCLED	8.3	57	105	5.9	388	1200	2.4	2.35
	CARB.	8.1	62	141	4.8	722	1545	3.3	2.40
C7/0.60/0	28	10.9	32	79	7.8	570	2120	3.1	2.26
	CYCLED	10.4	60	108	7.5	240	2150	2.9	2.26
	CARB.	10.4	53	157	7.4	545	2320	3.0	2.27
C10/0.60/50	28	11.1	23	67	7.7	298	4100	3.4	2.25
	CARB.	8.9	20	92	5.8	1240	4030	3.1	2.24
C11/0.54/0	28	12.4	23	52	6.7	2303	4113	5.8	2.18
	CYCLED	12.0	60	93	7.1	1075	2431	4.9	2.23
	CARB.	11.1	60	114	5.9	1266	2915	5.2	2.29
C15/0.54/50	28	12.9	23	64	8.2	2140	4640	4.7	2.18
	CARB.	11.7	64	136	8.1	3494	4586	3.6	2.24
C13/0.54/70	28	11.6	33	88	6.8	1463	4931	4.8	2.24
	CYCLED	8.4	15	45	4.6	2142	4670	3.8	2.27
	CARB.	11.7	24	155	7.1	530	1056	4.6	2.27
C18/0.45/0	28	8.8	28	58	6.1	430	4220	2.7	2.32
	CYCLED	6.6	42	65	4.8	140	4200	1.9	2.37
	CARB.	7.2	48	85	4.9	530	2740	2.3	2.38
C21/0.45/50	28	8.7	26	48	5.3	540	1243	3.4	2.34
	CYCLED	6.8	14	60	4.0	1266	1956	2.9	2.32
	CARB.	7.3	50	120	4.6	683	1632	2.7	2.41
C22/0.45/70	28	8.3	14	51	5.5	834	1411	2.8	2.37
	CYCLED	6.3	10	40	3.1	1075	1819	3.2	2.35
	CARB.	8.8	33	100	5.8	748	1337	3.0	2.35
C17/0.45/0	28	11.3	28	50	5.7	709	1115	5.5	2.25
	CYCLED	9.1	49	93	5.3	540	748	3.8	2.30
	CARB.	8.3	58	98	4.3	790	2345	4.0	2.37
C23/0.45/50	28	11.6	20	47	6.7	613	1115	4.9	2.21
	CARB.	8.9	20	100	4.0	2028	2968	5.0	2.37
C24/0.45/70	28	11.5	14	40	6.3	964	2028	5.2	2.23
	CYCLED	9.1	10	50	4.3	1056	1852	4.8	2.26
	CARB.	10.4	31	91	5.8	1037	2521	4.6	2.33
C27/0.35/0	28	6.8	31	45	4.9	92	510	1.9	2.42
	CYCLED	5.6	34	47	3.7	220	610	1.9	2.42
	CARB.	6.0	47	80	4.0	169	820	2.0	2.49
C28/0.35/50	28	6.6	18	35	4.0	152	411	2.6	2.42
	CARB.	5.6	32	54	3.2	222	550	2.4	2.44

Results of the MIP-test of concretes (continued)

			Capillary pore area			Mesopore area			
Mix/ w/b/ GBFS %	curing	Vtot [%]	top of the peak [nm]	end of the area [nm]	Vcap [%]	top of the peak [nm]	end of the area [nm]	Vres [%]	Density [g/cm^3]
C29/0.35/70	28	6.2	10	30	4.1	319	709	2.1	2.41
	CYCLED	4.4	10	40	2.5	502	735	1.9	2.38
	CARB.	5.8	27	52	3.5	376	624	2.3	2.43
C32/0.35/0	28	7.7	28	44	4.7	82	218	3.0	2.40
	CYCLED	6.4	33	50	4.9	411	591	1.6	2.38
	CARB.	7.0	43	74	5.3	182	404	1.7	2.43
C34/0.35/70	28	6.9	11	29	4.0	484	1037	2.9	2.39
	CYCLED	6.3	10	30	2.4	820	1000	3.8	2.34
	CARB.	6.5	28	80	3.4	442	1800	3.1	2.44

Results of the MIP-test of mortars

			Capillary pore area			Mesopore area			
Mix/ w/b/ GBFS %	curing	Vtot [%]	top of the peak [nm]	end of the area [nm]	Vcap [%]	top of the peak [nm]	end of the area [nm]	Vres [%]	Density [g/cm^3]
M7/0.60/0	28	18.7	45	108	12.9	397	776	5.8	1.97
	CARB.	16.9	50	160	11.8	400	650	5.1	2.04
	CYCLED	13.4	59	90	9.9	319	467	3.5	1.48
M10/0.60/50	28	23.1	40	100	12.3	100	540	10.9	1.88
	CARB.	22.7	80	160	13.4	343	570	9.3	1.94
	CYCLED	18.4	37	90	12.6	376	511	5.8	1.90
M70/0.60/70	28	23.5	19	100	11.0	581	881	12.5	1.87
	CARB.	24.7	40	150	12.4	570	776	12.3	1.89
	CYCLED	19.4	16	100	14.2	218	302	5.2	1.93
M18/0.45/0	28	14.5	42	62	11.0	160	500	3.5	2.11
	CARB.	12.2	52	78	9.4	252	345	2.8	2.20
	CYCLED	12.2	36	52	9.1	280	500	3.1	1.94
M21/0.45/50	28	17.0	24	50	9.6	88	240	7.4	2.02
	CARB.	15.4	32	50	8.1	104	199	7.3	2.11
	CYCLED	11.6	24	56	8.8	110	240	2.8	2.05
M22/0.45/70	28	17.8	22	45	9.6	118	239	8.2	2.03
	CARB.	17.9	22	70	10.1	144	257	7.8	2.08
	CYCLED	11.3	14	40	7.8	160	300	3.5	2.05
M27/0.35/0	28	13.1	39	49	8.8	90	300	4.3	2.18
	CARB.	10.8	51	68	8.4	90	200	2.4	2.24
	CYCLED	11.4	32	43	7.9	160	320	3.5	2.15
M28/0.35/50	28	9.0	21	60	6.5	160	800	2.5	2.28
	CARB.	8.2	38	90	6.0	260	600	2.2	2.32
	CYCLED	6.3	10	60	3.8	196	500	2.5	2.26
M29/0.35/70	28	10.4	16	60	6.5	650	1100	3.9	2.26
	CARB.	11.1	22	90	7.4	865	1156	3.7	2.32
	CYCLED	6.8	8	40	3.0	390	613	3.8	2.34

Results of the MIP-test of pastes

			Capillary pore area			Mesopore area			
Mix/ w/b/ GBFS %	curing	Vtot [%]	top of the peak [nm]	end of the area [nm]	Vcap [%]	top of the peak [nm]	end of the area [nm]	Vres [%]	Density [g/cm^3]
P7/0.60/0	28	34.0	64	175	26.6	390	570	7.5	1.43
	CARB.	31.4	76	180	20.7	411	602	10.7	1.54
	CYCLED	33.1	43	102	23.0	196	319	10.1	1.48
P10/0.60/50	28	39.3	58	166	23.7	602	805	15.6	1.34
	CARB.	39.6	86	240	23.5	570	762	16.1	1.47
	CYCLED	33.5	27	80	23.8	210	397	9.7	1.41
P70/0.60/70	28	43.9	30	200	22.9	1037	1692	21.0	1.30
	CARB.	44.4	100	220	21.5	964	1266	22.9	1.32
	CYCLED	38.9	20	200	28.2	624	1037	10.7	1.41
P18/0.45/0	28	25.4	50	75	20.1	240	600	5.3	1.68
	CARB.	20.8	48	83	17.6	160	400	3.2	1.85
	CYCLED	23.1	39	60	20.2			2.9	1.66
P21/0.45/50	28	30.2	38	141	22.4	434	550	7.8	1.54
	CARB.	28.6	88	182	22.9	390	581	5.7	1.69
	CYCLED	20.8	38	80	16.9	189	252	3.9	1.61
P22/0.45/70	28	35.9	26	149	24.8	581	834	11.1	1.49
	CARB.	33.8	90	220	25.6	502	683	0.0	1.57
	CYCLED	25.6	28	80	20.9	140	540	4.7	1.60
P27/0.35/0	28	21.2	37	47	15.3			5.9	1.83
	CARB.	17.2	45	64	15.7			1.5	2.00
	CYCLED	17.5	17	31	16.0			1.5	1.85

Definition of the capillary and the meso pore ranges

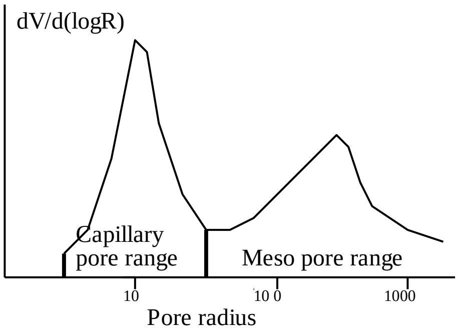

MIX PROPORTIONS OF PASTES

Paste	Binder composition [%]		Water/binder	water-reducer
	OPC	Slag	ratio	[% of binder]
P07	100	-	0.600	-
P10	50	50	0.600	-
P70	30	70	0.600	-
P18	100	-	0.446	0.37
P21	50	50	0.449	-
P22	30	70	0.449	-
P27	100	-	0.352	1.18

Mix proportions of mortars

Mortar	Aggregate/binder	Binder composition [%]		Water/binder	Water-reducer
	ratio	OPC	Slag	ratio	[% of binder]
M07	1.22	100	-	0.600	-
M10	1.22	50	50	0.600	-
M70	1.22	30	70	0.600	-
M18	1.35	100	-	0.454	0.37
M21	1.34	50	50	0.449	-
M22	1.34	30	70	0.449	-
M27	1.45	100	-	0.350	1.18
M28	1.44	50	50	0.351	1.36
M29	1.44	30	70	0.351	1.36

Grading of aggregates for mortars and concretes with the binder content of 400 kg/m3

Sieve size	Proportion passed [%]	
[mm]	Mortar mixes	Concrete mixes
0.125	5.0	2.9
0.25	22.0	6.9
0.5	34.1	13.1
1	71.0	17.3
2	100	28.8
4	100	45.8
8	100	64.5
16	100	100

Baseline-corrected freezing thermograms for pastes, w/b=0.60 APPENDIX H/1

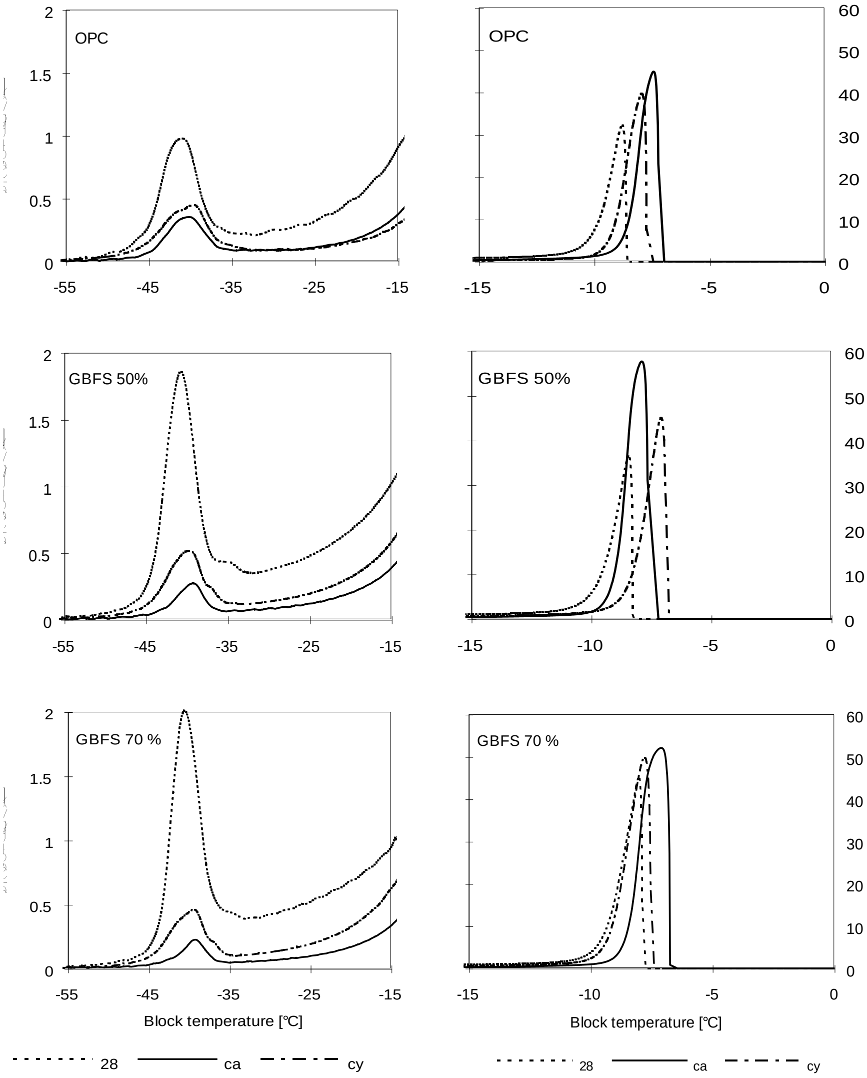

Baseline-corrected freezing thermograms for pastes, w/b=0.45 and 0.35

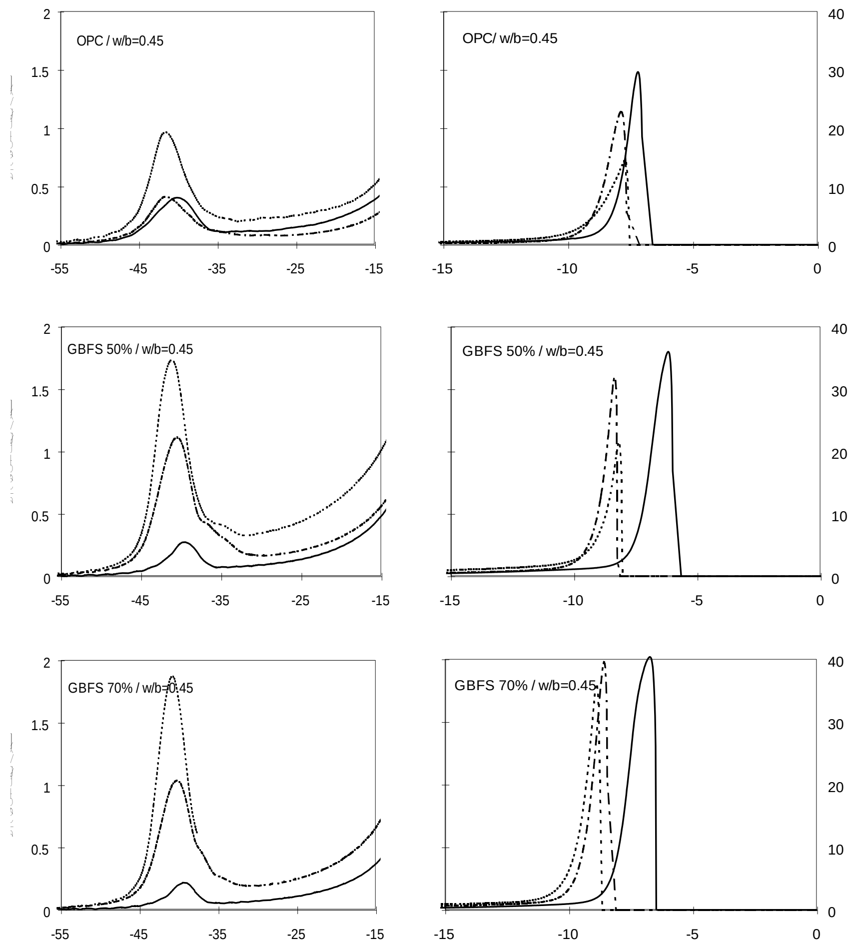

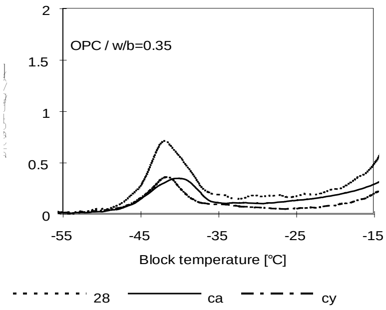
OPC / w/b=0.35
2
1.5
1
0.5
0
-55
-45
-35
-25
-15
Block temperature [ºC]
28
ca
cy

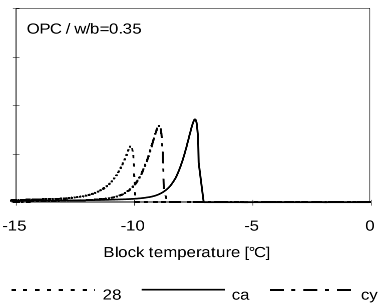
OPC / w/b=0.35
40
30
20
10
0
-15
-10
-5
0
Block temperature [ºC]
28
ca
cy

Baseline-corrected freezing thermograms for mortars, w/b=0.60 APPENDIX H/3

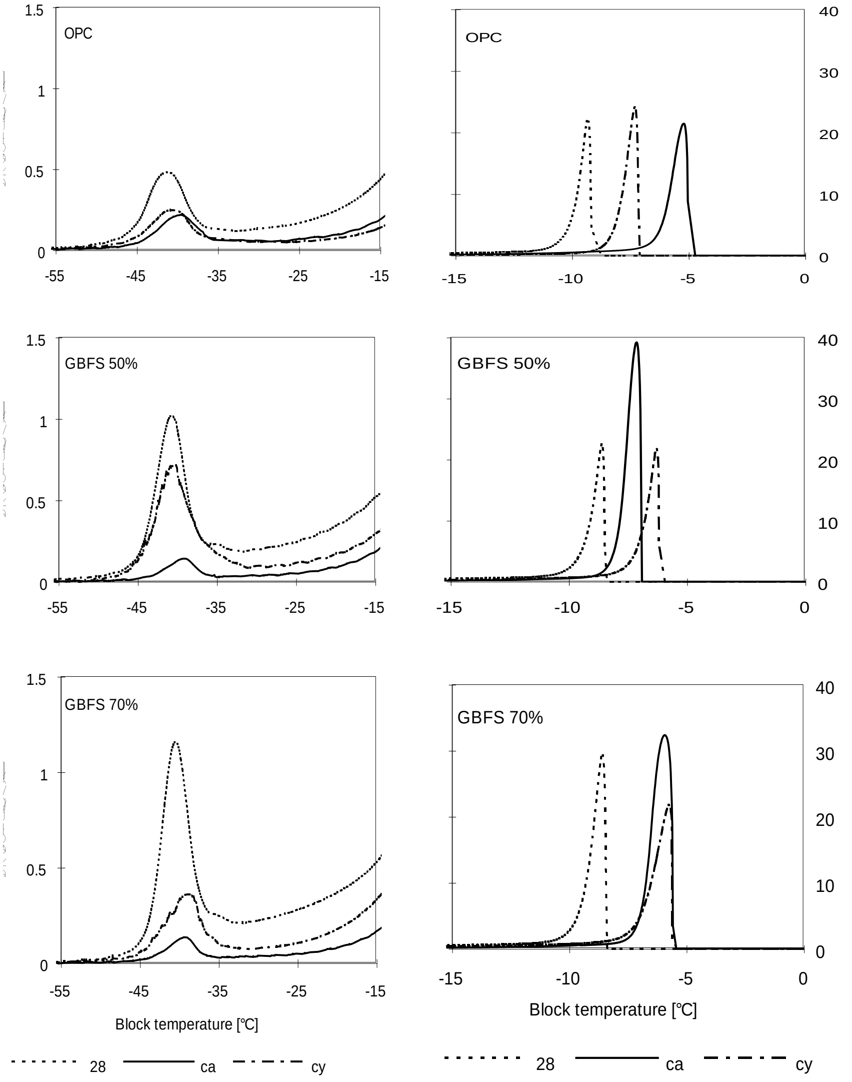

Baseline-corrected freezing thermograms for mortars, w/b=0.45 APPENDIX H/4

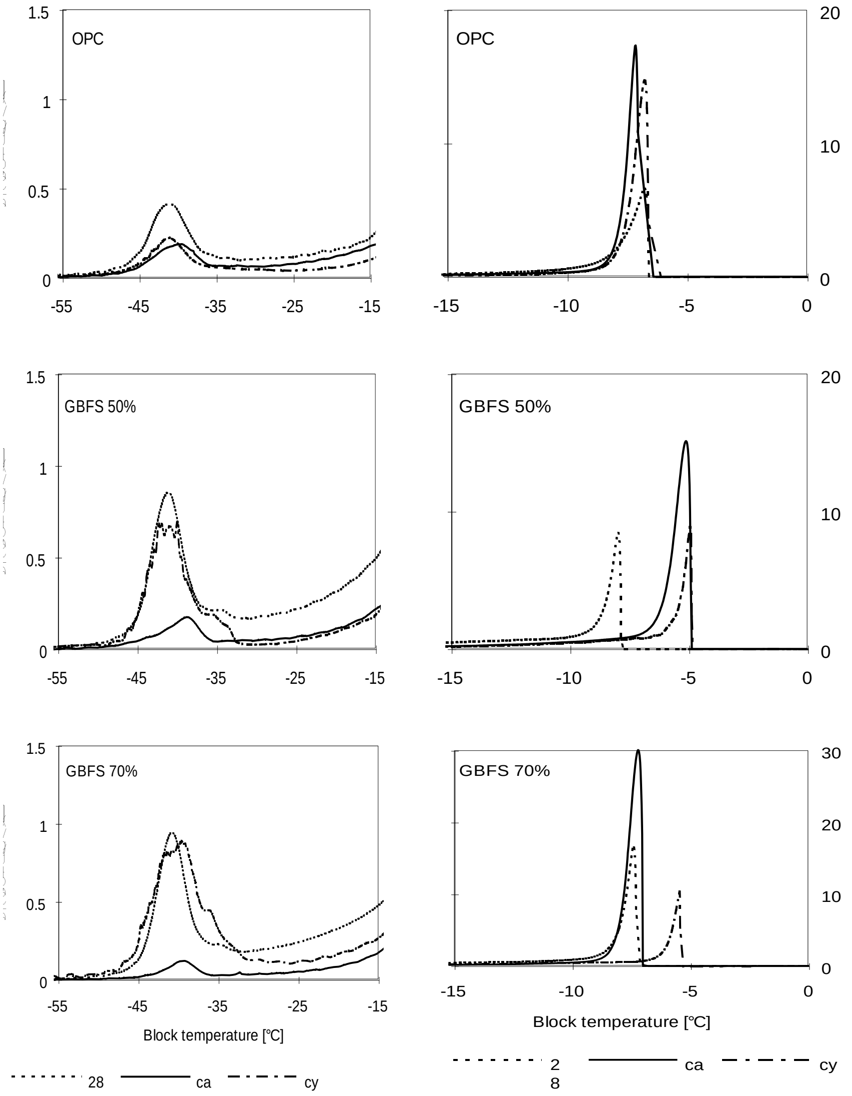

Baseline-corrected freezing thermograms for mortars, w/b=0.35 APPENDIX H/5

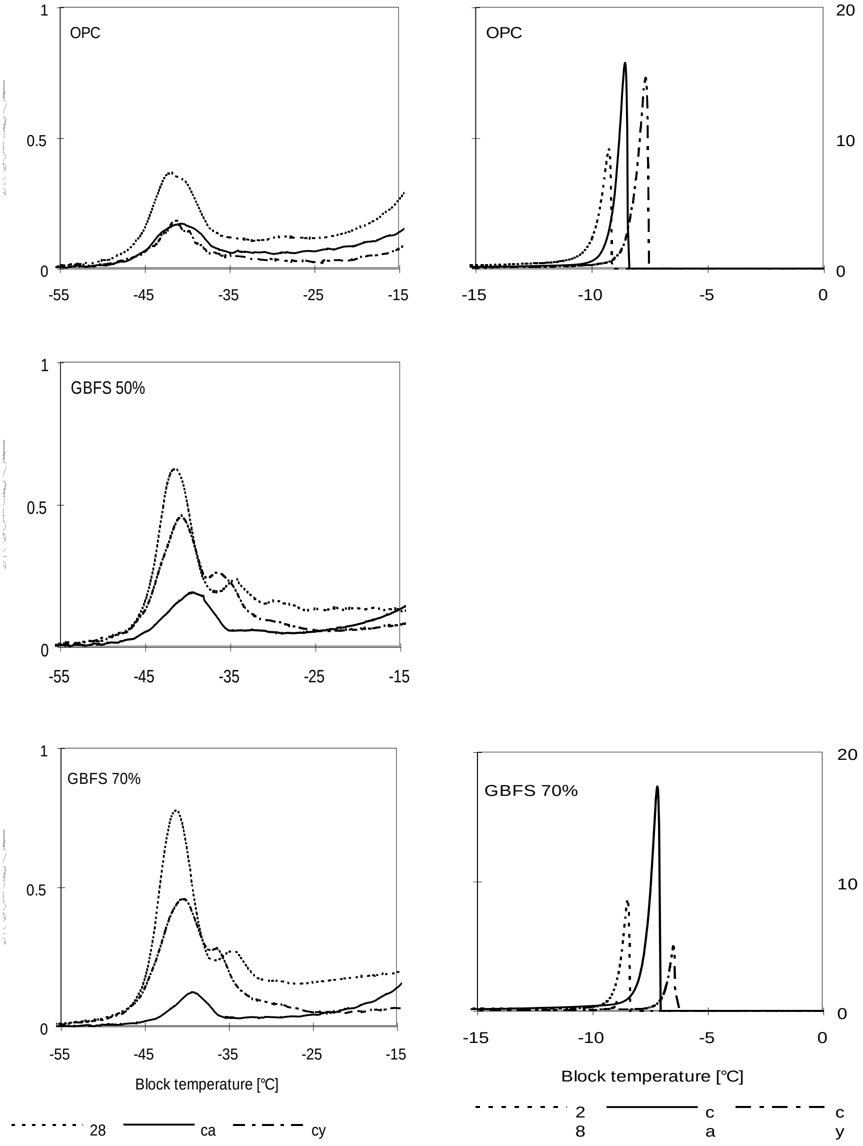

Fusion thermograms for pastes and mortars of w/b=0.60 APPENDIX H/6

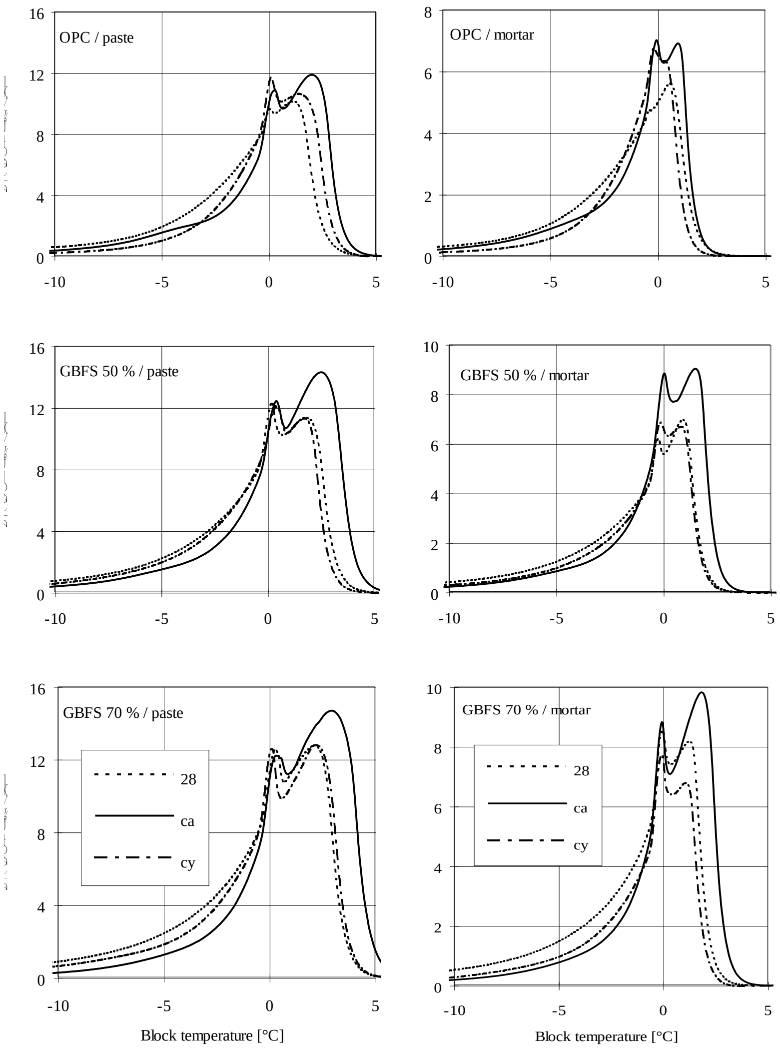

Fusion thermograms for pastes and mortars of w/b=0.45

APPENDIX H/7

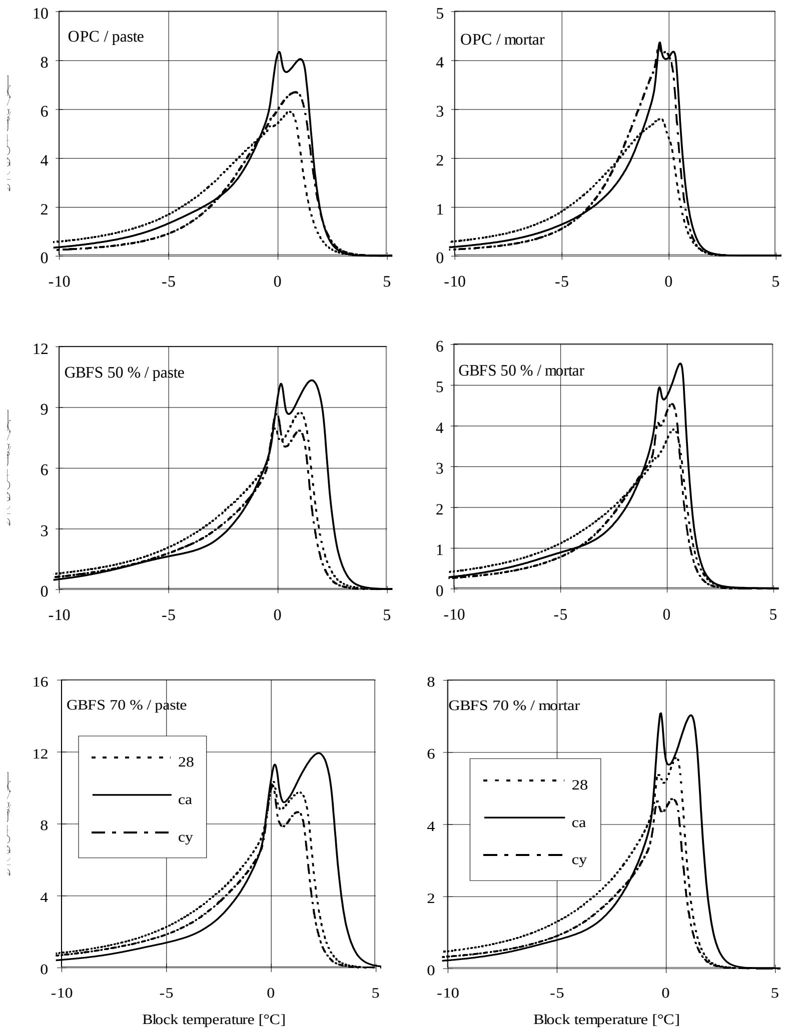

Fusion thermograms for pastes and mortars of w/b=0.35 APPENDIX H/8

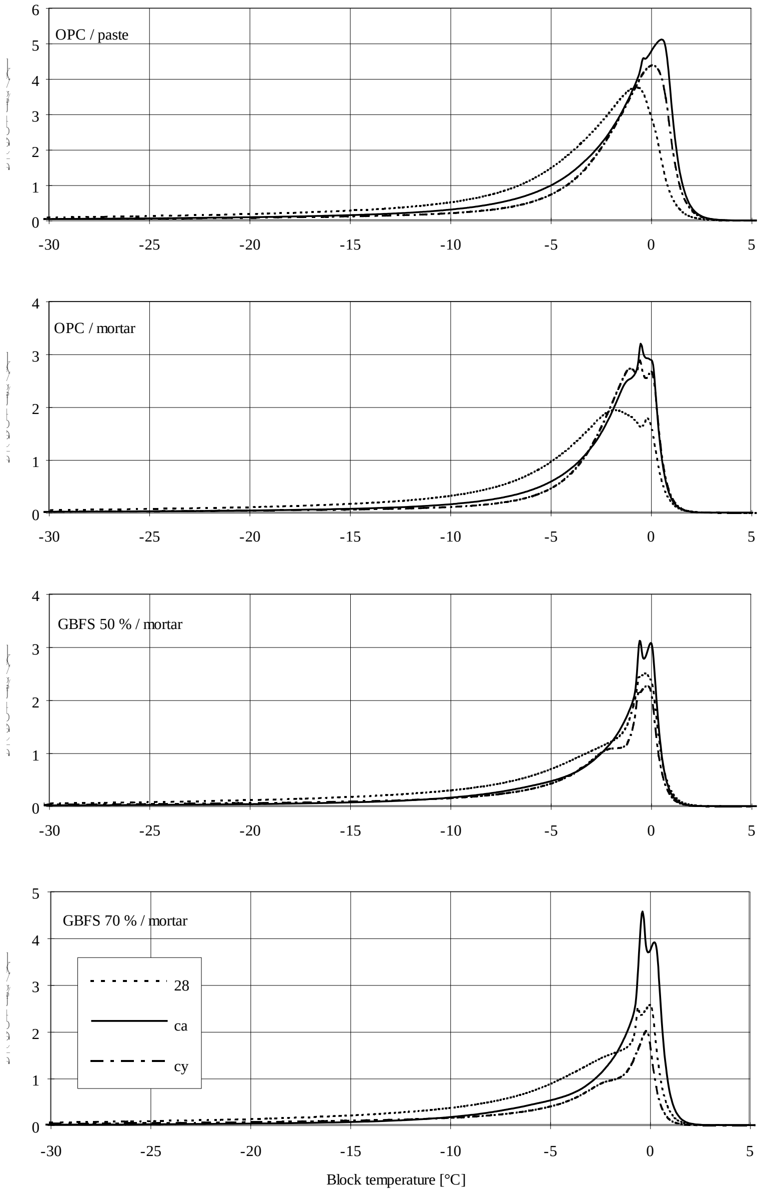

Cumulative freezable water as a function of pore size for pastes and mortars of w/b=0.60

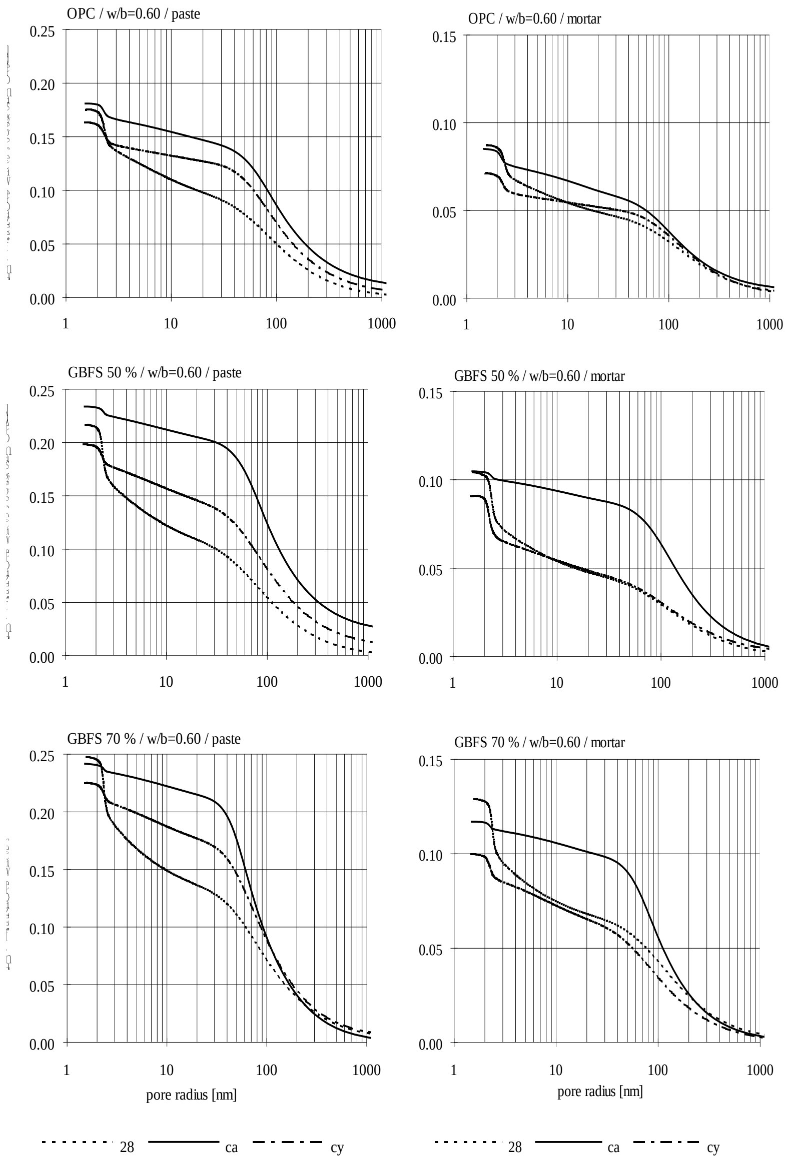

Cumulative freezable water as a function of pore size for pastes and mortars of w/b=0.45.

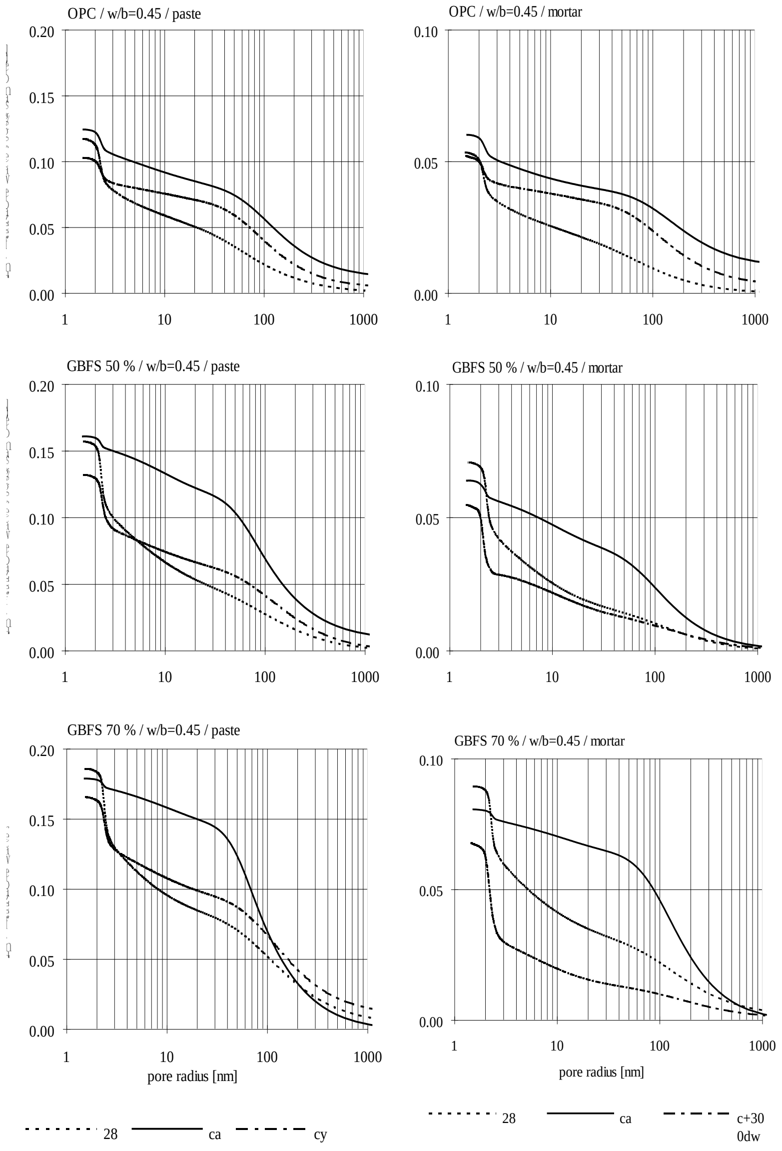

APPENDIX I/3

Cumulative freezable water as a function of pore size for pastes and mortars of w/b=0.35.

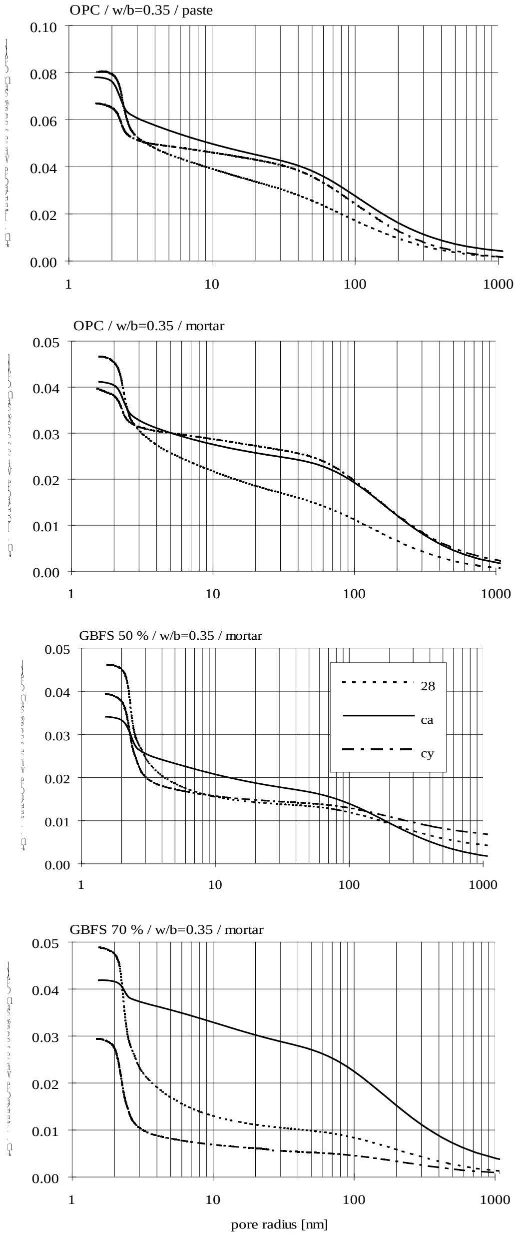

Table 1. Freezable and adsorbed water contents at different pore ranges according to the different pore models for the non-aged samples.

Mix	w/b	Total water porosity [g/g_{ssd}]	Freezable water [g/g_{ssd}]		Adsorbed water [g/g_{ssd}]											
					Spherical pore model			Cylindrical pore model			Layered pore model			Layered pore model /fine		
			1.5...4 [nm]	>4 [nm]	1.5...4 [nm]	>4 [nm]	<1.5 [nm]	1.5...4 [nm]	>4 [nm]	<1.5 [nm]	1.5...4 [nm]	>4 [nm]	<1.5 [nm]	1.5...4 [nm]	>4 [nm]	<1.5 [nm]
Pastes																
OPC	0.60	0.281	0.050	0.125	0.066	0.053	-0.012	0.034	0.035	0.037	0.012	0.019	0.076	0.023	0.017	0.066
GBFS 50%	0.60	0.291	0.075	0.142	0.101	0.062	-0.089	0.053	0.041	-0.020	0.019	0.022	0.033	0.035	0.018	0.022
GBFS 70%	0.60	0.304	0.077	0.170	0.104	0.071	-0.118	0.055	0.046	-0.045	0.020	0.025	0.011	0.036	0.021	0.000
OPC	0.45	0.223	0.047	0.070	0.070	0.031	0.005	0.038	0.020	0.048	0.014	0.011	0.081	0.022	0.009	0.076
GBFS 50%	0.45	0.240	0.071	0.085	0.099	0.044	-0.060	0.053	0.029	0.001	0.019	0.016	0.048	0.033	0.010	0.040
GBFS 70%	0.45	0.248	0.073	0.113	0.078	0.053	-0.069	0.038	0.036	-0.012	0.009	0.020	0.033	0.025	0.014	0.023
OPC	0.35	0.177	0.036	0.044	0.046	0.022	0.029	0.024	0.015	0.058	0.008	0.009	0.080	0.016	0.006	0.075
Mortar																
OPC	0.60	0.142	0.026	0.061	0.034	0.025	-0.004	0.018	0.017	0.021	0.006	0.009	0.040	0.012	0.008	0.035
GBFS 50%	0.60	0.148	0.041	0.063	0.055	0.029	-0.040	0.029	0.019	-0.005	0.011	0.011	0.022	0.019	0.008	0.017
GBFS 70%	0.60	0.163	0.043	0.085	0.057	0.036	-0.059	0.030	0.024	-0.020	0.010	0.013	0.010	0.020	0.011	0.004
OPC	0.45	0.108	0.022	0.031	0.035	0.014	0.006	0.019	0.009	0.027	0.007	0.005	0.042	0.010	0.004	0.041
GBFS 50%	0.45	0.116	0.036	0.035	0.050	0.019	-0.024	0.027	0.013	0.006	0.010	0.007	0.028	0.016	0.004	0.025
GBFS 70%	0.45	0.122	0.037	0.052	0.053	0.025	-0.045	0.029	0.016	-0.012	0.011	0.009	0.013	0.017	0.006	0.009
OPC	0.35	0.093	0.021	0.026	0.028	0.013	0.006	0.015	0.009	0.023	0.008	0.005	0.034	0.003	0.003	0.040
GBFS 50%	0.35	0.082	0.027	0.019	0.038	0.010	-0.012	0.020	0.007	0.009	0.008	0.004	0.024	0.012	0.002	0.022
GBFS 70%	0.35	0.084	0.032	0.017	0.044	0.011	-0.020	0.024	0.008	0.004	0.009	0.005	0.022	0.014	0.002	0.019

Table 2. Freezable and adsorbed water contents at different pore ranges according to the different pore models for the carbonated samples.

Mix	w/b	Total water porosity [g/g_{ssd}]	Freezable water [g/g_{ssd}]		Adsorbed water [g/g_{ssd}]											
					Spherical pore model			Cylindrical pore model			Layered pore model			Layered pore model /fine		
			1.5...4 [nm]	>4 [nm]	1.5...4 [nm]	>4 [nm]	<1.5 [nm]	1.5...4 [nm]	>4 [nm]	<1.5 [nm]	1.5...4 [nm]	>4 [nm]	<1.5 [nm]	1.5...4 [nm]	>4 [nm]	<1.5 [nm]
Pastes																
OPC	0.60	0.223	0.018	0.162	0.026	0.051	-0.035	0.014	0.033	-0.004	0.005	0.016	0.021	0.009	0.021	0.013
GBFS 50%	0.60	0.258	0.014	0.220	0.017	0.067	-0.060	0.009	0.043	-0.028	0.003	0.021	0.000	0.007	0.029	-0.011
GBFS 70%	0.60	0.281	0.011	0.230	0.016	0.071	-0.048	0.009	0.045	-0.015	0.003	0.022	0.014	0.006	0.029	0.004
OPC	0.45	0.167	0.024	0.101	0.034	0.035	-0.026	0.018	0.023	0.002	0.007	0.011	0.025	0.011	0.013	0.020
GBFS 50%	0.45	0.192	0.015	0.146	0.021	0.049	-0.039	0.011	0.031	-0.011	0.004	0.015	0.012	0.007	0.017	0.007
GBFS 70%	0.45	0.217	0.011	0.167	0.016	0.054	-0.031	0.008	0.034	-0.004	0.003	0.017	0.019	0.006	0.021	0.012
OPC	0.35	0.139	0.022	0.056	0.031	0.022	0.008	0.017	0.014	0.030	0.006	0.007	0.047	0.010	0.007	0.044
Mortar																
OPC	0.60	0.106	0.012	0.073	0.020	0.024	-0.023	0.011	0.015	-0.005	0.005	0.007	0.009	0.006	0.008	0.007
GBFS 50%	0.60	0.127	0.007	0.098	0.010	0.030	-0.017	0.005	0.019	-0.002	0.002	0.009	0.011	0.003	0.012	0.007
GBFS 70%	0.60	0.136	0.006	0.110	0.010	0.034	-0.024	0.005	0.021	-0.007	0.002	0.010	0.007	0.003	0.013	0.004
OPC	0.45	0.074	0.012	0.048	0.018	0.017	-0.020	0.010	0.011	-0.006	0.004	0.005	0.005	0.006	0.006	0.002
GBFS 50%	0.45	0.085	0.009	0.054	0.015	0.019	-0.013	0.008	0.012	0.001	0.004	0.006	0.012	0.005	0.006	0.011
GBFS 70%	0.45	0.100	0.006	0.074	0.009	0.023	-0.013	0.005	0.015	0.000	0.002	0.007	0.010	0.003	0.009	0.007
OPC	0.35	0.072	0.011	0.030	0.015	0.011	0.005	0.008	0.008	0.016	0.005	0.004	0.022	0.010	0.004	0.017
GBFS 50%	0.35	0.055	0.010	0.024	0.015	0.009	-0.003	0.008	0.006	0.007	0.003	0.003	0.015	0.005	0.003	0.013
GBFS 70%	0.35	0.054	0.006	0.036	0.008	0.012	-0.008	0.004	0.008	0.000	0.001	0.004	0.007	0.003	0.005	0.005

Table 3. Freezable and adsorbed water contents at different pore ranges according to the different pore models for the cycled samples.

Mix	w/b	Total water porosity [g/g_{ssd}]	Freezable water [g/g_{ssd}]		Adsorbed water [g/g_{ssd}]											
					Spherical pore model			Cylindrical pore model			Layered pore model			Layered pore model /fine		
			1.5...4 [nm]	>4 [nm]	1.5...4 [nm]	>4 [nm]	<1.5 [nm]	1.5...4 [nm]	>4 [nm]	<1.5 [nm]	1.5...4 [nm]	>4 [nm]	<1.5 [nm]	1.5...4 [nm]	>4 [nm]	<1.5 [nm]
Pastes																
OPC	0.60	0.253	0.025	0.138	0.038	0.044	0.008	0.020	0.028	0.041	0.008	0.014	0.068	0.011	0.018	0.060
GBFS 50%	0.60	0.246	0.028	0.170	0.040	0.058	-0.050	0.021	0.037	-0.011	0.008	0.019	0.021	0.013	0.021	0.013
GBFS 70%	0.60	0.271	0.025	0.200	0.033	0.067	-0.054	0.018	0.043	-0.015	0.006	0.022	0.018	0.012	0.026	0.007
OPC	0.45	0.200	0.022	0.080	0.034	0.027	0.036	0.018	0.017	0.061	0.007	0.009	0.081	0.010	0.011	0.077
GBFS 50%	0.45	0.204	0.048	0.084	0.069	0.034	-0.030	0.037	0.022	0.013	0.014	0.012	0.047	0.022	0.011	0.040
GBFS 70%	0.45	0.208	0.046	0.119	0.064	0.045	-0.067	0.034	0.030	-0.021	0.012	0.016	0.014	0.021	0.016	0.006
OPC	0.35	0.168	0.018	0.049	0.028	0.017	0.057	0.015	0.011	0.075	0.006	0.006	0.090	0.008	0.007	0.086
Mortar																
OPC	0.60	0.119	0.014	0.057	0.021	0.018	0.009	0.011	0.012	0.025	0.005	0.006	0.038	0.006	0.007	0.035
GBFS 50%	0.60	0.128	0.029	0.062	0.045	0.022	-0.030	0.025	0.014	-0.001	0.010	0.007	0.021	0.012	0.007	0.018
GBFS 70%	0.60	0.123	0.018	0.082	0.027	0.029	-0.033	0.015	0.018	-0.010	0.006	0.009	0.008	0.008	0.009	0.006
OPC	0.45	0.099	0.012	0.040	0.019	0.013	0.015	0.010	0.008	0.028	0.004	0.004	0.038	0.005	0.005	0.036
GBFS 50%	0.45	0.106	0.027	0.027	0.048	0.011	-0.007	0.026	0.007	0.018	0.011	0.003	0.038	0.012	0.003	0.037
GBFS 70%	0.45	0.107	0.041	0.027	0.068	0.012	-0.040	0.038	0.007	-0.005	0.016	0.004	0.021	0.018	0.003	0.019
OPC	0.35	0.083	0.009	0.030	0.015	0.010	0.019	0.008	0.006	0.029	0.003	0.003	0.038	0.005	0.004	0.035
GBFS 50%	0.35	0.066	0.022	0.017	0.034	0.007	-0.014	0.019	0.004	0.004	0.007	0.002	0.017	0.009	0.002	0.015
GBFS 70%	0.35	0.053	0.021	0.009	0.034	0.004	-0.014	0.019	0.002	0.002	0.008	0.001	0.014	0.009	0.001	0.014

Table 4. Specific surface area at different pore ranges according to the different pore models in the different curing methods.

Mix	w/b	Specific surface area [m^2/g] Spherical pore model						Specific surface area [m2/g] Cylindrical pore model						Specific surface area [m2/g] Layered pore model						Specific surface area [m2/g] Layered pore model / fine					
		Rp > 1.5 nm			Rp > 4 nm			Rp > 1.5 nm			Rp > 4 nm			Rp > 1.5 nm			Rp > 4 nm			Rp > 1.5 nm			Rp > 4 nm		
		28	ca	cy	28	ca	cy	28	ca	cy	28	ca	cy	28	ca	cy	28	ca	cy	28	ca	cy	28	ca	cy
Paste																									
OPC	0.60	169	72	94	27	16	13	84	36	47	15	9	8	32	14	17	6	4	3	49	27	31	16	15	14
GBFS 50%	0.60	248	55	108	33	18	23	123	28	54	19	10	13	46	11	21	8	5	6	66	30	34	18	21	16
GBFS 70%	0.60	256	55	96	36	21	25	127	29	49	20	12	14	48	11	19	9	5	6	69	27	36	20	19	20
OPC	0.45	169	87	83	18	14	10	83	43	41	10	8	6	30	16	15	4	3	2	40	25	24	8	10	8
GBFS 50%	0.45	241	64	162	29	20	16	119	33	80	16	12	9	44	13	29	7	5	4	58	21	42	12	12	10
GBFS 70%	0.45	207	52	155	29	18	20	103	27	77	16	11	11	39	11	29	7	5	5	57	21	45	15	14	14
OPC	0.35	110	78	65	12	10	6	54	38	32	7	6	3	20	14	12	3	3	1	30	20	19	7	6	6
Mortar																									
OPC	0.60	86	51	51	12	10	6	43	25	25	7	6	3	16	10	9	3	2	1	25	12	14	8	5	5
GBFS 50%	0.60	133	28	106	16	8	11	66	15	52	9	5	6	24	6	19	4	2	3	35	13	24	8	8	6
GBFS 70%	0.60	139	30	71	18	10	14	69	16	36	10	6	8	26	6	13	4	3	3	38	11	18	10	7	7
OPC	0.45	83	44	46	9	6	4	40	22	22	5	4	3	15	8	8	2	2	1	18	12	11	3	4	3
GBFS 50%	0.45	121	42	112	14	10	7	60	21	54	8	6	4	22	8	19	3	2	2	28	10	21	5	4	2
GBFS 70%	0.45	128	26	155	16	7	9	63	13	75	9	4	5	23	5	27	4	2	2	30	11	30	6	7	3
OPC	0.35	68	37	36	7	5	3	34	18	17	4	3	2	12	7	6	2	1	1	18	11	10	4	4	3
GBFS 50%	0.35	85	37	74	6	4	3	42	18	36	3	2	2	15	7	13	1	1	1	20	9	16	2	3	2
GBFS 70%	0.35	101	22	74	7	5	2	49	11	35	4	3	1	18	4	13	2	1	1	23	7	15	2	3	1

Table 5. Freezable water of LTC-samples

Mix	w/b	Total porosity (w_{105}/g_{ssd})			Total freezable water T>-55 ^{o}C (g/g_{ssd})			Freezable water T>-20 ^{o}C (g/g_{ssd})		
		28 days	carb.	cycled	28 days	carb.	cycled	28 days	carb.	cycled
Paste										
OPC	0.60	0.281	0.223	0.253	0.175	0.181	0.163	0.125	0.162	0.138
GBFS 50%	0.60	0.291	0.258	0.246	0.217	0.233	0.198	0.142	0.220	0.170
GBFS 70%	0.60	0.304	0.281	0.271	0.247	0.241	0.225	0.170	0.230	0.200
OPC	0.45	0.223	0.167	0.200	0.117	0.124	0.103	0.070	0.101	0.080
GBFS 50%	0.45	0.240	0.192	0.204	0.157	0.161	0.132	0.085	0.146	0.084
GBFS 70%	0.45	0.248	0.217	0.208	0.185	0.179	0.165	0.113	0.167	0.119
OPC	0.35	0.177	0.139	0.168	0.080	0.078	0.067	0.044	0.056	0.049
Mortar										
OPC	0.60	0.142	0.106	0.119	0.087	0.085	0.071	0.061	0.073	0.057
GBFS 50%	0.60	0.148	0.127	0.128	0.104	0.105	0.091	0.063	0.098	0.062
GBFS 70%	0.60	0.163	0.136	0.123	0.129	0.117	0.100	0.085	0.110	0.082
OPC	0.45	0.108	0.074	0.099	0.053	0.060	0.052	0.031	0.048	0.040
GBFS 50%	0.45	0.116	0.085	0.106	0.070	0.064	0.055	0.035	0.054	0.027
GBFS 70%	0.45	0.122	0.100	0.107	0.089	0.081	0.068	0.052	0.074	0.027
OPC	0.35	0.093	0.072	0.083	0.047	0.041	0.040	0.026	0.030	0.030
GBFS 50%	0.35	0.082	0.055	0.066	0.046	0.034	0.039	0.019	0.024	0.017
GBFS 70%	0.35	0.084	0.054	0.053	0.049	0.042	0.029	0.017	0.036	0.009

Table 6. Volume of paste porosities in LTC-test at different pore ranges (layered pore model).

		V_p (R_p<1.5 nm)		V_p(1.5>R_p<4nm)		V_p (R_p>4 nm)		V_p (total)	
Mix	w/b	Paste	Mortar	Paste	Mortar	Paste	Mortar	Paste	Mortar
28 days									
OPC	0.60	0.139	0.130	0.113	0.105	0.265	0.228	0.517	0.463
GBFS 50%	0.60	0.060	0.072	0.171	0.165	0.300	0.239	0.531	0.477
GBFS 70%	0.60	0.021	0.033	0.175	0.170	0.352	0.310	0.548	0.513
OPC	0.45	0.159	0.160	0.122	0.111	0.159	0.135	0.441	0.406
GBFS 50%	0.45	0.092	0.105	0.175	0.169	0.197	0.157	0.465	0.430
GBFS 70%	0.45	0.063	0.047	0.155	0.176	0.253	0.224	0.470	0.448
OPC	0.35	0.169	0.142	0.093	0.123	0.113	0.130	0.375	0.395
GBFS 50%	0.35		0.104		0.149		0.097		0.349
GBFS 70%	0.35		0.091		0.171		0.093		0.355
carbonated									
OPC	0.60	0.041	0.031	0.047	0.056	0.349	0.273	0.437	0.360
GBFS 50%	0.60	0.001	0.036	0.031	0.029	0.454	0.353	0.486	0.418
GBFS 70%	0.60	0.025	0.023	0.027	0.028	0.460	0.393	0.512	0.444
OPC	0.45	0.053	0.019	0.065	0.062	0.238	0.209	0.356	0.290
GBFS 50%	0.45	0.024	0.046	0.039	0.050	0.326	0.230	0.389	0.326
GBFS 70%	0.45	0.037	0.039	0.029	0.031	0.364	0.309	0.430	0.379
OPC	0.35	0.105	0.095	0.062	0.069	0.141	0.148	0.309	0.312
GBFS 50%	0.35		0.064		0.060		0.116		0.241
GBFS 70%	0.35		0.031		0.032		0.174		0.237
cycled									
OPC	0.60	0.127	0.127	0.062	0.060	0.286	0.211	0.476	0.398
GBFS 50%	0.60	0.041	0.068	0.068	0.126	0.358	0.225	0.466	0.420
GBFS 70%	0.60	0.034	0.028	0.057	0.078	0.410	0.299	0.501	0.404
OPC	0.45	0.164	0.146	0.059	0.061	0.179	0.169	0.403	0.375
GBFS 50%	0.45	0.093	0.140	0.124	0.142	0.192	0.114	0.410	0.397
GBFS 70%	0.45	0.028	0.077	0.114	0.209	0.263	0.114	0.404	0.400
OPC	0.35	0.191	0.160	0.051	0.052	0.115	0.141	0.358	0.353
GBFS 50%	0.35		0.073		0.127		0.086		0.287
GBFS 70%	0.35		0.063		0.124		0.043		0.230

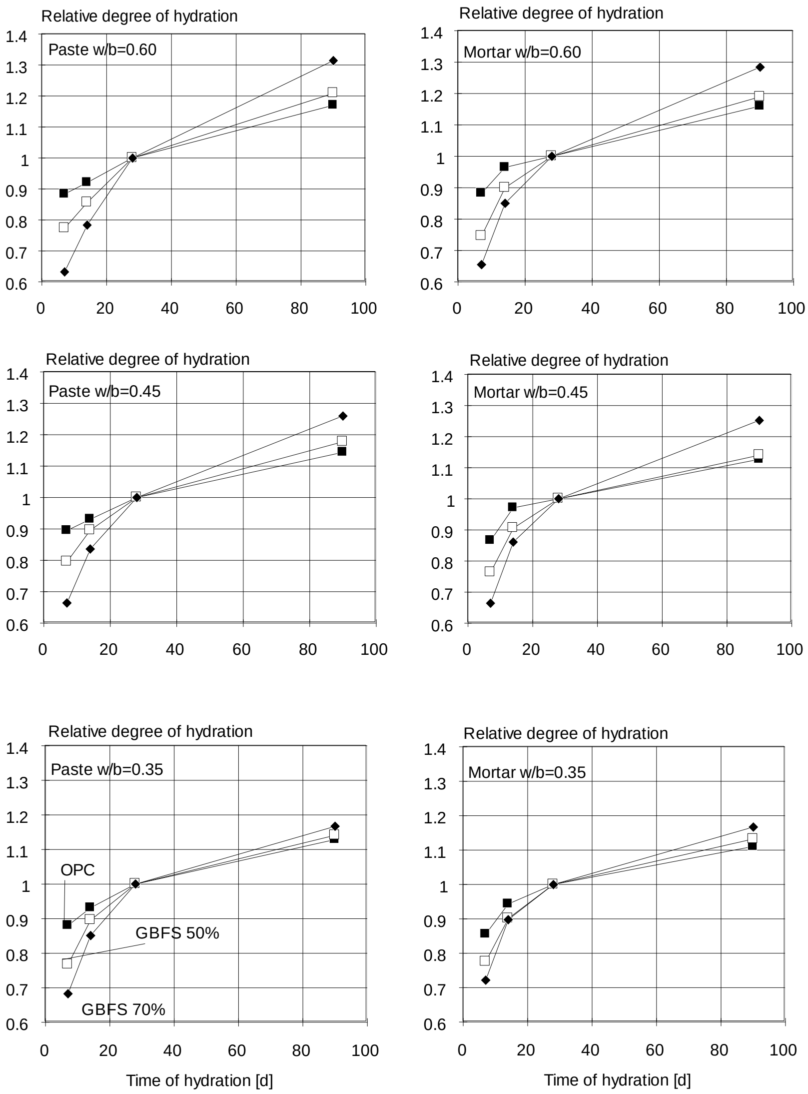

Fig. K1. The relative degree of hydration, α_t/α_{28} as a function of hydration time.

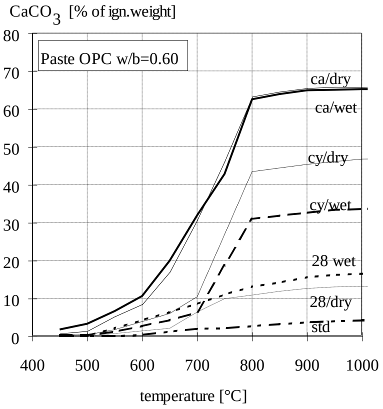
CaCO3 [% of ign.weight]
Paste OPC w/b=0.60
ca/dry
ca/wet
cy/dry
cy/wet
28 wet
28/dry
std
0
10
20
30
40
50
60
70
80
400
500
600
700
800
900
1000
temperature [°C]

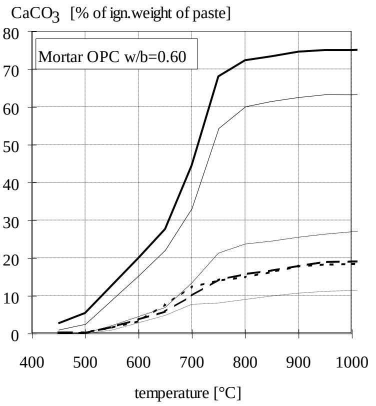
CaCO3 [% of ign.weight of paste]
Mortar OPC w/b=0.60
0
10
20
30
40
50
60
70
80
400
500
600
700
800
900
1000
temperature [°C]

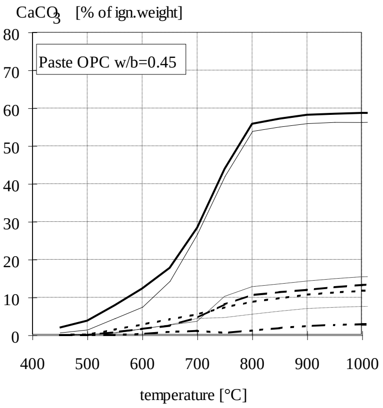
CaCO3 [% of ign.weight]
Paste OPC w/b=0.45
0
10
20
30
40
50
60
70
80
400
500
600
700
800
900
1000
temperature [°C]

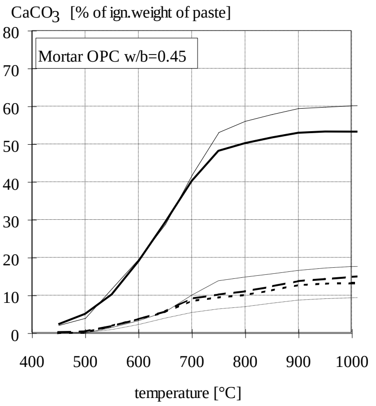
CaCO3 [% of ign.weight of paste]
Mortar OPC w/b=0.45
0
10
20
30
40
50
60
70
80
400
500
600
700
800
900
1000
temperature [°C]

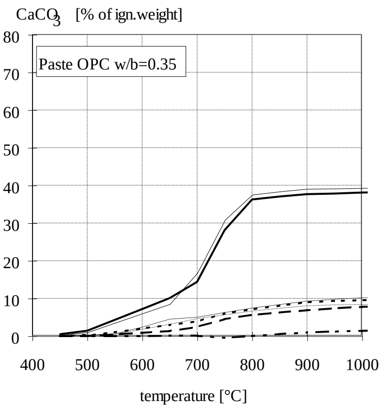
CaCO3 [% of ign.weight]
Paste OPC w/b=0.35
0
10
20
30
40
50
60
70
80
400
500
600
700
800
900
1000
temperature [°C]

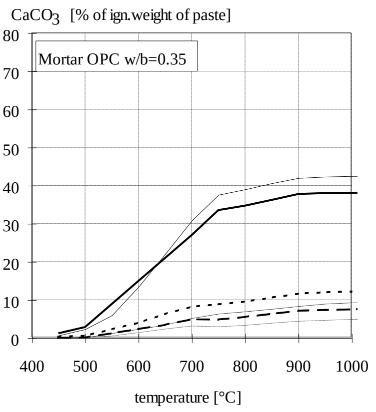
CaCO3 [% of ign.weight of paste]
Mortar OPC w/b=0.35
0
10
20
30
40
50
60
70
80
400
500
600
700
800
900
1000
temperature [°C]

Fig. K2. Cumulative decomposition of carbonates in OPC pastes and OPC mortars in the TG+EGA test.

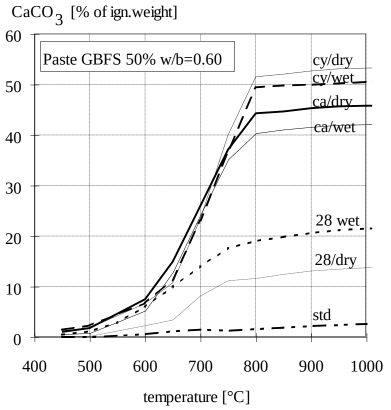
CaCO3 [% of ign.weight]
Paste GBFS 50% w/b=0.60
cy/dry
cy/wet
ca/dry
ca/wet
28 wet
28/dry
std
0
10
20
30
40
50
60
400
500
600
700
800
900
1000
temperature [°C]

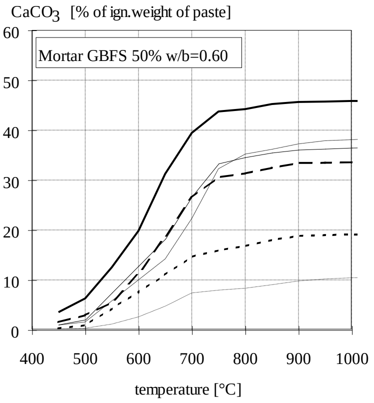
CaCO3 [% of ign.weight of paste]
Mortar GBFS 50% w/b=0.60
0
10
20
30
40
50
60
400
500
600
700
800
900
1000
temperature [°C]

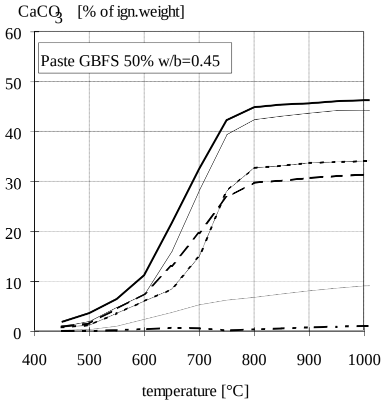
CaCO3 [% of ign.weight]
Paste GBFS 50% w/b=0.45
0
10
20
30
40
50
60
400
500
600
700
800
900
1000
temperature [°C]

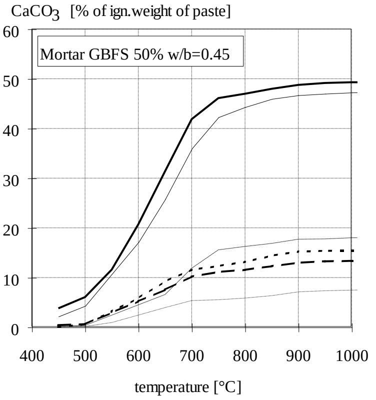
CaCO3 [% of ign.weight of paste]
Mortar GBFS 50% w/b=0.45
0
10
20
30
40
50
60
400
500
600
700
800
900
1000
temperature [°C]

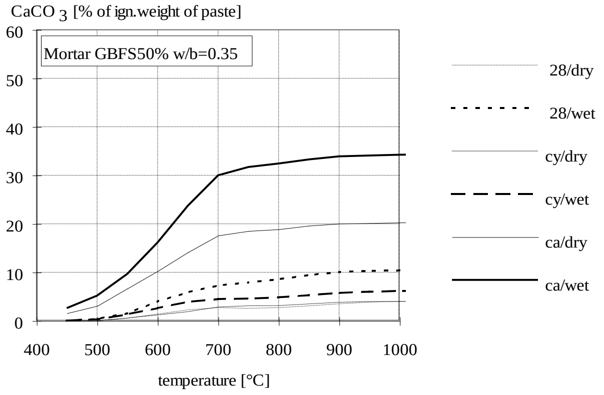
CaCO 3 [% of ign.weight of paste]
Mortar GBFS50% w/b=0.35
0
10
20
30
40
50
60
400
500
600
700
800
900
1000
temperature [°C]
28/dry
28/wet
cy/dry
cy/wet
ca/dry
ca/wet

Fig. K3. Cumulative decomposition of carbonates in GBFS 50% pastes and mortars in the TG+EGA test.

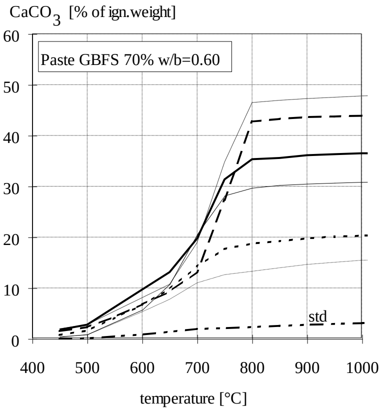
CaCO$_3$ [% of ign.weight]
Paste GBFS 70% w/b=0.60
std
0
10
20
30
40
50
60
400
500
600
700
800
900
1000
temperature [°C]

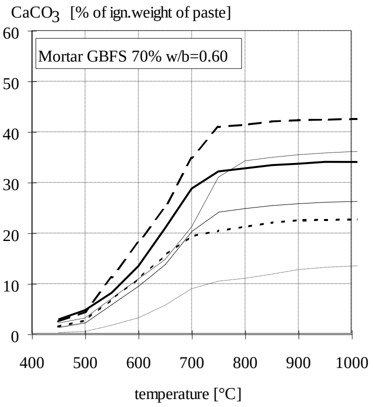
CaCO$_3$ [% of ign.weight of paste]
Mortar GBFS 70% w/b=0.60
0
10
20
30
40
50
60
400
500
600
700
800
900
1000
temperature [°C]

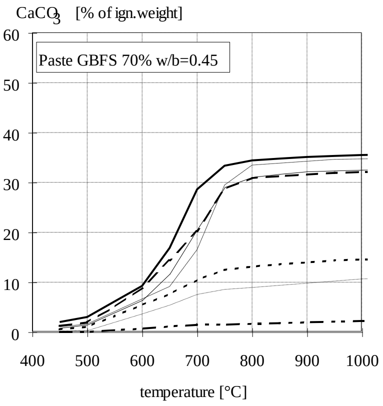
CaCO$_3$ [% of ign.weight]
Paste GBFS 70% w/b=0.45
0
10
20
30
40
50
60
400
500
600
700
800
900
1000
temperature [°C]

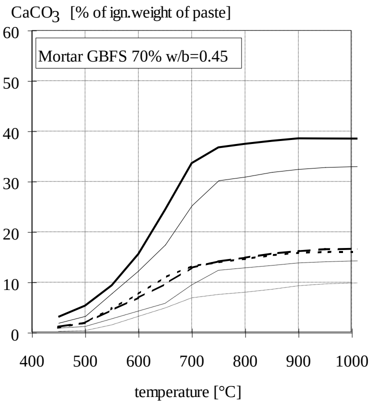
CaCO$_3$ [% of ign.weight of paste]
Mortar GBFS 70% w/b=0.45
0
10
20
30
40
50
60
400
500
600
700
800
900
1000
temperature [°C]

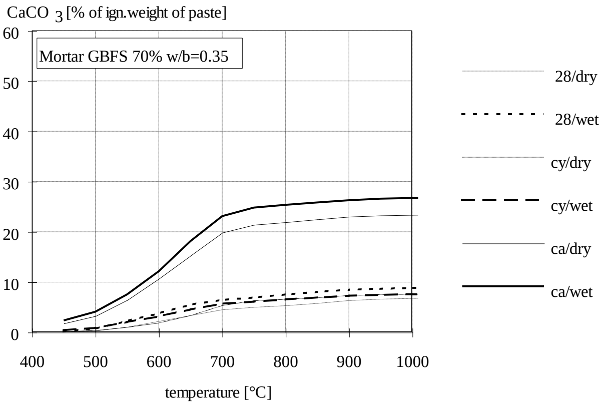
CaCO$_3$ [% of ign.weight of paste]
Mortar GBFS 70% w/b=0.35
0
10
20
30
40
50
60
400
500
600
700
800
900
1000
temperature [°C]
28/dry
28/wet
cy/dry
cy/wet
ca/dry
ca/wet

Fig. 4K. Cumulative decomposition of carbonates in GBFS 70% pastes and mortars in the TG+EGA test.

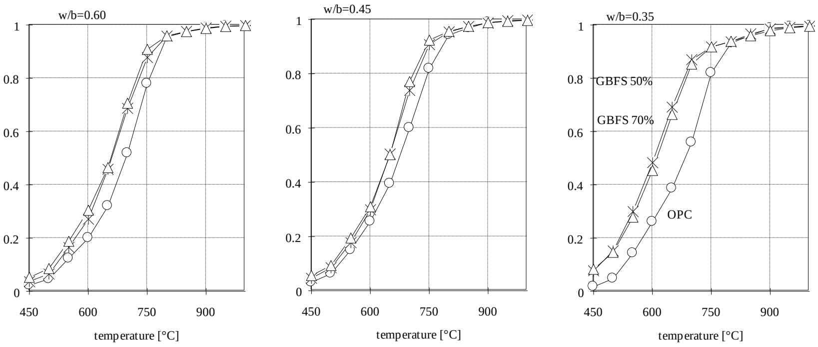

Fig. K5. Relative decomposition of carbonates for varyinf slag contents cured by the procedure "carbonated".

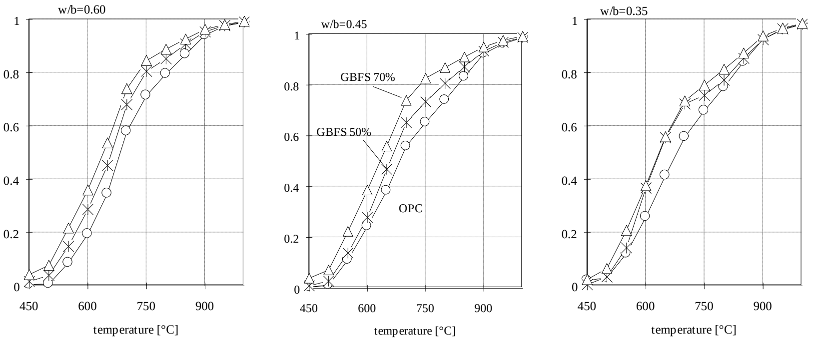

Fig. K6. Relative decomposition of carbonates for varyinf slag contents cured by the procedure "28 days".

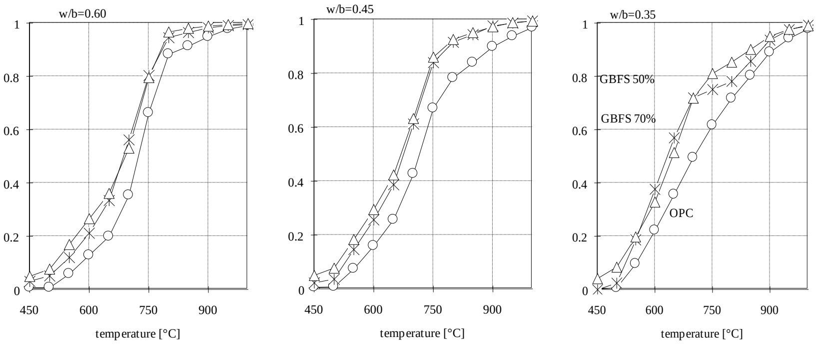

Fig. K7. Relative decomposition of carbonates for varyinf slag contents cured by the procedure "cycled".

Table 1. Results of the TG+EGA test, OPC, w/b=0.60.

	OPC, paste, w/b=0.60							OPC, mortar, w/b=0.60					
	28 d/ dry	28 d/ wet	std	cy / dry	cy/ wet	ca / dry	ca / wet	28 d/ dry	28 d/ wet	cy / dry	cy/ wet	ca / dry	ca / wet
CO_2-gas [% of ignited weight]													
T<500°C	0.03	0.07	0.00	0.16	0.14	0.64	1.45	-0.03	0.12	0.01	0.07	1.13	2.39
500°C<T<650°C	0.91	2.78	0.54	2.48	1.76	6.89	7.31	2.13	3.26	3.03	2.49	8.69	9.83
650°C<T<800°C	3.90	2.98	0.68	16.51	11.93	20.44	18.72	1.88	3.26	7.47	4.43	16.77	19.76
T>800°C	1.03	1.52	0.67	1.47	1.17	1.12	1.18	1.05	1.55	1.45	1.48	1.40	1.19
Total	5.87	7.36	1.89	20.62	14.99	29.08	28.66	5.03	8.18	11.95	8.47	27.99	33.17
origin from carb. of CH	1.99	2.27		7.42	5.89	7.24	7.24	2.06	4.24	3.39	3.87	7.33	7.33
origin from carb. of hydrates	2.85	3.56		11.73	7.93	20.72	20.24	1.92	2.39	7.12	3.12	19.26	24.65
$H_2$0-gas [% of ignited weight]													
110°C<T<1100°C	12.76	13.78	14.75	8.40	10.99	4.75	6.39	12.47	13.24	12.78	12.56	4.13	4.99
110°C<T<160°C	1.49	2.10	1.29	1.01	1.85	0.54	1.03	1.43	1.84	1.15	1.86	0.43	0.97
160°C<T<220°C	1.89	2.20	1.62	1.34	2.21	0.85	1.55	1.60	2.28	1.64	1.83	0.75	1.45
origin from CH	2.10	1.99	3.30	0.00	0.63	0.00	0.00	2.15	1.26	1.75	1.55	0.00	0.00
220°C<T<1100°C (CSH)	7.28	7.50	8.53	6.05	6.30	3.36	3.81	7.28	7.86	8.24	7.32	2.95	2.57
Total	16.28	23.52	17.57	11.13	17.48	6.70	9.41	17.05	19.18	15.54	18.91	5.14	7.62
Calcium hydroxide [% of ignited weight]													
Related to deg. of hydration	11.99		13.57	12.48		12.18		12.32		12.89		12.33	
Measured	8.64	8.17	13.57	0.00	2.58	0.00	0.00	8.85	5.18	7.18	6.38	0.00	0.00
SO_2-gas [% of ignited weight]													
Total	0.42	0.00	0.00	1.02	1.11	0.17	0.82	0.73	1.53	1.90	1.38	2.10	2.15
Degree of hydration	0.70		0.79	0.73		0.71		0.72		0.75		0.72	

Table 2. Results of the TG+EGA test, OPC, w/b=0.45.

	OPC, paste, w/b=0.45							OPC, mortar, w/b=0.45					
	28 d/ dry	28 d/ wet	std	cy / dry	cy/ wet	ca / dry	ca / wet	28 d/ dry	28 d/ wet	cy / dry	cy/ wet	ca / dry	ca / wet
CO_2-gas [% of ignited weight]													
T<500°C	0.04	0.06	0.00	0.04	0.00	0.66	1.68	0.08	0.07	0.00	0.21	1.78	2.23
500°C<T<650°C	1.19	1.80	0.40	1.15	1.16	5.69	6.12	1.70	2.37	2.46	2.49	10.98	10.64
650°C<T<800°C	1.23	2.07	0.17	4.51	3.70	17.55	16.73	1.36	2.03	4.08	2.51	12.07	9.20
T>800°C	0.91	1.29	0.75	1.17	1.22	1.04	1.25	1.07	1.37	1.23	1.77	1.80	1.34
Total	3.38	5.21	1.31	6.86	6.09	24.95	25.79	4.20	5.84	7.77	6.97	26.63	23.41
origin from carb. of CH	1.80	2.68		2.63	2.53	6.91	6.91	1.80	3.80	2.65	3.53	7.03	7.03
origin from carb. of hydrates	0.66	1.24		3.07	2.33	17.00	17.63	1.34	0.66	3.89	1.68	17.80	15.04
$H_2$0-gas [% of ignited weight]													
110°C<T<1100°C	11.59	11.46	12.86	12.09	11.53	5.04	4.26	10.94	13.29	10.69	12.07	4.73	4.98
110°C<T<160°C	1.18	1.67	1.02	1.33	1.72	0.42	1.54	1.98	1.93	1.19	1.74	0.40	0.92
160°C<T<220°C	1.72	1.85	1.42	1.68	1.89	0.69	0.67	0.52	2.10	1.31	2.19	0.86	1.48
origin from CH	1.99	1.64	3.05	1.81	1.85	0.00	0.00	2.01	1.19	1.65	1.29	0.00	0.00
220°C<T<1100°C (CSH)	6.70	6.30	7.36	7.27	6.07	3.93	2.05	6.42	8.07	6.55	6.85	3.47	2.58
Total	15.43	17.75	15.53	16.07	17.09	5.98	6.38	15.05	19.28	13.15	18.31	5.93	7.82
Calcium hydroxide [% of ignited weight]													
Related to deg. of hydration	11.23		12.55	11.88		11.62		11.30		11.22		11.83	
Measured	8.20	6.72	12.55	7.46	7.62	0.00	0.00	8.28	4.90	6.77	5.28	0.00	0.00
SO_2-gas [% of ignited weight]													
Total	0.99	0.70	0.70	0.80	1.67	0.60	0.62	1.19	1.65	1.42	1.90	1.88	1.66
Degree of hydration	0.61		0.68	0.64		0.63		0.61		0.61		0.64	

Table 3. Results of the TG+EGA test, OPC, w/b=0.35.

	OPC, paste, w/b=0.35							OPC, mortar, w/b=0.35					
	28 d/ dry	28 d/ wet	std	cy / dry	cy/ wet	ca / dry	ca / wet	28 d/ dry	28 d/ wet	cy / dry	cy/ wet	ca / dry	ca / wet
CO_2-gas [% of ignited weight]													
T<500°C	0.13	0.05	0.01	0.04	0.00	0.45	0.62	0.05	0.26	0.01	0.05	1.03	1.26
500°C<T<650°C	1.26	1.25	0.03	1.95	0.59	3.32	3.82	1.01	2.58	1.47	1.55	8.68	7.98
650°C<T<800°C	1.57	1.83	0.05	1.31	1.96	12.84	11.59	0.43	1.47	1.56	0.94	7.45	6.06
T>800°C	0.79	1.06	0.70	1.21	0.98	0.78	0.82	0.70	1.20	1.05	0.92	1.52	1.48
Total	3.75	4.19	0.68	4.51	3.53	17.39	16.85	2.19	5.52	4.09	3.46	18.68	16.78
origin from carb. of CH	1.87	2.09		2.65	2.03	5.47	5.47	1.29	2.94	1.54	1.08	5.76	5.76
origin from carb. of hydrates	1.09	1.04		0.65	0.53	11.14	10.56	0.20	1.38	1.50	1.46	11.39	9.53
H_20-gas [% of ignited weight]													
110°C<T<1100°C	9.04	9.53	10.88	11.00	11.78	5.39	6.46	10.17	10.58	10.17	12.72	6.31	6.74
110°C<T<160°C	1.14	1.52	0.87	1.21	1.55	0.56	0.97	1.01	1.25	0.78	1.89	0.53	0.79
160°C<T<220°C	1.53	1.72	1.62	1.36	1.87	0.72	1.41	1.11	1.60	0.92	1.46	0.82	1.39
origin from CH	1.23	1.14	2.27	1.31	1.57	0.00	0.00	1.51	0.84	1.52	1.70	0.00	0.00
220°C<T<1100°C (CSH)	5.14	5.15	6.13	7.12	6.80	4.12	4.08	6.54	6.89	6.94	7.67	4.96	4.56
Total	12.31	14.21	13.15	14.54	16.60	6.52	9.74	13.66	15.28	12.07	17.93	7.76	9.64
Calcium hydroxide [% of ignited weight]													
Related to deg. of hydration	8.20		9.31	9.85		9.21		8.39		8.82		9.69	
Measured	5.04	4.68	9.31	5.40	6.44	0.00	0.00	6.22	3.45	6.24	7.00	0.00	0.00
SO_2-gas [% of ignited weight]													
Total	0.37	0.65	0.84	0.70	1.03	0.32	0.80	1.01	2.27	1.74	2.03	2.25	1.85
Degree of hydration	0.52		0.59	0.62		0.58		0.53		0.56		0.61	

Table 4. Results of the TG+EGA test, GBFS 50%, w/b=0.60.

	GBFS 50%, paste, w/b=0.45							GBFS 50, mortar, w/b=0.45					
	28 d/ dry	28 d/ wet	std	cy / dry	cy/ wet	ca / dry	ca / wet	28 d/ dry	28 d/ wet	cy / dry	cy/ wet	ca / dry	ca / wet
CO_2-gas [% of ignited weight]													
T<500°C	0.06	0.50	0.01	0.81	1.01	0.37	0.79	0.15	0.42	0.72	1.30	0.93	2.77
500°C<T<650°C	1.43	3.89	0.50	3.94	4.01	5.32	5.77	1.98	4.47	5.63	6.94	7.16	10.96
650°C<T<800°C	3.66	4.01	0.21	18.01	16.69	12.16	12.89	1.60	2.56	9.36	5.61	7.21	5.69
T>800°C	0.94	1.09	0.45	0.76	0.46	0.77	0.66	0.93	1.02	1.29	0.98	0.84	0.72
Total	6.09	9.49	1.17	23.52	22.17	18.63	20.11	4.67	8.49	16.99	14.83	16.14	20.14
origin from carb. of CH	1.58	2.37		3.16	3.16	2.58	2.58	0.08	2.57	3.40	3.40	3.09	3.09
origin from carb. of hydrates	3.57	6.03		19.60	18.55	15.28	16.87	3.66	4.89	12.30	10.45	12.21	16.32
H_20-gas [% of ignited weight]													
110°C<T<1100°C	7.42	7.09	9.80	5.67	7.50	4.88	4.80	8.52	7.13	7.61	7.64	4.34	6.19
110°C<T<160°C	1.00	1.62	0.92	0.90	1.17	0.62	0.79	0.70	1.32	1.30	1.30	0.35	0.77
160°C<T<220°C	1.38	1.79	1.37	1.38	1.08	0.78	1.22	0.89	1.69	2.39	2.40	0.58	1.19
origin from CH	0.32	0.00	1.25	0.00	0.00	0.00	0.00	1.02	0.00	0.00	0.00	0.00	0.00
220°C<T<1100°C (CSH)	4.72	3.68	6.25	3.39	5.24	3.48	2.80	5.91	4.12	3.92	3.94	3.42	4.23
Total	10.49	12.40	12.03	7.28	13.32	6.01	6.49	10.60	11.44	9.70	12.97	5.47	8.66
Calcium hydroxide [% of ignited weight]													
Related to deg. of hydration	3.98		5.15	5.31		4.34		4.32		5.72		5.20	
Measured	1.32	0.00	5.15	0.00	0.00	0.00	0.00	4.19	0.00	0.00	0.00	0.00	0.00
SO_2-gas [% of ignited weight]													
Total	0.74	0.43	0.08	0.93	0.07	1.32	0.26	1.20	1.19	1.33	1.38	0.90	1.23
Degree of hydration	0.50		0.64	0.66		0.54		0.54		0.71		0.65	

Table 5. Results of the TG+EGA test, GBFS 50%, w/b=0.45.

	GBFS 50%, paste, w/b=0.45							GBFS 50, mortar, w/b=0.45					
	28 d/ dry	28 d/ wet	std	cy / dry	cy/ wet	ca / dry	ca / wet	28 d/ dry	28 d/ wet	cy / dry	cy/ wet	ca / dry	ca / wet
CO_2-gas [% of ignited weight]													
T<500°C	0.13	0.11	0.00	0.51	0.68	0.90	1.58	0.08	0.26	0.16	0.28	1.92	2.67
500°C<T<650°C	1.55	1.76	0.30	3.19	5.08	6.22	7.91	1.70	3.82	2.74	3.06	9.49	11.11
650°C<T<800°C	1.37	2.71	0.00	10.74	7.37	11.64	10.19	0.86	1.75	4.26	1.79	8.16	6.86
T>800°C	1.04	0.83	0.33	0.60	0.70	0.79	0.62	0.72	1.01	0.77	0.80	1.30	1.01
Total	4.09	5.40	0.48	15.04	13.82	19.54	20.30	3.35	6.84	7.94	5.94	20.88	21.65
origin from carb. of CH	0.71	1.23		2.86	2.86	2.58	2.58	0.14	2.51	2.24	2.85	3.13	3.13
origin from carb. of hydrates	2.34	3.34		11.58	10.26	16.17	17.10	2.49	3.31	4.92	2.29	16.46	17.52
$H_2$0-gas [% of ignited weight]													
110°C<T<1100°C	8.53	8.75	10.23	7.07	7.96	4.35	4.80	9.28	8.49	10.37	11.18	4.87	6.30
110°C<T<160°C	1.33	1.86	0.98	1.01	1.65	0.52	1.15	0.81	1.84	1.12	1.26	0.43	0.92
160°C<T<220°C	1.58	2.26	1.63	1.18	1.65	0.84	1.44	0.95	2.83	1.16	2.34	0.76	1.39
origin from CH	0.66	0.45	1.20	0.00	0.00	0.00	0.00	0.97	0.00	0.38	0.13	0.00	0.00
220°C<T<1100°C (CSH)	4.96	4.18	6.42	4.89	4.65	2.99	2.22	6.54	3.82	7.72	7.46	3.68	3.99
Total	11.67	13.89	12.54	8.94	12.41	5.43	7.00	12.01	13.48	12.74	16.26	6.11	8.85
Calcium hydroxide [% of ignited weight]													
Related to deg. of hydration	3.93		4.94	4.81		4.34		4.22		5.32		5.26	
Measured	2.73	1.85	4.94	0.00	0.00	0.00	0.00	3.99	0.00	1.55	0.52	0.00	0.00
SO_2-gas [% of ignited weight]													
Total	1.68	0.84	0.09	0.58	0.39	1.43	1.09	1.50	1.58	1.65	1.32	1.38	0.70
Degree of hydration	0.49		0.62	0.60		0.54		0.53		0.66		0.66	

Table 6. Results of the TG+EGA test, GBFS 70%, w/b=0.60.

	GBFS 70%, paste, w/b=0.60							GBFS 70, mortar, w/b=0.60					
	28 d/ dry	28 d/ wet	std	cy / dry	cy/ wet	ca / dry	ca / wet	28 d/ dry	28 d/ wet	cy / dry	cy/ wet	ca / dry	ca / wet
CO_2-gas [% of ignited weight]													
T<500°C	0.31	0.66	0.02	1.21	1.01	0.39	1.18	0.22	1.15	1.38	1.88	1.00	2.02
500°C<T<650°C	2.91	3.42	0.39	3.42	3.09	4.22	4.40	2.14	5.41	4.94	8.80	4.90	6.88
650°C<T<800°C	2.30	3.71	0.28	15.42	14.44	8.07	9.47	2.19	2.37	8.35	7.01	4.69	5.03
T>800°C	0.90	0.65	0.24	0.57	0.34	0.49	0.49	1.00	0.61	0.77	0.48	0.58	0.54
Total	6.42	8.44	0.93	20.61	18.87	13.16	15.54	5.55	9.53	15.45	18.16	11.17	14.47
origin from carb. of CH	0.60	0.60		0.84	0.74	0.65	0.60	0.04	0.67	0.95	0.95	0.68	0.68
origin from carb. of hydrates	4.92	7.20		19.21	17.80	12.02	14.45	4.52	8.25	13.73	16.73	9.91	13.25
$H_2$0-gas [% of ignited weight]													
110°C<T<1100°C	5.48	5.73	7.50	5.10	6.97	4.93	4.24	6.94	6.02	5.77	8.44	4.17	5.34
110°C<T<160°C	0.85	1.08	0.71	0.69	0.98	0.52	0.75	0.69	1.34	0.55	0.84	0.34	0.41
160°C<T<220°C	1.30	1.24	1.02	0.80	0.74	0.80	1.19	1.02	1.76	0.83	1.14	0.56	0.64
origin from CH	0.00	0.00	0.39	0.00	0.04	0.00	0.02	0.26	0.00	0.00	0.00	0.00	0.00
220°C<T<1100°C (CSH)	3.34	3.41	5.39	3.61	5.21	3.61	2.28	4.97	2.92	4.39	6.47	3.27	4.29
Total	7.90	10.48	9.35	6.40	10.83	6.06	6.31	9.44	10.54	7.22	12.01	5.14	6.95
Calcium hydroxide [% of ignited weight]													
Related to deg. of hydration	1.00		1.59	1.41		1.10		1.13		1.59		1.15	
Measured	0.00	0.00	1.59	0.00	0.17	0.00	0.09	1.07	0.00	0.00	0.00	0.00	0.00
SO_2-gas [% of ignited weight]													
Total	1.75	0.97	1.30	0.39	0.70	2.03	0.88	1.25	0.75	0.20	0.12	0.77	0.54
Degree of hydration	0.39		0.62	0.55		0.43		0.44		0.62		0.45	

Table 7. Results of the TG+EGA test, GBFS 70%, w/b=0.45.

	GBFS 70%, paste, w/b=0.45							GBFS 70, mortar, w/b=0.45					
	28 d/ dry	28 d/ wet	std	cy / dry	cy/ wet	ca / dry	ca / wet	28 d/ dry	28 d/ wet	cy / dry	cy/ wet	ca / dry	ca / wet
CO_2-gas [% of ignited weight]													
T<500°C	0.11	0.43	0.01	0.69	0.83	0.65	1.30	0.15	0.81	0.50	0.82	1.42	2.29
500°C<T<650°C	2.06	2.69	0.27	3.21	5.25	4.37	5.92	1.79	3.70	1.89	3.18	6.06	8.12
650°C<T<800°C	1.43	2.25	0.13	10.36	7.00	8.27	7.51	1.25	1.51	2.90	2.18	5.76	5.58
T>800°C	0.69	0.58	0.14	0.54	0.52	0.62	0.47	0.73	0.59	0.56	0.72	0.87	0.45
Total	4.30	5.95	0.54	14.80	13.60	13.91	15.20	3.93	6.61	5.85	6.90	14.12	16.43
origin from carb. of CH	0.64	0.78		1.00	0.79	0.83	0.83	0.04	0.88	1.23	1.23	0.98	0.98
origin from carb. of hydrates	2.96	4.59		13.27	12.29	12.46	13.89	3.16	5.14	4.06	4.95	12.27	15.01
H_20-gas [% of ignited weight]													
110°C<T<1100°C	6.42	6.45	7.93	5.57	6.96	4.01	4.52	5.84	7.02	9.32	8.91	3.74	4.08
110°C<T<160°C	0.97	1.25	0.83	0.76	0.99	0.48	0.81	0.56	1.15	0.75	2.29	0.41	0.66
160°C<T<220°C	1.24	1.40	1.05	1.50	1.23	0.70	0.64	0.93	1.39	0.96	0.87	0.58	0.97
origin from CH	0.06	0.00	0.48	0.00	0.09	0.00	0.00	0.35	0.00	0.00	0.00	0.00	0.00
220°C<T<1100°C (CSH)	4.15	3.80	5.57	3.31	4.66	2.84	3.07	4.01	4.48	7.61	5.74	2.75	2.45
Total	9.14	11.00	9.79	7.04	10.62	4.96	6.36	7.55	11.08	11.51	14.41	4.88	6.31
Calcium hydroxide [% of ignited weight]													
Related to deg. of hydration	1.31		1.98	1.68		1.40		1.49		2.07		1.65	
Measured	0.23	0.00	1.98	0.00	0.35	0.00	0.00	1.42	0.00	0.00	0.00	0.00	0.00
SO_2-gas [% of ignited weight]													
Total	2.17	0.97	1.05	1.51	0.66	1.61	1.47	1.02	0.71	0.68	0.84	1.46	1.21
Degree of hydration	0.40		0.59	0.50		0.42		0.45		0.62		0.50	

Table 8. Results of the TG+EGA test, GBFS 50% and GBFS 70%, w/b=0.35.

	GBFS 50%, mortar w/b=0.35							GBFS 70%, mortar w/b=0.35						
	28 d/ dry	28 d/ wet	cy / dry	cy/ wet	ca / dry	ca / wet	std	28 d/ dry	28 d/ wet	cy / dry	cy/ wet	ca / dry	ca / wet	std
CO_2-gas [% of ignited weight]														
T<500°C	0.04	0.18	0.02	0.13	1.39	2.30	0.00	0.11	0.29	0.15	0.35	1.39	1.74	0.03
500°C<T<650°C	0.98	2.45	0.86	1.61	4.88	8.19	0.46	1.17	1.87	1.14	1.41	5.08	5.96	0.62
650°C<T<800°C	0.21	1.21	0.56	0.40	2.09	3.85	0.04	0.76	0.79	1.26	0.76	2.80	3.06	0.47
T>800°C	0.57	0.81	0.37	0.59	0.61	0.80	0.59	0.56	0.50	0.39	0.41	0.62	0.58	0.49
Total	1.80	4.65	1.81	2.74	8.97	15.14	1.08	2.59	3.45	2.94	2.93	9.88	11.34	1.61
origin from carb. of CH	0.03	1.68	0.05	0.54	1.68	1.68		0.11	0.72	0.40	0.56	0.78	0.78	
origin from carb. of hydrates	1.20	2.16	1.34	1.62	6.67	12.65		1.93	2.23	2.15	1.96	8.49	9.98	
H_20-gas [% of ignited weight]														
110°C<T<1100°C	7.84	7.19	6.21	8.15	3.35	4.13	9.45	6.11	6.88	4.76	4.86	4.55	4.07	7.46
110°C<T<160°C	0.79	1.26	0.63	1.15	0.31	0.64	1.12	0.42	0.98	0.53	0.79	0.43	0.49	0.94
160°C<T<220°C	0.90	1.64	0.88	1.15	0.47	1.13	1.14	0.87	1.21	0.64	1.04	0.62	0.66	1.06
origin from CH	0.70	0.02	0.22	0.02	0.00	0.00	0.97	0.25	0.00	0.07	0.00	0.00	0.00	0.34
220°C<T<1100°C (CSH)	5.46	4.26	4.48	5.84	2.58	2.35	6.21	4.57	4.69	3.52	3.03	3.50	2.91	5.12
Total	9.95	10.93	7.82	12.22	4.29	6.13	11.84	8.05	10.59	6.04	7.25	5.64	5.68	9.45
Calcium hydroxide [% of ignited weight]														
Related to deg. of hydration	2.93		0.99		2.83			1.21		0.94		1.31		
Measured	2.88	0.10	0.90	0.09	0.00	0.00	3.98	1.03	0.00	0.27	0.00	0.00	0.00	1.41
SO_2-gas [% of ignited weight]														
Total	1.02	1.41	0.67	1.08	0.61	0.93	1.55	0.56	1.10	0.26	0.89	0.49	0.80	1.77
Degree of hydration	0.45		0.43		0.43		0.60	0.52		0.41		0.57		0.73

APPENDIX M

Volume fractions of phases (% of paste volume) in LTC samples calculated according to the results of the TG+EGA test

Binder	w/b	slag%	DH	DC	V(unhyd)	V($CaCO_3$)	V(CH)	V(CSH)	V(pore)
Paste "28 days"									
OPC	0.60	0	0.70	0.20	10.0	6.5	3.9	27.9	51.7
OPC	0.45	0	0.61	0.17	15.7	5.5	3.8	30.8	44.1
OPC	0.35	0	0.52	0.16	22.4	5.1	3.1	31.9	37.5
GBFS 50%	0.60	50	0.50	0.41	17.8	8.6	0.0	20.5	53.1
GBFS 70%	0.60	70	0.39	0.48	21.9	7.7	0.0	15.6	54.8
GBFS 50%	0.45	50	0.49	0.23	21.0	5.7	1.1	25.8	46.5
GBFS 70%	0.45	70	0.40	0.33	25.2	6.3	0.0	21.5	47.0
Mortar "28 days"									
OPC	0.60	0	0.72	0.22	10.3	7.9	2.7	31.5	47.7
OPC	0.45	0	0.61	0.19	16.4	6.5	2.9	32.6	41.6
OPC	0.35	0	0.53	0.20	21.0	6.5	2.2	30.6	39.7
GBFS 50%	0.60	50	0.54	0.33	17.7	8.4	0.0	24.1	49.9
GBFS 70%	0.60	70	0.44	0.48	20.6	8.9	0.0	17.8	52.7
GBFS 50%	0.45	50	0.53	0.28	20.3	7.6	0.0	28.0	44.2
GBFS 70%	0.45	70	0.45	0.33	24.1	7.3	0.0	22.7	45.9
GBFS 50%	0.35	50	0.45	0.22	27.5	6.0	0.1	30.2	36.3
GBFS 70%	0.35	70	0.52	0.15	24.5	4.5	0.0	34.0	37.1
Paste "carbonated"									
OPC	0.60	0	0.71	0.78	9.8	25.8	0.0	20.7	43.7
OPC	0.45	0	0.63	0.80	15.3	28.0	0.0	21.0	35.6
OPC	0.35	0	0.58	0.56	19.8	21.1	0.0	28.2	30.9
GBFS 50%	0.60	50	0.54	0.79	16.3	18.4	0.0	16.7	48.6
GBFS 70%	0.60	70	0.43	0.80	20.5	14.2	0.0	14.1	51.2
GBFS 50%	0.45	50	0.54	0.79	19.0	21.7	0.0	20.5	38.9
GBFS 70%	0.45	70	0.42	0.80	24.5	16.3	0.0	16.2	43.0
Mortar "carbonated"									
OPC	0.60	0	0.72	0.89	10.8	33.9	0.0	17.5	37.8
OPC	0.45	0	0.64	0.71	16.6	28.4	0.0	24.1	30.9
OPC	0.35	0	0.61	0.53	18.1	20.7	0.0	29.1	32.1
GBFS 50%	0.60	50	0.65	0.66	13.7	20.2	0.0	22.1	44.0
GBFS 70%	0.60	70	0.45	0.72	21.9	14.6	0.0	16.6	46.8
GBFS 50%	0.45	50	0.66	0.70	15.3	24.9	0.0	25.8	34.0
GBFS 70%	0.45	70	0.50	0.74	22.8	18.9	0.0	18.8	39.5
GBFS 50%	0.35	50	0.43	0.74	30.3	20.9	0.0	23.0	25.8
GBFS 70%	0.35	70	0.57	0.44	24.2	16.1	0.0	33.8	25.8
Paste "cycled"									
OPC	0.60	0	0.73	0.40	9.2	13.4	1.2	28.7	47.6
OPC	0.45	0	0.64	0.18	14.6	6.6	4.4	34.1	40.3
OPC	0.35	0	0.62	0.11	17.7	4.4	4.3	37.8	35.8
GBFS 50%	0.60	50	0.66	0.71	11.8	20.0	0.0	21.6	46.6
GBFS 70%	0.60	70	0.55	0.76	15.8	16.9	0.1	17.2	50.1
GBFS 50%	0.45	50	0.60	0.49	16.5	14.7	0.0	27.8	41.0
GBFS 70%	0.45	70	0.50	0.60	20.3	14.2	0.2	24.9	40.4
Mortar "cycled"									
OPC	0.60	0	0.75	0.22	9.9	8.9	3.6	35.2	42.3
OPC	0.45	0	0.61	0.22	17.0	7.9	3.2	33.0	38.8
OPC	0.35	0	0.56	0.12	20.3	4.2	4.5	35.1	35.9
GBFS 50%	0.60	50	0.71	0.44	11.3	15.0	0.0	29.4	44.3
GBFS 70%	0.60	70	0.62	0.65	15.1	18.4	0.0	23.8	42.7
GBFS 50%	0.45	50	0.66	0.19	14.5	6.6	0.3	37.6	40.9
GBFS 70%	0.45	70	0.62	0.25	16.8	7.8	0.0	34.0	41.3
GBFS 50%	0.35	50	0.43	0.14	30.8	3.8	0.1	34.4	30.9
GBFS 70%	0.35	70	0.41	0.16	34.8	4.4	0.0	35.2	25.6

DH = Degree of hydration, DC = Degree of carbonation, V(unhyd) =volume of unhydrated binder
V($CaCO_3$) = volume of carbonates, V(CH) = volume of calcium hydroxide, V(pore) = total porosity

RESULTS OF THE X-RAY DIFFRACTION TEST

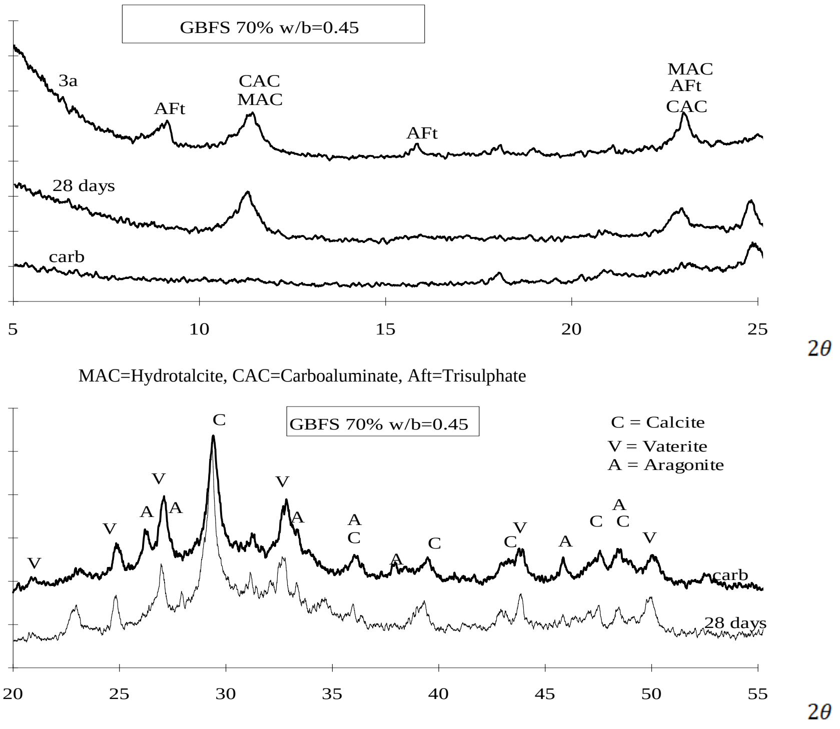

Figure. N1. X-ray patterns for GBFS paste samples with w/b ratios of 0,45.

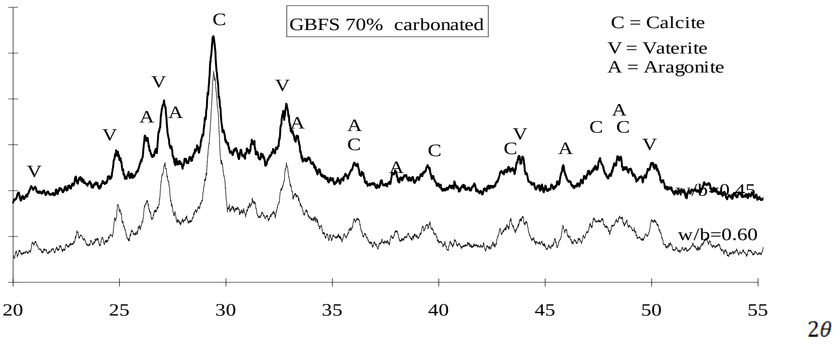

Figure. N2. X-ray patterns for carbonated GBFS paste samples.

APPENDIX N/2

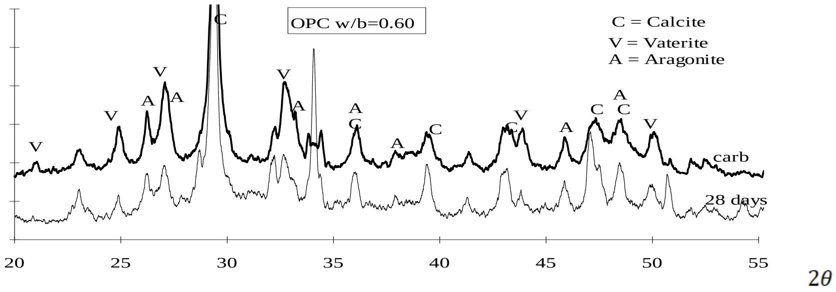
OPC w/b=0.60
C = Calcite
V = Vaterite
A = Aragonite
V
V
A
V
A
C
V
A
A
C
A
C
C
V
A
C
A
C
V
carb
28 days
20
25
30
35
40
45
50
55
2θ

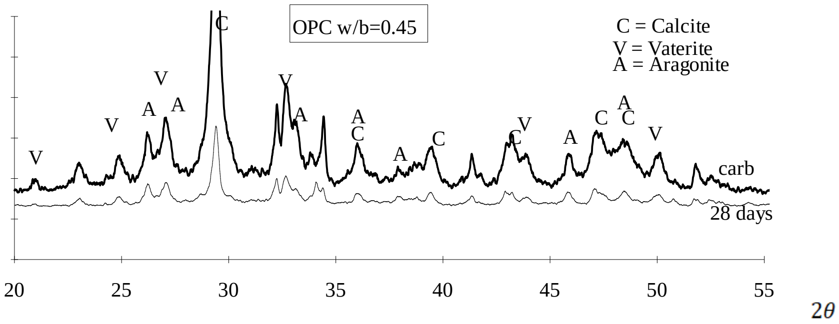
OPC w/b=0.45
C = Calcite
V = Vaterite
A = Aragonite
V
V
A
V
A
C
V
A
A
C
A
C
C
V
A
C
A
C
V
carb
28 days
20
25
30
35
40
45
50
55
2θ

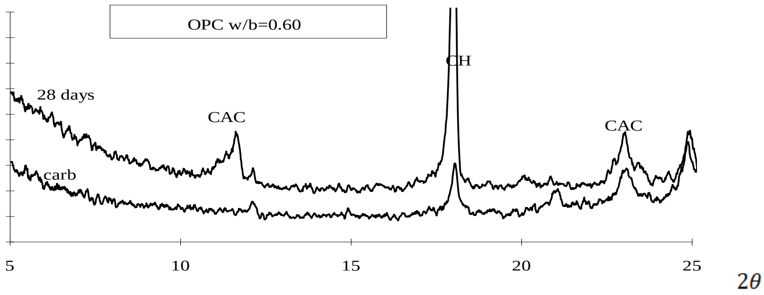
OPC w/b=0.60
28 days
carb
CAC
CH
CAC
5
10
15
20
25
2θ

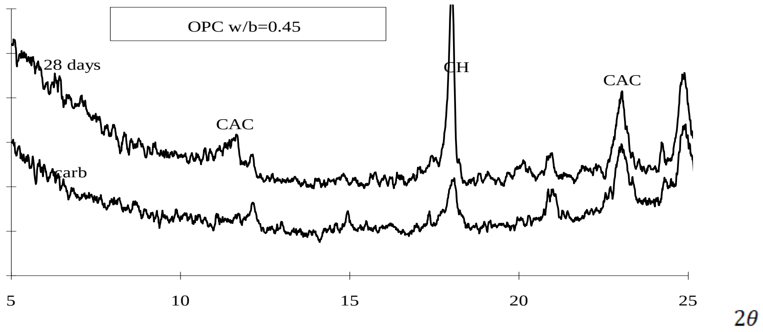
OPC w/b=0.45
28 days
carb
CAC
CH
CAC
5
10
15
20
25
2θ

Figure. N3. X-ray patterns for OPC paste samples with w/b ratios of 0,45.

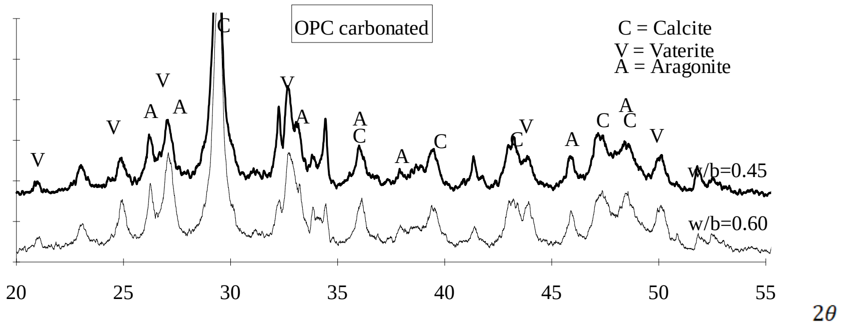

Figure. N4. X-ray patterns for carbonated OPC paste samples.